Marina Filonovich

Faculdade de Ciências e Tecnologia
Universidade Nova de Lisboa

NUMERICAL MODELLING OF COMPOUND CHANNEL FLOW

Dissertação para obtenção do Grau de Doutor em
Engenharia Civil

Orientador: João Gouveia Aparicio Bento Leal
Assistant Professor, FCT/UNL,Portugal
Professor, Universitetet i Adger, Norway

Co-orientador: Luis R. Rojas-Solórzano
Associate Professor
Nazarbayev University, Kazakhstan

Juri:

Presidente: Prof. Fernando Manuel Anjos Henriques

Arguentes: Prof. Rui Miguel Lage Ferreira
Prof. José Manuel Paixão Conde

Vogais: Prof. Mário Jorge Rodrigues Pereira de Franca
Prof. Maria Rita Lacerda Morgado
Fernandes de Carvalho Mesquita David

FACULDADE DE CIÊNCIAS E TECNOLOGIA
UNIVERSIDADE NOVA DE LISBOA

Abril 2015

N^{0} de

Arquivo_____

*Copyright*_____

[Numerical Modelling of Compound Channel Flow]

In memory of my parents

Acknowledgements

I would like to thank both the Civil Engineering Department of the Faculty of Sciences and Technology of New University of Lisbon (FCT/UNL) and the Foundation of Science and Technology (FCT) for providing the necessary resources and financial support through the scholarship SFRH/BD/64337/2009 and through the projects PTDC/ECM/70652/2006, PTDC/ECM/117660/2010 and RECI/ECM-HID/0371/2012 for the duration of this PhD.

There are numerous people that I would like to thank, both academically and socially, for enriching my life over the last four years.

First of all, I would like to express gratitude to my supervisors, Prof. João Gouveia Aparicio Bento Leal and Prof. Luis R. Rojas-Solórzano, for their guidance, enthusiasm and criticism, which allowed all of this to be possible. To both of them, for their great support and encouragement, for sharing with me your wealth of knowledge, for helpful discussions in person and remotely, I give my sincere and heartfelt thanks.

Prof. Rui Ferreira and Prof. Mário Franca deserve a special mention for organising the International Workshops. Thank you for introducing me and having the opportunity to discuss and to have a feedback on my research work from the experts in fluvial hydraulics community and CFD modelling (Koji Shiono, Vladimir Nikora, Thorsten Stoesser, Wim Uijttewaal, Dubravka Pokrajac, to mention a few). Special gratitude to the experts for willing to share with us their invaluable experience. I am also grateful to George Constantinescu and Weiming Wu for their invaluable feedback on my research that took place at Master Class of the River Flow 2012 Congress in Costa Rica; and special thanks to Rafael Murillo, the organiser of the Congress, for making possible for me to attend this Master class.

Special thanks to our Travelling Nerds group (Stephan Spiller, Inés Mera Rico, Helena Nogueira, Ana Margarida Ricardo, Bruño Fraga, Sándor Baranya and Mona Jafarnejad) for spending unforgettable time in Costa Rica. It was a fantastic trip despite the earthquake, heavy rains and tropical virus. This was an adventure that will be remembered forever! Thank you for sharing with me this part of your lives, your Tovarisch!

I would like to express special thanks to my friends Matthew Wilkinson and his lovely wife Elizabete for enriching my social life and my English. Thank you for delightful dinners, barbecues and lots of parties. Matthew, your mushroom risotto and baked goat cheese will be always my favourite dish.

My thanks to Ian Paterson and Katarzyna Wojtyczka for inviting me and my family for the Christmas party, where we had a chance to know and become friends with these amazing and joyful people, Przemek Jankowski, Aleksandra Kawalek and Kenny Walker. Thanks to all of you for the wonderful time that we spent together during these several months. It is not much but it seems like we know each other forever and is so easy and comfortable to chat with you that time just flies (like during the Easter). Special thanks to Kenny for sharing with me the typical Portuguese recipe that most Portuguese people do not know. It was the best Arroz de Pato ever!

My thanks to João Fernandes, Hugo Biscaia and Noel Franco at this difficult final stage for your help, support and understanding. I would also like to thank Ricardo Azevedo for providing me with the experimental data for validating my numerical simulations. To Moises Brito, Silvia Saggiori, Sílvia Rute Amaral, Ricardo Birjukov Canelas, Olga Birjukova Canelas, Edgar Ferreira, Rui Aleixo, Pawel Jerzy Wojcik, Iwona Bernacka-Wojcik many thanks for your help, support and just for sharing with me your experience and friendship.

I would also like to express my appreciation to people from Civil Engineering Department who contributed to the possibility for me joining the academic environment, for providing good conditions for the research, helping and supporting me at various times of my life. In

particularly, I'm grateful to Prof. Manuel A. J. Gonçalves de Silva, Prof. João C. G. Rocha de Almeida, Prof. Fernando M. A. Henriques, Prof. Válter J. G. Lúcio, Prof. António M. Pinho Ramos and all others who not been specifically mentioned here. Special thanks to Carla Teixeira and to Maria da Luz Sousa for being not only good professionals but also good persons willing always to help and to listen.

The last months were not easy for me…being far away from my beloved husband and daughter and finishing the PhD thesis, but I could always count on my friends Andrey Lyubchik and his gorgeous wife Elena Lygina. I'm very grateful to them for helping me with my daily problems in this difficult period of my life, for supporting and understanding.

I would also like to express my deep gratitude to my parents in-law for their encouragement and believing in me. Undoubtely, the completion of this research would not have been possible without their support.

At last but not least I would like to thank my husband Sergej for his love and care, patience, responsibility and understanding. Thank you for being tolerant when I was in a bad mood. You are the best husband and I'm so lucky to have you! Я тебя люблю!

Very special thanks to my daughter Anastacia. When you smile my day becomes brighter and happier. You are my little sunshine. Thank you for being such a wonderful daughter! I love you, my beautiful princess Anastacia!

Abstract

The main objectives of the present study are to evaluate the performance of most common RANS turbulence closure models in simulating river flows, where secondary currents play an important role, and to contribute to the understanding of the relative importance of the underlying physical hypotheses enclosed in each model. Guidelines for CFD users are also proposed, regarding mesh independence and computational domain approach.

For that purpose, ANSYS-CFX package was used allowing the simulation of uniform flows in straight asymmetric trapezoidal and rectangular compound channels with several different RANS turbulence closure models. Namely, isotropic k-ε and shear stress transport (SST) models and anisotropic explicit algebraic Reynolds stress models (EARSM) and Reynolds stress models (RSM). In anisotropic models two approaches were used for the near-wall region, one was the standard k-ε model and the other a modified k-ω model (BSL). Also different pressure-strain rate models were used: LRR-IP, LRR-IQ and SSG.

Verification and validation of the numerical solutions was performed using Grid Convergence Index method together with linear regression analysis. Local mesh refinement of regions of interest improved significantly the convergence of the turbulent field. The comparison of the simulations with existing experimental data showed better agreement for anisotropic models. Nevertheless, some discrepancies were observed and further analysed. The transport terms revealed to be important, which invalidates the hypothesis of negligible anisotropy diffusion implicit in the weak equilibrium condition of EARSM. The anisotropy convection and streamline curvature corrections, established for flow in rotating frames, did not improve the EARSM results. The RSM performs better than EARSM, but still presents problems due to limitations of the near-wall and free-surface modelling, of the adopted transport/diffusion and pressure-strain rate models, and to the isotropic dissipation rate assumption. The two former seem to have a higher impact on the quality of the solution.

Keywords: compound channel, main channel, floodplain, turbulence model, Reynolds stresses, secondary flow.

Resumo

Os objectivos deste estudo foram a avaliação da performance de modelos de turbulência (acoplados às equações RANS) na simulação de escoamentos fluviais com correntes secundárias e contribuir para o conhecimento sobre a validade das hipóteses simplificativas de cada modelo. Propuseram-se ainda procedimentos para utilizadores de CFD relativos à independência da malha e à implementação do domínio de cálculo.

Foi utilizada a aplicação ANSYS-CFX na simulação de escoamentos uniformes em canais rectos com secção composta assimétrica (rectangular e trapezoidal). Usaram-se modelos de turbulência isotrópicos, *k*-ε e shear stress transport (SST), e anisotrópicos, explicit algebraic Reynolds stress models (EARSM) e Reynolds stress models (RSM). Nestes últimos testaram-se duas abordagens para a região da parede, uma baseada no modelo *k*-ε e a outra num modelo *k*-ω modificado (BSL). Testaram-se ainda diferentes modelos para a correlação da pressão com a taxa de deformacão: LRR-IP, LRR-IQ e SSG.

A verificação e validação das soluções numéricas foi efectuada usando o método Grid Convergence Index juntamente com análise de regressão linear. O refinamento local da malha nas regiões de interesse melhorou significativamente a convergência do campo turbulento. A comparação das simulações com dados experimentais existentes mostrou melhores resultados para os modelos anisotrópicos. Nestes, os termos de transporte revelaram-se importantes, invalidando a hipótese de difusão anisotrópica desprezável, implicita no EARSM. As correcções da convecção da anisotropia e da curvatura das linhas de corrente, estabelecidas para escoamentos com rotacão, não melhoraram a qualidade dos resultados do EARSM. O RSM apresenta melhores resultados, mas ainda assim subsistem problemas relacionados com o tratamento das regiões da parede e da superfície livre, com os modelos dos termos de transporte e de correlação da pressão com a taxa de deformação e com a hipótese de taxa de dissipação turbulenta isotrópica. Os dois primeiros parecem ter maior impacto na qualidade da solução.

Palavras-chave: canal de secção composta, leito principal, leito de cheia, modelo de turbulência, tensões de Reynolds, correntes secundárias.

Contents

List of Figures

List of Tables

List of Abbreviations and Symbols

Latin alphabet

Symbol	Description	Units
A	Cross sectional area; coefficient matrix	[m^2]; [-]
A_3'	Coefficient from EARSM	[-]
a_{ij}	Reynolds stress anisotropy tensor	[-]
B	Total channel top width; constant in the logarithmic velocity law	[m]; [-]
B_{fp}	Floodplain width	[m]
B_{mc}	Main channel top width	[m]
b	Main channel half bottom width in symmetric compound channels; main channel bottom width in asymmetric compound channels	[m]; [m]
C	Volume fraction	[-]
C_D	Model constant	[-]
C_{Diff}	Constant from EARSM	[-]
$C_{\varepsilon 1}$, $C_{\varepsilon 2}$, C_{μ},	Empirical constants in the k-ε model	[-]
C_S	Coefficient from the gradient-diffusion model	[-]
C_1, C_2	Rotta constant and constant from LRR-IP and LRR-QI models	[-]
C_1'	Constant from EARSM	[-]
C_{S1}, C_{S2}, C_{r1}, C_{r2}, C_{r3}, C_{r4}, C_{r5}	Constants in the LLR-IP, LLR-QI and SSG models	[-]
e_a^{21}, e_a^{32}	Approximate relative error between meshes 1 and 2, and between meshes 2 and 3, respectively	[-]
F_s	Factor of safety	[-]
F_1	Blending function	[-]
f	Darcy-Weisbach friction factor	[-]
f_1, f_2, f_3	Fine-, medium- and coarse grid solution of the variable of interest obtained with grid spacing h_1, h_2 and h_3, respectively	[]
g	Gravitational acceleration	[m/s^2]

H	Water depth	[m]
h_b	Main channel bankfull height	[m]
h_{fp}	Floodplain water depth	[m]
h_1, h_2, h_3,	grid size of fine-, medium- and coarse grid, respectively	[m]
h_r	Relative depth	[-]
I	turbulence intensity	[-]
k	Turbulence kinetic energy	[m^2/s^2]
L	Length of compound channel; largest length scales (eddy size)	[m]; [m]
l	Turbulence length-scale	[m]
N	Total number of cells of the calculation domain; shorthand notation in the EARSM expression; shape function	[-]; [-]; [-]
Δn_j	Discrete outward surface vector	[-]
P	Wetted perimeter	[m]
P_{ij}	Production term	[m^2/s^3]
p	Instantaneous pressure field; apparent order of accuracy	[Pa]; [-]
Δp	Pressure change	[Pa]
Q	Flow discharge	[m^3/s]
R	Hydraulic radius	[m]
R^2	Correlation coefficient	[-]
R_{ij}	Traceless pressure-strain rate correlation	[m^2/s^3]
r^n	Residual	[-]
Re	Reynolds number	[-]
$RSxx$, $RSyy$, $RSzz$	Normal Reynolds stresses	[N/m^2]
$RSxy$, $RSxz$, $RSyz$	Tangential Reynolds stresses	[N/ m^2]
r_{21} and r_{32}	Refinement factor between fine mesh 1 and medium mesh 2, and between medium mesh 2 and coarse mesh 3, respectively	[-]
S_{ij}	Mean strain-rate tensor normalized with the turbulent time-scale	[-]
S_0	Bed slope	[-]
S_ϕ	Source term	[]
s	Side slope of the channel	[-]

T_{kij}	Reynolds stress flux	[m^3/s^3]
$T_{kij}^{(u')}$, $T_{kij}^{(p')}$, $T_{kij}^{(\nu)}$	Turbulent transport, pressure transport and viscous diffusion	[m^3/s^3]
t	Time	[s]
U_d	Depth-averaged streamwise velocity	[m/s]
u	Instantaneous streamwise velocity	[m/s]
u_*	Friction velocity	[m/s]
$\bar{U}$	Time-averaged streamwise velocity	[m/s]
u'	Streamwise fluctuation velocity	[m/s]
$\overline{u_i' u_j'}$	Reynolds stress tensor	[m^2/s^2]
V_d	depth-averaged spanwise velocity	[m/s]
v	Instantaneous spanwise velocity	[m/s]
$\bar{V}$	Time-averaged spanwise velocity	[m/s]
v'	Spanwise fluctuation velocity	[m/s]
ΔV_i	Volume of the i^{th} cell	[m^3]
W_d	Depth-averaged vertical velocity	[m/s]
w	Instantaneous vertical velocity	[m/s]
$\bar{W}$	Time-averaged vertical velocity	[m/s]
w'	Vertical fluctuation velocity	[m/s]
x	Cartesian coordinate in the streamwise direction; longitudinal distance from inlet	[m]; [m]
y	Cartesian coordinate in the spanwise direction	[m]
z	Cartesian coordinate in the vertical direction	[m]
z^+	Non-dimensional vertical coordinate	[-]
II_S, II_Ω, III, IV, V	Invariants of S_{ij} and Ω_{ij}	[-]

Greek alphabet

Symbol	Description	Units
Φ_1, Φ_2, Φ_3	Empirical coefficients of the Wilcox model, of the transformed k-ε model and of BSL model, respectively	[-]

Γ	Secondary current term	[N/m^2]
Γ_ϕ	Diffusion coefficient	[-]
Π_{ij}	Pressure-strain correlation	[m^2/s^3]
Ω_{ij}	Vorticity tensor normalized with the turbulent time-scale	[-]
α, α_3	Constants from *k*-ω and BSL models, respectively	[-]
β, β', β_3	Constants from *k*-ω and BSL models, respectively	[-]
β_1, …, β_{10}	Coefficients from the Reynolds stress anisotropy tensor	[-]
δ_{ij}	The Kronecker delta	[-]
ε	Dissipation rate of TKE	[m^2/s^3]
ε_{ij}	Dissipation tensor	[m^2/s^3]
ϕ	Any variable of interest	[]
η	Kolmogorov length scale	[m]
κ	Von Kármán constant	[-]
λ	Dimensionless eddy viscosity	[-]
μ	Molecular viscosity	[kg/(ms)]
π	Pi	[-]
ν	Kinematic viscosity	[m^2/s]
ν_t	Eddy viscosity	[m^2/s]
ρ	Density of the fluid	[kg/m^3]
σ_k, σ_ε, σ_ω	Constants (turbulent Schmidt number) from *k*-, ε- and ω-equations	[-]
$\sigma_{\omega 2}$, $\sigma_{\omega 3}$	Constants (turbulent Schmidt number) from BSL model	[-]
τ	Time-scale; shear stress	[s]; [N/m^2]
τ_a	Apparent shear stress	[N/m^2]
ω	Specific dissipation rate or turbulence frequency or turbulence vorticity	[s^{-1}]

Subscripts

Symbol	Description
b	Bed

d	Depth-averaged value
fp	Floodplain
i	Stands for local values in the i^{th} cell or node
ip	Integration point
l	Logarithmic region
max	Maximum
mc	Main channel
min	Minimum
r	Refined
s	Sublayer
t	Turbulent
up	Upwind
w	Wall

Superscripts

Symbol	Description
+	Variable scaled by viscous and velocity scales, ν/ u_* and u_*
′	Fluctuating quantity
-	Time-averaged or global variable
(*eq*)	Equilibrium value
(*h*)	Harmonic
nb	Neighbour
(*r*)	Rapid
(*s*)	Slow

Abbreviations and Acronims

Symbol	Description
ASM	Algebraic stress model

BSL	Menter's baseline k-ω model
CC	Curvature correction/corrected
CFD	Computational fluid dynamics
COHM	Coherence method
DNS	Direct numerical simulation
EARSM	Explicit algebraic Reynolds stress model
FCF	Flood channel facility
FEM	Finite element method
FLT	Fu, Launder and Tselepidakis model
FP	Floodplain
FVM	Finite volume method
GCI	Grid convergence index
HFA	Hot film anemometer
LDA	Laser Doppler anemometry
LDV	Laser Doppler velocimetry
LES	Large eddy simulation
LHS	Left hand side
LRR	Launder-Reece-Rodi pressure-strain rate correlation model
LRR-IP	Isotropization of production model of the LRR
LRR-QI	Quasi-isotropic LRR
MC	Main channel
PBC	Periodic boundary conditions
PISO	Pressure implicit solution by split operator method
PIV	Particle image velocimetry
RANS	Reynolds-averaged Navier Stokes (equations)
RHS	Right hand side
RMS	Root mean square
RSM	Reynolds stress model
SERC	Science and Engineering Research Council
SIMPLE	Semi implicit method for pressure linked equations

SIMPLEC	SIMPLE consistent
SIMPLER	SIMPLE revised
SKM	Shiono and Knight method
SST	Menter’s shear-stress transport model
SSG	Speziale-Sarkar-Gatski pressure-strain rate correlation model
TKE	Turbulence kinetic energy
VOF	Volume of fluid
WDCM	Weighted divided channel method
1D, 2D, 3D	One-, two- and three-dimensional

CHAPTER 1

INTRODUCTION

Contents

1 INTRODUCTION

1.1 BACKGROUND AND MOTIVION

Rivers are the arteries of the Earth, and they are of enormous importance. Although they contain only about 0.0001% of the total amount of water in the world, the rivers drain nearly 75% of the earth's land surface to the sea (Hebert and Ontario 2013).

Since the ancient times the rivers have attracted people. Rivers have been used as a source of drinking water, as a source of food and building materials (sand and gravel) and for transportation. It is therefore no surprise that the river banks, also called floodplains, have attracted the ancients to establish their settlements there. These settlements have become big cities. Nowadays, most of the major cities of the world are situated on the banks of the rivers.

Floods are one of the most frequent natural hazards and occur in almost every country in the world. They account for about a third of all natural disasters (*i.e*. floods, earthquakes or storms) world-wild, but are responsible for over half the deaths (Berz 2000). The floods are generally considered among the deadliest natural disasters ever recorded, and almost certainly the deadliest of the 20th century (*cf*. Table 1.1).

In the period from 1998 to 2009 floods and storms were considered the most costly hazards (EEA). From the Table 1.2 it is evident that the floods caused the highest economic losses over the past decades. This is an outcome from the increase of population and the growth of assets on the river floodplains.

Table 1.1: Top 10 important flood disasters for the period 1900 to 2014. (Source: EM-DAT: The OFDA/CRED International Disaster Database, Universite catholique de Louvain, Brussels, Belgium)

	Country	***Date***	***Nº killed***
1	China	July 1931	3,700,000
2	China	July 1959	2,000,000
3	China	July 1939	500,000
4	China	1935	142,000
5	China	1911	100,000
6	China	July 1949	57,000
7	Guatemala	October 1949	40,000
8	China	August 1954	30,000
9	Venezuela	15 of December 1999	30,000
10	Bangladesh	July 1974	28,700

Table 1.2: The most devastating flood disasters. Top 10 at economic losses for the period 1900 to 2014. (Source: EM-DAT: The OFDA/CRED International Disaster Database, Universite catholique de Louvain, Brussels, Belgium)

	Country	***Date***	***Damage* (000 US$)**
1	Tailand	05 / 08 / 2011	40,000,000
2	China	01 / 07 / 1998	30,000,000
3	China	29 / 05 / 2010	18,000,000
4	North Korea	01 / 08 / 1995	15,000,000
5	Germany	28 / 05 / 2013	12,900,000
6	China	30 / 06 / 1996	12,600,000
7	USA	24 / 06 / 1993	12,000,000
8	Germany	11 / 08 / 2002	11,600,000
9	USA	09 / 06 / 2008	10,000,000
10	Pakistan	28 / 07 / 2010	9,500,000

At present it is not possible to prevent flood disasters, thus a comprehensive understanding of the flood phenomenon has to be considered. Thus, in 1986 the Science and Engineering Research Council (SERC) and Hydraulics Research Ltd (HR) have constructed the Flood Channel Facility (FCF) to provide a database for validating the numerical models and to enable engineers to understand the hydraulic processes involved in river flooding. Most floods originate a so-called compound channel flow, where the flow is deeper and faster in a main channel (inbank flow) and shallower and slower in lateral floodplains (overbank flow).

The European Commission adopted the Directive 2007/60/EC that aims to reduce and manage the risks that floods pose to human health, the environment, cultural heritage and economic activity. The directive applies to all types of floods and will be implemented with a preliminary assessment of the river basin's flood risk, as well as associated coastal zones and then followed by the development of flood hazard maps and flood risk maps by 2013 (European Environmental Agency 2010).

Predicting the discharges and maximum water levels is a challenge for engineers in flood modelling. The fundamental link between discharge and water level is important, since flood risk maps should give and accurate estimate of water levels and possible inundation areas (Knight 2013). Determining the stage-discharge relationship for channels with complex cross-section, like compound channel, is not a simple matter (Knight and Shamseldin 2006; Knight *et al*. 2010). For reliable predictions of stage-discharge relationships, the modeller needs adequate turbulence data and complete understanding of the flow behaviour.

Practitioners, in general, still use 1D models for assessing flow conditions in real rivers setups, where a roughness coefficient accounts for all 3D effects (Morvan *et al*. 2008), making it case sensitive and implicitly increasing modelling uncertainty. Recently, 2D (streamwise and lateral directions) models are being used more often. They explicitly can account for significant variations in the cross-section shape and area, which includes floodplain flow and meandering channels (Wright 2001). Despite that, the roughness coefficients still bear some uncertainty, since they have to account for all the vertical processes that are not modelled (Morvan *et al*. 2008). These can be relevant when secondary flow (*i.e*. flow circulations transverse to the main downstream flow direction also known as helical flow) is important, like the ones occurring in channel bends, floodplain/channel interactions and to a lesser extent in straight channels (Wright 2001).

Although, the use of 3D models in real river configurations is still rare, both the increase of computational capacity and the need for more physically based predictions will push forward their use in the near future. Moreover, 3D models provide more reliable estimates of bed shear stress and other more useful information, such as the three-dimensional flow field important for mixing processes (*cf*. Lane *et al*. 1999). In this context, the use of CFD commercial codes seems more probable to occur, rather than the use of research codes developed in the academia. Mainly, because the former are user-friendly and incorporate most of the turbulence closure models, starting from the simplest one- or two-equation models to a more advanced large eddy simulation (LES). It is important to notice that the majority of commercial codes stemmed from aerodynamics industrial applications. They often present additional shortcomings, like "hidden" default strategies (Knight 2013), using default values for the empirical coefficients that sometimes cannot be changed. Nevertheless, commercial models have demonstrated their ability in simulating laboratory open-channel flows, giving results in good agreement with the experiments (Morvan *et al*. 2002, Morvan 2005). Even so, their validation within river flow configurations is still far to be considered fully accomplished.

Even if a CFD commercial package is available, the user will have to face a critical choice about the model that should be used. The choice is usually a compromise between the accuracy of the results and the computational time required. At present, the use of LES and Direct Numerical Simulation, DNS (this one is not usually available in commercial packages), can be discarded, due to the large quantity of data to manage and to the exceptionally high computational time required. This leaves as viable alternatives the models based on Reynolds Averaged Navier-Stokes (RANS) equations coupled with a turbulence closure model. Within this "family" of models, one can choose from less demanding one- or two-equation models to the more demanding models based on Reynolds stress transport equations.

In the context of river flow modelling, and more precisely of compound-channel flow, it is important to assess which model will have the best binomial accuracy *vs*. computational time.

1.2 OBJECTIVES AND METHODOLOGY

The main objectives of the present study are:

i) to provide users of commercial CFD packages modelling guidelines regarding mesh resolution and computational domain modelling approach;
ii) to provide users of commercial CFD packages a clear picture of the performance of most common RANS turbulence closure models in simulating river flows with non-negligible secondary currents;
iii) to contribute to the understanding of the relative importance of the underlying physical hypotheses implicitly enclosed in each model in the prediction of secondary flows.

To achieve these objectives 3D simulations of laboratorial compound channel flows, where turbulence data was available (Tominaga and Nezu 1991 and Azevedo *et al*. 2012), were performed using the commercial package ANSYS-CFX. The simulated experiments correspond to asymmetric compound channel configurations with high flow stages (relative depth, defined as the relation between the flow depth in the floodplain and the one in the main channel, equal to 0.5), since this configuration is known to produce strong secondary flow (*e.g*. Nezu 1994).

Since the main focus was on accuracy *vs*. computational time required for different turbulence closure models, it was decided to start with the less time demanding, and most used, k-ε model and then continue with the use of more complex and time demanding turbulence closure models. At the end, six different turbulence models were used, which are, in increasing order of complexity (details on each model can be consulted in Chapter 2): k-ε model; shear stress transport model (SST) that uses a mixture of both k-ε and k-ω models; explicit algebraic Reynolds stress model coupled with an ε-equation and LRR-IP pressure-strain rate correlation model (EARSM); explicit algebraic Reynolds stress model coupled with a modified ω-equation and LRR-QI pressure-strain rate correlation model (BSL EARSM); Reynolds stress model coupled with an ε-equation and SSG pressure-strain rate correlation model (SSG RSM), and Reynolds stress model coupled with a modified ω-equation and LRR-QI pressure-strain rate correlation model (BSL RSM).

The choice of using more complex turbulent models was based on the comparison of less complex models and on the physical interpretation of the main discrepancies. The latter were evaluated by comparison of experimental data and also by performing a budget analysis of

transport equations, identifying the relevant terms. Some corrections available in the CFD package, mostly developed for air flows, where tested and evaluated, namely the ones regarding the EARSM.

In terms of computational domain it was decided to start by modelling the entire experimental flume, specifying the exact laboratorial inlet and outlet conditions, and to use a two fluid (water + air) domain, avoiding the specification of free-surface boundary conditions. With the increase of turbulence model complexity it was necessary, due to computational time constrains, to adopt a smaller computational domain. This was accomplished by using a single phase fluid (water), being the free-surface modelled as a rigid lid with free slip conditions (see Chapter 3 for details). Also periodic boundary conditions were imposed at the inlet and outlet, allowing to shorten the length of the computational domain.

For reaching solid conclusions on the accuracy of each model and comparing different simulations it was also necessary to establish verification and validation criteria for the latter, ensuring that the turbulent velocity field was converged. For that purpose several meshes were used, starting with a coarser one and refining it locally, in the regions of interest (*i.e.* bottom, walls, free-surface and interface between main channel and floodplain), until reaching an acceptable convergence of the turbulent field.

1.3 THESIS OUTLINE

The present work is divided into six chapters and two appendixes. Since the results originated a sum of papers with self-contained introductions and references, and independent pagination, notation and text style, it was decided to present them in Appendix A as the original published papers.

Chapter 1 introduces the reader to the studied topic, giving a background that motivated this study, stating the main objectives and a brief description of the methodology used to accomplish them, and presenting the outline of the thesis.

In Chapter 2 a brief review of the governing equations and turbulence closure models is presented together with some problems and limitations in turbulence modelling. This chapter allows readers not familiar with turbulence closures models to have an overview of the main characteristics of the models used in the thesis.

Chapter 3 aims to introduce the reader to the computational fluid dynamics (CFD), structure of the CFD package, the algorithms and numerical techniques used in this study. This chapter also presents the definitions of errors and uncertainties in CFD models.

Chapter 4 encloses some significant contributions concerning numerical modelling of the inbank flow in straight rectangular and trapezoidal open channels, and then the main aspects on numerical modelling of rectangular and trapezoidal compound channel flows are briefly summarised. This chapter aims to give the reader a picture of the turbulent field in compound channel flows and the different numerical approaches used previously by other authors in their simulations.

Chapter 5 summarizes the results of each individual research paper, allowing the reader to have an overall view of the link between research papers and its sequence.

Chapter 6 resumes the main conclusions and findings of this thesis and suggests topics for further research.

As stated before Appendix A contains the original research papers. Four papers are presented, one was published in an international scientific journal (Research Paper I), two were published in the proceeding of international scientific conferences (Research Papers II and III), and one submitted to an international scientific journal (Research Paper IV). Appendix B presents some additional results concerning the use of VOF technique for free-surface modelling, demonstrating that the adopted modelling approach is adequate.

1.4 REFERENCES

Azevedo, R., Rojas-Solórzano, L. R. and Leal, J. B. 2012 Experimental characterization of straight compound-channel turbulent field. In *Proc. of 2nd European IAHR Congress*. 27-29 June, Munich, Germany.

Berz, G. 2000 Flood disasters: Lessons from the past – worries for the future. *Proc. Inst. Civil Eng. Water and Maritime Engineering*, London **142** (1), 3-8.

Directive 2007/60/EC of the European Parliament and of the Council of 23 October 2007 on the assessment and management of flood risks (Text with EEA relevance).

European Environmental Agency 2010 *Mapping the impacts of natural hazards and technological accidents in Europe. An overview of the last decade*. Technical report ISSN 1725-2237, **13**, 1-144.

European Environmental Agency *Disasters in Europe: more frequent and causing more damage* (http://www.eea.europa.eu/highlights/natural-hazards-and-technological-accidents)

Hebert, P. and Ontario, B. 2013 River. Retrieved from http://www.eoearth.org/view/article/155760

Knight, D. W. 2013 River hydraulics – a view from midstream. *Journal of Hydraulic Research* **51** (1), 2-18.

Knight, D. W. and Shamseldin, A. 2006 *River basin modelling for flood risk mitigation*. Taylor & Francis, Leiden.

Knight, D. W., Tang, X., Sterling, M., Shiono, K. and McGahey, C. 2010 Solving open channel flow problems with a simple lateral distribution model. In River Flow 2010, *Proc. Int. Conf. on Fluvial Hydraulics*, 41-48, A. Dittrich, K. Koll, J. Aberle, P. Geisenhainer, eds. Braunschweig.

Lane, S. N., Bradbrook, K. F., Richards, K. S., Biron, P. A. and Roy, A. G. 1999 The application of computational fluid dynamics to natural river channels: three-dimensional versus two-dimensional approaches. *Geomorphology* **29** (1), 1-20.

Morvan, H. P. 2005 Channel shape and turbulence issues in flood flow hydraulics. *Journal of Hydraulic Engineering*, **131** (10), 862-865.

Morvan, H., Knight, D., Wright, N., Tang, X. and Crossley, A. 2008 The concept of roughness in fluvial hydraulics and its formulation in 1D, 2D and 3D numerical simulation models. *Journal of Hydraulic Research* **46** (2), 191-208.

Morvan, H. P., Pender, G., Wright, N.G. and Ervine, D. A. 2002 Three-dimensional hydrodynamics of meandering compound channels. *Journal of Hydraulic Engineering* **128** (7), 674-682.

Nezu, I. 1994 Compound open-channel turbulence and its role in river environment. *Keynote Address of 9th APD-IAHR Congress*, Delft, The Netherlands, 1-24.

Tominaga, A. and Nezu, I. 1991 Turbulent structure in compound open-channel flows. *Journal of Hydraulic Engineering* **117** (1), 21-40.

Wright, N. G. 2001 *Conveyance implications for 2D and 3D modelling*. Specialist Review for Scoping Study for Reducing Uncertainty in River Flood Conveyance, R & D Technical Report by HR Wallingford to DEFRA/Environment Agency.

CHAPTER 2

BASIC CONCEPTS IN TURBULENCE MODELLING

Contents

2 BASIC CONCEPTS IN TURBULENCE MODELLING

2.1 INTRODUCTION

In this chapter a brief review of the governing equations valid for constant-property (*e.g.* density and viscosity) Newtonian fluids and isothermal flows under a constant gravitational field are presented. A detailed review of several turbulence models used to closure the Reynolds Averaged Navier-Stokes (RANS) equations is also presented, focusing on the main assumed hypotheses that can have impact on the numerical results.

Equations in the following Subchapters use Cartesian index notation, where $i = 1$ is for x - direction (along the flow) and streamwise velocity component u, $i = 2$ is for y - direction (across the flow) and transversal velocity component v, and $i = 3$ is for z (orthogonal to the fluid bed) and vertical velocity component w.

2.2 GOVERNING EQUATIONS AND REYNOLDS AVERAGING

The basic system of governing equations for incompressible fluid flows is based on the conservation laws of physics:

- conservation of mass (*i.e.* continuity equation),
- conservation of momentum (Newton's second law).

The mass-conservation or continuity equation for an incompressible fluid can be written as (*e.g.* Pope 2000):

$$\operatorname{div}\mathbf{u} = \frac{\partial u}{\partial x} + \frac{\partial v}{\partial y} + \frac{\partial w}{\partial z} = 0 \ \text{ or } \frac{\partial u_i}{\partial x_i} = 0 \tag{2.1}$$

The second equation, conservation of momentum, states that the rate of change of momentum equals the sum of the forces on a fluid element. For a constant-property (*e.g.* density and viscosity) Newtonian fluid and isothermal flow under a constant gravitational field can be written (*e.g.* Pope 2000):

$$\frac{\partial u_i}{\partial t} + u_j \frac{\partial u_i}{\partial x_j} = -\frac{1}{\rho}\frac{\partial p}{\partial x_i} + \frac{\partial}{\partial x_j}\left(\nu \frac{\partial u_i}{\partial x_j}\right) + f_i \tag{2.2}$$

where p is instantaneous pressure field, ρ is the fluid density, ν is the fluid kinematic viscosity and f_i are body forces. Equations (2.2) are known as Navier-Stokes equations for constant-property Newtonian fluids.

Equations (2.2) completely describe the laminar-turbulent field and may, in principle, be solved directly in so called direct numerical simulation (DNS). However, the numerical solution is extremely difficult, since the significantly different length and time scales in a turbulent field need to be resolved, and thus the stable solution requires such a fine mesh resolution that the computational effort grows rapidly with increasing Reynolds number. Thus, practically in most turbulent flows the flow-field variables are decomposed into the mean and fluctuating parts. This process is known as the Reynolds decomposition and can be expressed as:

$$u_i = \overline{U_i} + u_i' \tag{2.3}$$

where u_i is the instantaneous velocity component, u_i' is the fluctuating part for which $\overline{u_i'} = 0$ and $\overline{U_i}$ is the mean velocity. Note that this mean value should be obtained from classic statistics knowing the probability density function of the random variable (velocity field). However, a very common approach, also adopted here, is to consider that the flow is statistically stationary (*i.e.* all statistics are invariant under a shift in time). This allows estimating the statistical mean by performing a time-average (over a time interval). For statistically stationary flows, the time-averaged value tends to the statistical mean value as the used time interval tends to infinity (*e.g.* Pope 2000).

Substituting the decomposition (2.3) for velocity and pressure into the continuity and momentum equations (Eqs. (2.1) and (2.2)), and then by averaging all the terms in the equations and taking into account that $\overline{u_i'} = 0$ and $\overline{\overline{U_i}} = \overline{U_i}$, the Reynolds averaged Navier-Stokes equations (RANS) for constant-property Newtonian fluids are obtained (*e.g.* Pope 2000):

$$\frac{\partial U_i}{\partial x_i} = 0 \tag{2.4}$$

$$\frac{\partial U_i}{\partial t} + U_j \frac{\partial U_i}{\partial x_j} = -\frac{1}{\rho}\frac{\partial P}{\partial x_i} + \frac{\partial}{\partial x_j}\left(\nu \frac{\partial U_i}{\partial x_j}\right) - \frac{\partial \overline{u_i' u_j'}}{\partial x_j} \tag{2.5}$$

For brevity, the overbars indicating the averaged values are dropped from U_i and P from here on. The last term in equation (2.5) is new compared to equation (2.2). An extra term in equation (2.5), $-\overline{u_i' u_j'}$, is the fluctuating contribution to the nonlinear convective acceleration term in the momentum equation (2.2), also called the apparent stress arising from the fluctuating velocity field (Pope 2000). This apparent stress tensor is $-\overline{u_i' u_j'}$ which statistically represents the

correlation matrix between fluctuating components of the velocity field, is also denominated the Reynolds stress tensor.

2.3 PROBLEMS AND LIMITATIONS IN TURBULENCE MODELLING

Turbulence can either be resolved or modelled. Resolving implies proper solution of the governing equations (at all scales) with no modelling or empirical assumptions. Modelling implies a solution that uses some degree of approximation and empiricism.

There are three levels of resolving turbulence: fully resolved, partially resolved, and unresolved. Direct Numerical Simulation (DNS) is one technique that attempts to fully resolve turbulent flow by solving the Navier-Stokes equations at all length and time scales. In DNS turbulence or empirical models are not required.

The ample variation in length and time scales is an important characteristic of turbulent flows which is in part responsible for the difficulty encountered in the numerical and theoretical analysis of turbulent flows. The largest length scales (eddy sizes), given by *L*, in the flow account for most of the transport of momentum and energy. The size of these eddies is constrained by the physical boundaries of the flow. Thus, for compound channel flow the largest eddies can have the size of the channel width.

Kinetic energy from large eddies is transferred to the smaller eddies during the cascading process until it is dissipated into heat (Pope 2000). As we approach smaller and smaller length scales, the viscous effects become more important. Thus, the size of the smallest eddies, η, at which this energy is dissipated depends on the dissipation rate, ε, and viscosity, ν, and is defined as:

$$\eta = \left(\frac{\nu^3}{\varepsilon} \right)^{1/4} \tag{2.6}$$

This length scale is called the Kolmogorov length scale and it characterizes the smallest dissipative eddies. Therefore, it corresponds to the smallest length scale needed to properly resolve turbulent flow.

The time scale, τ, of the smallest eddies is:

$$\tau = \left(\frac{\nu}{\varepsilon} \right)^{1/2} \tag{2.7}$$

The ratio of largest to smallest length scales and time scales in the flow is proportional to the Reynolds number raised to the 3/4 and 1/2 power, respectively. For example, in a flow with a

Reynolds number of 10^5, the ratio L/η is proportional to $10^{15/4}$. Thus, to resolve the entire range of length scales in 3D turbulent flow, we would need a computational domain that consists of at least 10^{10} grid points. The amount of information resulting from such simulation would exceed the capacity of any existing computer. This becomes even clearer when the unsteady, transient nature of turbulence is considered. Thus, the problem with DNS is that it consumes enormous computational resources since the grid resolution must be on the order of the Kolmogorov scales as indicated in previous paragraphs. Currently, DNS is a research tool and is only feasible for simple flows at lower Reynolds numbers (Kim *et al*. 1987).

Large Eddy Simulation (LES) attempts to partially resolve turbulence. The fundamental idea is that the small scales of turbulence (close to the Kolmogorov scales) can be modelled by a subgrid model, while the larger scales are resolved by the governing equations. Grid resolution is on the order of the turbulent scale that wants to be solved, thus in LES the computational demands are considerably smaller than in DNS. The LES has become more and more popular and shows good results when compared to experimental data (*e.g*. Thomas and Williams 1995, Cater and Williams 2008, Stoesser 2010, Kara *et al*. 2012). Nevertheless, its application to real setups is still impractical, due to the exceptionally high computational effort required.

The most practical and still the most popular method of dealing with turbulence is that based on RANS equations. Only mean flow quantities are resolved. In the RANS method, all scales of turbulence are modelled; grid resolution is in the order of the mean flow scale - not a turbulent scale. This offers huge computational savings when compared to both DNS and LES. The complexity of RANS models ranges from purely algebraic or zero-equation models to a more complex Reynolds stress models.

Reynolds stresses appearing in RANS have to be related to the mean motion itself before the equations can be solved, since the number of unknowns and number of equations must be equal.

From equations (2.4) and (2.5) we have 10 unknowns (P, U_1, U_2, U_3, and six Reynolds stresses $\overline{u_i' u_j'}$) and only 4 equations, which configures an unclosed mathematical problem. The absence of these additional equations is often referred to the turbulence closure problem. To close these equations, *i.e*. have the same number of equations and unknowns, extra equations are introduced through the different turbulence models, which will be described in the next subchapters.

2.4 EDDY VISCOSITY MODELS

In this subchapter the so-called eddy viscosity turbulence models are briefly discussed. The models can be divided in three categories; zero-, one- and two-equation models. These models use the Boussinesq eddy viscosity concept (Boussinesq 1877). In analogy to viscous stresses in

laminar flow, the turbulent stresses are assumed to be proportional to the mean velocity gradients (*e.g.* Nezu and Nakagawa 1993). The Reynolds stress tensor is then related to the mean flow field through:

$$-\overline{u_i' u_j'} = \nu_t \left(\frac{\partial U_i}{\partial x_j} + \frac{\partial U_j}{\partial x_i} \right) - \frac{2}{3} k \delta_{ij} \tag{2.8}$$

where v_t is the eddy viscosity; δ_{ij} is the Kronecker delta ($\delta_{ij} = 1$ for $i = j$; and $\delta_{ij} = 0$ for $i \neq j$); and k is the turbulence kinetic energy, defined as $k = \overline{u_i' u_i'}/2$.

As will be shown in later subchapters, the primary goal of many turbulence models is to find some estimation for the eddy viscosity to model the Reynolds stresses. These may range from the relatively simple algebraic models, to the more complex models such as the k-ε model, where two additional transport equations are solved in addition to the mean flow equations. Here only two-equation models will be presented (more details of zero- or one-equation models can be found in standard books like Rodi (1993), Pope (2000) or Wilcox (2006).

The two-equation models are the simplest complete models, since these models provide independent transport equations for both variables, the turbulence kinetic energy and the turbulence length scale, or some equivalent parameter.

Kolmogorov (1942) and Prandtl (1945) suggested determining the distribution of k by solving a model transport equation for this quantity, which can be obtained by introducing the Reynolds decomposition in the Navier-Stokes equations, multiplying by the velocity and taking time-average of the resulting equation (*e.g.* Pope 2000). The resulting transport equation for k can be written as:

$$\underbrace{\frac{\partial k}{\partial t}}_{\substack{\text{Rate of} \\ \text{change} \\ \text{of } k}} + \underbrace{U_i \frac{\partial k}{\partial x_i}}_{\substack{\text{Convective} \\ \text{transport} \\ \text{of } k}} = \underbrace{-\frac{\partial}{\partial x_i} \left[\overline{u_i' \left(\frac{u_j' u_j'}{2} + \frac{p'}{\rho} \right)} \right]}_{\text{Turbulent transport of } k} - \underbrace{\overline{u_i' u_j'} \frac{\partial U_i}{\partial x_j}}_{\substack{P = \text{turbulence} \\ \text{production}}} - \underbrace{\nu \overline{\frac{\partial u_i'}{\partial x_j} \frac{\partial u_i'}{\partial x_j}}}_{\substack{\varepsilon = \text{rate of} \\ \text{dissipation} \\ \text{of } k}} \tag{2.9}$$

Equation (2.9) is the exact k-equation and is of no use in the turbulence model since new unknown correlations appear in the turbulent transport and dissipation terms. To obtain a closed set of equations, model assumptions must be introduced for these terms. Thus, turbulent transport term is often modelled with a gradient-diffusion concept (2.10). The reader should keep in mind that gradient-diffusion hypothesis is applicable to high Reynolds number flows and is not valid in certain flow regions, such as the viscous sublayer near walls.

Assuming that the turbulent transport of k is proportional to the gradient of k (Rodi 1993):

$$-\overline{u_i'\left(\frac{u_j'u_j'}{2}+\frac{p'}{\rho}\right)}=\frac{\nu_t}{\sigma_k}\frac{\partial k}{\partial x_i} \tag{2.10}$$

where σ_k is the turbulent Schmidt number that does not have a universal value and empirical values have been used in different studies in the range of 0.2 - 1.3 (Tominaga and Stathopoulos 2007). The selected value of σ_k has a significant effect on the prediction of the results. Thus, Tominaga and Stathopoulos (2007) recommended that σ_k should be determined by considering the dominant flow structures for each case. However, σ_k generally takes value around 1.0 (*e.g.* Nezu and Nakagawa 1993, Pope 2000, Rodi 1993).

Taking into account the above mentioned assumptions in (2.8) and (2.10), equation (2.9) reads:

$$\underbrace{\frac{\partial k}{\partial t}}_{\substack{\text{Rate of}\\ \text{change}\\ \text{of } k}}+\underbrace{U_i\frac{\partial k}{\partial x_i}}_{\substack{\text{Transport}\\ \text{of } k \text{ by}\\ \text{convection}}}=\underbrace{\frac{\partial}{\partial x_i}\left(\frac{\nu_t}{\sigma_k}\frac{\partial k}{\partial x_i}\right)}_{\substack{\text{Turbulent transport}\\ \text{of } k}}+\underbrace{\nu_t\left(\frac{\partial U_i}{\partial x_j}+\frac{\partial U_j}{\partial x_i}\right)\frac{\partial U_i}{\partial x_j}}_{\substack{P=\text{turbulence}\\ \text{production}}}-\underbrace{\varepsilon}_{\substack{\text{rate of}\\ \text{dissipation}\\ \text{of } k}} \tag{2.11}$$

The choice of the second variable in two-equation models is arbitrary and many proposals have been presented. Thus, Davidov (1961), Harlow and Nakayama (1968) and Jones and Launder (1972) suggested an equation for the dissipation rate $\varepsilon = k^{3/2}/l$, being l a turbulence length-scale; Rotta (1951) proposed an equation for kl; Kolmogorov (1942) an equation for the turbulence frequency $\omega = k^{1/2}/l$; Saffman (1970) an equation for turbulence vorticity $\omega^2 = k/l^2$ and Speziale *et al*. (1992) an equation for the turbulent time-scale $\tau = l/k^{1/2}$. Two of the most popular dependent variables for the second variable have been the dissipation rate ε and the specific dissipation rate ω. These models will be discussed in more details since they have been applied to calculate compound channel flow in this study (see Research Paper II).

The k-ε model is the best-known two-equation turbulence model and is incorporated in most commercial CFD codes. The most used formulation of the k-ε model, referred as the "standard" k-ε model, is of Jones and Launder (1972). Those authors proposed the following transport equation for the dissipation rate:

$$\underbrace{\frac{\partial \varepsilon}{\partial t}}_{\substack{\text{Rate of}\\ \text{change}\\ \text{of } \varepsilon}}+\underbrace{U_i\frac{\partial \varepsilon}{\partial x_i}}_{\substack{\text{Transport}\\ \text{of } \varepsilon \text{ by}\\ \text{convection}}}=\underbrace{\frac{\varepsilon}{k}\left(C_{\varepsilon 1}P-C_{\varepsilon 2}\varepsilon\right)}_{\substack{\text{Production and dissipation}\\ \text{rate of } \varepsilon}}+\underbrace{\frac{\partial}{\partial x_i}\left(\frac{\nu_t}{\sigma_\varepsilon}\frac{\partial \varepsilon}{\partial x_i}\right)}_{\substack{\text{Turbulent transport}\\ \text{of } \varepsilon}} \tag{2.12}$$

where the eddy viscosity used in the model is specified as:

$$\nu_t = C_\mu k^2 / \varepsilon \tag{2.13}$$

It should be referred that equation (2.12) is not the exact transport equation for ε, but rather an entirely empirical equation that can account better for the fact that ε is determined by the large-scale motions (energy cascade) instead of motions in the dissipative range (*cf*. Pope 2000).

The *k*-ε model involves the five empirical constants C_μ, $C_{\varepsilon 1}$, $C_{\varepsilon 2}$, σ_k and σ_ε. Their standard values for open-channel flows are presented in the Table 2.1. The choice of these constants is based on the compatibility of the model to the logarithmic velocity distribution near the wall in channel flows with Von Kármán constant $\kappa = 0.41$ (Nezu and Nakagawa 1993).

In open-channel flows, vertical fluctuations, *w*′, are damped by the free-surface, which results in ν_t approaching to zero near the free-surface (Nezu and Nakagawa 1993). This surface damping can be accounted for in the *k*-ε model by decreasing C_μ near the free-surface by means of damping functions, or surface-proximity function (Celik and Rodi 1984).

Table 2.1: Values of the constants in the *k*-ε model for open-channel flows (Nezu and Nakagawa 1993)

C_μ	$C_{\varepsilon 1}$	$C_{\varepsilon 2}$	σ_k	σ_ε
0.09	1.44	1.92	1.2	1.2

Another popular two-equation model is the *k*–ω model (being the turbulence frequency $\omega = \varepsilon/k$), which will be presented here in the form given by Wilcox (1988). The *k*-ω model solves the *k*-transport equation (2.11) and a transport equation for ω, instead of the ε-equation (2.12). The *k*-transport equation, re-written replacing $\varepsilon = k\omega$, and the transport equation for ω can be written (Wilcox 1988):

$$\frac{\partial k}{\partial t} + U_i \frac{\partial k}{\partial x_i} = \frac{\partial}{\partial x_i}\left(\frac{\nu_t}{\sigma_k} \frac{\partial k}{\partial x_i} \right) + P - \beta' k\omega \tag{2.14}$$

$$\frac{\partial \omega}{\partial t} + U_i \frac{\partial k}{\partial x_i} = \frac{\partial}{\partial x_i}\left(\frac{\nu_t}{\sigma_\omega} \frac{\partial k}{\partial x_i} \right) + \alpha \frac{\omega}{k} P - \beta \omega^2 \tag{2.15}$$

and the eddy viscosity is given:

$$\nu_t = k/\omega \tag{2.16}$$

The *k*-ω model involves five empirical constants β*'*, β, α, σ_k and σ_ω. Their standard values are presented in Table 2.2.

Table 2.2: Values of the constants in the *k*- ω model (Wilcox 1988).

β'	β	α	σ_k	σ_ω
0.09	0.075	5/9	2	2

Another two-equation model was proposed by Menter (1994), which combines the best behaviour of the *k*-ε and *k*-ω models (*k*-ω performs better near the wall region and *k*-ε performs better in the fully turbulent region). This model is implemented into ANSYS CFX and it is known as the Baseline (BSL) *k*-ω model. This model will be discussed here in more details, since it was used for the calculations in the present study (Research Papers III and IV).

The BSL model proposed by Menter (1994) suggested a hybrid model using a transformation of the *k*-ε model into *k*-ω model in the near-wall region and the standard *k*-ε model in the fully turbulent region far from the wall. Thus, Wilcox model (Eq. (2.14)) is multiplied by a "blending function" F_1 and the transformed *k*-ε model by a function (1-F_1). Close to the walls the blending function F_1 is equal to one (leading to a standard ω- equation) and decreases to a value of zero outside the boundary layer (corresponding to the standard ε- equation). The blending functions are used to achieve a smooth transition between the two models, yielding to the BSL model:

$$\frac{\partial \omega}{\partial t} + U_i \frac{\partial k}{\partial x_i} = \frac{\partial}{\partial x_i}\left(\frac{\nu_t}{\sigma_{\omega 3}} \frac{\partial k}{\partial x_i} \right) + \alpha_3 \frac{\omega}{k} P - \beta_3 \omega^2 + (1 - F_1) \frac{2}{\sigma_{\omega 2} \omega} \frac{\partial k}{\partial x_i} \frac{\partial \omega}{\partial x_i} \qquad (2.17)$$

An extra source term, called cross-diffusion term, appears on the right hand side (RHS), which arises during the transformation. The model constants, Φ_3 (being Φ either σ_ω, α or β), are related through a linear combination of a set of constants Φ_1 and Φ_2 (where subscripts 1 and 2 correspond to constants of *k*-ω and of *k*-ε models presented in Table 2.2 and Table 2.1, respectively):

$$\Phi_3 = F_1 \Phi_1 + (1 - F_1) \Phi_2 \qquad (2.18)$$

Blending function F_1 is defined as:

$$F_1 = \tanh\left(\arg_1^4 \right) \qquad (2.19)$$

with

$$\arg_1 = \min\left(\max\left(\frac{\sqrt{k}}{\beta' \omega z}, \frac{500\nu}{z^2 \omega} \right), \frac{4k}{CD_{k\omega} \sigma_{\omega 2} z^2} \right) \qquad (2.20)$$

where *z* is the distance to the nearest wall.

$$CD_{k\omega} = \max\left(\frac{2}{\sigma_{\omega 2}\omega}\frac{\partial k}{\partial x_i}\frac{\partial \omega}{\partial x_i}, 10^{-10}\right) \tag{2.21}$$

For completeness, all BSL constants are listed again in the Table 2.3.

Table 2.3: Values of the coefficients in the BSL *k*- ω model.

Φ_1	β'	β_1	α_1	σ_{k1}	$\sigma_{\omega 1}$
	0.09	0.075	5/9	2	2
Φ_2	β'	β_2	α_2	σ_{k2}	$\sigma_{\omega 2}$
	0.09	0.0828	0.44	1	1/0.856

Another two-equation model which has become very popular is the Shear Stress Transport (SST) *k*-ω model proposed also by Menter (1993). The *k*-ω based SST model accounts for the transport of the turbulent shear stresses, according to modifications introduced to the original *k*-ω model by Menter. One of these modifications is referred to obtain a limiter for the formulation of the eddy viscosity, given by:

$$\nu_t = \frac{a_1 k}{\max(a_1 \omega, SF_2)} \tag{2.22}$$

where $S = \sqrt{2S_{ij}S_{ij}}$, a_1 is a constant and F_2 is a blending function similar to F_1.

$$F_2 = \tanh\left(\arg_2^2\right) \tag{2.23}$$

$$\arg_2 = \max\left(\frac{2\sqrt{k}}{\beta' \omega z}, \frac{500\nu}{z^2 \omega}\right) \tag{2.24}$$

A disadvantage of standard two-equation turbulence models is the excessive production of turbulence kinetic energy, *P*. Therefore, another formulation of limiters for the production term in the turbulence equations was suggested by Menter (1994) as:

$$P = \min\left(P, 10\beta' k\omega\right) \tag{2.25}$$

In conclusion, two-equation models have proven that they perform reasonably well for a wide range of flows of engineering interest, with some limitations that may be accounted with the use of special bounding or damping functions. Their major advantage is the simplicity, and the low computational cost compared to more complex models, such as RSM or LES.

Generally, neither two-equation model, *k*-ε or *k*-ω model, is capable of giving quantitatively

good results for more complicated flows. As pointed out by Wilcox (2006), these models can fail drastically for flows with sudden changes in mean strain rate, curved surfaces, secondary motions, rotation, or if the flow is highly 3D. Regretfully, most flows of interest include some or all of these features. While two-equation models may be able to give qualitative results for such flows, generally a further level of complexity is needed in the model to obtain close agreement with experiments (as will be shown in Research Paper II).

2.5 REYNOLDS STRESS MODELS

As it was mentioned in previous subchapter, the eddy viscosity approximation for determining the Reynolds stresses is not a good model for complex flows. Thus, the Boussinesq hypothesis is abandoned here and the unknown Reynolds stress components are obtained directly from the solution of differential Reynolds stress transport equations.

The Reynolds stress models (RSM) are thus more complicated than the eddy viscosity models. They provide a more accurate representation of the turbulence and are valid over a wider range of flows. They can capture many of the complex effects encountered in nature and in engineering practice.

The basic concepts of the RSM were defined by Chou (1945). A few years later, Rotta (1951) made an important and lasting contribution to Reynolds stress modelling. In the 1970s the RSM gained more attention with the contribution of Hanjalić and Launder (1972) and of Launder *et al*. (1975). Since then, many researchers have contributed and proposed models of different level of complexity.

Reynolds stress models and algebraic Reynolds stress models used in this study are presented in the next Subchapters.

2.5.1 Reynolds Stress model

The Reynolds Stress models (RSM), also known as the Reynolds stress transport models, second-order closure, second moment closure and second-order modelling, are higher level, elaborate turbulence models. In the RSM, transport equations are solved for the individual Reynolds stresses. Thus, in general 3D mean flows six equations need to be solved, due to symmetry in the Reynolds stress tensor, and an additional equation for the turbulence length-scale or equivalent.

The exact transport equation for the Reynolds stresses in Cartesian tensor notation reads as (*e.g*. Pope 2000):

$$\frac{\mathrm{D}\overline{u_i' u_j'}}{\mathrm{D}t} + \frac{\partial}{\partial x_k} T_{kij} = P_{ij} + R_{ij} - \varepsilon_{ij} \tag{2.26}$$

The first term on the left hand side (LHS) is the mean-flow convection of Reynolds stresses. It is directly related to the unknowns, $\overline{u_i' u_j'}$, and therefore needs no modelling:

$$\frac{\mathrm{D}\overline{u_i' u_j'}}{\mathrm{D}t} = \frac{\partial \overline{u_i' u_j'}}{\partial t} + U_k \frac{\partial \overline{u_i' u_j'}}{\partial x_k} \tag{2.27}$$

In statistically steady (stationary) flows this is equal to the rate of change of Reynolds stresses due to convection by the mean flow (last term in Eq. (2.27)).

P_{ij} is the production term. It represents the rate at which energy is fed from the mean flow to each stress component. The production term can be computed directly from the stress and the mean-flow strain-rate components and thus needs no modelling. P_{ij} reads:

$$P_{ij} = -\overline{u_i' u_k'} \frac{\partial U_j}{\partial x_k} - \overline{u_j' u_k'} \frac{\partial U_i}{\partial x_k} \tag{2.28}$$

Both, convection and production terms need no modelling, but all the other terms in equation (2.26) need additional modelling.

ε_{ij} is the dissipation tensor. It represents the dissipation rate of Reynolds stresses due to molecular viscous action.

$$\varepsilon_{ij} = 2\nu \overline{\frac{\partial u_i'}{\partial x_k} \frac{\partial u_j'}{\partial x_k}} \tag{2.29}$$

The dissipation rate tensor ε_{ij} is usually decomposed into an isotropic part and the deviation from that, $\varepsilon_{ij} = \varepsilon(e_{ij} + 2/3\delta_{ij})$. The total dissipation rate ε is modelled through a transport equation, similar to the ε equation in the k–ε models (Eq. (2.12)). The dissipation rate anisotropy e_{ij} is typically explicitly modelled in terms of the Reynolds stress anisotropy a_{ij} or can be included into the modelling of the pressure strain rate, which will be discussed later. At high Reynolds numbers and sufficiently far from the solid walls ε_{ij} is expected to approach an isotropic state $2/3\varepsilon\delta_{ij}$. Thus, most current RSM employ an isotropic assumption for the dissipation rate tensor. Close to the walls, the dissipation rate becomes substantially anisotropic and different models are appropriate to model it, such as the simple model from Rotta (1951), a more accurate approximation to ε_{ij} by Launder and Reynolds (1983) and Kebede *et al*. (1985), a more complicated proposal by Hanjalić and Jakirlić (1993) and Launder (1996). Jakirlić and

Hanjalić (2002) proposed a new model for the transport equation of the turbulence energy dissipation rate ε and for the anisotropy of the dissipation rate tensor ε_{ij} for near-wall turbulent flows, which yields better agreement with DNS data.

T_{kij} is the Reynolds stress flux. It represents the rate of spatial transport of Reynolds stresses by the action of turbulent fluctuations, pressure fluctuations and viscous diffusion.

$$T_{kij} = T_{kij}^{(u')} + T_{kij}^{(p')} + T_{kij}^{(\nu)} \tag{2.30}$$

where the three fluxes are turbulent transport

$$T_{kij}^{(u')} = \overline{u_i' u_j' u_k'} \tag{2.31}$$

pressure transport

$$T_{kij}^{(p')} = \frac{1}{\rho}\left(\overline{u_i' p'}\delta_{jk} + \overline{u_j' p'}\delta_{ik}\right) \tag{2.32}$$

and viscous diffusion

$$T_{kij}^{(\nu)} = -\nu \frac{\partial \overline{u_i' u_j'}}{\partial x_k} \tag{2.33}$$

The contribution of the viscous diffusion term (Eq. (2.33)) to the total rate of transport of $\overline{u_i' u_j'}$ is negligible at high Reynolds numbers, except in the viscous wall region. The term is in closed form, thus, no further modelling is needed.

The pressure transport (Eq. (2.32)) originates from decomposition of the velocity-pressure-gradient tensor Π_{ij} (*cf.* Pope 2000) into the traceless pressure-strain correlation R_{ij} (will be mentioned further) and the pressure transport term as:

$$\Pi_{ij} = R_{ij} - \frac{\partial}{\partial x_k} T_{kij}^{(p')} \tag{2.34}$$

In most RSM, the pressure transport (Eq. (2.32)) is either neglected, since it is very small, or it is modelled (implicitly or explicitly) together with the turbulent transport by a gradient-diffusion assumption. In homogeneous turbulence the pressure transport is zero, and thus, $\Pi_{ij} = R_{ij}$. From now on, the pressure-strain correlation R_{ij} will be mentioned in equations as Π_{ij}.

The gradient-diffusion model was proposed by Daly and Harlow (1970) and can be said to be the standard transport submodel. It uses the Reynolds-stress tensor to define anisotropic diffusion coefficient:

$$\overline{u_i' u_j' u_k'} = -C_s \frac{k}{\varepsilon} \overline{u_k' u_l'} \frac{\partial \overline{u_i' u_j'}}{\partial x_l} \tag{2.35}$$

where C_s is an empirical model coefficient typically set equal to 0.22 (Launder 1990). The pressure and turbulent transport can also be modeled using the simplest gradient-diffusion model due to Shir (1973):

$$-\frac{\partial T_{lij}^{(p)}}{\partial x_l} - \frac{\partial T_{lij}^{(t)}}{\partial x_l} = \frac{\partial}{\partial x_l}\left(\underbrace{\frac{\nu_t}{\sigma_k}}_{\substack{\text{diffusion} \\ \text{coefficient}}} \frac{\partial \overline{u_i' u_j'}}{\partial x_l} \right) \tag{2.36}$$

where the diffusion coefficient is considered to be equal to the diffusion coefficient of turbulence kinetic energy $k = \overline{u_i' u_i'}/2$. In this model the diffusion coefficient is considered isotropic, which increases the model robustness.

Alternative models for the turbulent transport exist, but they all are considerably more complex than Daly and Harlow's model without necessarily producing better overall performance. Examples of such models are Hanjalić and Launder (1972) and Lumley and Khajeh-Nouri (1974).

Π_{ij} is the redistribution term. It represents the redistribution of the available turbulence kinetic energy between the stress components. It is also commonly known as the pressure-strain term, because it is a correlation between fluctuating pressure and strain rate.

$$\Pi_{ij} = \overline{\frac{p'}{\rho}\left(\frac{\partial u_i'}{\partial x_j} + \frac{\partial u_j'}{\partial x_i} \right)} \tag{2.37}$$

In addition to the dissipation, the redistribution term needs to be modelled with care. The modelling of the pressure-strain term is based on the classical decomposition of the formal solution of the Poisson equation for the fluctuating pressure field into three contributions: the rapid pressure $p^{(r)}$, the slow pressure $p^{(s)}$ and the harmonic contribution $p^{(h)}$, which satisfies Laplace's equation $\nabla^2 p^{(h)} = 0$ (*e.g.* Pope 2000). The rapid part responds immediately to changes in the mean flow field while the source term for the slow part does not contain any mean flow field information.

Obviously, the pressure-strain term can also be decomposed into three contributions, $\Pi_{ij}^{(r)}$, $\Pi_{ij}^{(s)}$ and $\Pi_{ij}^{(h)}$. The harmonic part, $\Pi_{ij}^{(h)}$, is zero in homogeneous turbulence, and it is rather

unimportant also in inhomogeneous flows except in the immediate vicinity of walls (Pope 2000).

Rotta (1951) proposed the simplest model for pressure-strain term in decaying homogeneous anisotropic turbulence, where the pressure-strain term is due entirely to the slow pressure, *i.e.* $\Pi_{ij} = \Pi_{ij}^{(s)}$, which is modelled linearly:

$$\Pi_{ij}^{s} = -C_1 \frac{\varepsilon}{k}\left(\overline{u_i' u_j'} - \frac{2}{3} k \delta_{ij}\right) = -C_1 \varepsilon a_{ij} \tag{2.38}$$

where C_1 is the "Rotta constant", usually assigned the value in the range of 1.5 - 2.0, and a_{ij} is the Reynolds stress anisotropy tensor, and is defined as:

$$a_{ij} = \frac{\overline{u_i' u_j'}}{k} - \frac{2}{3}\delta_{ij} \tag{2.39}$$

Rotta's model corresponds to a linear return to isotropy. This type of modelling has been adopted by most modellers and was used in the present study (Research Papers III and IV). Thus, Launder *et al*. (1975) proposed the basic model LRR-IP which is based on the combination of Rotta's model and isotropization of production (IP) model of Naot *et al*. (1970), where pressure-stain term is modelled linearly:

$$\Pi_{ij} = -C_1 \varepsilon a_{ij} - C_2\left(P_{ij} - \frac{2}{3} P \delta_{ij}\right) \tag{2.40}$$

where P_{ij} is production, defined in equation (2.28). P is given by $0.5P_{ii}$. The values of two coefficients are $C_1 = 1.8$ and $C_2 = 3/5$.

The first term in equation (2.40) is Rotta's model for $\Pi_{ij}^{(s)}$, and the second term is the IP model for $\Pi_{ij}^{(r)}$ proposed by Naot *et al*. (1970). This combination of models is one of two models proposed by Launder *et al*. (1975). The second model is the LRR-QI, where QI stands for quasi-isotropic and differs from the IP model in the formulation of the rapid term:

$$\begin{aligned}\Pi_{ij}^{(r)} = &-\frac{C_2 + 8}{11}\left(P_{ij} - \frac{2}{3} P \delta_{ij}\right) - \frac{30C_2 - 2}{55} k\left(\frac{\partial U_i}{\partial x_j} + \frac{\partial U_j}{\partial x_i}\right) \\ &- \frac{8C_2 - 2}{11}\left(D_{ij} - \frac{2}{3} P \delta_{ij}\right)\end{aligned} \tag{2.41}$$

where D_{ij} is given by:

$$D_{ij} = -\overline{u_i' u_k'} \frac{\partial U_k}{\partial x_j} - \overline{u_j' u_k'} \frac{\partial U_k}{\partial x_i} \tag{2.42}$$

Subsequent to the work of Launder *et al*. (1975), Lumley (1978) demonstrated the need for nonlinear terms in models for the pressure-strain term. Many nonlinear models have been proposed, including the SL model of Shih and Lumley (1985), Haworth and Pope (1986), Speziale (1987), Reynolds (1987), the FLT model of Fu *et al*. (1987), the SSG model of Speziale *et al*. (1991) and Sjögren and Johansson (2000). The SL and FLT models were derived in order to satisfy strong form of realizability: when a principal Reynolds stress component vanishes, its time rate must also vanish and its second derivative must be positive (see Lumley 1978).

The SSG model (Speziale *et al*. 1991) is the higher order model which is nonlinear in the Reynolds stress anisotropy and satisfies a weak form of realizability, was used in this study (Research Paper III), and thus will be presented herein. This model is only quadratically nonlinear in the anisotropy tensor for the pressure-strain correlation.

In order to compare the pressure-strain terms for the three previous models described in this subchapter, a general form can be derived based on the anisotropy tensor a_{ij} and the mean strain rate tensor and vorticity tensor, S_{ij} and Ω_{ij}, respectively. The general form reads:

$$\Pi_{ij}^{(s)} = -\varepsilon\left[C_{s1} a_{ij} + C_{s2}\left(a_{ik} a_{kj} - \frac{1}{3} a_{mn} a_{mn} \delta_{ij} \right) \right] \tag{2.43}$$

$$\begin{aligned} \Pi_{ij}^{(r)} &= -C_{r1} P a_{ij} + C_{r2} k S_{ij} - C_{r3} k S_{ij} \sqrt{a_{mn} a_{mn}} \\ &+ C_{r4} k\left(a_{ik} S_{jk} + a_{jk} S_{ik} - \frac{2}{3} a_{kl} S_{kl} \delta_{ij} \right) + C_{r5} k\left(a_{ik} \Omega_{jk} + a_{jk} \Omega_{ik} \right) \end{aligned} \tag{2.44}$$

where the mean strain rate tensor is defined as:

$$S_{ij} = \frac{1}{2}\left(\frac{\partial U_i}{\partial x_j} + \frac{\partial U_j}{\partial x_i} \right) \tag{2.45}$$

and vorticity tensor as:

$$\Omega_{ij} = \frac{1}{2}\left(\frac{\partial U_i}{\partial x_j} - \frac{\partial U_j}{\partial x_i} \right) \tag{2.46}$$

This general form can be used to model linear and quadratic terms by using the appropriate values for the constants. The constants are listed in the Table 2.4 for each model.

Table 2.4: Values of the constants in the LRR-IP, LRR-QI and SSG models.

Model	C_{S1}	C_{S2}	C_{r1}	C_{r2}	C_{r3}	C_{r4}	C_{r5}
LRR-IP	1.8	0.0	0.0	0.8	0.0	0.6	0.6
LRR-QI	1.8	0.0	0.0	0.8	0.0	0.873	0.655
SSG	1.7	-1.05	0.9	0.8	0.65	0.625	0.2

Speziale *et al*. (1990, 1991) have tested the LRR, SSG and FLT (Fu *et al*. 1987) models in homogeneous shear flows with and without rotation. The results showed that the SSG model outperforms the linear LRR and nonlinear FLT models in predicting the time evolution of turbulence kinetic energy, except for the most energetic homogeneous shear flow with rotation ($\Omega/S = 0.25$). The SSG model is not significantly more complicated than the LRR model, and is substantially simpler than the proposed nonlinear SL and FLT models of Shih and Lumley (1985) and of Fu *et al*. (1987), respectively.

Abid and Speziale (1993) have compared LRR, SL, SSG and FLT models for homogeneous shear flow and for the log-layer of channel flow. They observed that the SSG and FLT models gave the best agreement with the experimental data for homogeneous flow. For the log-layer channel flow the SSG model provided the equilibrium values that were in a close range of the experimental data. The FLT model did not perform well in channel flow. The SSG model performs reasonably well, and is superior to some other existing second-order models (Speziale *et al*. 1991).

2.5.2 Omega-based Reynolds stress models

It is known that common RSM perform better than the eddy viscosity models in many flows. Most advanced RSM employ ε-equation (2.12), which is known to perform poorly in the wall bounded flows in the very near-wall region. Wilcox (1993) illustrated that an ω-based Reynolds stress model provides better results thus making the ω-equation (2.15) an ideal choice for the near wall flow.

In this study Baseline Reynolds Stress model (BSL RSM) was used. The BSL RSM is a Reynolds stress model based on the ω–equation (2.17) used in the BSL *k*-ω model, which was discussed earlier in subchapter 2.4.

The exact Reynolds stress transport equation for the BSL RSM is given in previous subchapter by equation (2.26) and ω-equation is given by equation (2.17). The constitutive relation for the pressure-strain term in BSL RSM is given by LRR-QI model and is presented as:

$$\Pi_{ij} = \beta' C_1 \omega \left(-\overline{u_i' u_j'} + \frac{2}{3} k \delta_{ij} \right) - \frac{C_2 + 8}{11} \left(P_{ij} - \frac{2}{3} P \delta_{ij} \right) - \frac{60 C_2 - 4}{55} k \left(S_{ij} - \frac{1}{3} S_{kk} \delta_{ij} \right) - \frac{8 C_2 - 2}{11} \left(D_{ij} - \frac{2}{3} P \delta_{ij} \right) \tag{2.47}$$

where the values of $C_1 = 1.8$ and $C_2 = 0.52$. The coefficients in the BSL RSM of ω-equation are blended using the relationship (2.18) and are presented in the Table 2.3.

2.5.3 Algebraic Reynolds stress models

The classical Algebraic Reynolds stress model (ARSM) was developed from the modelled equation for the Reynolds stress by Rodi (1972, 1976). The basic assumption of Rodi (1972, 1976) is that the convection minus diffusion/transport in the transport equation for the Reynolds stress is proportional to the convection minus diffusion/transport in the kinetic energy equation (Taulbee 1992):

$$\frac{\mathrm{D}\overline{u_i' u_j'}}{\mathrm{D}t} - \frac{\partial T_{ijl}}{\partial x_l} = \frac{\overline{u_i' u_j'}}{k} \left(\frac{\mathrm{D}k}{\mathrm{D}t} - \frac{\partial T_l^{(k)}}{\partial x_l} \right) = \frac{\overline{u_i' u_j'}}{k} \left(P - \varepsilon \right) = P_{ij} + \Pi_{ij} - \varepsilon_{ij} \tag{2.48}$$

thus, turning the equation for the Reynolds stresses into algebraic one. Here, T_{ijl} and $T_l^{(k)} = T_{jjl}/2$ are the transport (turbulent and molecular) of the Reynolds stress and turbulence kinetic energy, respectively. P_{ij} and P are production terms, ε_{ij} is dissipation rate tensor and Π_{ij} is pressure-strain, which were defined in subchapter 2.5.1.

An alternative development of this assumption results in the exact transport equation for the Reynolds stress anisotropy tensor:

$$k \frac{\mathrm{D}a_{ij}}{\mathrm{D}t} - \left(\frac{\partial T_{ijl}}{\partial x_l} - \frac{\overline{u_i' u_j'}}{k} \frac{\partial T_l^{(k)}}{\partial x_l} \right) = -\frac{\overline{u_i' u_j'}}{k} \left(P - \varepsilon \right) + P_{ij} + \Pi_{ij} - \varepsilon_{ij} \tag{2.49}$$

The traditional idea of ARSM is equivalent to neglecting convection and diffusion/transport terms (weak-equilibrium hypothesis *cf.* Rodi 1972, 1976) in the exact transport equation for the Reynolds stress anisotropy a_{ij} (Eq. (2.49)). Thus, the ARSM assumption leads to the following implicit algebraic equation for a_{ij}:

$$\frac{\overline{u_i' u_j'}}{k} \left(P - \varepsilon \right) = P_{ij} + \Pi_{ij} - \frac{2}{3} \varepsilon \delta_{ij} \tag{2.50}$$

In the case of quasi-linear pressure-strain model (LRR-QI) the implicit algebraic equation for the Reynolds stress anisotropy tensor may be written as:

$$\left(C_1 - 1 + \frac{P}{\varepsilon}\right)a_{ij} = -\frac{8}{15}S_{ij} + \frac{7C_2 + 1}{11}\left(a_{ik}\Omega_{kj} - \Omega_{ik}a_{kj}\right) - \frac{5 - 9C_2}{11}\left(a_{ik}S_{kj} + S_{ik}a_{kj} - \frac{2}{3}a_{kl}S_{lk}\delta_{ij}\right) \tag{2.51}$$

where S_{ij} and Ω_{ij} denote the strain-rate and vorticity tensors, respectively, normalized with the turbulent time-scale, $\tau \equiv k/\varepsilon$, and they are defined as:

$$S_{ij} = \frac{1}{2}\tau\left(\frac{\partial U_i}{\partial x_j} + \frac{\partial U_j}{\partial x_i}\right) \tag{2.52}$$

$$\Omega_{ij} = \frac{1}{2}\tau\left(\frac{\partial U_i}{\partial x_j} - \frac{\partial U_j}{\partial x_i}\right) \tag{2.53}$$

Algebraic equation system (2.51), in principle, can be solved iteratively. However, an iterative solution is found to be numerically troublesome in practical flow problems. One should note that although the equation (2.51) is tensorially linear, it represents a nonlinear relation since $P/\varepsilon = -a_{kl}S_{lk}$. Therefore, multiple roots exist, and iteration may converge to a non-physical root. To overcome this problem, an exact explicit solution can be found for equation (2.51) with the aid of the Caley-Hamilton theorem (*e.g.* Pope 1975).

2.5.4 Explicit algebraic Reynolds stress models

The implicit relation for a_{ij} in the ARSM (Eq. (2.51)) has been found to be numerically and computationally cumbersome. The computational effort for many applications has been found to be too large, and the advantage of using ARSM instead of the full RSM was then lost.

Pope (1975) was the first to propose a methodology for obtaining a solution for system of equations (2.51). This methodology, which leads to explicit algebraic stress models (EARSM), is based on the use of the integrity basis from linear algebra.

The most general form for a_{ij} in terms of S_{ij} and Ω_{ij} consists of ten tensor groups (Hellsten and Wallin 2009):

$$
\begin{aligned}
a_{ij} &= \beta_1 S_{ij} + \beta_2\left(S_{ik}S_{kj} - \frac{1}{3} II_S \delta_{ij} \right) + \beta_3\left(\Omega_{ik}\Omega_{kj} - \frac{1}{3} II_\Omega \delta_{ij} \right) + \\
&\beta_4\left(S_{ik}\Omega_{kj} - \Omega_{ik}S_{kj} \right) + \beta_5\left(S_{ik}S_{kl}\Omega_{lj} - \Omega_{ik}S_{kl}S_{lj} \right) + \\
&\beta_6\left(S_{ik}\Omega_{kl}\Omega_{lj} + \Omega_{ik}\Omega_{kl}S_{lj} - \frac{2}{3} IV \delta_{ij} \right) + \\
&\beta_7\left(S_{ik}S_{kl}\Omega_{lp}\Omega_{pj} + \Omega_{ik}\Omega_{kl}S_{lp}S_{pj} - \frac{2}{3} V \delta_{ij} \right) + \\
&\beta_8\left(S_{ik}\Omega_{kl}S_{lp}S_{pj} - S_{ik}S_{kl}\Omega_{lp}S_{pj} \right) \\
&+ \beta_9\left(\Omega_{ik}S_{kl}\Omega_{lp}\Omega_{pj} - \Omega_{ik}\Omega_{kl}S_{lp}\Omega_{pj} \right) + \\
&\beta_{10}\left(\Omega_{ik}S_{kl}S_{lp}\Omega_{pq}\Omega_{qj} - \Omega_{ik}\Omega_{kl}S_{lp}S_{pq}\Omega_{qj} \right)
\end{aligned}
\tag{2.54}
$$

where S_{ij} and Ω_{ij} are the normalized strain-rate and vorticity tensors, respectively, defined in equations (2.52) and (2.53). The β-coefficients may be functions of the five independent invariants of S_{ij} and Ω_{ij}, which can be written as:

$$
\begin{aligned}
II_S &= \mathrm{tr}\left\{\mathbf{S}^2\right\} = S_{ij}S_{ji} \\
II_\Omega &= \mathrm{tr}\left\{\mathbf{\Omega}^2\right\} = \Omega_{ij}\Omega_{ji} \\
III &= \mathrm{tr}\left\{\mathbf{S}^3\right\} = S_{ij}S_{jk}S_{ki} \\
IV &= \mathrm{tr}\left\{\mathbf{S}\mathbf{\Omega}^2\right\} = S_{ij}\Omega_{jk}\Omega_{ki} \\
V &= \mathrm{tr}\left\{\mathbf{S}^2\mathbf{\Omega}^2\right\} = S_{ij}S_{jk}\Omega_{kl}\Omega_{li}
\end{aligned}
\tag{2.55}
$$

The solution procedure for obtaining complete EARSM in general 3D mean flow is then to substitute equation (2.54) into equation (2.51) and reduce high-order terms, obtained by the multiplication of a_{ij} with S_{ij} and Ω_{ij}, with the aid of the Cayley-Hamilton theorem (Atiyah and MacDonald 1969).

Pope (1975) was the first to propose this methodology. But due to the severe complexity of the algebra he restricted his analysis to 2D flows. Thus, in 2D flows, there are only three independent tensor groups in equation (2.54), *i.e.* the $\beta_{1,2,4}$ groups, and two independent invariants II_S and II_Ω. Later this approach was extended and solved to 3D mean flows by Gatski and Speziale (1993) for general linear pressure-strain model and by Taulbee (1992) for the special case when $C_2 \approx 5/9$. By setting $C_2 = 5/9$ (Lumley 1978, Shabbir and Shih 1992) the last term in equation (2.51) is zero, and a simplified but still implicit equation is obtained:

$$
\left(C_1 - 1 + \frac{P}{\varepsilon} \right) a_{ij} = -\frac{8}{15} S_{ij} + \frac{4}{9}\left(a_{ik}\Omega_{kj} - \Omega_{ik}a_{kj} \right) \tag{2.56}
$$

The removal of the last term in equation (2.51) simplifies substantially the solution, especially in 3D flows. The simplified implicit algebraic Reynolds stress equation (2.56) is then multiplied by 9/4, and is written in the next form (Wallin and Johansson 2000):

$$Na_{ij} = -\frac{6}{5}S_{ij} + \left(a_{ik}\Omega_{kj} - \Omega_{ik}a_{kj}\right) \tag{2.57}$$

where N is related to the production to dissipation ratio as:

$$N = C_1^{'} + \frac{9}{4}\frac{P}{\varepsilon} \tag{2.58}$$

and

$$C_1^{'} = \frac{9}{4}\left(C_1 - 1\right) \tag{2.59}$$

C_1, the Rotta coefficient, is set here to 1.8. With the simplifications made the equation system becomes quasi-linear, as the tensor equation for the a_{ij} is linear and the corresponding scalar equation for N is nonlinear.

The procedure to solve this equation system is to insert the general form for a_{ij} (Eq. (2.54)) into the simplified ARSM equation (2.57) where N is not yet determined. This results in a linear equation system for the β-coefficients which can be solved by reducing the higher-order tensor groups using the Cayley-Hamilton theorem. The β-coefficients are now functions of production to dissipation ratio, P/ε, or N. Thus, there are only two non-zero β-coefficients for 2D mean flows in the simplified solution of the ARSM, which can be expressed as:

$$\beta_1 = -\frac{6}{5}\frac{N}{N^2 - 2II_\Omega}, \quad \beta_4 = -\frac{6}{5}\frac{1}{N^2 - 2II_\Omega} \tag{2.60}$$

The final step of the solution is to formulate and solve the nonlinear scalar equation for N. The nonlinear equation for N in 2D mean flow can be derived by inserting the solution of a_{ij} for 2D mean flow into the definition of N (Eq. (2.57)). This results in a cubic equation and can be written following Wallin and Johansson (2000):

$$N^3 - C_1^{'}N^2 - \left(\frac{27}{10}II_S + 2II_\Omega\right)N + 2C_1^{'}II_\Omega = 0 \tag{2.61}$$

which can be solved in a closed form with the solution for the positive root being:

$$N=\begin{cases}\dfrac{C_1^{'}}{3}+\left(P_1+\sqrt{P_2}\right)^{1/3}+\operatorname{sign}\left(P_1-\sqrt{P_2}\right)\left|P_1-\sqrt{P_2}\right|^{1/3}, & P_2\geq 0\\ \dfrac{C_1^{'}}{3}+2\left(P_1^2-P_2\right)^{1/6}\cos\left(\dfrac{1}{3}\arccos\left(\dfrac{P_1}{\sqrt{P_1^2-P_2}}\right)\right), & P_2<0\end{cases} \tag{2.62}$$

where the arcos function should return an angle between 0 and π, and

$$\begin{aligned}P_1&=\left(\frac{1}{27}C_1^{'2}+\frac{9}{20}II_S-\frac{2}{3}II_\Omega\right)C_1^{'}\\ P_2&=P_1^2-\left(\frac{1}{9}C_1^{'2}+\frac{9}{10}II_S+\frac{2}{3}II_\Omega\right)^3\end{aligned} \tag{2.63}$$

The solution N remains real and positive for all possible values of II_S and II_Ω (Wallin and Johansson 2000). The production to dissipation ratio may then be found from equation (2.58) and the system is completely solved.

For 3D mean flows only five tensor groups are remained from the general form for a_{ij}, *i.e.* $\beta_{1,3,4,6,9}$ groups (Taulbee 1992). Thus, the solution for the β-coefficients in the simplified solution of the ARSM can be expressed as (Wallin and Johansson 2000):

$$\begin{aligned}\beta_1&=-\frac{N\left(2N^2-7II_\Omega\right)}{Q}\\ \beta_3&=-\frac{12N^{-1}IV}{Q}\\ \beta_4&=-\frac{2N\left(N^2-2II_\Omega\right)}{Q}\\ \beta_6&=-\frac{6N}{Q}\\ \beta_9&=\frac{6}{Q}\end{aligned} \tag{2.64}$$

where the denominator is calculated as:

$$Q=\frac{5}{6}\left(N^2-2II_\Omega\right)\left(2N^2-II_\Omega\right) \tag{2.65}$$

The denominator Q cannot become singular since II_Ω is always negative. The nonlinear equation for N is then obtained by introducing the above solution (2.64) for a_{ij} into the definition of N of the simplified ARSM (Eq. (2.57)). The resulting equation is of sixth order and can be written, according to Wallin and Johansson (2000), as:

$$N^6 - C_1' N^5 - \left(\frac{27}{10} II_S + \frac{5}{2} II_\Omega \right) N^4 + \frac{5}{2} C_1' II_\Omega N^3 + \left(II_\Omega^2 + \frac{189}{20} II_S II_\Omega - \frac{81}{5} V \right) N^2 - C_1' II_\Omega^2 N - \frac{81}{5} IV^2 = 0 \tag{2.66}$$

This equation cannot be solved in a closed form. According to Hellsten (2004), in 3D mean flows, the solution of N may in practice be approximated using the solution of the cubic equation (2.61).

The extended formulation of the EARSM was included in the text since this model was used in this study (Research Papers I-IV). The implemented EARSM into ANSYS CFX is based on the EARSM of Wallin and Johansson (2000) in the form given by Hellsten (2004). The EARSM used in this study was coupled together with the k-ε model (Research Papers I and II) and the BSL model (Research Papers III and IV).

The differences between the EARSM of Wallin and Johansson (2000) presented above and the EARSM used in this study will be presented further in Research Paper IV.

The EARSM is about as robust and easy to use as the linear eddy viscosity models. When compared to standard eddy viscosity two-equation models, the computational cost is increased by less than 10%. The EARSM involves higher level of physical description and can include many of the same features as the RSMs. Thus, the EARSM was the turbulence model adopted in the present study, and much of the research was focused on verifying its validity in the simulation of Prandtl's second kind secondary flows.

2.6 REFERENCES

Abid, R. and Speziale, C. G. 1993 Predicting equilibrium states with Reynolds stress closures in channel flow and homogeneous shear flow. *Phys. Fluids* A**5**, 1151-1158.

Atiyah, M. F. and MacDonald, I. G. 1969 *Introduction to Commutative Algebra*. Oxford: Westview Press.

Baldwin, B. S. and Lomax, H. 1978 Thin-layer approximation and algebraic model for separated turbulent flows. *AIAA*, Paper78-257.

Boussinesq, J. 1877 Essai sur la th´eorie des eaux courantes. *M´em. pr´es. Acad. Sci.*, 3rd ed., Paris XXIII, 46.

Cater, J. E. and Williams, J. J. R. 2008 Large eddy simulation of a long asymmetric compound channel. *J. Hydraulic Res*. **46** (4), 445-453.

Celik, I. and Rodi, W. 1984 Simulation of free-surface effects in turbulent channel flows. *Physicochemical Hydrodynamics* **5**, 217-227.

Chou, P. Y. 1945. On velocity correlations and the solution of the equations of turbulent fluctuation. *Quart. Appl. Math.* **3**, 38-54.

Daly, B. J. and Harlow, F. H. 1970 Transport equations in turbulence. *Phys. Fluids* **13**, 2634-2649.

Davidov, B. I. 1961 On the statistical dynamics of an incompressible turbulent fluid. *Dokl. Akad. Nauk S.S.S.R*. **136**, 47-50.

Fu, S., Launder, B. E. and Tselepidakis, D. P. 1987 Accomodating the effects of high strain rates in modelling the pressure-strain correlation. *UMIST Mech. Engng Dept Rep*. TFD/87/5.

Gatski, T. and Speziale, C. 1993 On explicit algebraic stress models for complex turbulent flows. *J. Fluid Mech.* **254**, 59-78.

Hanjalić, K. and Launder, B. E. 1972 A Reynolds stress model of turbulence and its application to thin shear flows. *J. Fluid Mech.* **52** (4), 609–638.

Hanjalić, K. and Jakirlić, S. 1993 A model of stress dissipation in second-moment closures. *Appl. Sci. Res*. **51**, 513-518.

Harlow, F. H. and Nakayama, P. I. 1968 Transport of turbulence energy decay rate. University of California Report LA-3854, Los Alamos Scientific Laboratory.

Haworth, D. C. and Pope, S. B. 1986 A generalized Langevin model for turbulent flows. *Phys. Fluids* **29**, 387-405.

Hellsten, A. 2004 *New two-equation turbulence model for aerodynamics applications*. Thesis (PhD). Helsinki University of Technology,Espoo, Finland ISBN 951-22-6933-3 (print), 951-22-6934-1 (pdf, available at http://lib.hut.fi/Diss/).

Hellsten, A. and Wallin, S. 2009 Explicit algebraic Reynolds stress and non-linear eddy-viscosity models. *Int. J. Compt. Fluid Dyn.* **23** (4), 349-361.

Jakirlić, S. and Hanjalić, K. 2002 A new approach to modelling near-wall turbulence energy and stress dissipation. *J. Fluid Mech*. **459**, 139-166.

Jones, W. P. and Launder, B. E. 1972 The prediction of laminarization with a two-equation model of turbulence. *Int. J. Heat Mass Transfer* **15**, 301-314.

Kara, S., Stoesser, T. and Sturm, T. W. 2012 Turbulence statistics in compound channels with deep and shallow overbank flows. *J. Hydraulic Research* **50** (5), 482-493.

Kebede, W., Launder, B. E. and Younis, B. A. 1985 Large-amplitude periodic pipe flow: a second-moment closure study. In F. Durst (Ed.), In *Proc. Fifth Symp.Turbulent Shear Flows*, Ithaca, Cornell University, 16.23-16.29.

Kim, J., Moin, P. and Moser, R. 1987 Turbulence statistics in fully developed channel flow at low Reynolds number. *J. Fluid Mech*. **177**, 133-166.

Kolmogorov, A. N. 1942 The equations of turbulent motion in an incompressible fluid. *Izvestia Academy of Sciences, USSR; Physics* **6**, 56–58 (in Russian).

Launder, B. E. 1990 Phenomenological modelling: present… and future? In J.L. Lumley (Ed.), *Whither Turbulence? Turbulence at the Crossroads*, 439-485.Berlin: Springer-Verlag.

Launder, B. E. 1996 An introduction to single-point closure methodology. In Gatski, T. B., Hussaini, M. Y. and Lumley, J. L. (Eds.) *Simulation and Modeling of Turbulent Flows*. Chapter 6, 243-310. New York: Oxford University Press.

Launder, B. E., Reece, G. J. and Rodi, W. 1975 Progress in the development of a Reynolds-stress turbulence closure. *J. Fluid Mech.* **68**, 537–566.

Launder, B. E. and Reynolds, W. C. 1983 Asymptotic near-wall stress dissipation rates in a turbulent flow, *Phys. Fluids* **26**, 1157-1158.

Lumley, J. L. 1978 Computational Modeling of Turbulent Flows. *Adv. Appl. Mech*. **18**, 123-176.

Lumley, J. L. and Khajeh-Nouri, B. 1974 Computational Modelling of Turbulent Transport, *Adv. Geophys*. **18**A, 169-192.

Menter, F. R. 1993 Zonal Two Equation *k*-ω Turbulence Models for Aerodynamic Flows. In 24th *Fluid Dynamics Conference* (Orlando), AIAA Paper 93-2906.

Menter, F. R. 1994 Two-equation eddy-viscosity turbulence models for engineering applications. *AIAA* **32** (8), 1598 – 1605.

Naot, D., Shavit, A. and Wolfshtein, M. 1970 Interactions between components of the turbulent velocity correlation tensor due to pressure fluctuations. *Israel J. Technol*. **8**, 259-269.

Nezu, I and Nakagawa, H. 1993 *Turbulence in open-channel flows*. In: IAHR Monograph Series. Rotterdam: Balkema.

Pope, S. B. 1975 A more general effective-viscosity hypothesis. *J. Fluid Mech*. **72**, 331-340.

Pope, S. B. 2000 *Turbulent flows*. Cambridge University Press, Cambridge, United Kingdom. ISBN 0–521–59886–9.

Prandtl, L. 1925 Bericht über die Entstehung der Turbulenz. *Z. Angew. Math. Mech*. **5**, 136-139.

Prandtl, L. 1945 Über ein neues Formelsystem für die ausgebildete Turbulenz. *Nachr. Akad.Wiss. Göttingen Math-Phys*. K**1**, 6-19.

Reynolds, W. C. *1987 Fundamentals of Turbulence for Turbulence Modelling and Simulation*. Lecture Notes for Von Karman Institute, AGARD Lecture Series No.86. NATO.

Rodi, W 1972 The prediction of free turbulent boundary layers by use of a two equation model of turbulence. PhD thesis, University of London.

Rodi, W. 1976 A new algebraic relation for calculating the Reynolds stresses. *Z. Angew. Math. Mech*. **56**, T219-221.

Rodi, W. 1980 *Turbulence models and their application in hydraulics: a state of the art review*. IAHR book publications, Delft.

Rodi, W. 1993 *Turbulence models and their application in hydraulics.* A. A. Balkema, Netherlands.

Rotta, J. C. 1951 Statistische Theorie nichthomogener Turbulenz. *Zeitschrift für Physik* **129**, 547–572.

Saffman, P. G. 1970 A model for inhomogeneous turbulent flow. In *Proc. R. Soc. London Ser. A* **317,** 417-433.

Shabbir, A. and Shih, T. H. 1992 Critical assessment of Reynolds stress turbulence models using homogeneous flows. *NASA TM* 105954; *ICOMP*-92-24; *CMOTT*-92-12.

Shih, T. H. and Lumley, J. L. 1985 Modelling of pressure correlation terms in Reynolds stress and scalar flux equations. *Tech. Rep.* FDA-85-3. Cornell University.

Shir, C. C. 1973 A preliminary study of atmospheric turbulent flow in idealized planetary boundary layer. *Journal Atmospheric Science*, **30**, 1327-1339.

Sjögren, T. and Johansson, A.V. 2000 Development and calibration of algebraic nonlinear models for terms in the Reynolds stress transport equations. *Phys. Fluids.* **12**, 1554-1572.

Smith, A. M. O. and Cebeci, T. 1967 Numerical solution of the turbulent boundary layer equations. Report DAC 33735, Douglas Aircraft Division.

Speziale, C. G. 1987 Second-order closure models for rotating turbulent flows. *Q. Appl. Maths* 45, 721-733.

Speziale, C. G. 1990 Discussion of turbulence modelling: Past and future. In *Whither Turbulence? Turbulence at the Crossroads* (ed. J. L. Lumley). Lecture Notes in Physics, **357**, 354-368. Springer.

Speziale, C. G., Abid, R. and Anderson, E. C. 1992 Critical evaluation of two-equation models for near-wall turbulence. *AIAA* **30**, 324-331.

Speziale, C. G., Gatski, T. B. and Mac Giolla Mhuiris, N. 1990 A critical comparison of turbulence models for homogeneous shear flows in a rotating frame. *Phys. Fluids* A**2**, 1678-1684.

Speziale, C. G., Sarkar, S. and Gatski, T. B. 1991 Modelling the pressure-strain correlation of turbulence: an invariant dynamical systems approach. *J. Fluid Mech*. **227**, 245-272.

Stoesser, T. 2010 Physically realistic roughness closure scheme to simulate turbulent channel flow over rough beds within the framework of LES. *J. Hydraulic Eng.* **136** (10), 812-819.

Taulbee, D. B. 1992 An improved algebraic Reynolds stress model and corresponding nonlinear stress model. *Phys. Fluids* A**4**, 2555-2561.

Thomas, T. G. and Williams, J. J. R. 1995 Large eddy simulation of turbulent flow in an asymmetric compound open channel. *J. Hydraulic Research*. **33** (1), 27-41.

Tominaga, Y. and Stathopoulos, T. 2007 Turbulent Shmidt number for CFD analysis with various types of flowfield. *Atmospheric Environment* **41**, 8091-8099.

Wallin, S. and Johansson, A. V. 2000 An explicit algebraic Reynolds stress model for incompressible and compressible turbulent flows. *J. Fluid Mech.* **403**, 89–132.

Wilcox, D. C. 1988 Reassessment of the scale-determining equation for advanced turbulence models. *AIAA* **26**, 1299–1310.

Wilcox, D. C. 1993 *Turbulence modeling for CFD*. La Cañada, CA: DCW Industries.

Wilcox, D.C. 1994 Simulation of Transition with a Two-Equation Turbulence Model. *AIAA* **32**, 247–255.

Wilcox, D.C. 2006 *Turbulence Modeling for CFD*. 3rd Edition, San Diego, California: Birmingham Press, Inc.

CHAPTER 3

MODELLING APPROACH

Contents

3 MODELLING APPROACH

3.1 INTRODUCTION TO COMPUTATIONAL FLUID DYNAMICS (CFD)

Fluid dynamics is the branch of fluid mechanics which studies fluids in motion. There are three ways of studying the fluid flow: experimentally, theoretically and numerically (computational fluid dynamics (CFD)).

Computational fluid dynamics (CFD) is a branch of fluid mechanics that uses numerical methods to solve fluid flow governing differential equations by means of computer-based simulations. The fundamental bases of almost all CFD problems are the Navier-Stokes equations, which were defined earlier in Chapter 2.

One of the earliest types of calculations resembling modern CFD are those by Lewis Fry Richardson (1881-1953). For these calculations he used finite difference approximations and divided the physical space into grid cells. Although they were not fully accurate, these calculations together with Richardson's book (1965) set the basis for modern CFD.

The computer power available accelerated the pace of development of 3D methods. Probably, the first work using computers to model fluid flow, as governed by the Navier-Stokes equations, was performed at Los Alamos National Labs, in the T3 group (Harlow 2004). This group was led by Francis H. Harlow, who is widely considered as one of the pioneers of CFD. During the 1960s, this group developed a variety of numerical methods to simulate transient 2D fluid flows, such as: Particle-in-cell (PIC) method (Harlow 1955), Fluid-in-cell method (Gentry *et al*. 1966), Vorticity stream function method (Fromm 1963), Marker-and-cell method (Harlow and Welch 1965), k-ε turbulence model (Harlow and Nakayama 1968), *etc*.

During the 1970s, a research team working under Brian Spalding at Imperial College of London, developed: code for parabolic flows GENMIX (Spalding 1977), TEACH code, Upwind numerical scheme, Finite Volume methodology (FVM), code based on the stream-function and vorticity variables, hybrid method (Runchal 1972), the SIMPLE algorithm (Patankar and Spalding 1972), *etc*.

Most of the successful commercial CFD codes even today employ the SIMPLE algorithm or its variations at least as one of the available options. After retiring Spalding devoted his full attention to the development of the PHOENICS code, which debuted in 1978 and was the first commercially available software tool in CFD (Runchal 2009).

Nowadays, there are many commercial and open source software available, such as: PHOENICS (UK), STAR-CD and STAR-CCM+ (USA), FLOW- 3D (USA), SCRYU/TETRA (Japan), OpenFOAM (UK), SSIIM (Norway), TELEMAC (France), ANSYS (USA), which has acquired Fluent (UK and USA), CFX (UK and Canada), POLYFLOW (Belgium) and many more.

CFD has seen enormous growth over the last several decades. This technology has widely spread to various engineering applications such as automobile and aircraft design, building HVAC (heating, ventilation, and air conditioning), chemicals and petrochemicals, medicine, energy and power generation, oil and gas industry, product design and optimization, weather science, environmental pollution, civil engineering and oceanography, among others. CFD codes can produce an extremely large volume of computed results and cost much less than experiments because physical modifications of facilities are not necessary. CFD analysis complements testing and experiments and it reduces the total effort required in the laboratory.

Below, an overall structure of ANSYS-CFX, the CFD workbench used in this study, is presented and the role of the individual structure blocks is discussed.

3.2 STRUCTURE OF THE ANSYS CFX

All CFD workbench codes, as well as ANSYS-CFX, are user friendly and have a sophisticated graphical interface where one can input the initial and boundary conditions for the determined physical process of the region of interest and then to examine the results. Hence all codes contain three main elements: a pre-processor, a solver and a post-processor (Versteeg and Malalasekera 2007).

Pre-processing consists of the input of a flow problem to CFD workbench code. More exactly, this stage involves: the definition of the geometry of the region of interest (computational domain), grid generation or meshing, definition of fluid properties, selection of the physical phenomena that need to be modelled, definition of the initial and boundary conditions and the selection of the turbulence model to be used for the simulation of the flow. The structure of ANSYS-CFX can be presented as a system of five cells (Table 3.1).

In present study the geometry was created in the DesignModeler module incorporated into ANSYS-CFX. However, in CFX the geometry also can be imported from most major CAD packages that will output a SAT, STL, Parasolid, STEP or IGES file (ANSYS-CFX 2010).

Table 3.1: Structure of ANSYS CFX

Elements of code	Cell	Function
Pre-processor	Geometry	Generation of the geometry
	Mesh	Grid generation
	Setup	Definition of initial and boundary conditions and turbulence model
Solver	Solution	Definition of the run and monitoring of the convergence
Post-processor	Results	Visualization of the results and their treatment

After the geometry has been defined the next step is to mesh the computational domain. The objective of meshing is to divide the domain into a number of smaller elements (control volumes). The accuracy of a CFD solution partially depends on the number of cells and on the quality of the mesh. Optimal meshes are often non-uniform: finer in areas where high velocity gradients occur and coarser in regions with relatively little change (Versteeg and Malalasekera 2007). When creating the mesh, one should keep in mind that balance should exist between the accuracy of a solution through the number of grid elements generated and its cost in terms of necessary computer hardware and calculation time. The mesh quality analysis of the present study will be discussed further in Research Paper I.

The most basic form of mesh classification is based upon the connectivity of the mesh: structured (Figure 3.1(a)) and unstructured (Figure 3.1(b)). The structured mesh is considered when cells (nodes) are arranged in rows and columns (not necessary equally spaced, but following the same pattern as the geometry), thus, limiting the type of elements to quadrilaterals (for 2D geometries) and hexahedrons (for 3D geometries). Unstructured mesh is considered when cells and nodes are not arranged in rows and columns (Figure 3.1(b)). In unstructured meshes for 3D geometries the next types of elements can be generated: prisms, pyramids and tetrahedrons. Tetrahedral mesh might use up to six times as many elements as hexahedral one, thus resulting in more computationally expensive mesh for the same number of nodes (Chu *et al.* 2009). The disadvantages of structured grid are that it is limited to simple geometries and it is time consuming to create a high quality mesh, while unstructured grid can be generated very fast for very complex geometries. The advantage of structured grid is that structured grid calculations usually take less time than an unstructured grid calculation, for the same number of nodes. Another reason to use structured grids is that unstructured grids are often (but not always) very dissipative compared to a high resolution structured mesh. Thus, the use of unstructured grid is therefore unsuitable for some applications. One of these applications is the compound channel flow. A test case was performed for an asymmetric compound channel flow

using unstructured grid with prisms elements. This test case is not reported here, however, it demonstrated that secondary flows were dissipated due to the use of unstructured grid. Thus, in present study only non-uniform hexahedral mesh was generated for the computational domain.

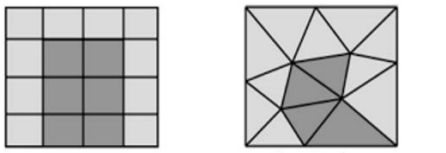

a) Structured grid b) Unstructured grid

Figure 3.1: Structured and unstructured grids (adapted from https://confluence.oceanobservatories.org).

The next and final step of the pre-processing is to create input required by the Solver, such as fluid properties, initial and boundary conditions, turbulence model, numerical scheme for the advection term, convergence criteria and monitoring.

The numerical schemes implemented into CFX and boundary conditions will be discussed in more details in subchapter 3.3.

The component that solves the CFD problem is called **Solver**. The numerical algorithm consists of the following steps:

1. The governing differential equations of fluid flow are integrated over all the (finite) control volumes of the region of interest.
2. Discretisation - the integral equations are converted into a system of algebraic equations.
3. The system of algebraic equations is solved iteratively.

An iterative approach is required because of the non-linear nature of the equations. The solution is converged when so-called residuals - measures of the overall conservation of the flow properties - are very small. A moderate-large number of iterations are usually required to reach a converged solution.

There is no convergence theory for the solution of the discrete RANS equations (ERCOFTAC 2000). The ideal level of convergence is to drive all the residuals down to machine accuracy, but in practice it is not used due to time constraints. Thus, before applying the **Solver**, it is necessary to define the convergence criteria and specify additional quantities which should be monitored during the simulation.

In the present study the simulations were stopped when the convergence criteria were met. The level of convergence was evaluated based on average values of the residuals. Typically for practical simulations the aim is to decrease the residuals to an order of 10^{-4}. However,

depending on the class of problem under investigation, it may be necessary to decrease the residuals further to 10^{-6} or even more (Knight *et al*. 2005). One of the convergence criteria met in the present study was that the root mean square (RMS) normalized values of all the equation residuals were below the residual target value of 10^{-6}. Another additional criterion was used, such as defining monitor points throughout the computational domain and checking if quantities of interest (*e.g*. three velocity components and pressure) have reached steady values and kept constant for at least 500 iterations. At the end of the run the global balances are reported. The simulation is assumed to be converged if two previous criteria met and if global mass and momentum unbalances are less than 0.01%.

The Solver produces a results file that is then passed to the **post-processor** where the resulting solution can be visualised and analysed. At the end of the simulation the user has to judge whether the results are "good enough". It can be done by comparing the numerical results with the experimental data. The validation of a CFD simulation was performed in this study and is presented in more details in Research Paper I.

Anyone wishing to use CFD in a serious way must realise that it is not a substitute for experiments, but a very powerful complementary problem solving tool.

3.3 DISCRETISATION AND SOLUTION THEORY

The CFD algorithms based on discretization of the computational domain stand on four numerical solution techniques: finite difference, finite volume, finite element and spectral methods. There are also some CFD algorithms in the field of numerical simulation that do not require discretization of the simulation domain, which are called mesh-free methods. Here we will focus on the finite volume method, and the special formulation that is used in ANSYS-CFX. The order of accuracy will be highlighted, while numerical differential schemes are presented, implementation of boundary conditions and near-wall modelling in ANSYS CFX is described and errors and uncertainties in CFD modelling are also reviewed.

3.3.1 Finite volume method (FVM)

CFX uses Finite-Element-based Finite Volume method (FVM). In this variant, the control volumes are vertex-centred, where the solution variables are calculated and stored at the vertices (nodes) of the mesh. This type of mesh is called non-staggered, or co-located, grid. The Finite Element (FE) basis comes from the use of shape functions (also known as trial functions, interpolation functions or basis functions, Chung 2002), common in FE techniques, to describe the way a variable changes across each element.

The objective of the FVM is the transformation of the partial differential equations into the system of algebraic equations, which then should be solved. The process of the discretisation consists of two steps: discretisation of the computational domain and discretisation of the equations.

For discretisation of the computational domain the mesh should be generated, where the control volumes are constructed. A typical 2D control volume is presented in Figure 3.2.

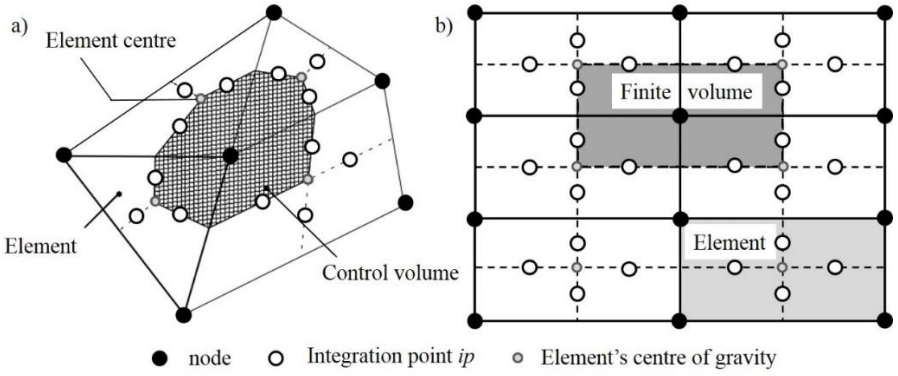

Figure 3.2: Control volume around grid node in 2D mesh: (a) unstructured; (b) structured.

A control volume (the shaded area in Figure 3.2(a) and the light grey area in Figure 3.2(b)) is constructed around each mesh node using medians. It is defined by lines joining the centres of the edges and element centres surrounding the node.

All the conservation equations can be written in the same general convection-diffusion form:

$$\underbrace{\frac{\partial}{\partial x_j}\left(\rho U_j \phi\right)}_{\text{Convection term}} = \underbrace{\frac{\partial}{\partial x_j}\left(\Gamma_\phi\left(\frac{\partial \phi}{\partial x_j}\right)\right)}_{\text{Diffusion term}} + \underbrace{S_\phi}_{\text{Source term}} \tag{3.1}$$

where ϕ is any variable of interest, Γ_ϕ is the diffusion coefficient, and S_ϕ is a source term.

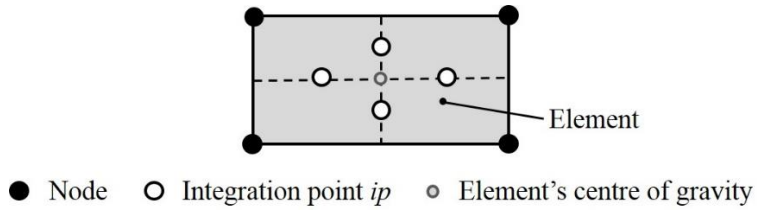

Figure 3.3.: Mesh element.

After the computational domain has been discretised, governing equations (3.1) are integrated over each control volume (step 1 in p. 50):

$$\int_S \rho U_j \phi dn_j = \int_S \Gamma_\phi \left(\frac{\partial \phi}{\partial x_j} \right) dn_j + \int_V S_\phi dV \tag{3.2}$$

where V and S denote volume and surface regions of integration, respectively, and dn_j are the differential Cartesian components of the outward normal surface vector. Equation (3.2) represents the flux balance in a control volume.

The next step in the numerical algorithm is to discretise the volume and surface integrals from equation (3.2). To illustrate this step, let's consider an element like the one shown in Figure 3.3.

Volume integrals are converted into surface integrals using Gaussian divergence theorem. Surface integrals are discretised at the integration points (ip_n) located at the centre of each surface segment within an element and then distributed to the adjacent control volumes (step 2 in p. 50). The surface integrals are locally conservative because they are equal and opposite for control volumes adjacent to the integration points.

After discretising the volume and surface integrals the integral equation (3.2) becomes:

$$\sum_{ip} \left(\rho U_j \Delta n_j \right)_{ip} \phi_{ip} = \sum_{ip} \left(\Gamma_\phi \left(\frac{\partial \phi}{\partial x_j} \right) \Delta n_j \right)_{ip} + \overline{S_\phi} V \tag{3.3}$$

where the subscript *ip* denotes evaluation at an integration point (summations are over all integration points of the control volume), Δn_j is the discrete outward surface vector, $(\rho U_j \Delta n_j)_{ip}$ is the mass flow rate across the surface of the control volume estimated at the integration point, ϕ_{ip} denotes the value of the variable at the integration point, V is the control volume and $\overline{S_\phi}$ is the average value of S_ϕ throughout the volume.

Solution fields and other properties are stored at the mesh nodes. However, to evaluate many of the terms, the solution field or solution gradients must be approximated at the integration points. ANSYS-CFX uses finite element linear shape functions to perform these approximations.

Finite-element shape functions describe the variation of the variable ϕ within an element as follows:

$$\phi = \sum_{i=1}^{N_{node}} N_i \phi_i \tag{3.4}$$

where N_i is the shape function for node *i* and ϕ_i is the value of ϕ at node *i*. The summation is over all nodes of the element.

Key properties of shape functions include:

$$\sum_{i=1}^{N_{node}} N_i = 1 \tag{3.5}$$

In other words, shape functions assume the value of one at the node under consideration and zero at the other nodes, linearly varying in between.

In a few situations when gradients are required at node, ANSYS CFX uses a form of the Gauss' divergence theorem to evaluate these control volume gradients:

$$\nabla\phi = \frac{1}{V}\sum_{ip}\left(\phi\Delta\vec{n}\right)_{ip} \tag{3.6}$$

where $\Delta\vec{n}$ is the outward surface vector at integration point *ip*.

Equation (3.6) requires the use of the finite element shape functions for evaluation of ϕ at integration point *ip*.

3.3.2 Numerical differentiation schemes

There are many differencing schemes available, but more accurate schemes tend to be less robust or slower. Some of the differencing schemes offered by CFX are described in this subchapter.

The advection term requires the integration point values ϕ_{ip} to be approximated in terms of the nodal values of ϕ. The advection schemes implemented into ANSYS CFX can be written in the next form:

$$\phi_{ip} = \phi_{up} + \beta\nabla\phi\Delta\vec{r} \tag{3.7}$$

where ϕ_{up} is the value at the upwind node and $\vec{r}$ is the vector from the upwind node to the *ip*. The choice of β and $\nabla\phi$ yields different schemes as described below.

The **central differencing scheme** is one of the schemes that has been used widely to represent the diffusion terms in steady diffusion problems. It can be obtained by setting β to 1

and $\nabla\phi$ to the local element gradient. The central differencing scheme has second order accuracy, but it not able to identify the flow direction, which makes it not suitable for general-purpose flow calculations, and thus creating the need for other schemes. This type of schemes allows to reproduce steep spatial gradients more accurately than first order schemes, but they generate non-physical oscillations (numerical dispersion) in regions of rapid solution variation.

The particular choice of $\beta = 0$ yields the **upwind differencing scheme**. The convected value of ϕ at a cell face is taken to be equal to the value at the upstream node, *i.e.* $\phi_{ip} = \phi_{up}$. The upwind differencing scheme is only first-order accurate but it accounts for the flow direction. The scheme is very robust, but it will introduce diffusive discretization errors that tend to smear steep spatial gradients. These errors are referred as a false diffusion. The false diffusion is most serious when the grid lines are inclined at 45º to the flow direction (Patankar 1980). In high Reynolds number flows, false diffusion can be large enough to produce physically erroneous results (Leschziner 1980, Huang *et al*. 1985). However, the amount of false diffusion can be reduced by refining the mesh size and by aligning the grid lines with the flow direction (Patankar 1980). Although, the upwind differencing scheme is not entirely appropriate for accurate flow calculations, it is very robust and is the best scheme to start the calculations with.

By choosing the value for β between 0 and 1 and by setting $\nabla\phi$ equal to the average of the adjacent nodal gradients, the discretisation errors associated with the upwind differencing scheme are reduced. This scheme in ANSYS CFX is called **specified blend factor**. The term $\beta\nabla\phi\Delta\vec{r}$ in equation (3.7) is called numerical advection correction and may be viewed as an anti-diffusive correction applied to the upwind scheme.

The **high resolution scheme** uses a special non-linear recipe for β at each node. The advective flux is evaluated using the values of β and $\nabla\phi$ from the upwind node. The recipe for β is based on the boundedness principals used by Barth and Jesperson (1989). This methodology involves computing of ϕ_{min} and ϕ_{max} at each node (including the node itself). Then, for each integration point around the node, equation (3.7) is solved for β to ensure that ϕ_{ip} does not go below ϕ_{min} and does not exceed ϕ_{max}. The nodal value for β is taken to be the minimum value of all integration point values surrounding the node. The value of β is also not allowed to exceed 1 (ANSY CFX - Solver Theory Guide 2010).

The higher order schemes are more accurate but at the same time are less stable, and they increase computational time of the simulation. It is recommended to start calculations with first order upwind scheme and to switch over to higher order schemes after several hundreds of iterations. This provides a good combination of stability and accuracy. This recommendation was taken into account in the present study for the calculations. In the beginning, first order

upwind scheme was used and then switched to a high resolution scheme or to specified blend factor with $\beta = 1$.

3.3.3 Pressure-velocity coupling

In subchapter 3.3.1 we saw how convection-diffusion equations can be solved. Such equations are available for all variables, except for the pressure.

Transport equations for each velocity component (momentum equations) can be derived from the general transport equation (3.1) by replacing variable ϕ by u, v and w, respectively. Every velocity component appears in the momentum equations (2.2), and also must satisfy the continuity equation (2.1). Pressure gradients appear in all three momentum equations, thus the pressure field needs to be calculated in order to be able to solve these equations.

These equations are hard to solve due to non-linear terms in momentum equations and interdependence of the pressure term in all equations. If the flow field is compressible, the continuity equation (2.1) may be used as the transport equation for density and the energy equation - for temperature. The pressure may then be obtained from density and temperature. However, if the flow is incompressible, the pressure is independent of density. So there is no explicit equation for pressure. The so-called pressure-velocity coupling algorithms are used to derive equations for the pressure from the momentum equations and continuity equation.

A widely used pressure-velocity coupling algorithm is the SIMPLE (Semi Implicit Method for Pressure Linked Equations) algorithm proposed by Patankar and Spalding (1972). It is an iterative procedure for the calculation of pressure and velocity fields. Many CFD books describe the SIMPLE algorithm in detail (Patankar 1980, Ferziger and Peric 2001, Versteeg and Malalasekera 2007 and others), thus it will not be presented here. There are also improved versions of SIMPLE algorithm such as SIMPLER (SIMPLE Revised) algorithm of Patankar (1980), SIMPLEC (SIMPLE Consistent) algorithm of Van Doormal and Raithby (1984) and PISO (Pressure Implicit solution by Split Operator method) algorithm proposed by Issa (1986) which have been implemented in numerous CFD codes.

The mentioned above algorithms for pressure-velocity coupling use staggered grid to avoid problems associated with pressure field oscillations. In a staggered grid the velocity components are stored at the centres of the faces and pressure is stored at the grid nodes (centre of the control volume). CFX uses co-located (non-staggered) grid arrangement, where all the variables are stored at the same locations (element nodes), thus all control volumes are identical for all transport equations. An advantage of co-located grid layout is that all geometrical data is only stored once, thus saving computational time and memory of the calculations. However, this arrangement does also have some disadvantages. As discussed by Patankar (1980), co-located

methods can lead to a decoupled (checkerboard) pressure field. To overcome this problem Rhie and Chow (1983) proposed the momentum interpolation method. In this approach, the cell-face velocities in the continuity equation are evaluated by linearly interpolating the discretised momentum equations for the neighbouring cell-centred velocities. This procedure results in a strong velocity–pressure coupling. Later this method was modified by Majumdar (1988) and Miller and Schmidt (1988). They have removed the problem of under-relaxation parameter dependency of the results and the dependence of the steady-state solution on the time-step, observed in Rhie and Chow's formula. A similar strategy is adopted in ANSYS CFX.

The FVM of discretising the governing equations of fluid flow results in a system of linear algebraic equations which need to be solved, as was discussed previously in subchapter 3.3.1. In ANSYS CFX the system of equations can be written in the next form:

$$\sum_{nb_i} a_i^{nb} \phi_i^{nb} = b_i \tag{3.8}$$

where ϕ is the solution, a the coefficients of the equation, b the right hand side term, i is the identifying number of the control volume or node, nb stands for neighbour.

For 3D mass-momentum equation set, the terms from (3.8) can be expressed as:

$$a_i^{nb} = \begin{bmatrix} a_{uu} & a_{uv} & a_{uw} & a_{up} \\ a_{vu} & a_{vv} & a_{vw} & a_{vp} \\ a_{wu} & a_{wv} & a_{ww} & a_{wp} \\ a_{pu} & a_{pv} & a_{pw} & a_{pp} \end{bmatrix}_i^{nb} \qquad \phi_i^{nb} = \begin{bmatrix} u \\ v \\ w \\ p \end{bmatrix}_i^{nb} \qquad b_i = \begin{bmatrix} b_u \\ b_v \\ b_w \\ b_p \end{bmatrix}_i \tag{3.9}$$

The finite volume solution method can either use a segregated (uncoupled) or a coupled solution procedure.

The segregated solution method is the default method in most commercial finite volume codes. Segregated solvers like in ANSYS Fluent solve the momentum equations (u, v and w velocity) sequentially, then using the updated velocity field they calculate the pressure correction equation for continuity. This is repeated until convergence is reached. With segregated methods an equation for a certain variable is solved for all cells, and then the equation for the next variable is solved for all cells, *etc*.

Coupled solvers like ANSYS-CFX have all three momentum equations and the pressure equation in the same matrix so they are solved together. It does not need pressure-velocity coupling as that is taken care of in the matrix solution. With coupled methods, for a given cell equations for all variables are solved, and then the process is repeated for the rest of the cells.

Coupled solvers take more time per iteration and use more memory as the matrix is bigger, but they usually converge much faster since they are converging only the non-linear terms. Segregated solvers need to converge both the non-linear terms and the pressure-velocity coupling.

3.3.4 Linear equation solution and multigrid technique

The solution of each set of equations (3.9) in ANSYS-CFX consists of two numerical operations:

1. Coefficient generation: the non-linear equations are linearized and assembled into the solution matrix.
2. Equation solution: the linear equations are solved using an algebraic multigrid method.

ANSYS CFX uses a Multigrid (MG) accelerated Incomplete Lower Upper (ILU) factorisation technique for solving the discrete system of linearized equations. It is an iterative solver, thus, the exact solution of the equations is approached during the course of several iterations.

The linearized system of discrete equations described above can be written in the general matrix form:

$$[A][\phi]=[b] \tag{3.10}$$

where [A] is the coefficient matrix, [ϕ] is the solution vector and [b] is the right hand side.

Equation (3.10) can be solved iteratively by starting with an approximate solution, ϕ^n, which is to be improved by a correction, ϕ', to yield a better solution, ϕ^{n+1}, that is:

$$\phi^{n+1} = \phi^n + \phi' \tag{3.11}$$

where ϕ' is a solution of:

$$A\phi' = r^n \tag{3.12}$$

where r^n is the residual, obtained from:

$$r^n = b - A\phi^n \tag{3.13}$$

This algorithm repeats until the solution reaches the desired accuracy.

The convergence of these iterative linear solvers can be accelerated significantly by involving coarser grids. This strategy is called multigrid technique. This process involves

running early iterations on a fine mesh and later iterations on progressively coarser virtual ones. The results are then transferred back from the coarser mesh to the original fine mesh.

The simplest way of obtaining the coarse grid is to merge cells. Thus, for 3D analysis one coarse grid control volume is constructed from every eight fine grid control volumes (Figure 3.4).

Since, the accuracy of the solution strongly depends on the discretization it is required that our final solution is determined only by the finest grid. The coarse grid is used to estimate only fine level errors. Thus, any approximations made in the coarse level problem have an effect on the convergence rate only and not on the final finest grid solution.

Geometric multigrid procedure is widely used in commercial CFD solvers. This method agglomerates fine level cells to obtain the grid geometry of a coarse level cell in order to solve the linear system of equations.

ANSYS CFX uses a particular implementation of algebraic multigrid called additive correction multigrid (Hutchinson and Raithby 1986). The main difference of this method from the geometric multigrid procedure is that it agglomerates the equations at the fine level cells to directly obtain the linear equation corresponding to that coarse cell.

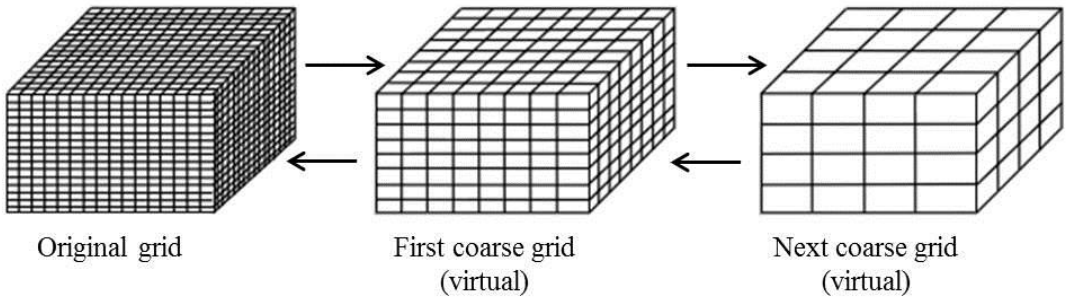

Figure 3.4: Coarsening for 3D grid (adapted from http://www.bakker.org/dartmouth06/engs150/05-solv.pdf).

Algebraic multigrid technique significantly improves the convergence rates and is less expensive than other multigrid methods.

3.3.5 Boundary conditions and near-wall modelling

When solving the Navier-Stokes (or RANSs equations coupled with a turbulence model) and continuity equations, appropriate initial and boundary conditions have to be applied. The process of solving the fluid flow can be seen in a simplified way as the extrapolation of a set of data defined on a boundary contour or surface into the domain interior (Versteeg and

Malalasekera 2007). Thus, it is of extreme importance to specify correctly physically realistic boundary conditions, otherwise it will lead to incorrect results.

In this subchapter a brief description of the next types of boundary conditions used in the present study will be presented:

- Inflow boundary (inlet)
- Outflow boundary (outlet)
- Periodic boundary conditions (PBC)
- Wall

At inflow boundary the distribution of all flow variables, ϕ, needs to be specified. In CFX the magnitude of the uniform profile of the inlet velocity, U, is specified and the direction is taken to be normal to the boundary. The turbulence intensity, $I = \sqrt{(\overline{u'^2} + \overline{v'^2} + \overline{w'^2})/3} \Big/ \sqrt{U^2 + V^2 + W^2}$ is selected to be 5% at the inlet. Thus, turbulence kinetic energy is calculated using:

$$k_{inlet} = \frac{3}{2} I^2 U^2 \tag{3.14}$$

and the turbulence dissipation is calculated using:

$$\varepsilon_{inlet} = \rho C_\mu \frac{k^2}{\mu_t} \tag{3.15}$$

where $\mu_t = 1000 I\mu$.

It is very important to place outflow boundary at the appropriate location such that the conditions downstream have no influence on the solution. Thus, outlet should be placed far away from the inlet or any geometric obstacles such that the flow reaches a fully developed state. At the outlet, the gradients of all variables (except pressure) are zero in the flow direction. In the present study a hydrostatic pressure is specified at the outflow boundary.

Periodic boundary conditions (PBC) are used to simulate fluid flow by modelling a small part of the computational domain, thus reducing essentially computational time and effort.

Periodic flow occurs when the physical geometry of interest and the expected pattern of the flow solution have a periodically repeating nature. PBC mean that the flow entering the computational domain through one periodic plane is identical to the flow exiting the domain through the opposite periodic plane.

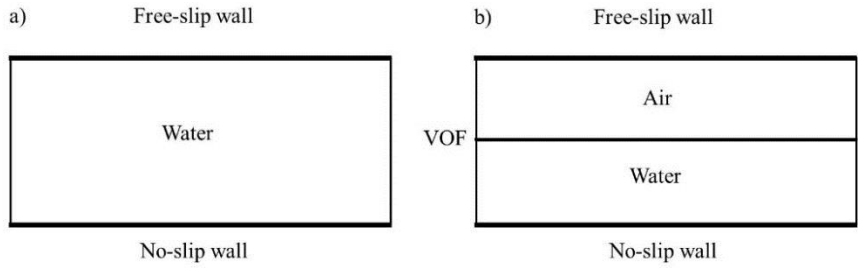

Figure 3.5: Wall boundary conditions: (a) single fluid domain; (b) two-fluid domain.

Two types of periodic flow can be modelled in CFX:

1. no pressure drop occurs across the rotational and translational periodic boundaries, *i.e.* $\Delta p = 0$;
2. a pressure drop occurs across translational periodic boundaries only, Δp = const.

In the present study the second type of PBC was used for simulations. This PBC allows modelling fully developed flow in the streamwise direction by specifying either a mean pressure drop per period (Research Papers III and IV) or net mass flow rate (Research Papers I and II).

Turbulent water flow can be bound by a solid wall or (and) by free-surface. Free-surface in the present study was modelled as a rigid lid and by applying a volume of fluid method (VOF). The rigid lid was specified for a single-fluid domain (Research Papers III and IV) by applying a *free slip* wall boundary condition (Figure 3.5(a)), where the velocity normal to the wall and the wall shear stress are set to zero ($U_{n,Wall} = 0$ and $\tau_w = 0$). For a calculation domain with water and air (Research Papers I and II) the VOF method was used to calculate the free surface (Figure 3.5(b)).

The Volume of Fluid (VOF) method is based on the idea of volume fraction C (Hirt and Nichols 1981). The water volume fraction C is used to identify mesh cells that contain such a fluid. A free surface cell (i, j) is defined as a cell containing a nonzero value of C and having at least one neighboring cell, (i+1,j) or (i,j+l), that contains a zero value of C. Basically, a unit value of C would correspond to a cell full of fluid, while a zero value would indicate that the cell contained no fluid. The value $C = 0.5$ is used to detect the free-surface position (for details see Appendix B).

The wall is the most common boundary condition in bounded fluid flow problems. The *no-slip* condition, where the velocity of fluid at the wall boundary is set to zero ($U_{Wall} = 0$), is the appropriate condition for the velocity components at solid walls.

The implementation of wall boundary condition in turbulent flows starts with the evaluation of the dimensionless distance from the wall from the nearest-to-boundary node:

$$z^+ = \frac{\Delta z u_*}{\nu} \tag{3.16}$$

where Δz is the distance of the near-wall node to the solid boundary, ν is kinematic viscosity of the fluid and u_* is the friction velocity defined as:

$$u_* = \sqrt{\frac{\tau_w}{\rho}} \tag{3.17}$$

where τ_w is the wall shear stress and ρ is the density of the fluid.

A near-wall treatment depends on the position of the nearest-to-the-boundary node. If $z^+ \leq$ 11.06 the laminar viscous sublayer must be resolved (Figure 3.6). In order to resolve in all the details a viscous sublayer a very fine mesh is required, with distance from the wall to the first node $z^+ \approx 1$, which will lead to excessive computational effort being devoted to the near-wall region.

If $z^+ > 11.06$ the nearest-to-boundary node lies in the buffer layer where flow is turbulent the wall function approach is used. The wall function approach in ANSYS CFX is an extension of Launder and Spalding (1972) method. The idea of this approach is to apply boundary conditions some distance away from the wall. The wall function boundary conditions are applied in the log-law region ($z^+ > 30$), where the near wall velocity is related to the wall shear stress by the logarithmic law of the wall due to von Kármán (1930):

$$U^+ = \frac{U}{u_*} = \frac{1}{\kappa}\ln\left(z^+\right) + B \tag{3.18}$$

Equation (3.18) is known as the log-law where B is the integral constant and κ is the von Kármán constant. For the wall layers in open-channel flows, $\kappa = 0.41$ and $B = 5.29$ (*cf.* Nezu and Nakagawa 1993).

The intersection of the linear profile $U^+ = z^+$ and the log-law (Eq. (3.18)) gives us the exact value of $z^+ = 11.06$. This point lies in the buffer layer, the region between the viscous sublayer ($z^+ < 5$) and the log-law region ($z^+ > 30$). The buffer layer is a transition region between the laminar and turbulent parts of the flow (Figure 3.6).

One of the major drawbacks of the wall function approach is that predictions depend on the location of the mesh point nearest to the wall and are sensitive to the near-wall meshing. Refining the mesh does not mean that a unique solution of high accuracy will be given (Grotjans and Menter 1998). The problem of inconsistencies in the wall function approach, in the case of fine meshes, can be overcome with the use of the **Scalable Wall Function**

formulation developed by ANSYS CFX. The scalable wall function is implemented into ANSYS CFX and was used in the present study together with the SSG RSM in Research Paper III for the near-wall modelling.

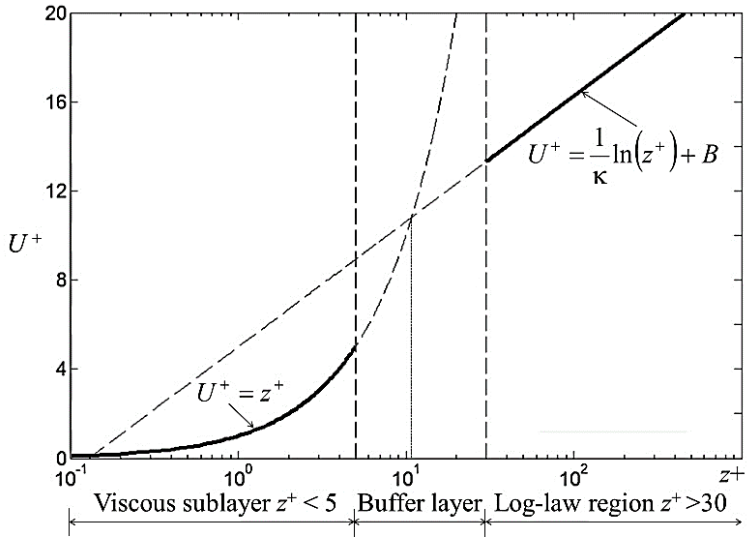

Figure 3.6: Subdivisions of the near-wall region (Modified from http://www.computationalfluiddynamics.com.au/).

The idea of the scalable wall function approach is to limit the z^+ value used in the logarithmic formulation (Eq. (3.18)) by a lower value of $\tilde{z}^+ = \max(z^+, 11.06)$, where 11.06 is the value of z^+ at the intersection between the logarithmic and the linear near-wall profiles mentioned earlier. The computed $\tilde{z}^+$ is not allowed to fall below this limit. Therefore, all mesh points are outside the viscous sublayer and all fine mesh inconsistencies are avoided.

The above mentioned wall function approaches are based on the assumptions which are problematic for flows at low *Re* number ($Re < 10^5$), as the viscous sublayer is neglected in the mass and momentum balance. For omega-based models ANSYS CFX implemented a formulation which will automatically switch from wall functions to a low-*Re* near-wall formulation as the mesh is refined. The *k*-ω model of Wilcox (Eq. (2.15)) and ω–based models, such as BSL EARSM and BSL RSM used in this study, have the advantage that the analytical expression is known for ω in the viscous sublayer. This advantage can be used in the **Automatic Wall Function** formulation. In the present study the automatic wall function approach for near-wall modelling was used together with the BSL EARSM and BSL RSM in Research Papers III and IV. The main idea behind this formulation is to blend the wall value for ω between the logarithmic and near-wall formulation. In order to achieve a smooth blending and to avoid cyclic convergence behaviour, the following expression is used:

$$\omega_{\omega} = \omega_s \sqrt{1 + \left(\frac{\omega_l}{\omega_s} \right)^2} \tag{3.19}$$

where ω_{ω} is a blend between the analytical expression for ω_l in the logarithmic region and the value ω_s in the sublayer.

While in the wall function formulation, the first node is treated as being outside of the viscous sublayer (and preferably also outside the buffer layer); in the low-*Re* approach, the location of the first mesh point is virtually moved down through the viscous sublayer as the mesh is refined. The physical location of the first node is at the wall ($z = 0$). However, the first mesh point is treated as if it were Δz away from the wall. The error in the wall function formulation results from this virtual shift. This error is always present in this wall function model.

3.3.6 Errors and uncertainty in CFD modelling

In both academic and industrial applications there is a question mark on how certain or credible are CFD numerical results on the basis of the RANS equations even with most popular or common turbulence models. The solution is always approximate since in turbulent flows the effects of turbulence are modelled by approximate theories and empirical constants, only valid on very special conditions, which generally do not match entirely the problem to be solved. Thus, there is a need to deal with uncertainties arising from the turbulence modelling.

The deficiencies or inaccuracies of CFD simulations can be related to a wide variety of errors and uncertainties. The AIAA Guide for the Verification and Validation of Computational Fluid Dynamics Simulations (AIAA 1998) and Oberkampf and Trucano (2002) provided the following definitions of error and uncertainty in CFD model:

- Error: a recognisable deficiency that is not due to lack of knowledge.
- Uncertainty: a potential deficiency that is due to lack of knowledge.

Typical known errors are:

- Numerical errors - round-off errors, iterative convergence errors, discretisation errors
- Coding errors - mistakes or “bugs” in the software
- User errors - human errors due to incorrect use of the software

Uncertainties arise because of incomplete knowledge of physical characteristics of the flow problem. The main sources of uncertainty are application uncertainties and physical model uncertainties, as for example those appearing when modelling turbulence and multiphase flows.

Application uncertainties arise due to a complex application and the precise data that is needed for the simulation which is not always available. Examples of these are uncertainties in the precise geometry definition for a computer simulation (*i.e.* simplifications of the complex geometries may be a source of error), uncertain data for boundary conditions (turbulence intensity, length scale or velocity profile at the inlet), initial guess of the flow field, the physical properties that need to be specified for the fluid and whether the flow is steady or unsteady.

Model uncertainties arise due to the difference between the real flow and the solution of the model equations. This includes errors from turbulence modelling due to the fact that the exact governing equations are not solved but are replaced with a simplified model since there is no generally valid universal model of turbulence (ERCOFTAC 2000).

Coding and user errors are the most treacherous types of errors. **Code errors** are difficult to find, as CFD software is very complex and typically involves hundreds of thousands of lines of code for a commercial product. Even a relatively simple typing error can result in disastrous consequences when incorporated into a line code.

In CFD the human factor plays an important role, since the results depend on the competence and experience of the user. The errors may arise from mistakes and carelessness of the user. The **user errors** commonly decrease with increasing experience of the user.

Discretisation errors arise due to the difference between the exact solution and a numerical solution on a chosen time and space mesh resolution. The discretisation error (or truncation error) is inherent in discretisation. This type of errors can be reduced by using progressively refined time step and space mesh size, or by using higher-order discretization schemes, when available. Finely spaced isotropic mesh distributions are ideal, but they will require an increasing amount of memory and computing time. Thus, an alternative strategy for reducing the discretisation errors is to generate anisotropic meshes with fine spacing in directions of most rapid solution variations and relatively coarse spacing in other directions. For example, the typical boundary layer meshes are compressed in the direction of the rapid solution variation, *i.e.* normal to the wall.

Discretisation errors also are affected by poor geometrical mesh quality. The error source contributions increase with anisotropic meshes. Thus, high orthogonality and low element-to-element side expansion factors are recommended in boundary layer meshes where diffusive transport dominates.

Round-off errors contribute to the numerical error in CFD result. This type of errors is due to the fact that the small difference between two values of a parameter is below the machine accuracy, where the limited number of computer digits is available for storage of a given value (around 8 for single-precision and around 16 for double-precision). In situations where these

small arithmetical differences become relevant, cancellation due to round-off may lead to severe errors. To avoid this, ANSYS CFX calculates pressure relative to a reference value, thus ensuring that the pressure values within the calculation domain are of the same order, or a double-precision is used for the calculations.

The iteration or **convergence errors** arise due to the difference between a fully converged solution and the current solution (not fully converged) after *n* number of iterations. This difference reduces as the number of iterations increases. The equations solved by CFD methods are usually iterative, and starting from the initial approximation they iterate to a final result. However, in practice the iteration process is stopped at a certain level in order to reduce the numerical effort. This level is called normalized residual target and in many CFD codes is set by default to 10^{-4}, which is considered a relatively loose convergence. For sensitive problems, such as the compound channel flow of the present study, and in order to obtain more accurate results, a residual target of 10^{-6} is required.

A measure of how well the solution is converged may be obtained by evaluation of the RMS (root mean square) or maximum-point values of the residuals. In most CFD methods, the residual is normalised allowing the comparison between different applications with different scaling. In ANSYS CFX the level of convergence is judged by RMS normalised values of the residuals, which are obtained by taking all of the residuals throughout the domain, squaring them, taking the mean, and then taking the square root of the mean. When the value of the RMS residuals becomes smaller than the residual target the simulation stops.

Since the errors and uncertainties are unavoidable aspects of CFD modelling, it is necessary to develop methods for quantifying the level of accuracy of the results. When discussing the credibility a clear distinction must be done between the meaning of the terms verification, validation and calibration. The definition of these terms is given by AIAA (1998), Roache (1998) and by Oberkampf and Trucano (2002) as:

- Verification: procedure to ensure that the program solves the equations correctly. This process quantifies the errors.
- Validation: procedure to test the extent to which the model accurately represents reality. This process quantifies the uncertainty.
- Calibration: procedure to assess the ability of a CFD code to predict global quantities of interest for specific geometries of engineering design interest. It is also used to describe the process of adjusting the values of the coefficients of a turbulence model to provide better agreement with experimental data.

The process of verification involves quantification of the errors. The code errors and user errors are ignored, it is assumed that the code is correct and the user is experienced.

The round-off errors can be estimated by comparing CFD results obtained using single-precision and double-precision machine accuracy.

The iterative or convergence error can also be estimated by investigating the residuals for quantities of interest, such as pressure drop or mass flow rate and the velocity components at several locations of interest. Difference between the values of variables of interest at various iterations provides a quantitative measure of how close the current solution is to a converged asymptotic solution.

The discretisation error is quantified by space and time refining (for transient analysis). To quantify the numerical error a Grid Convergence Index (GCI) technique was proposed by Roache (1997). For high quality CFD work three levels of mesh refinement are necessary. The discretisation error should reduce monotonically with the refining of the mesh space and time step.

The validation involves quantification of the uncertainties. Thus, Oberkampf and Trucano (2002) stated that a comparison of the CFD results with high-quality experimental data or available DNS results is necessary for quantitative assessment of the physical modelling uncertainties. If the difference between computed and experimental values is sufficiently small the CFD model is considered to be validated.

In the present study verification and validation procedures are performed for compound channel flow and will be presented further in more detail in Research Paper I.

3.4 REFERENCES

AIAA 1998 *Guide for the Verification and Validation of Computational Fluid Dynamics Simulations*. AIAA Guide G-077-1998.

ANSYS CFX 2010 *ANSYS-CFX – Introduction*. USA: ANSYS CFX Release 13.0.

ANSYS CFX 2010 *ANSYS-CFX – Solver Theory Guide*. USA: ANSYS CFX Release 13.0

Barth, T. J. and Jesperson, D. C. 1989 The design and application of upwind schemes on unstructured meshes. *AIAA* paper 89-0366.

Chapra, S. C. and Canale, R. P. 2006 *Numerical Methods for Engineers*. 5th Ed. McGraw Hill Higher Education, N.Y.

Chu, A., Fu, C. W., Hanson, A. J., and Heng, P. A. 2009 GL4D: A GPU-based Architecture for Interactive 4D Visualization. *IEEE Transactions On Visualization And Computer Graphics* **15** (6), 1587-1594.

Chung, T. J. 2002 *Computational Fluid Dynamics*. Cambridge University Press, N.Y.

ERCOFTAC 2000 *Best practice guidelines, Version 1.0*, M. Casey and T. Wintergerste (eds), ERCOFTAC Special Interest Group on "Quality and Trust Industrial CFD".

Ferziger, J. H. and Peric, M. 2001 *Computational Methods for Fluid Dynamics*. 2nd ed., Springer-Verlag.

Fromm, J. E. and Harlow, F. H. 1963 Numerical solution of the problem of vortex street development. *Physics of Fluids* **6**, 975-982.

Gentry, R. A., Martin, R. E., and Daly, J. B. 1966 An Eulerian differencing method for unsteady compressible flow problems. *J. Comput. Phys*. **1** (1), 87–118.

Grotjans, H. and Menter, F. R. 1998 Wall functions for general application CFD codes. In K. D. Papailiou et al., editor, *ECCOMAS 98 Proceedings of the Fourth European Computational Fluid Dynamics Conference*, John Wiley & Sons, 1112-1117.

Harlow, F. H. 1955 *A Machine Calculation Method for Hydrodynamic Problems*. Los Alamos Scientific Laboratory report LAMS-1956.

Harlow, F. H. 2004 Fluid dynamics in Group T-3 Los Alamos National Laboratory:(LA-UR-03-3852). *J. Comput. Phys*. **195** (2), 414–433.

Harlow, F. H. and Nakayama, P. I. 1968 *Transport of turbulence energy decay rate*. University of California Report LA-3854, Los Alamos Scientific Laboratory.

Harlow, F. H. and J. E. Welch, J. E. 1965 Numerical calculation of time-dependent viscous incompressible flow of fluid with a free surface. *Physics of Fluids* **8**, 2182–2189.

Hirt, C. W. and Nichols, B. D. 1981 Volume of fluid (VOF) method for the dynamics of free boundaries. *J. Comput. Phys.* **39** (1), 201-225.

Huang, P. G., Launder, B. E. and Leschziner, M. A. 1985 Discretisation of non-linear convection processes: a broad-range comparison of four schemes. *Comput. Methods Appl. Mech. Eng*. **48**, 1-24.

Hutchinson, B. R. and Raithby, G. 1986 A multigrid method based on the additive correction strategy. *Numer. Heat Transfer* **9**, 511-537.

Issa, R. I. 1986 Solution of the implicitly discretised fluid flow equations by operator-splitting. *J. Comput. Phys*. **62**, 40-65.

Knight, D. W., Wright, N. G. and Morvan, H. P. 2005 *Guidelines for applying commercial CFD software to open channel flow*. Report based on the research work conducted under EPSRC Grants GR/R43716/01 and GR/R43723/01.

Launder, B. E. and Spalding, D. B. 1972 *Mathematical models of turbulens*. London: Academic Press.

Leschziner, M. A. 1980 Practical evaluation of three finite difference schemes for the computation of steady-state recirculating flows. *Comput. Methods Appl. Mech. Eng*. **23**, 293-312.

Majumdar, S. 1988 Role of underrelaxation in momentum interpolation for calculation of flow with non-staggered grids. *Numerical Heat Transfer* **13**, 125-132.

Miller, T. F. and Schmidt, F. W. 1988 Use of a pressure-weighted interpolation method for the solution of the incompressible Navier–Stokes equations on a non-staggered grid system. *Numerical Heat Transfer* **14**, 213–233.

Nezu, I and Nakagawa, H. 1993 *Turbulence in open-channel flows*. In: IAHR Monograph Series. Rotterdam: Balkema.

Oberkampf, W. L. and Trucano, T. G. 2002 Verification and Validation in Computational Fluid Dynamics, *Prog. Aerosp. Sci*. **38**, 209-272.

Patankar, S. V. 1980 *Numerical Heat Transfer and Fluid Flow*. Hemisphere Publishing Corporation, Taylor & Francis Group, New York.

Patankar, S. V. and Spalding, D. B. 1972 A calculation procedure for heat, mass and momentum transfer in three-dimensional parabolic flows. *Int. J. Heat and Mass Transfer* **15** (10), 1787-1806.

Rhie, C. M. and Chow, W. L. 1983 A numerical study of the turbulent flow past an isolated airfoil with trailing edge separation, *AIAA* **21**, 1525-1532.

Richardson, L. F. and Chapman, S. 1965 *Weather prediction by numerical process*. Dover Publications.

Roache, P. J. 1997 Quantification of uncertainty in computational fluid dynamics. *Annual Review of Fluid Mechanics* **29**, 123-160.

Roache, P. J. 1998 *Verification and validation in computational science and engineering*. Hermosa Publishers, Albuqurque, NM.

Runchal, A. K. 1972 Convergence and accuracy of three finite difference schemes for a two dimensional conduction and convection problem, *Int. J. Num. Methods Eng*. **4,** 540–550.

Runchal, A. K. 2009 Brian Spalding: CFD and reality – A personal recollection. *Int. J. Heat and Mass Transfer* **52**, 4063-4073.

Spalding, D. B. 1977 *Genmix: a general computer program for two-dimensional parabolic phenomena*, Pergamon Press, Oxford.

Van Doormal, J. P. and Raithby, G. D. 1984 Enhancements of the SIMPLE method for predicting incompressible fluid flows. *Numer. Heat Transfer* **7**, 147-163.

Versteeg, H. K. and Malalasekera, W. 2007 *An introduction to computational fluid dynamics. The finite volume method*. 2nd Ed., Pearson Pearson Education Ltd., UK.

von Kármán, T. 1930 Mechanische Ähnlichkeit und Turbulenz. In *Proc. Third Int. Congr. Applied Mechanics*, Stockholm, 85-105.

CHAPTER 4

LITERATURE REVIEW

Contents

4 LITERATURE REVIEW

4.1 INTRODUCTION

This chapter presents an overview of the most important research carried out up-to-date concerning numerical modelling of open-channel flow.

A good understanding of the historical development of certain fundamental concepts in modelling open-channel flows is essential for the present study. There are many books dealing with the fundamentals of computational fluid dynamics (CFD) and specific characteristics of the open-channel flows, *e.g.* Chow 1959, Rodi 1980, Nezu and Nakagawa 1993, Pope 2000, Versteeg and Malalasekera 2007, to name a few.

In the past open-channel flows have been modelled using one-dimensional (1D) Saint-Venant equations (Saint-Venant 1871). It is a simplification from two-dimensional shallow water equations, which are also known as the two-dimensional Saint-Venant equations. These 1D models contain high level of empiricism which has been investigated experimentally, namely work carried out on the Flood Channel Facility (FCF) by Knight and Sellin (1987), Knight and Shiono (1990) and Knight (1992). Based on these experimental results a number of 1D methods were developed, such as Coherence Method (COHM) of Ackers (1993a, b), the Weighted Divided Channel Method (WDCM) of Lambert and Myers (1998) and the Shiono and Knight Method (SKM) of Shiono and Knight (1991). With advances in computer power, the interest has risen in applying more complex tree-dimensional (3D) models. However, according to Wright (2001), most of the models applied to open-channel flow are either 1D or 2D with few applications of 3D models due to the inherent difficulties found in applying CFD in natural river channels.

It should be noticed that not all the aspects of numerical modelling of open-channel flows will be highlighted in this chapter. The explanations are kept as brief as possible since all of the topics discussed can be found in more details in the textbooks mentioned above or in peer-reviewed research papers (Knight and Shiono 1990, Shiono and Knight 1991, Tominaga and Nezu 1991, Thomas and Williams 1995a, b, Sterling *et al*. 2008 and others).

The main focus of this research is the numerical modelling of compound channel flow. Most natural rivers have compound cross-section consisting of the main channel and one or more floodplains on the lateral sides, as shown in Figure 4.1.

For most of the time water flows only in the main channel. However, during floods the flow can overtop the river banks, inundating the floodplains and originating a compound section configuration.

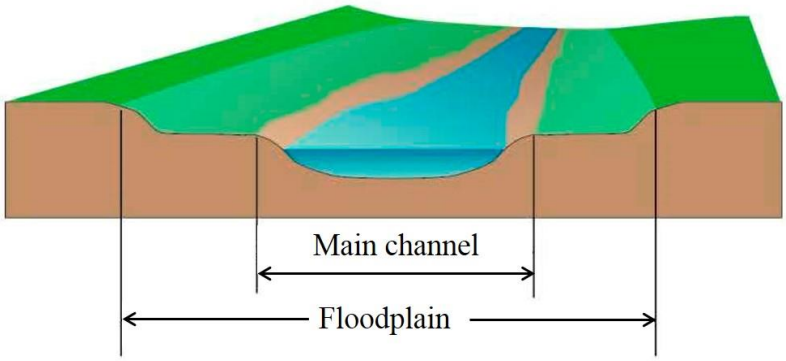

Figure 4.1: Schematic representation of natural river (adapted from http://mavensnotebook.com/dpg/Tables_Graphics.html Web. August 2014).

Compound channel flow is characterised by complicated 3D flow structures. These structures are called secondary flows and have been classified into two categories by Prandtl (1952). He distinguished the secondary flows of the first kind, which are derived from the mean flow skewing and by the centrifugal forces in curved or meandering channels, and the secondary flows of the second kind, which are generated by the non-homogeneity[1] and anisotropy[2] of turbulence (*e.g.* Nezu and Nakagawa 1993).

There are several approaches for studying secondary flows (for an overview see Nikora and Roy 2012). One of the approaches, which is widely used by researchers, is based on time-averaged streamwise vorticity equation. This equation stems from Navier-Stokes (momentum) equation (2.7) and can be derived by eliminating the pressure term through cross differentiation (Nezu and Nakagawa 1993). These authors focused their study of Prandtl's second kind secondary flows, based on equation for streamwise vorticity Ω_1, which, for steady and uniform flows in straight channels, *i.e.* $\partial/\partial t = 0$ and $\partial/\partial x = 0$, can be expressed as:

$$U_2\frac{\partial\Omega_1}{\partial x_2}+U_3\frac{\partial\Omega_1}{\partial x_3}=\frac{\partial^2}{\partial x_2\partial x_3}\left(\overline{u_3'u_3'}-\overline{u_2'u_2'}\right)+\left(\frac{\partial^2}{\partial {x_2}^2}-\frac{\partial^2}{\partial {x_3}^2}\right)\overline{u_2'u_3'}+\nu\nabla^2\Omega_1 \quad (4.1)$$

where

[1] Turbulence is said to be homogeneous when the fluctuating velocity field is statistically homogeneous (*i.e.* all statistics are invariants under a shift in position or, in other words, under translations) (*e.g.* Pope 2000).

[2] Turbulence is said to be isotropic when the fluctuating velocity field is statistically invariant to both, translations (homogeneous), rotations and reflections (*i.e.* all statistics are invariants) which implies zero mean velocity gradients (*e.g.* Pope 2000).

$$\Omega_1 = \frac{\partial U_2}{\partial x_3} - \frac{\partial U_3}{\partial x_2} \tag{4.2}$$

Nezu and Nakagawa (1993) concluded that secondary currents of the second kind are generated as a result of differences between the first and the second RHS terms of equation (4.1). The magnitude of the secondary flows of the second type is about 2-3% of the maximum streamwise velocity (Nezu and Rodi 1985), however, they have a major impact on the mean flow and turbulence structures.

In order to understand the behavior of these secondary flow structures, it is helpful to investigate simpler cases, such as the inbank flow in straight rectangular and trapezoidal open-channels. Hence, the main aspects on numerical modelling of straight simple and compound channel flows are briefly summarised in this chapter. However, it should be kept in mind that natural river channels are usually neither rectangular, nor prismatic.

4.2 INBANK FLOWS IN STRAIGHT CHANNELS

In order to understand the more complex 3D turbulent structures of compound channel flow, a basic understanding of inbank flows is essential. The aspect ratio, *B*/*H*, defined as the ratio between the width of the channel *B* and the depth of the flow *H*, and the geometry have an impact on the flow structures in open-channel flows. The main characteristics of flow in straight inbank channels are briefly reviewed in this subchapter.

4.2.1 Rectangular open-channels

The secondary currents in closed air ducts have been measured by several researchers, e.g. Brundrett and Bains (1964), Gessner and Jones (1965) and Perkins 1970) using Hot Wire Anemometer (HWA) and Melling and Whitelaw (1976) using a Laser Doppler Anemometry (LDA). These results contributed to the future development of Algebraic Stress Model (ASM) and Reynolds Stress Model (RSM).

Accurate measurements of secondary currents in rectangular open-channel flow have been carried out by Nezu and Rodi (1985). They have measured streamwise (*u*) and vertical (*w*) velocities using LDA and calculated the transverse velocity (*v*) from the equation of continuity for fully developed flow. The results are presented in Figure 4.2.

Secondary flow pattern in closed duct is symmetric, representing two symmetric contra-rotating secondary cells with regard to the corner bisector (Figure 4.2(a)). In open-channel flow two main secondary cells are observed. Near the free surface ($z/h \geq 0.6$), a large-scale secondary-current cell called “free-surface vortex” is generated which transports momentum

and energy from the side wall towards the channel centre (Figure 4.2(b)). At the channel bottom, a smaller secondary cell called "bottom vortex" is formed which rotates in the opposite direction to the free-surface vortex.

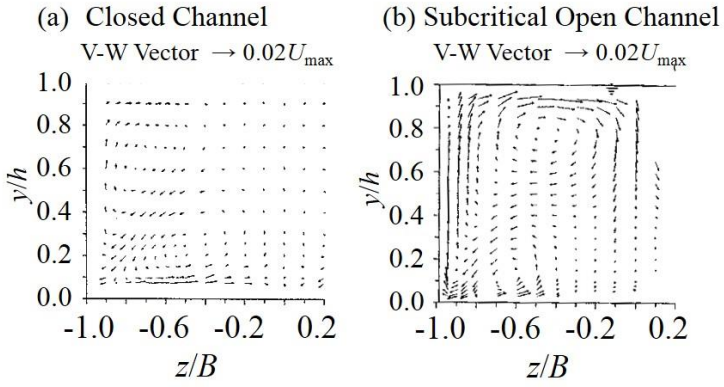

Figure 4.2: Measured secondary-current velocity vectors at a section in: (a) closed duct; (b) open-channel (after Nezu 2005).

Nezu and Rodi (1985) found that the cause for the velocity dip at the channel center is the free-surface vortex due to the transport of momentum from the free surface to the mid-depth of the channel. They also noticed that the pattern of the secondary flows depends on the aspect ratio, and hence classified rectangular channel as narrow (B/H < 5) or as wide (B/H > 5) channels.

Further investigations on the secondary currents in rectangular channels were followed up by Tominaga *et al*. (1989) using Hot Film Anemometry (HFA). They studied the effects of geometry and wall roughness on the pattern of secondary currents. Figure 4.3 shows the distribution of streamwise velocity and secondary currents in rectangular open-channel. These authors concluded that the streamwise velocity, the turbulence intensities, the Reynolds stresses and the boundary shear stress are affected by the secondary currents. The maximum value of the secondary flows was nearly equal to $0.015U_{max}$.

Naot and Rodi (1982) simulated rectangular open-channel flows using the ASM and investigated the effect of the aspect ratio on the isovels of the streamwise velocity and on the formation of the secondary currents. The calculated secondary current streamlines are illustrated in Figure 4.4. The numerical results agree well with the experimental data shown in Figure 4.2. The pattern of secondary currents simulated by ASM shows a strong free-surface vortex, which

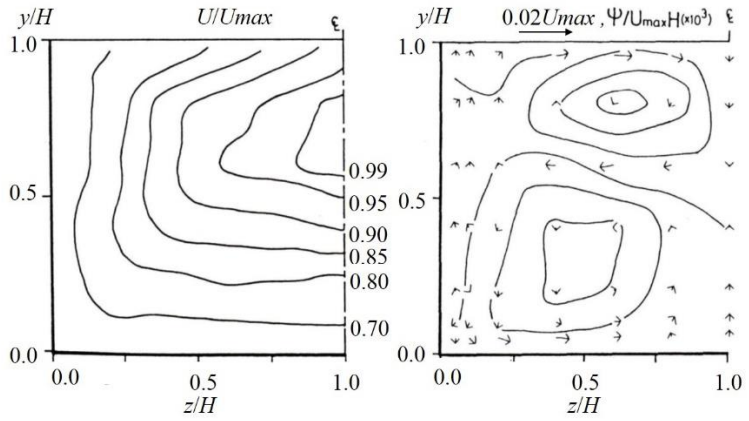

Figure 4.3: Isovels of streamwise velocity and secondary currents in rectangular open-channel for aspect ratio 2 (adapted from Tominaga *et al*. 1989).

transports high momentum from the water surface downwards, and a weak bottom vortex, which transports low momentum from near the walls towards the channel centre. As the aspect ratio increases, the free-surface vortex becomes stronger and suppresses the lower bottom vortex. For aspect ratios below 2 the bottom vortex becomes dominant. When the aspect ratio is below 1, then the free-surface vortex splits into smaller and weaker vortices.

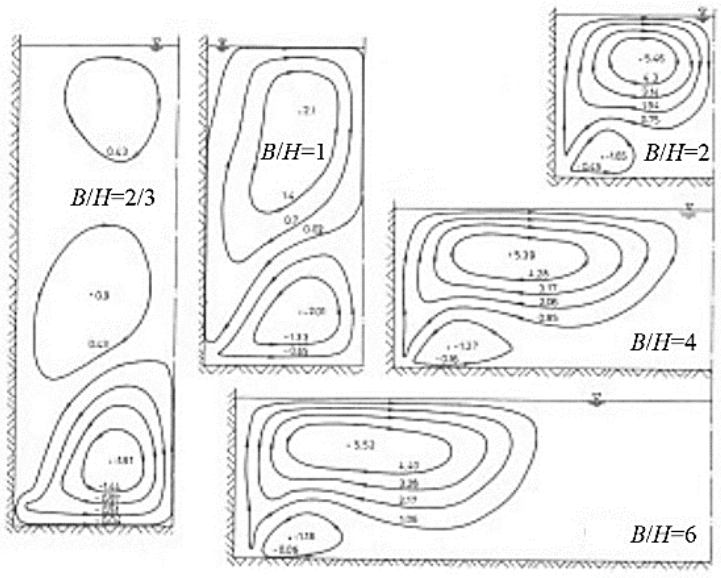

Figure 4.4: Calculated secondary current streamlines in open-channels under various aspect ratios (after Naot and Rodi 1982).

Following Naot and Rodi (1982), many researches simulated open-channel flows using ASM (Krishnappan and Lau 1986, Naot *et al*. 1993, Naot *et al*. 1996). For numerical simulations of 3D turbulent open-channel flows, the *k*-ε model has been the preferred choice (Fischer-Antze *et al*. 2001, Wu *et al*. 2000, Rameshwaran and Naden 2003). However, according to Pezzinga (1994) and Cokljat and Younis (1995) the *k*-ε model cannot reproduce secondary flows.

Reece (1977) was the first who simulated square duct and open-channel flow using RSM based on the work of Launder *et al*. (1975). Later, Cokljat and Younis (1995) have simulated rectangular open-channel flow for three aspect ratios using RSM and compared their results with the experimental data of Tominaga *et al*. (1989). The calculated and measured secondary-velocity vectors are shown in Figure 4.5. The RSM model of Cokljat and Younis (1995) agrees well with the experimental data of Tominaga *et al*. (1989). This RSM was able to predict the number and the pattern of the secondary flows, namely free-surface vortex and bottom vortex. Cokljat and Younis (1995) noticed that with the increase of the aspect ratio the free-surface vortex elongates until it separates into two contra-rotating vortices. This behaviour was well captured by the experiment and reproduced by model.

Cokljat and Younis (1995) also studied the effect of the secondary flows on the primary velocity field. Figure 4.6 presents the predicted and measured contours of the streamwise velocity.

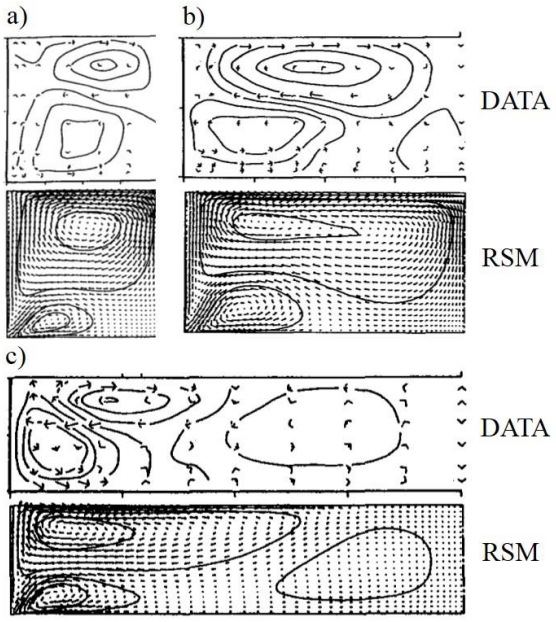

Figure 4.5: Predicted (RSM) and measured seconary flow in rectangular open-channel: Aspect ratios (a) 2; (b) 3.94; (c) 8 (adapted from Cokljat and Younis 1995).

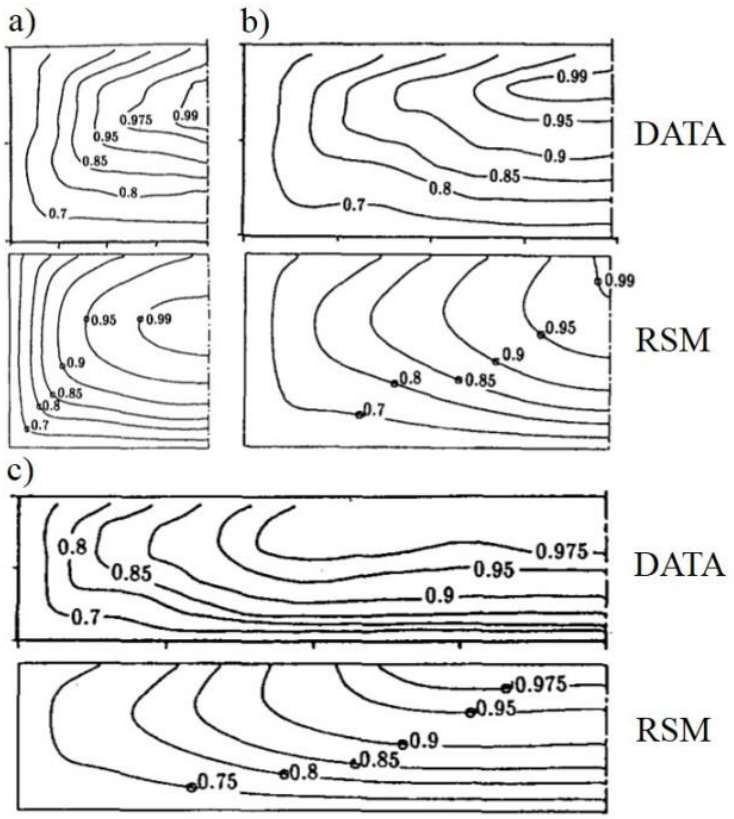

Figure 4.6: Contours of primary velocity in rectangular open-channel: Aspect ratios (a) 2; (b) 3.94; (c) 8 (adapted from Cokljat and Younis 1995).

The free-surface vortex transports the slow fluid from the vicinity of the side walls into the centre of the channel causing the distortion of the isovels, and thus, the maximum velocity occurs below the free surface. In this study Cokljat and Younis (1995) have concluded that for $B/H = 2$ the position of the maximum velocity predicted by RSM was slightly over predicted in comparison to the experimental data, and that for higher aspect ratios the agreement was less satisfactory.

Cokljat and Younis (1995) also have studied the effect of the normal-stress anisotropy since the anisotropy is the driving force for the secondary currents (see Eq. (4.1)). They pointed out the shaded line in Figure 4.7, which is a zone where $\overline{v'v'}$ and $\overline{w'w'}$ are equal. They noticed that in closed ducts this line would lie along the corner bisector. But the presence of the free surface in the model adds an asymmetry to the flow. The position of this shaded line predicted by the model matched the measured one, however some overprediction was observed near the free surface.

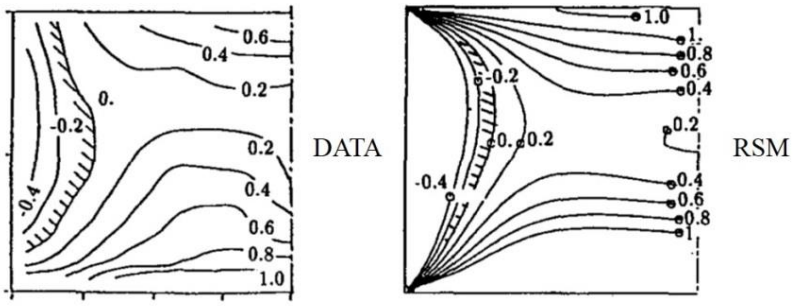

Figure 4.7: Predicted (RSM) and measured turbulence anisotropy for open rectangular channel with aspect ratio = 2 (adapted from Cokljat and Younis 1995).

Besides the already known free-surface vortex and bottom vortex, Grega *et al*. (1995) and Hsu *et al*. (2000) have reported the existence of the inner secondary currents in the rectangular open-channels, which occur at the junction of the free surface and side wall. Despite the magnitude of this small-sized vortex is about 1% of the mean streamwise velocity, it affects the mean flow and turbulence structures (Grega *et al*. 1995).

Kang and Choi (2006a) continued the study of the rectangular open-channels using RSM. The purpose of their study was to develop a RSM that is capable to reproduce detailed mean flow and turbulence structure including inner vortex. The results, simulated by RSM of Kang and Choi (2006a), were compared with experimental data by Nezu and Rodi (1985) and also with another RSM results by Cokljat (1993) and with Large Eddy Simulation (LES) results by Shi *et al*. (1999).

The isovels of the streamwise mean velocity predicted by RSM of Kang and Choi (2006a) were in a good agreement with the experimental data and with other numerical models, and bulged towards the juncture between the sidewall and free surface (see Figure 4.8). This bulging was due to the presence of the inner vortex that was not seen in other models and measurements.

In the secondary current vectors (Figure 4.8) the free surface vortex and the bottom vortex are observed. The overall pattern and the magnitude of the secondary currents simulated by the Kang and Choi (2006a) RSM are in a good agreement with measured data and other RSM and LES models. The maximum magnitude of the secondary flows is around 2% of the maximum streamwise velocity, which is consistent with the previous studies by Naot and Rodi (1982), Tominaga *et al*. (1989) and Cokljat and Younis (1995).

However, the inner vortex is observed only in the Figure 4.8(a), *i.e*. the RSM results produced by Kang and Choi (2006a). Experimental data and two other numerical models did not

reveal this small inner vortex probably due to poor resolution in the experiments and coarse computational grid (Hsu *et al*. 2000).

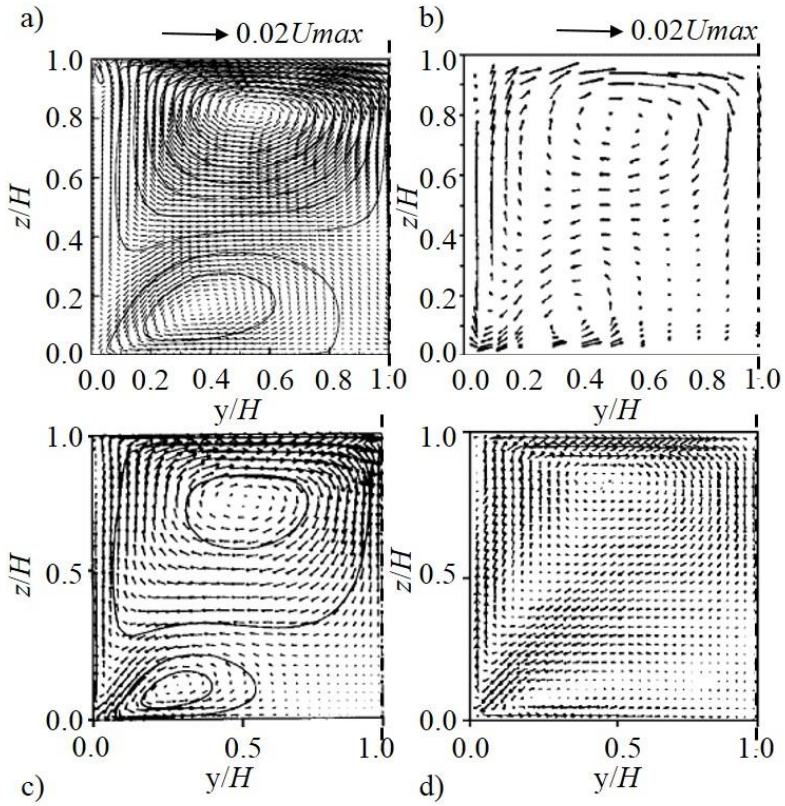

Figure 4.8: Secondary current vectors: (a) RSM by Kang and Choi (2006a); (b) experiment Nezu and Rodi (1985); (c) RSM by Cokljat (1993); and (d) LES by Shi *et al*. (1999) (adapted from Kang and Choi 2006a).

A good agreement was also observed by Kang and Choi (2006a) between turbulence intensities u' and w' and experimental data. Profiles of the bed shear stress at the side wall were analysed. The shear stress at the free surface was 60% higher than the mean value as a result of the inner secondary current occurring at that region, *i.e*. at the juncture of the free surface and the side wall.

4.2.2 Trapezoidal open-channels

In addition to the rectangular channels, Tominaga *et al*. (1989) also measured three dimensional flow in open smooth trapezoidal channels with different side slope angles (Figure 4.9).

They observed that one more vortex is generated between the side wall and the free-surface vortex. Tominaga *et al*. (1989) concluded that when the side slope angle reduces, the free-surface vortex gets weaker and the bottom vortex expands. They did not observe the velocity

dip phenomenon observed in rectangular channels. It was revealed that the maximum value of the secondary currents was of the same magnitude as that in the rectangular channel.

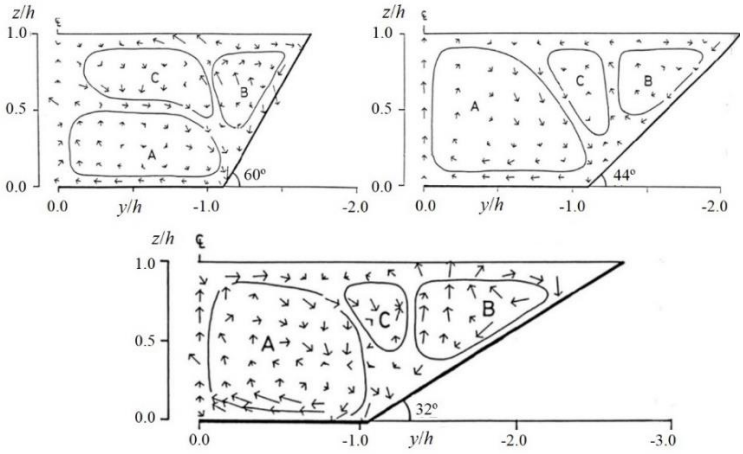

Figure 4.9: Secondary current vectors in smooth trapezoidal channels (adapted fromTominaga *et al*. 1989).

Knight *et al*. (2007) have applied the Shiono and Knight method (SKM) to calculating the lateral distributions of depth-averaged velocity U_d and boundary shear stress τ_b for flows in straight prismatic trapezoidal channels. During this study they obtained accurate distributions of U_d, however distributions of τ_b did not always match the experimental data due to the use of a constant value of friction factor, f, within each panel. To achieve a high accuracy in the analytical τ_b results, Knight *et al*. (2007) have adopted linearly varying f values and two additional panels for the modelling. They also have concluded that the number of secondary current cells in a simple trapezoidal channel depends on the aspect ratio $2b/H$ (for definition of b and H see Figure 4.12). For aspect ratios less than 2.2, three secondary current cells were observed; two of them were located at the side slope and one over the bottom of the channel. For $2b/H \geq 4$, the number of the secondary cells was found to be four, with two cells situated over the side slope and two over the flat bottom. The schematic representation of the pattern of the secondary current cells is presented in Figure 4.10.

Knight *et al*. (2005) applied a state-of-the-art CFD workbench software to explore the physics within open-channel flows. In their research work they applied three different turbulent models, namely the *k*-ε, Reynolds Stress model by Speziale, Sarkar and Gatski (SSG) by Speziale *et al*. (1991) and Reynolds Stress ω or SMC-ω (implemented in ANSYS-CFX) models to trapezoidal channel. The three models were compared with LES by Wright *et al*. (2004). The results revealed that *k*-ε did not show any recirculation, while some bulging of the velocity isovels was

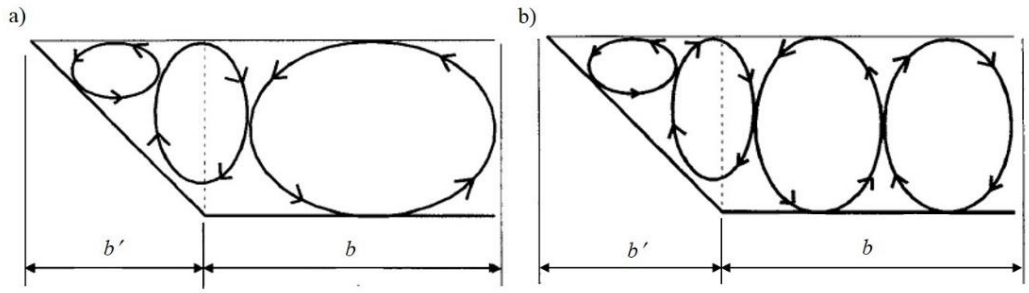

Figure 4.10: Secondary flow cells pattern in smooth trapezoidal channels with different aspect ratio: (a) $2b/H \leq 2.2$; (b) $2b/H \geq 4$ (adapted fromKnight *et al*. 2007).

observed in the SSG, and the bulging in the SMC-ω was found to be more prominent at the middle of the side slope; the three secondary cells were present for the Reynolds stress models. However, there was no evidence of the velocity dip phenomenon.

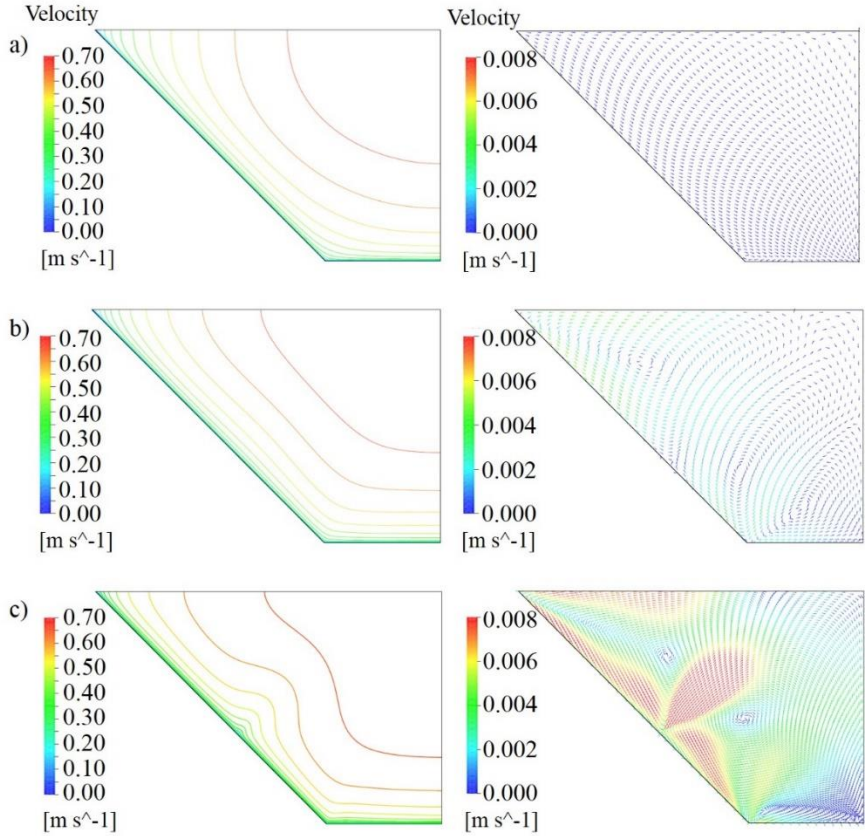

Figure 4.11: Velocity contours and secondary velocity vectors in smooth trapezoidal channels: (a) *k*-ε; (b) SSG; (c) SMC-ω (adapted from Knight *et al*. 2005).

To overcome this issue, a modified free surface boundary condition was applied in their study, based on Celik and Rodi (1984), which yields a higher value for turbulent eddy dissipation and reduces turbulence kinetic energy near the free surface. The use of modified free surface boundary condition, affected the location of the secondary flows and the position of the bulging in SMC-ω was slightly shifted up than before. In the SSG results was verified that the maximum of the velocity was beneath the water surface. The results from three models using the modified boundary condition are presented in Figure 4.11. The LES results showed a similar bulging of the isovels on the side slope of the trapezoidal channel as in the SMC-ω model. LES results also revealed an additional bulging near the bottom of the channel, and the magnitude of the *v* and *w* velocity components was greater than the results obtained by other models in this research.

4.3 FLOWS IN STRAIGHT COMPOUND CHANNELS

Since the 1960s, compound channels have been studied intensively and a brief summary of the main findings in straight compound channels is presented in this subchapter. The complexity of turbulent structures in compound channel flow is higher than in a single rectangular or trapezoidal open-channel. The straight compound channels are classified into symmetric or asymmetric, and according to the shape of the cross-section – into rectangular or trapezoidal.

A schematic representation of compound channels and the geometric variables are presented in Figure 4.12, namely, the total channel width, B; the top main channel width, B_{mc}; the floodplain width, B_{fp}; the half of the main channel bottom width in symmetric channels and the

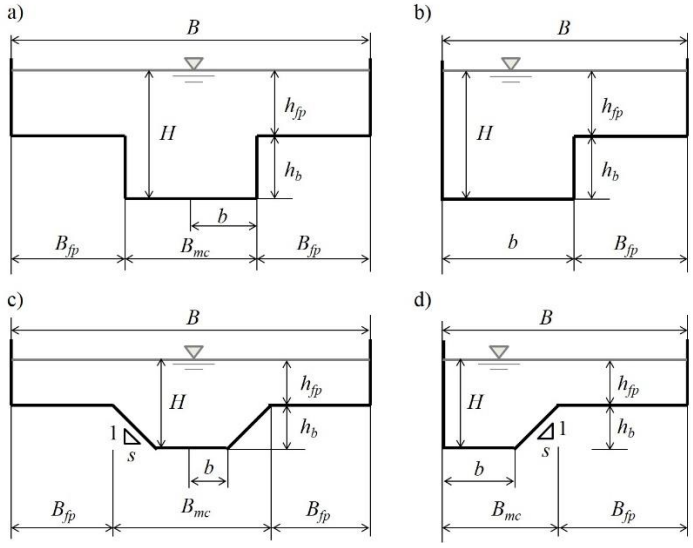

Figure 4.12: Schematic representation of compound channel: (a) symmetric rectangular compound channel; (b) asymmetric rectangular compound channel; (c) symmetric trapezoidal compound channel and (d) asymmetric trapezoidal compound channel.

main channel bottom width in asymmetric channels, b; and the side slope of the main channel 1:s = vertical:horizontal. Furthermore, H and h_{fp} correspond to the main channel and the floodplain water depths, and h_b denotes the main channel bankfull height.

Figure 4.13 represents the typical hydraulic parameters and turbulent structures in symmetric prismatic compound channel (after Shiono and Knight 1991). A strong lateral shear layer is present due to the difference between the faster flow in the deeper main channel and the slower flow in the shallower floodplain. This shear layer produces horizontal vortices with vertical axes at the edge between the main channel and the floodplain, which transport the high momentum fluid from the main channel towards the floodplain. These vertical vortices were first identified and photographed by Sellin (1964). There are also streamwise vortices (Prandtl's second kind secondary flows) with horizontal axes present in the main channel, which also contribute to the momentum exchange between the main channel and the floodplain.

Relative depth, $h_r = h_{fp} / H$, plays an important role in compound channel flows. Depending on the relative depth value, one form of the vortices may dominate another. Thus, for $h_r < 0.3$, the horizontal vortices are dominant, which can extend to the entire width of the floodplain, even in natural rivers (Knight 2013). For higher relative depths, that is, $h_r > 0.4$, the streamwise vortices tend to dominate the flow, thus making horizontal vortices smaller, as presented in Figure 4.13.

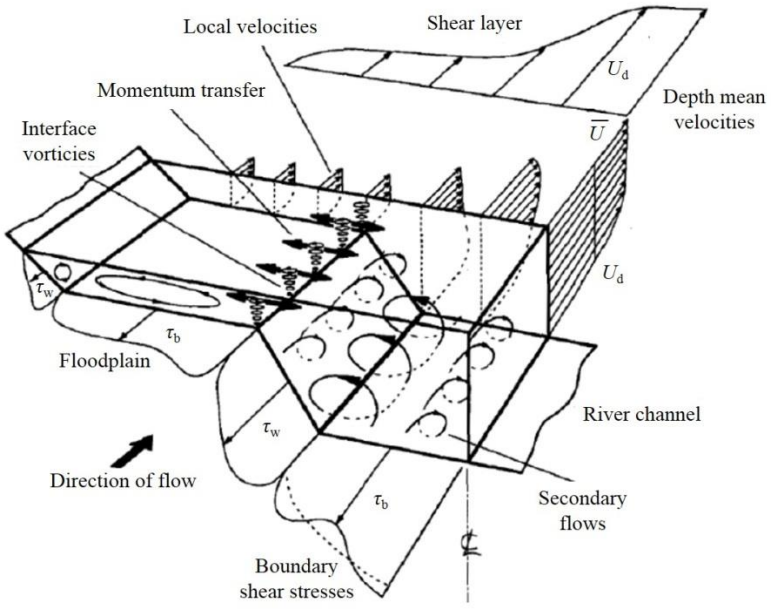

Figure 4.13: Hydraulic parameters associated with overbank flow in a trapezoidal compound channel (after Shiono and Knight 1991).

4.3.1 Rectangular compound channels

Much research has focused on rectangular compound channels. This type of channel has been studied by many researches to understand the interaction mechanisms at the interface region between the main channel and the floodplain.

Myers (1978) measured the shear stress distributions across the entire cross-section of the compound channel using a Preston tube. He considered the entire cross-section in equilibrium and identified the acting forces. Taking into account a momentum balance separately in the main channel and in the floodplain, Myers (1978) identified an additional shear stress acting in the vertical interface between the main channel and the floodplain due to momentum transfer from the main channel to the floodplain and called it apparent shear stress, τ_a. He also found that the apparent shear stress is higher at the lowest depth and suggested that the apparent shear stress may represent the intensity of the vorticity in the mixing region.

The apparent shear stress, τ_a, may be obtained by the integration over the width of a subsection, the floodplain (B_{fp}) or the main channel (B_{mc}), of the depth-averaged momentum equation in the streamwise direction (which stem from the continuity equation (2.6) by integrating over the flow depth). In the vertical interface between the main channel and the floodplain τ_a is defined as (more details can be found in Fernandes 2013):

$$\tau_a = -\rho\left(\overline{u_1' u_2'}\right)_d\Big|_{B_{mc}} + \rho U_d V_d\big|_{B_{mc}} \tag{4.3}$$

The first RHS term of equation (4.3) represent the contribution of the shear layer to the overall shear stress in each subsection, and the second term represents the secondary flow contribution (*cf.* Shiono and Knight 1991).

Modern techniques have enabled the measurements of secondary currents in compound channel flows. Tominaga and Nezu (1991) performed accurate measurements using fiber-optic two-component LDA and investigated the three-dimensional turbulent structure in rectangular compound channel. They have studied four cases, namely, three relative depths, h_r = 0.25; 0.5 and 0.75, with smooth boundaries and one relative depth, h_r = 0.5, with rough floodplain.

For h_r = 0.25 and h_r = 0.5, a pair of longitudinal vortices was recognised near the interface region, namely a main channel and a floodplain vortex, as well as a free surface vortex observed near the side wall of the main channel. For h_r = 0.75, the floodplain vortex appeared stronger and reached the free surface. They found that the magnitude of the secondary flows reaches approximately 4% of the maximum streamwise velocity. This magnitude is higher than the magnitude of secondary currents observed in the inbank case, which reaches typically 2-3%, as was seen in subchapter 4.1. Turbulence intensities, Reynolds stresses and bed shear stress were

also obtained. Using the results of turbulence intensities, they calculated the turbulence kinetic energy (TKE) and anisotropy of turbulence. The TKE results revealed that the total magnitude of turbulence increases in the vicinity of the interface between the main channel and the floodplain. The anisotropy of turbulence determines the structure of secondary currents driven by turbulence showing a complicated behaviour near the junction. Tominaga and Nezu (1991) concluded that the roughened floodplain did not affect the structure of the secondary currents.

Nezu (1994, 1996) extended the study of Tominaga and Nezu (1991) to various geometries and roughness using fiber-optic two-component LDA. His results agree well with those of Tominaga and Nezu (1991).

Nezu *et al*. (1999) using LDA and Particle Image Velocimetry (PIV) measurements studied further the pattern and the strength of the coherent horizontal vortices for various relative depths between 0.16 and 0.67. They found that for relative depths higher than 0.375, a pair of horizontal vortices is observed near the junction. For lower h_r, a unique horizontal vortex develops at the interface region between the main channel and the floodplain (*cf*. Figure 4.14).

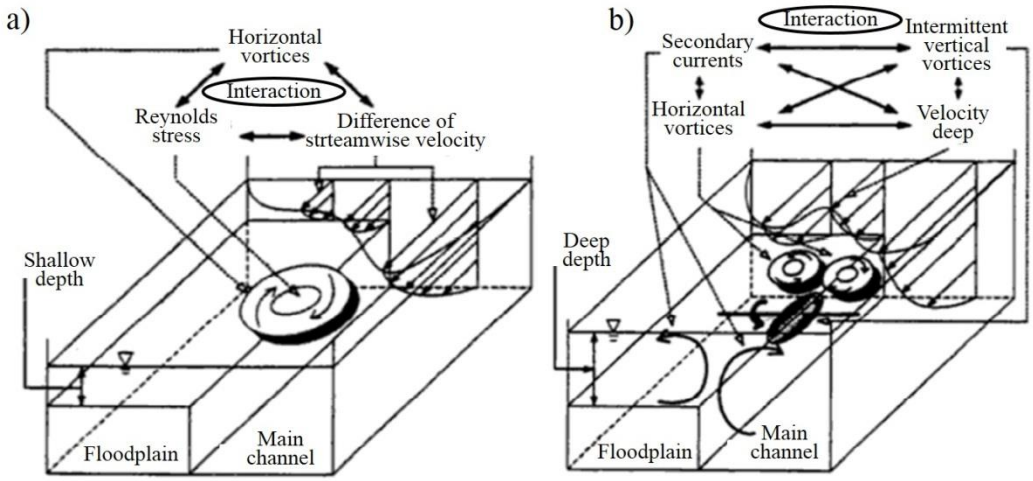

Figure 4.14: Schematic representation of flow field in: (a) a shallow depth flow; (b) deep depth flow (adapted from Nezu *et al*. 1999).

Keller and Rodi (1989) were the first to incorporate a two-dimensional depth-averaged form of the *k*-ε model in a numerical study to predict flow characteristics in compound channels. They modelled symmetric and asymmetric rectangular compound channels and compared the depth-averaged velocity and bed shear stress against the existing laboratory data. The agreement between the predicted distributions and the experimental data was generally quite good. However, there was some deviation in the interaction region from the experimental data. They

concluded that this deviation results from the under-prediction of transverse mixing in regions with an abrupt change in depth and that it cannot be accounted for correctly in their model.

The non-linear *k*-ε model, first proposed by Speziale (1987), has employed to predict secondary currents in compound channel flows by Pezzinga (1994), Lin and Shiono (1995) and Sofialidis and Prinos (1998). The latter used a low-Reynolds non-linear *k*-ε model. Although these models successfully predicted both streamwise velocity and the secondary currents, especially the two vortices generated at the interface between the main channel and the floodplain, they could not accurately simulate the velocity-dip phenomenon. The non-linear *k*-ε model did not predict correctly the strength of the secondary currents. The measured and predicted isovels of the streamwise velocity are presented in Figure 4.15.

Naot *et al*. (1993) extended the ASM of Naot and Rodi (1982) to simulate asymmetric rectangular compound channel flows with smooth and rough floodplain and symmetric smooth and wide compound channels with relative depth ratios of h_r = 0.25, 0.50, 0.75. They compared the predicted results of streamwise velocity, wall shear stress distribution, TKE and secondary currents with experimental data of Tominaga and Nezu (1991). The results were in a good agreement although some differences were recognised in the secondary currents. For h_r = 0.5 comparison revealed that calculated values of *k* are too small due to the choice of the model coefficients adopted in their model.

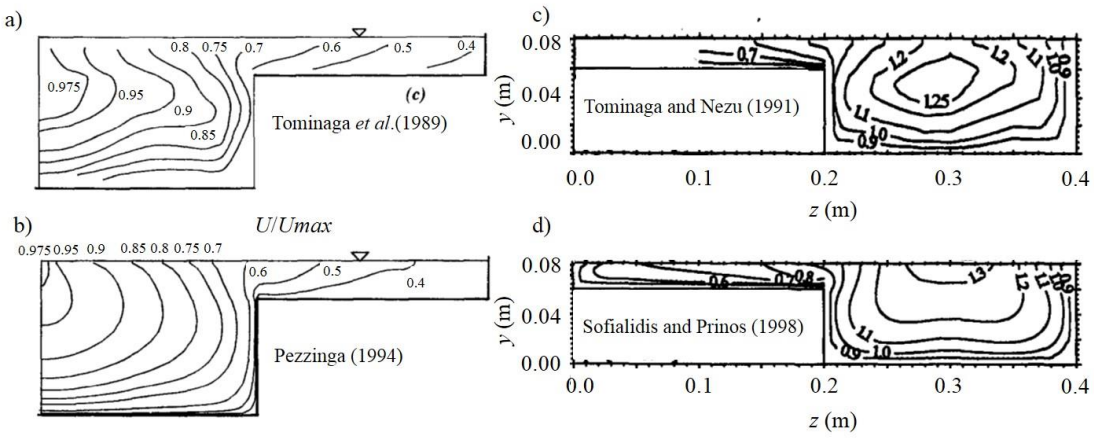

Figure 4.15:Experimental and computed contours of the streamwise velocity: (a) data by Tominaga *et al*. (1989); (b) model by Pezzinga (1994); (c) data by Tominaga and Nezu (1991) and (d) model by Sofialidis and Prinos (1998) (adapted from Pezzinga (1994) and Sofialidis and Prinos (1998)).

Shiono *et al*. (2003) studied the effect of secondary flows on solute transport processes in a compound channel using linear *k*-ε model and the ASM by Launder and Ying (1973). The previous study by Lin and Shiono (1995), where they investigated solute transport in a

compound channel comparing the linear and non-linear *k*-ε models, revealed a significant difference in solute distributions with and without secondary flows. Shiono *et al*. (2003) concluded that the streamwise velocity and secondary flow in the shear layer using ASM of Lin and Shiono (1995) were in a good agreement with the experimental data. However, the inclination angle of two vortices from the junction between the main channel and the floodplain was steeper than the measured one. The linear *k*-ε model did not predict secondary flows and gave poor quality predictions. For shallow flow, both models failed in predicting two concentration peaks. Shiono *et al*. (2003) highlighted the importance of secondary currents modelling in order to accurately predict the primary velocity.

Cokljat and Younis (1995) applied their RSM to symmetric and asymmetric compound channels. The experimental data from Tominaga and Ezaki (1988) and Tominaga and Nezu (1991) were used for the model validation. It was found that RSM captured the secondary currents and even smaller vortices. The position, where free surface and main channel vortices meat, was predicted almost exactly by the model. The effect that secondary currents have on the primary flow was well predicted, where a significant bulging of the isovels at the junction between the main channel and the floodplain was present (*cf*. Figure 4.16). The velocity-dip phenomenon was captured by the RSM. Cokljat and Younis (1995) suggested that the latter was not reproduced in the work of Naot *et al*. (1993) due to underprediction of the levels of turbulence anisotropy by that model. They also compared the predicted and measured boundary shear stress distribution for the symmetric compound channel. The correspondence was fairly satisfactory, especially for the floodplain, where the RSM reproduced the waviness of the experimental data. The variation of the total discharge with different relative depths was well predicted.

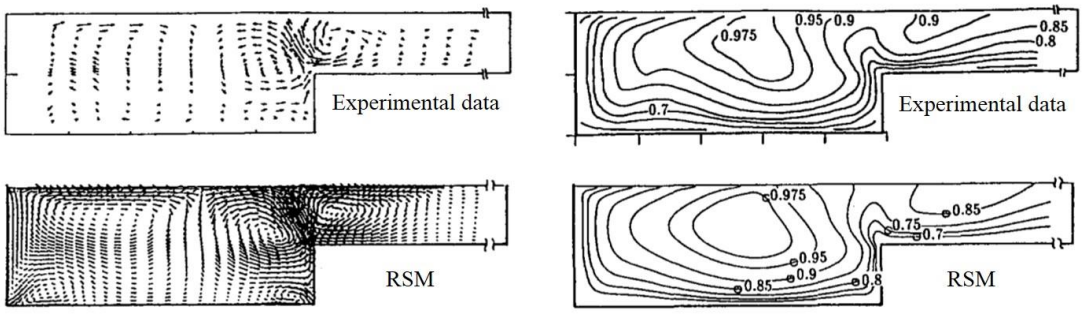

Figure 4.16: Vector plots of the secondary currents and contours of the primary velocity in asymmetric compound channels for h_r = 0.5 (adapted from Cokljat and Younis 1995).

Similar calculations have been made by Kang and Choi (2006b). Their RSM was capable of predicting the velocity dip, number and position of the secondary currents and the distribution of the streamwise velocity. It also produced results that were in good agreement with experimental data of Tominaga and Nezu (1991). The maximum magnitude of the secondary currents was about 3% for the h_r = 0.5. The authors have noticed that the secondary currents at the junction between the main channel and the floodplain become weakened as the relative depth decreases. This aspect is reflected in the angle of inclination of the upflow at the junction, which increases with decreasing the relative depth (Kang and Choi 2006b). For shallow flow, h_r = 0.25, the vertical structure in the main channel becomes similar to that observed in the rectangular channel (*cf.* Figure 4.8). The main channel vortex increases its intensity and the floodplain vortex decreases with the decrease of the relative depth. Kang and Choi (2006b) also compared the wall shear stress distribution and concluded that the RSM overestimates bottom shear stress in the main channel. However, in the floodplain, the simulated bottom shear stress was in a good agreement with the experimental data.

Thomas and Williams (1995a) were the first to apply LES to study the flow and turbulence structure in a compound open-channel. Their work has been complemented by the study of Cater and Williams (2008). Both of these studies simulated an asymmetric rectangular compound channel using LES for a relative depth of h_r = 0.5. The difference between these models lied in the longer calculation domain and in finer mesh for Cater and Williams (2008) in comparison to the model of Thomas and Williams (1995a). They have predicted mean streamwise velocity distribution, secondary currents, bed shear stress distribution, turbulence intensities, TKE, and calculated lateral distribution of apparent shear stress. In general, the results were in a good agreement with the experimental data of Tominaga and Nezu (1991). However, some deviation from the data was observed. Namely, the bed shear stress predicted by LES, as well as the ASM of Naot *et al*. (1993), differ significantly from the experimental data. The position and number of secondary currents was captured by LES in both studies. The maximum magnitude of the secondary flows was around 3.7% of the maximum primary velocity. The upflow at the junction between the main channel and the floodplain was inclined at the angle of 20º from the vertical. The authors of both studies have noticed that the distortion of the isovels is more pronounced in the experimental data (*cf.* Figure 4.17).

The previous studies of Thomas and Williams (1995a) and Cater and Williams (2008) have been complemented by the work of Kara *et al*. (2012). The latter have employed LES to study the effects of the floodplain depth on the flow in an asymmetric compound channel. They have studied two relative depths, namely, h_r = 0.25 and h_r = 0.5. With an increase in recent years in the computational power, this study was run with finer mesh compared to the previous cases.

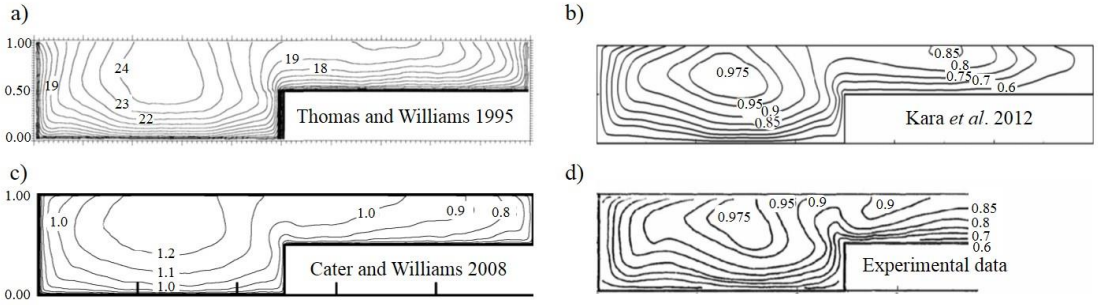

Figure 4.17: Contours of the streamwise velocity in asymmetric compound channels for h_r = 0.5 (adapted from Thomas and Williams 1995a, Cater and Williams 2008, Kara *et al*. 2012).

Kara *et al*. (2012) predicted secondary currents, the time-averaged streamwise velocity, distribution of shear Reynolds stresses and bed shear stress distribution.

Overall a good agreement between the experimental data of Tominaga and Nezu (1991) and simulated results was obtained, confirming the accuracy of the method for these flows (*cf.* Figure 4.17). Kara *et al*. (2012) compared the depth-averaged streamwise velocities obtained by LES with calculated by analytical solution of Shiono and Knight Method (SKM), and concluded that the analytical approach to their problem requires calibration of the lateral eddy viscosity coefficient, λ, and the secondary current parameter, Γ. The authors have examined the terms contributing to the lateral momentum transport and quantified the anisotropy, generation term of streamwise vorticity and apparent shear stress.

Kara *et al*. (2012) demonstrated that the anisotropy in compound channel at the interface between the main channel and the floodplain leads to the formation of a vortex pair. The apparent shear stress (see Eq. (4.3)) was greater for the shallow floodplain case. The generation term (first RHS term in Eq. (4.1)) was found to be more significant at the interface for shallow case, where the peak values extend to the free surface. The authors suggested that the extent and magnitude of the secondary current generation term influences the angle of inclination of secondary currents.

Furthermore, recently Xie *et al*. (2013) used LES to simulate asymmetric rectangular compound channel. In this study the distributions of the mean velocity and secondary flows, boundary shear stress, turbulence intensities, TKE and Reynolds stresses were in a good agreement with the experimental data. They investigated the instantaneous flow fields and large-scale vortical structures, and concluded that a stronger turbulent flow occurs in the near-wall region and a significant lateral transport of momentum is present.

4.3.2 Trapezoidal compound channels

For the purposes of establishing an experimental database for validating open-channel flow phenomena in numerical models, the Science and Engineering Research Council (SERC) built the Flood Channel Facility (FCF) in 1986 at Hydraulic Research ltd., located in Wallingford, UK. A large number of detailed measurements of various channel geometries, including trapezoidal compound channel, were carried out at the FCF flume. For the details of the facility and on the experiments the reader can consult Knight and Sellin (1987).

One of the first outputs of this program was the work presented by Knight and Shiono (1990). This study includes highly accurate measurements of the primary velocity, the turbulent intensities, TKE and the Reynolds stresses. One of the main conclusions of their study was the significance of the secondary currents contribution to the lateral transfer of momentum despite their small values. Longitudinal vortices have been found by those authors to be important for relative depths as low as 0.25. The vertical distribution of the shear stress τ_{zu} was found to be highly non-linear in the interface zone, indicating strong secondary currents development. With an increase of the relative depth, the spreading of the shear layer onto the floodplain decreases.

Very recently, Azevedo *et al*. (2012) have measured the streamwise and vertical velocity components and turbulent intensities, using a 2D Laser Doppler Velocimetry (LDV) in asymmetric compound channel with trapezoidal cross-section. Their data is used in the present study for validating the turbulence models, which will be discussed in Research Papers I and II.

Since the introduction of the analytical SKM by Shiono and Knight (1988), a number of studies have been carried out to show its accuracy in predicting lateral distributions of the depth-averaged velocity and the boundary shear stress distribution. In this SKM Shiono and Knight (1988) ignored the secondary flow effects. Shiono and Knight (1991) improved their earlier work by including the effects of secondary flow.

SKM has been among the most popular methods used by researchers (Lambert and Sellin 1996, Ervine *et al*. 2000, Bousmar and Zech 2004, Rezaei and Knight 2009, Yang *et al*. 2013). Previous research (*e.g*. Knight and Shiono 1996, Abril and Knight 2004, McGahey *et al*. 2006) has demonstrated that the SKM is capable of determining the lateral distributions of depth averaged velocity and boundary shear stress across rivers and channels of various cross-sections both accurately and with a minimum of computational effort (Sharifi *et al*. 2009). However, for a successful simulation using SKM, in addition to the inputs of the shape of cross-section, number of sub-areas (panels) and longitudinal bed slope, correctly specified values of three parameters are required, namely, the lateral distribution of friction factor, *f*, dimensionless eddy viscosity, λ, and a sink term which represents the effect of the secondary flow, Γ. The calibration of these parameters had to be done for different types of channels. Based on the

experimental studies, Knight and Abril (1996) and Abril and Knight (2004) derived equations for estimating the value of f, λ and Γ in compound channels; Chlebek and Knight (2006) provided initial guidance on choosing suitable parameters for prismatic rectangular channels. Based on the analysis of the calibration results, Knight *et al*. (2007) and Sharifi *et al*. (2008, 2009) provided guidelines for calculating the values of the calibration parameters for hydraulically smooth trapezoidal channels.

A two-dimensional depth-averaged k-ε model has been applied to trapezoidal compound channel by Keller and Rodi (1988). They calculated the depth-averaged velocity and the bed shear stress distributions. The agreement between the predicted distributions and the experimental data were quite good. However, some deviations were present in the interaction region between the main channel and the floodplain due to not sufficient transverse mixing and too low eddy viscosity, which can cause under-prediction of turbulence generation. To account for this production a more refined bed shear stress and turbulence model is required.

A LES was used to calculate velocity and bed shear stress distribution and secondary currents in symmetric compound channel of trapezoidal cross-section by Thomas and Williams (1995b). The results were compared with experimental data from the SERC-FCF. The pattern of the secondary cells was in close agreement with data of Shiono and Knight (1990) for the lower relative depth, h_r = 0.15. The predicted bed shear stress distribution was in a good agreement with the experimental data. The streamwise velocity was overpredicted at most by approximately 8% and deviated from the logarithmic profile. The authors concluded that the main deficiency in their simulation was too coarse mesh spacing in streamwise direction of the flow due to the limitations in their computational resources at the moment.

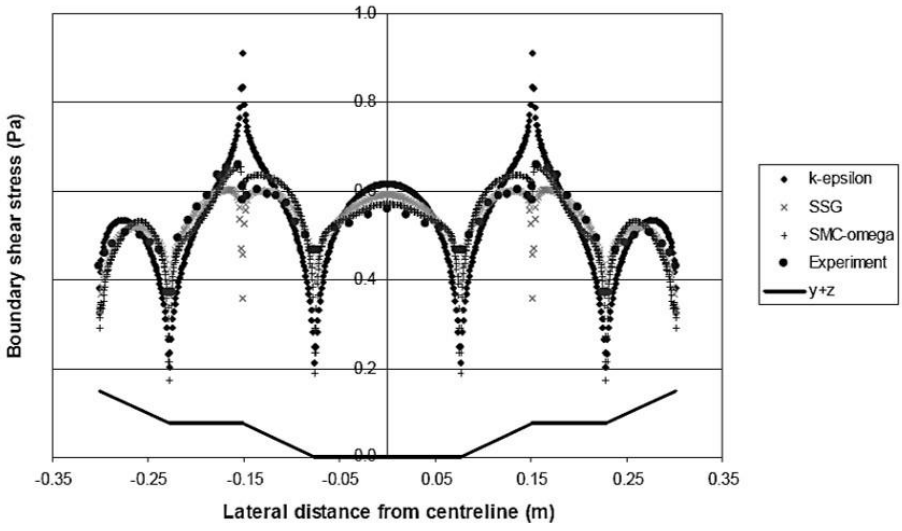

Figure 4.18: Boundary shear stress in symmetric compound channel with trapezoidal cross-section (after Knight *et al*. 2005).

Knight *et al*. (2005) continued their research work in applying state-of-the-art CFD workbench software to compound channel flow. They have tested *k*-ε model, SSG and SMC-ω model and compared the predicted streamwise velocity and boundary shear stress distributions with experimental data by Yuen (1989). Both models, SSG and SMC-ω, predict the presence of four secondary cells where the strongest is located about the junction between the main channel and the floodplain. In the case of bed boundary shear stress distribution, the SMC-ω predictions were in the closest match to the experimental data (*cf*. Figure 4.18). The authors have noticed that the predicted mass flow rate was higher than the experimental value. This is due to the fact that whilst the experiments were considered with relatively smooth walls, there was still some roughness to account for. This was reflected in CFD simulations through applying a small roughness (0.5 mm) in the cases of *k*-ε and SSG model. The introduction of roughness did not have any impact on the velocity contours or the boundary shear stress profiles. The *k*-ε model failed in predicting secondary currents and overestimated the boundary shear stress. The main conclusion from this research work has been that there are limitations as to what can be achieved with a turbulence model in the case of steady uniform flow (Knight *et al*. 2005).

Evidence gathered from the literature review permits to assume that besides DNS, much more complex models, such as LES, are necessary for simulating the fully 3D multi-scale phenomena in open-channel flows. However, despite the fact that LES produces accurate results, it increases computational cost further beyond typical engineering time and resource framework, which often leads to rejection of this method. Thus, a compromise is needed between capturing the complexity of anisotropic 3D secondary flows with accuracy and using moderate computational cost yet. Accessible computational cost may dictate the usefulness or not of new models to develop engineering analyses for which, for example, design optimization is mandatory and hundreds or even thousands of simulations are required before determining the best solution. For such a purpose the author of the present study will apply several turbulence models to compound channel flow, perform mesh independence analyses, compare numerical results to experimental data and discuss the advantages and drawbacks of the used models (see Research Papers I - IV).

4.4 REFERENCES

Abril, J. B. and Knight, D. W. 2004 Stage-discharge prediction for rives in flood applying a depth-averaged model. *J. Hydraulic Research* **42** (6), 616–629.

Ackers, P. 1993a Flow formulae for straight two-stage channels. *J. Hydraulic Research* **31** (4), 509–531.

Ackers, P. 1993b Stage-discharge functions of two-stage channels: The impact of new research. *J. Institution of Water and Environmental Management* **7** (1), 52-61.

Azevedo, R., Rojas-Solórzano, L. R. and Leal, J. B. 2012 Experimental characterization of straight compound-channel turbulent field. In *Proc. of 2nd European IAHR Congress*. 27-29 June, Munich, Germany.

Bousmar, D. and Zech, Y. 2004 Velocity distribution in non-prismatic compound channels. In *Proc. Inst. Civil Eng. Water Manage*. **157**, 99–108.

Brundrett, E. and Bains, W. D. 1964 The production and diffusion of vorticity in duct flow. *J. Fluid Mech.* **19**, 375-394.

Cater, J. E. and Williams, J. J. R. 2008 Large eddy simulation of a long asymmetric compound open-channel. *J. Hydraulic Research* **46** (4), 445-453.

Celik, I. and Rodi, W. 1984 Simulation of free-surface effects in turbulent channel flows. *PCH Physico Chemical Hydrodynamics* **5**(3/4), 217-227.

Chlebek, J. and Knight, D. W. 2006 A new perspective on sidewall correction procedures, based on SKM modeling. In Ferreira, R. M. L., Alves, E. C. T. L., Leal, J. G. A. B. And Cardoso, A. H. (eds) *Proc. RiverFlow 2006*, Taylor & Francis, Lisbon, **1,** 135–144.

Chow, V. T. 1959 *Open-channel hydraulics*. McGraw-Hill, New-York.

Cokljat, D. 1993Turbulence models for non-circular ducts and channels. PhD thesis, Department of Civil Engineering, City University, London, England.

Cokljat, D. and Younis, B. A. 1995 Second-order closure study of open-channel flows. *J. Hydraulic Eng.* (ASCE) **121** (2), 94-107.

Ervine, D. A., Babaeyan-Koopaei, K. and Sellin, H. J. 2000 Two-dimensional solution for straight and meandering overbank flows. *J. Hydraulic Eng.* **126** (9), 653–669.

Fernandes, J.N. 2013 Compound Channel Uniform and Non-Uniform Flows With and Without Vegetation in the Floodplain. PhD Thesis in Civil Engineering, Instituto Superior Técnico, Universidade de Lisboa.

Fischer-Antze, T., Stoesser, T., Bates, P. and Olsen, N. R B. 2001 3D numerical modeling of open-channel flow with submerged vegetation. *J. Hydraulic Research* **39** (3), 303-310.

Gessner, F. B. and Jones, J. B. 1965 On some aspects of fully-developed turbulent flow in rectangular channels. *J. Fluid Mech.* **23**, 689-713.

Grega, L. M., Wei, T., Leighton, R. I. and Nevens, J. C. 1995 Turbulent mixed boundary flow in a corner formed by a solid wall and a free surface. *J. Fluid Mech.* **294**, 17-46.

Hsu, T. Y., Grega, L. M., Leighton, R. I. and Wei, T. 2000 Turbulent kinetic energy transport in a corner formed by a solid wall and a free surface. *J. Fluid Mech.* **410**, 343-366.

Kang, H. and Choi, S.-U. 2006a Reynolds stress modelling of rectangular open-channel flow. *Int. Journal for Numerical Methods in Fluids* **51**, 1319-1334.

Kang, H. and Choi, S.-U. 2006b Turbulence modelling of compound open-channel flows with and without vegetation on the floodplain using the Reynolds stress model. *Advances in Water Resources* **29**, 1650-1664.

Kara, S., Stoesser, T. and Sturm, T. W. 2012 Turbulence statistics in compound channels with deep and shallow overbank flows. *J. Hydraulic Research* **50** (5), 482-493.

Keller, R. J. and Rodi, W. 1989 Prediction of flow characteristics in main channel/flood plain flows. *J. Hydraulic Research* **26** (4), 425-441.

Kim, J., Moin, P. and Moser, R. 1987 Turbulence statistics in fully developed channel flow at low Reynolds number. *J. Fluid Mech.* **177**, 133-166.

Knight, D. W. 1992 *SERC Flood Channel Facility experimental data – Phase A*, Vols. **1-15**, School of Civil Engineering, The University of Birmingham: Birmingham.

Knight, D. W. 2013 River hydraulics – a view from midstream. *J. Hydraulic Research* **51** (1), 2-18.

Knight, D.W. and Abril, B. 1996 Refined calibration of a depth-averaged model for turbulent flow in a compound channel. In *Proc. of the Institution of Civil Engineers, Water, Maritime and Energy Division* **118** (3), 151-159.

Knight, D. W. and Sellin, R. H. J. 1987 The SERC Flood Channel Facility. *J. of the Institution of Water and Environmental Management* **1** (2), 198-204.

Knight, D. W. and Shiono, K. 1990 Turbulence measurements in a shear layer region of a compound channel. *J. Hydraulic Research* **28** (2), 175-196.

Knight, D. W. and Shiono, K. 1996 River channel and floodplain hydraulics. *In Floodplain Processes* (ed. in M. G. Anderson, D. E. Walling and P. D. Bates), 139–181. John Wiley & Sons, New York, ch 5.

Knight, D. W., Wright, N. G. and Morvan, H. P. 2005 *Guidelines for applying commercial CFD software to open channel flow*. Report based on the research work conducted under EPSRC Grants GR/R43716/01 and GR/R43723/01.

Knight, D. W., Omran, M. and Tang, X. 2007 Modelling depth-averaged velocity and boundary shear in trapezoidal channels with secondary flows. *J. Hydraulic Eng.* (ASCE) **133** (1), 39-47.

Krishnappan, B. G. and Lau, Y. L. 1986 Turbulence modelling of flood plain flows. *J. Hydraulic Eng.* (ASCE) **112**(4), 251-266.

Lambert, M. F. and Myers, W. R. 1998 Estimating the discharge capacity in straight compound channels, In *Proc. of the Institution of Civil Engineers - Water, Maritime and Energy* **130**, 84–94.

Lambert, M. F. and Sellin, R. H. J. 1996 Discharge prediction in straight compound channels using the mixing length concept. *J. Hydraulic Research* **34** (3), 381–394.

Launder, B. E. and Ying, W. H. 1973 Prediction of flow and heat transfer in ducts of square cross section, In *Proc. Inst. Mech. Engrs*. **187**, 455-461.

Lin, B. and Shiono, K. 1995 Numerical modelling of solute transport on compound channel flows. *J. Hydraulic Research* **33** (6), 773-788.

McGahey, C., Samuels, P. G. and Knight, D. W. 2006 A practical approach to estimating the flow capacity of rivers-application and analysis. In *Proc. Int. Conf. on Fluvial Hydraulics (River Flow 2006), Lisbon, Portugal, September* (ed. in R. M. L. Ferreira, E. C. T. L. Alves, J. G. A. B. Leal and A. H. Cardoso), **1**, 303–312. Taylor & Francis, London.

Melling, A. and Whitelaw, J. H. 1976 Turbulent flow in a rectangular duct. *J.Fluid Mech.* **78**, 289-315.

Myers, W. R. C. 1978 Momentum transfer in a compound channel. *J. Hydraulic Research* **16** (2), 139-150.

Naot, D. and Rodi, W. 1982 Calculation of secondary currents in channel flow. *J. Hydraulic Div.* (ASCE) **108** (8), 948-968.

Naot, D., Nezu, I. and Nakagawa, H. 1993 Hydrodynamic behavior of compound rectangular open channels. *J. Hydraulic Eng.* (ASCE) **122** (11), 625-633.

Naot, D., Nezu, I. and Nakagawa, H. 1996 Hydrodynamic behavior of partly vegetated open channels. *J. Hydraulic Eng.* (ASCE) **119** (3), 390-408.

Nezu, I. 1994 Compound open-channel turbulence and its role in river environment. *Keynote Address of 9th APD-IAHR Congress*, Delfft, The Netherlands, 1-24.

Nezu, I. 1996 Experimental and numerical study on 3-D turbulent structures in compound open-channel flows. *Flow modelling and turbulence measurements*, C. J. Chen *et al*., eds., Balkema, Rotterdam, The Netherlands, 65-74.

Nezu, I. 2005 Open-Channel Flow Turbulence and Its Research Prospect in the 21st Century. *J. Hydraulic Eng.* (ASCE) **131** (4), 229-246.

Nezu, I and Nakagawa, H. 1993 *Turbulence in open-channel flows*. In: IAHR Monograph Series. Rotterdam: Balkema.

Nezu, I., Onitsuka, K. and Iketani, K. 1999 Coherent horizontal vortices in compound open-channel flows. *In Hydraulic modelling* (ed. I. W. Seo V. P. Singh and J. H. Sonu). Water Resources Publications, Colorado, USA, 17–32

Nezu, I. and Rodi, W. 1985 Experimental study on secondary currents in open channel flow, In *Proc. 21st IAHR Congress, Melbourne, Australia*, 114–119.

Nikora, V. and Roy, A. G. 2012 Secondary flows in rivers: Theoretical framework, recent advances, and current challenges. *Gravel-bed Rivers: Processes, Tools, Environments*. M. Church, P.M. Biron, A.G. Roy, eds. John Wiley & Sons, USA, 3-22.

Perkins, H. J. 1970 The formation of streamwise vorticity in turbulent flow. *J. Fluid Mech*. **44**, 721-740.

Pezzinga, G. 1994 Velocity distribution in compound channel flows by numerical modelling. *J. Hydraulic Eng.* (ASCE) **120** (10), 1176-1198.

Pope, S. B. 2000 *Turbulent flows*. Cambridge University Press, Cambridge, United Kingdom. ISBN 0–521–59886–9.

Prandtl, L. 1952 *Essentials of Fluid Dynamics*, Hafner Publishing Co., New York.

Rameshwaran, P. and Naden, P. S. 2003 Three dimensional numerical simulation of compound channel flows. *J. Hydraulic Eng.* (ASCE) **129** (8), 645-652.

Reece, G. J. 1977 *A generalized Reynolds stress model of turbulence*. PhD thesis, Imperial College, University of London, London, England.

Rezaei, B., and Knight, D. W. 2009 Application of the Shiono and Knight method in compound channels with non-prismatic floodplains. *J. Hydraul. Eng.* **47** (6), 716–726.

Rodi, W. 1980 *Turbulence models and their application in hydraulics: State of the art paper*. IAHR, Delft.

Saint-Venant, A. 1871 Theorie du mouvement non permanent des eaux, avec application aux crues des rivieres et a l'introduction de marees dans leurs lits. Comptes rendus des seances de l'Academie des Sciences.

Sellin, R. H. J. 1964 A laboratory investigation into the interaction between the flow in the channel of a river and that over its flood plain. *La Houille Blanche*, Paris, France, **7**, 793-802.

Sharifi, S., Knight, D. W. and Sterling, M. 2008 Modelling flow using SKM and a multi-objective evolutionary algorithm. In: Altinakar, M. S., Kokpinar, M. A., Aydin, I., Cokgar, S. and Kirkgoz, S. (eds) In *Proc. RiverFlow 2008, Cesme, Turkey*, **3**, 2149–2158.

Sharifi, S., Knight, D. W. and Sterling, M. 2009 A novel application of a multi-objective evolutionary algorithm in open channel flow modelling. *J. of Hydroinformatics* **11** (1), 31-50.

Shi, J., Thomas, T. G. and Williams, J. J. R. 1999 Large eddy simulation of flow in a rectangular open channel. *J. Hydraulic Research* **37** (3), 345-361.

Shiono, K. and Knight, D. 1988 Two dimensional analytical solution for a compound channel. In *Proc. 3rd Intl Symp. on Refined Flow Modelling and Turbulence Measurements*, Tokyo, Japan, July (eds. Y. iwasa, N., Tamai and A. Wada), 503-510.

Shiono, K. and Knight, D. W. 1991 Turbulent open-channel flows with variable depth across the channel. *J. Fluid Mech*. **222**, 617-646.

Shiono, K., Scott, C. F. and Kearney, D. 2003 Predictions of solute transport in a compound channel using turbulence models. *J. Hydraulic Research* **41** (3), 247-258.

Sofialidis, D. and Prinos, P. 1998 Compound open-channel flow modelling with nonlinear low-Reynolds *k*-ε models. *J. Hydraulic Eng.* **124** (3), 253-262.

Speziale, C. G. 1987 On nonlinear *k*-*l* and *k*-ε models of turbulence. *J. Fluid Mech*. **178**, 459-475.

Speziale, C. G., Sarkar, S. and Gatski, T. B. 1991 Modelling the pressure-strain correlation of turbulence: an invariant dynamical systems approach. *J. Fluid Mech*. **277**, 245-272.

Sterling, M., Beaman, F., Morvan, H. and Wright, N. 2008 Bed-Shear Stress Characteristics of a Simple, Prismatic, Rectangular Channel. *J. Eng. Mech*. **134** (12), 1085–1094.

Thomas, T. G. and Williams, J. J. R. 1995a Large eddy simulation of turbulent flow in an asymmetric compound channel. *J. Hydraulic Research* **33** (1), 27-41.

Thomas, T. G. and Williams, J. J. R. 1995b Large eddy simulation of a symmetric trapezoidal channel at a Reynolds number of 430,000. *J. Hydraulic Research* **33** (6), 825-841.

Tominaga, A. and Ezaki, K. 1988 Hydraulic characteristics of compound channel flow. In *Proc. 6th Cong. Asian and Pacific Regional Div*., Int. Assoc. for Hydr. Res., Kyoto, Japan.

Tominaga, A., Ezaki, K., Nezu, I. and Nakagawa, H. 1989 Three-dimensional turbulent structure in straight open channel flows. *J. Hydraulic Research* **27** (1), 149–173.

Tominaga, A. and Nezu, I. 1991 Turbulent structure in compound open-channel flows. *J. Hydraulic Eng.* **117** (1), 21-40.

Versteeg, H.K. and Malalasekera, W. 2007 *An introduction to computational fluid dynamics. The finite volume method*. 2nd Ed., Pearson Pearson Education Ltd., UK.

Wright, N. G. 2001 *Conveyance implications for 2D and 3D modelling*. Specialist Review for Scoping Study for Reducing Uncertainty in River Flood Conveyance, R & D Technical Report by HR Wallingford to DEFRA/Environment Agency.

Wright, N. G., Crossley, A. J., Morvan, H. P. and Stoesser, T. 2004 Detailed validation of CFD for flows in straight channels, In *Proc. River Flow 2004*, Naples, Italy.

Wu, W., Rodi, W. and Wenka, T. 2000 3D numerical modelling of flow and sediment transport in open channels. *J. Hydraulic Eng.* (ASCE) **126** (1), 4-15.

Xie, Z., Lin, B. and Falconer, R. A. 2013 Large-eddy simulation of the turbulent structure in compound open-channel flows. *Advances in Water Resources* **53**, 66-75.

Yang, K., Nie, R., Liu, X. and Cao, S. 2013 Modeling Depth-Averaged Velocity and Boundary Shear Stress in Rectangular Compound Channels with Secondary Flows. *J. Hydraulic Eng.* (ASCE) **139** (1), 76-83.

Yuen, K. W. H. 1989 *A study of boundary shear stress flow resistance and momentum transfer in open channels with simple and compound trapezoidal cross-section*, in Department of Civil Engineering, University of Birmingham: Birmingham.

CHAPTER 5

SUMMARY OF RESULTS

Contents

5 SUMMARY OF RESULTS

Four research papers are attached to this thesis. This chapter resumes the results of each research paper. The papers are not presented in the chronological order. The order was chosen to provide a straightforward structure for this thesis. Research Paper I introduces a Grid Convergence Index (GCI) technique and linear regression analysis for estimating the mesh quality. Research Papers II to III present a comparison of several turbulence closure models with experimental data. Research Paper IV discusses the influence of the terms in the governing equations in predicting secondary flows. References in subchapters, figures and equations are directed to the indicated paper in the Appendix A.

5.1 RESEARCH PAPER I: CREDIBILITY ANALYSIS OF COMPUTATIONAL FLUID DYNAMIC SIMULATIONS FOR COMPOUND CHANNEL FLOW

This paper was published in the international research journal:

Filonovich, M. S., Azevedo, R., Rojas-Solórzano, L. R. and Leal, J. B. 2013. Credibility analysis of computational fluid dynamic simulations for compound channel flow. *J. Hydroinformatics* **15** (3): 926-938. (doi: 10.2166/hydro.2013.187).

The aim of this paper was to evaluate the level of accuracy of the Explicit Algebraic Reynolds Stress model (EARSM) calculations performed for trapezoidal compound channel flow (the choice of the model results from the conclusions of Research Paper II). For such purpose, the credibility analysis of the numerical model was performed, which consisted in verification and validation of solution.

The asymmetric trapezoidal compound channel flow results of Azevedo *et al*. (2012) for a relative depth h_r = 0.5 were simulated with the EARSM coupled with the transport equation for the dissipation rate (ε-equation, Eq. (2.12)). The dissipation/transport terms were modelled with the standard isotropic formulation of Shir (1973) (see Eq. (2.36)) and the pressure-strain rate correlation was modelled with LRR-IP from Launder *et al*. (1975) (see Eq. (2.40)). The computational domain exactly matched the experimental flume and a biphasic flow was considered (*i.e*., water and air, being the free-surface captured by the VOF technique referred in subchapter 3.3.5).

For solution verification, a number of techniques and methods may be used. The Grid Convergence Index (GCI) method proposed by (Celik *et al*. 2008) to evaluate the numerical uncertainty associated with grid resolution was adopted in this paper. The simulations were run

on three different sets of grids with a global constant refinement factor between the coarse and fine grids. The GCI values have been calculated for three velocity components, turbulence kinetic energy (TKE), dissipation and Reynolds stresses. The lowest absolute values of GCI were for the *u* velocity component, while the highest GCI values were for *v* and *w* velocity components, and Reynolds stresses *RSxy* and *RSyz*. In order to reduce GCI values further refinement of the medium and fine meshes was performed. The refinement was made in the horizontal direction near the lateral wall and in the mixing layer region, and in the vertical direction near the bottom and free-surface region (*cf*. Figures B.1 and B.2, Appendix B). After refinement the GCI values improved for three velocity components, but increased for higher order variables. The contours of GCI presented for all variables after refinement revealed that areas of GCI higher than 5% were localized in the same positions as for the non-refined meshes, except for TKE and dissipation. Comparison of the contours of Reynolds stress *RSxy* before (Figure 3 in Research Paper I) and after refinement (Figure 4 in Research Paper I), concluded that the area, where the GCI is higher than 5%, has decreased significantly according to the mesh refinement performed in the mixing (shear) layer region. However, the averaged GCI value for Reynolds stress *RSxy* has increased in comparison to the non-refined mesh results (Tables 1 and 2 in Research Paper I, respectively). The paper suggests that the difference in these results is due to the non-uniform spatial procedure of grid refinement and the high sensibility of this low magnitude variable to numerical inaccuracies. Analysing the results of GCI, it was concluded that the numerical scheme had an acceptable accuracy for the *u* velocity component, where the GCI value is less than 1%. However, for the secondary variables, like *v* and *w* components of velocity, and Reynolds stresses *RSxy* and *RSyz*, the GCI values were high. This conclusion raised a question to which variable a scheme should be verified on. If the aim of the study is to capture only the primary flow, it can be assumed that the scheme has converged and the numerical accuracy is acceptable. However, if the aim is to capture the processes of mass and momentum transfer between the main channel and the floodplain and secondary flows, the numerical accuracy of the scheme might not be enough to predict it. In such case, a further mesh refinement is necessary or the use of a higher order of the numerical scheme.

Before trying a further mesh refinement it was proposed to verify mesh quality using a different method. Thus, a linear regression analysis was performed between three data sets. The comparison of the GCI values with the correlation coefficient and line slope revealed that for *u* velocity component both methods gave good results. Thus, the results of streamwise velocity are mesh independent. However, for *v* and *w* velocity components and turbulence quantities, there was a fair agreement between the meshes with regression line slopes around 1 in apparent contradiction with the GCI results. It was suggested in the paper that for the compound channel

case one cannot rely only on the GCI method in verifying the mesh quality, since the GCI method is very sensitive when calculating low magnitude values, resulting in very large errors. However, both methods together are good for evaluating the numerical uncertainty associated with grid resolution, and the use of both methods can overcome some drawbacks of GCI analysis.

For validation of the solution, comparison of numerical results of the *u* and *w* velocity components based on the refined mesh with the experimental data measured by a Laser Doppler Velocimeter (LDV) was performed. The paper showed similar behaviour between numerical results and measured data, namely: 1) the significant bulging of the *u* isovels upward near the upper interface is present as a result of secondary flow cells generated by wall turbulence anisotropy; 2) the positive and negative *w* velocities are almost in the same locations; and 3) the presence of two counter-rotating secondary cells in the interface region between the main channel and the floodplain is observed. The paper showed the main differences between numerical results and experimental data, namely: 1) that the numerical model was not able to capture the effect of free surface, where the maximum velocities occur below the free surface (Nezu 1994), due to the missing modelling of free surface; 2) the intensity of the secondary cell generated at the interface between the main channel and the floodplain was slightly higher for the experimental results, which confirmed the fact that Algebraic Stress Models underestimate the secondary flow (Bradshaw 1987). The paper also presented linear regression analysis for *u* and *w* velocity components obtained experimentally and numerically. The comparison of the streamwise velocity suggests a good level of agreement. The major discrepancies were found for the lower *u* velocities near the walls where the numerical model overestimates the experimental data, indicating that the model did not capture well what was happening near the walls. The comparison of the *w* velocity component revealed a distinct area of the disagreement of the results. It was observed that generally the numerical model underestimates the experimental vertical velocity.

5.2 RESEARCH PAPER II: SIMULATION OF THE VELOCITY FIELD IN COMPOUND CHANNEL FLOW USING DIFFERENT CLOSURE MODELS

This paper was presented at the 1st IAHR European Congress in Edinburgh, UK, 2010:

> Filonovich, M. S., Azevedo, R., Rojas-Solórzano, L. R. and Leal, J. B. 2010 Simulation of the velocity field in compound channel flow using different closure models. *In Proc. of 1st European Congress, Edinburgh, UK., 2010,* FMIIIb in USB flash drive.

This paper is based on the numerical results performed using commercial 3D CFD code (ANSYS CFX) in the beginning of the present study. The aim of this study was to evaluate the

ability of ANSYS CFX accurately predict the primary flow and position of the free surface by applying mass flow rate as initial condition known from the experiments. Additional results regarding the free-surface modelling with VOF can be seen in Appendix B. The paper shows the comparison of the numerical results obtained by different turbulence models for compound trapezoidal channel flow with experimental data.

Like in Research Paper I, the asymmetric trapezoidal compound channel flow results of Azevedo *et al*. (2012) for a relative depth h_r = 0.5 were simulated. Again, the computational domain exactly matched the experimental flume and a biphasic flow was considered (*i.e*., water and air, being the free-surface capture by the VOF technique referred in subchapter 3.3.5).

Three turbulence models were used in this paper for comparison, where two of the models were isotropic models, *k*-ε model and Shear Stress Transport model (SST), and the third was anisotropic EARSM with the transport equation for the dissipation rate (ε-equation, Eq. (2.12)) presented in Chapter 2. The diffusion/transport and the pressure-strain rate correlation terms were modelled like in Research Paper I. The computational domain also covered the entire flume length and a biphasic (water + air) flow was also considered.

The paper shows the comparison of measured and simulated by *k*-ε, SST and EARSM vertical profiles of time-averaged primary velocity, *U*, in the floodplain, in the upper and lower interfaces, and in the middle of the main channel. These results revealed that all models give similar results and good agreement with experimental data in the inner layer and in the middle of the main channel and in the floodplain, except near the free surface (Figure 5 in Research Paper II). In the outer region in the interface verticals EARSM gave results closer to the experimental data, however, slightly overestimated. The main conclusion from this part of the paper is that isotropic models can accurately reproduce the mean primary velocity in the floodplain region far from the lateral walls. However, in the interface region between the main channel and the floodplain, where the turbulence anisotropy is generated by the geometry of the compound cross-section, isotropic models fail in reproducing the profile of the *U* and EARSM shows better agreement with the experimental data.

The paper also presents the analysis of the cross-section contours of the streamwise velocity and turbulence kinetic energy (TKE) for three models and secondary flow vectors obtained by EARSM. The paper showed that EARSM was able to reproduce significant bulging of the isovels towards the free surface at the upper interface as a result of secondary flow cells generated by turbulence anisotropy. The isotropic models did not show this behaviour, since they assume isotropic turbulence. The secondary flow vectors of EARSM (Figure 8 in Research Paper II) confirmed the presence of secondary flow cells causing the inflection of the isovel lines. The comparison of the TKE results showed more realistic results performed by EARSM

despite of the similar behaviour of the *k*-ε and EARSM close to the free surface and better performance of SST near the walls. Thus, the main conclusion of this paper was that EARSM was able to simulate Prandtl's second kind secondary flows. The quality of this simulation will be discussed in the next papers, as well as the influence of the mesh size on the accuracy of the results obtained by EARSM was analysed in more details in Research Paper I.

5.3 RESEARCH PAPER III: PREDICTION OF COMPOUND CHANNEL SECONDARY FLOWS USING ANISOTROPIC TURBULENCE MODELS

This paper was presented at the River Flow 2014 – the 7th International Conference on Fluvial Hydraulics at EPFL, Lausanne, Switzerland, 2014.

Filonovich, M. S., Rojas-Solórzano, L. R. and Leal, J. B. 2014 Prediction of compound channel secondary flows using anisotropic turbulence models. *In Proc. of River Flow 2014* – the 7th International Conference on Fluvial Hydraulics, Lausanne, Switzerland, 2014, 163-170.

From the previous Research Paper II it was concluded that EARSM performs better when compared to isotropic models, such as *k*-ε and SST. Thus, a question has arisen how EARSM would behave when compared to Reynolds Stress Models (*i.e.*, that directly use the Reynolds stress transport equations), such as Baseline Reynolds Stress model (BSL RSM, where a modified ω-equation (Eq. 2.17) is used, which is a mixture of *k*-ε and *k*-ω models) and Speziale-Sarkar-Gatski Reynolds Stress model (SSG RSM, where a standard ε-equation (Eq. (2.12)) is used). The SSG RSM uses a different model for the pressure-strain correlation terms (see Eqs. (2.43) and (2.44), and the different coefficients presented in Table 2.4).

The objective of this study was to use anisotropic models based on Reynolds stresses transport equations (namely, BSL EARSM, BSL RSM and SSG RSM) to examine the differences in results produced by each model. Validation of the numerical results was performed with the experimental data of Tominaga and Nezu (1991) for an asymmetric rectangular compound channel with relative depth of h_r = 0.5. Since fully developed flow conditions were assumed, the computational domain was shortened and periodic boundary conditions were used, thus reducing the computational time. Contrary to the experimental flume, the computational domain was horizontal and the flume slope (*i.e.* energy slope, since the flow was uniform) was taken into account by a corresponding pressure drop between the inlet and the outlet cross-sections. A single fluid was considered (water) and the free-surface was modelled as a rigid lid with free-slip condition (see subchapter 3.3.5).

The simulations have reproduced the complex flow pattern of primary velocity field, secondary currents, Reynolds stresses, anisotropy of turbulence and production term of secondary currents in the streamwise equation of vorticity (Eq. (4.1)).

The three turbulence models were able to reproduce significant bulging of the isovels at the interface upwards due to secondary flows. However, the bulging was more pronounced in the BSL's models than in the SSG (Figure 2 in Research Paper III) due to a different near-wall treatment between the models (subchapter 3.3.5). The presence of the secondary flow cells as well as the free surface vortex was confirmed by the three models. However, the latter was reproduced with much lower magnitude and not extending until the middle of the main channel as observed in the experimental data.

The pattern of turbulence anisotropy, ($\overline{v'v'} - \overline{w'w'}$), for numerical models (Figure 6(b-d) in Research Paper III) slightly differs from the experimental. At the junction between the main channel and the free surface and in the corners of the main channel, secondary flow cells are formed (Figure 2(b-d) in Research Paper III), where the values of turbulence anisotropy change the sign (Figure 6 (b-d) in Research Paper III). The paper showed that BSL's models, and especially EARSM, reproduced higher values of the turbulence anisotropy than the SSG model due to a different near-wall treatment (subchapter 3.3.5).

The analysis of the normalised normal Reynolds stress profiles revealed that all models underestimated the experimental normal stresses $\overline{u'u'}$ near the bed until $z/H < 0.4$ (Figure 7 in Research Paper III) due to a wall treatment for SSG model and due to insufficient mesh refinement close to the walls for the BSL's models. Production term of the secondary currents in the streamwise equation of vorticity (Figure 8 in Research Paper III) presented the extreme values at the junction edge, in the corners of the main channel and the floodplain as well as in the wall-free-surface corners with positive and negative peaks alternatively. This gradient becomes a driving force in generation of secondary flows at these regions. Although BSL EARSM is able to reproduce this at some extent, still some discrepancies were found. Therefore in Research Paper IV a deeper analysis on the validity of the underlying hypotheses of EARSM is performed. Moreover, since a more complex pressure-strain rate correlation model (SSG RSM) did not improve the results, the focus of the next research paper is on the role of diffusion/transport terms.

5.4 RESEARCH PAPER IV: OPEN-CHANNEL SECONDARY FLOW SIMULATION WITH RSM AND EARSM

This research paper was submitted to Engineering Applications of Computational Fluid Mechanics:

Filonovich, M. S., Rojas-Solórzano, L. R. and Leal, J. B. 2015 Open-channel secondary flow simulation with RSM and EARSM. Submitted to *Engineering Applications of Computational Fluid Mechanics.*

Conclusions of Research Paper III triggered the need in further investigation of BSL models, namely BSL EARSM and BSL RSM, on predicting Prandtl's secondary flow. Thus, the main aims of this paper were to evaluate the differences between EARSM and RSM results for compound channel of Tominaga and Nezu (1991) and to identify which simplifications in the EARSM cause the differences in the results. For such purpose four simulations were run: 1) BSL RSM; 2) BSL EARSM_1 non-corrected; 3) BSL EARSM_2 with diffusion correction; 4) BSL EARSM_3 with streamline curvature correction.

The comparison of experimental and numerical results demonstrated overall a good agreement for the Reynolds stresses. However, the models failed in reproducing the velocity dip phenomenon, where the maximum velocity occurs below the free-surface (Figure 2 in Research Paper IV).

The budget of Reynolds stresses transport equations was performed in this paper. Analysis of these results performed by BSL RSM revealed high turbulent production P_{ij} (Eq. (6) in Research Paper IV) of primary normal Reynolds stress $\overline{u_1' u_1'}$ near the walls, which was balanced by both pressure-strain rate correlation Π_{ij} and dissipation rate ε_{ij} (Eqs. (10) and (9) in Research Paper IV, respectively). The secondary normal stresses $\overline{u_2' u_2'}$ and $\overline{u_3' u_3'}$ showed a different budget (see Figure 3 in Research Paper IV), where the dissipation rate at the walls was mainly balanced by the pressure-strain rate, except near the corners and channel centre where turbulent production is important. At the corners of the channel production of secondary normal Reynolds stresses had opposite signs which reflected the generation of secondary flows. The production of wall-normal Reynolds stresses $\overline{u_1' u_2'}$ and $\overline{u_1' u_3'}$ was balanced by the pressure-strain correlation near the vertical walls and near the bottom, respectively. The turbulent transport and viscous diffusion D_{ij} was relevant at the corners and in the interface region for all Reynolds stresses but with smaller order of magnitude. The budget of Reynolds stresses transport equations performed by non-corrected EARSM_1 showed significant differences when compared to RSM budget for all P_{ij}, Π_{ij} and slightly for D_{ij} (Figure 4 in Research Paper IV). The major differences occurred for production of $\overline{u_1' u_1'}$, $\overline{u_1' u_2'}$ and for $\overline{u_1' u_3'}$, where the EARSM overpredicts the normal and underpredicts the wall-normal Reynolds stresses production, which would influence the turbulence anisotropy and hence secondary flow pattern.

The budget of anisotropy tensor transport equations was also presented in this paper. The RSM results (Figure 5 in Research Paper IV) showed that the convection of anisotropy had the lowest magnitude than the diffusion term and the turbulent production and viscous dissipation contribution from TKE. These results pointed out that neglecting the anisotropy convection (Eq. (1) in Research Paper IV) was a valid approach, whereas rejecting the anisotropy diffusion (Eq. (2) in Research Paper IV) was not valid since its value was particularly high near the corners of the channel. These conclusions were in line with the work of Taulbee (1992) and Qiu *et al*. (2008), where they directed attention to the important role of diffusion in the near-wall region.

The effect of the EARSM diffusion correction on the results was studied. An exceptionally high value $C_{Diff} = 10$, compared to the $C_{Diff} = 2.2$ proposed by Wallin and Johansson (2000), was used. Comparison of the results of the corrected EARSM_2 (Figure 6 in Research Paper IV) with the RSM (Figure 5 in Research Paper IV) showed similar patterns of anisotropy diffusion, although the magnitude was higher for the RSM. The diffusion correction increased the secondary flow, however did not improve the contours inflection of the primary velocity in the centre of the main channel observed in RSM.

In order to evaluate the importance of streamline curvature correction on the results, the EARSM_3 was performed. The diffusion terms for the corrected EARSM_3 (Figure 7 in Research Paper IV) showed the similar pattern when compared with RSM (Figure 3 in Research Paper IV) and with EARSM_2 (Figure 6 in Research Paper IV), although their magnitude was smaller than of the latter ones. Therefore, it was concluded that for compound channel flow the diffusion correction was more relevant than the streamline curvature correction.

The simplifications included in the EARSM were also studied in the paper. The explicit polynomial a_{ij}^{CFX} in CFX (Eq. (23) in Research Paper IV) is an approximation of the exact polynomial a_{ij}^{WJ} of Wallin and Johansson (2000) (Eq. (20) in Research Paper IV), where β_9^{WJ} is neglected and β_4^{CFX} uses the value for 2D flows. Figure 8 in Research Paper IV presents the relative errors between a_{ij}^{CFX} and a_{ij}^{WJ}. The research paper shows the significant differences (± 50%) in the region of lateral walls and channel bottom. It was concluded that neglecting the β_9^{WJ} term gave errors below 5%, thus highlighting that the major source of error lied in the assumption of the 2D value for β_4^{CFX}.

The validity of the approximation for *N*, by using the solution of the cubic equation obtained for 2D flows, was evaluated by comparing the exact value *N* (Eq. (18) in Research Paper IV) with the approximated value N^{ap} (Eq. (27) in Research Paper IV), both computed with non-corrected EARSM_1 results. The *N* relative error showed higher values in the regions where the

secondary flow cells interact, but in the order of 5%. Thus, it was concluded that N approximation gave reasonably good results.

An overall conclusion from this paper states that RSM is the preferable choice when Prandtl's second kind secondary flow is to be accurately predicted, although improvements should be done for the free-surface modelling and for the turbulent transport term, such as the use of a more complex gradient-diffusion model for the latter one (*e.g*. Daly and Harlow 1970).

CHAPTER 6

CONCLUSIONS AND FUTURE RESEARCH

Contents

6 CONCLUSIONS AND FUTURE RESEARCH

6.1 CONCLUSIONS

In the present study several numerical RANS simulations of laboratorial flows measured by other authors in straight rectangular and trapezoidal compound channel were performed using a commercial CFD package (ANSYS-CFX). The results from the simulations were presented in four research papers (Appendix A) and allowed to fulfil the three main objectives defined in subchapter 1.2.

Regarding modelling guidelines (objective i) in p. 8), the following conclusions can be listed:

- the quality of mesh resolution should be checked using GCI method complemented with a linear regression analysis of the low magnitude variables (see the methodology presented in Research Paper I) to insure the convergence of the turbulent field;
- local mesh refinement, close to the walls and in the interface region (mixing layer), improves the results without increasing too much the computational time (see the refinement procedure proposed in Research Paper I);
- for the specific case studies, where free-surface gradients were small, the VOF technique for domain with two fluids (water + air) is able to reproduce accurately the free-surface level throughout the channel (see results presented in Research Papers I and II, and also in Appendix B);
- a domain with single fluid (water) with a rigid lid representing the free-surface and with inlet and outlet periodic boundary conditions represented by a pressure drop, allows the reduction of mesh size and, consequently, of the computational time, rendering similar results to the biphasic fluid domain (compare results in Research Papers I and II to the ones in Research Papers III and IV).

Regarding the turbulence closure models performance in simulating flows with secondary currents (objective ii) in p. 8) and the relative importance of their underlying physical hypotheses (objective iii) in p. 8), the following conclusions can be listed:

- the two-equation models, k-ε and SST (mixture of k-ε and k-ω models), give similar results confirming that the assumption of turbulence isotropy, rendering nonexistent Prandtl's secondary flow, is much more limitative than the near-wall treatment (see results in Research Paper II);

- the EARSM allows to simulate the secondary currents, but significant discrepancies are seen when compared with experimental results (see results in all Research Papers), which are mainly caused by the hypothesis of negligible anisotropy diffusion implicit in the weak equilibrium condition (see Research Paper IV);
- the anisotropy convection and streamline curvature corrections, that were established for flow in rotating frames, proved to be inefficient in increasing the EARSM results quality (see Research Paper IV);
- the RSM gives better results than EARSM, but still some discrepancies are noticed when comparing them with experimental data (see Research Paper IV), which are due to limitations of the near-wall and free-surface modelling (BSL modified ω closure equation), on the adopted pressure-strain rate correlation and diffusion models and to the isotropic dissipation rate assumption (see Research Paper IV);
- the near-wall treatment (*i.e.* ε-equation *vs*. BSL modified ω-equation) seems to have a higher impact on the quality of the solution than the pressure-strain rate correlation model (LRR-IP *vs*. LRR-QI *vs*. SSG) (compare EARSM results in Research Paper III and RSM results in Research Papers III and IV).

Resuming, although the EARSM seems an attractive model due to its low computational cost, the RSM is the preferable choice when Prandtl's second kind secondary flow is to be accurately predicted. However, RSM models also have limitations in predicting turbulence. Due to important role of turbulent transport terms, it is recommended to represent them in RSM with a more complex gradient-diffusion model. An additional modelling is also necessary, *e.g.* damping functions, near the free surface to reproduce the velocity dip. Unfortunately, these methods are not usually available in commercial codes, since they steamed from aerodynamics industrial applications, and their implementation is difficult. Local mesh refinement is advised near the walls and in the shear layer when the aim of the study is to capture secondary flows and all the processes of mass and momentum transfer between the main channel and the floodplain.

6.2 FUTURE RESEARCH

In the present work, several turbulence models have been validated for simple experiments, comprising uniform flows in straight asymmetric trapezoidal and rectangular smooth compound channel, both in high flood conditions ($h_r = 0.5$).

Even for these simple cases, the more complex RANS modelling (*i.e.* RSM) renders non-negligible differences in the prediction of secondary flows observed in the experiments. Therefore, improvement of near-wall and free-surface modelling (namely for the dissipation rate and pressure-strain correlation terms) as well as the diffusion/transport terms is needed.

This can be accomplished by using an open source CFD package, where code changes can be introduced.

In terms of mesh refinement, since the location of the secondary cells is previously known, it could be interesting to evaluate the effect of refining the mesh in the region where adjacent secondary cells interact near the corners.

The simulations should be extended to lower relative depth cases, were the strength of the mixing layer at the interface between main channel and floodplain is known to increase. The subsequent interaction of the mixing layer with the secondary flow would render quite different turbulence anisotropic state, and therefore the performance of the models can change significantly.

Extending the simulations to rough boundaries seems also a natural step towards the representation of real river flow cases, where rough boundaries are common. The effect of rough boundaries on the turbulence anisotropy generation surely will raise some problems to the near-wall modelling and can render different performance of the models.

In the same line as the previous suggestion, future simulations should cover meandering compound-channels, where Prandtl's first kind secondary flows are known to occur. These, contrary to the second kind, are not turbulence driven, but their joint interaction would be interesting to assess and model.

Finally, in a broader approach, simulations of compound channel flows with vegetation, sediment or pollutant transport would highlight the importance of turbulence driven secondary flow prediction and evaluation of the ability of RANS models in giving accurate results.

APPENDIX A

RESEARCH PAPERS

Paper I

CREDIBILITY ANALYSIS OF COMPUTATIONAL FLUID DYNAMIC SIMULATIONS FOR COMPOUND CHANNEL FLOW

Marina Filonovich, Ricardo Azevedo, Luis R. Rojas-Solórzano, João Bento Leal

Published in *Journal of Hydroinformatics* **15** (3), 2013 (doi: 10.2166/hydro.2013.187)

Credibility analysis of computational fluid dynamic simulations for compound channel flow

M. S. Filonovich, R. Azevedo, L. R. Rojas-Solórzano and J. B. Leal

ABSTRACT

In this paper, verification and validation of a turbulence closure model is performed for an experimental compound channel flow, where the velocity and turbulent fields were measured by a Laser Doppler Velocimeter (LDV). Detailed Explicit Algebraic Reynolds Stress Model (EARSM) simulations are reported. There are numerous methods and techniques available to evaluate the numerical uncertainty associated with grid resolution. The authors have adopted the Grid Convergence Index (GCI) approach. The velocity components, the turbulence kinetic energy (TKE), the dissipation rate and the Reynolds stresses were used as variables of interest. The GCI results present low values for the *u* velocity component, but higher values in what concerns the *v* velocity component and *w* velocity component (representing secondary flows) and for Reynolds stresses *RSxy* and *RSyz*. This indicates that the mean flow has converged but the turbulent field and secondary flows still depend on grid resolution. Based on GCI values distribution, the medium and fine meshes were further refined. In addition to GCI analysis, the authors have performed linear regression analysis for estimating the mesh quality in what concerns small value variables. Comparison of numerical and experimental results shows good agreement.

Key words | compound channel flow, Grid Convergence Index (GCI), Reynolds stresses, validation and verification, velocity components

M. S. Filonovich (corresponding author)
R. Azevedo
J. B. Leal
Department of Civil Engineering,
Faculdade de Ciências e Tecnologia da Universidade Nova de Lisboa,
Campus de Caparica,
2829-516, Caparica,
Portugal
E-mail: *m.filonovich@fct.unl.pt*

M. S. Filonovich
J. B. Leal
CEHIDRO,
Instituto Superior Técnico,
Av. Rovisco Pais,
1049-001, Lisbon,
Portugal

L. R. Rojas-Solórzano
Department of Energy Conversion and Transport,
Universidad Simón Bolívar,
AP 1080, Caracas,
Venezuela

NOTATION

h_1, h_2, h_3	grid size of fine-, medium- and coarse-grid, respectively, m;	i	subscript that stands for local values in the ith cell;
ΔV_i	volume of ith cell, m^3;	p	apparent order of accuracy;
N	total number of cells of the calculation domain;	H	water level above channel bottom, m;
r_{21}, r_{32}	refinement factor between fine mesh 1 and medium mesh 2, and between medium mesh 2 and coarse mesh 3, respectively;	h_b	bankfull level above channel bottom, m;
		S_0	bed slope of the flume;
		B	section width, m;
		b	main channel bottom width, m;
e_a^{21}, e_a^{32}	approximate relative error between meshes 1 and 2, and between meshes 2 and 3, respectively;	z^+	non-dimensional vertical coordinate;
		h_r	relative flow depth;
f_1, f_2, f_3	fine-, medium- and coarse-grid solution of a variable of interest obtained with grid spacing h_1, h_2 and h_3, respectively;	u, v, w	longitudinal, transversal and vertical velocity components, respectively, m/s;
		TKE	turbulence kinetic energy per unit mass, m^2/s^2;
F_s	safety factor;	dissipation	dissipation rate per unit mass, m^2/s^3;

doi: 10.2166/hydro.2013.187

RSxy, *RSxz*, *RSyz*	tangential Reynolds stresses, N/m^2;
GCI21, GCI32	Grid Convergence Index values between meshes 1 and 2, and between meshes 2 and 3, respectively;
GCI21r, GCI32r	Grid Convergence Index values between refined meshes 1 and 2, and between mesh 2 refined and mesh 3, respectively;
R	correlation coefficient;
–	overbar operator that stands for global (cross-section averaged) values.

INTRODUCTION

During recent decades, there has been an incredible increase in computer simulations of practical fluid dynamics problems. There are currently many commercial and in-house computational fluid dynamics (CFD) codes that simulate the behaviour of turbulent flows. A CFD code is expected to be a very powerful tool, as far as it can help solving very important but difficult to measure flows. Furthermore, nowadays in many applications of CFD it is no longer enough just to produce a solution; the credibility analysis of the numerical model should be performed. This analysis consists of two fundamental steps: verification and validation (V&V).

Verification is principally a mathematical and computer science issue (Roache 1998a), which consists of two steps:

1. Code verification, its assessment consists of accumulating evidence certifying that the code does not have algorithmic or programming errors.
2. Solution verification is based on the accumulation of evidence that a specific calculation is correct and accurate, and requires confirmation of grid convergence (Oberkampf & Trucano 2002).

Validation is primarily a physical sciences issue (Roache 1998a), which shows the assessment of the accuracy of a computational model by comparison with experimental data, direct numerical simulation (DNS) or analytical solution, when available. In other words, according to Roache (1994) verification is 'solving the equations right' and validation is 'solving the right equations'.

CFD was one of the first fields to seriously begin developing concepts and procedures for V&V methodology. There are a number of authors who have contributed to the verification of CFD solutions, like Celik *et al.* (1993), Roache (1997, 1998a, b) and many others. Some of these authors have contributed highly accurate numerical solutions, while others have contributed analytical solutions useful for verification. A large number of researches through the years have conducted the work in validation methodology and validation experiments (e.g., Celik *et al.* 1994; Oberkampf 1994; Coleman & Stern 1997; Roache 1998a).

The first quality-control measures in the CFD area were issued by the editors of the American Society of Mechanical Engineers (ASME) *Journal of Fluids Engineering* (JFE) in 1986 by publishing a brief policy statement (Roache *et al.* 1986) which was expanded in 1993 (Freitas 1993). Since then, for further improvement of quality of publications in the CFD community, the discretization error estimation is required to publish numerical results in many CFD journals. There are recommended procedures and guidelines to be followed in order to make sure that a numerical solution has reached a certain level of accuracy. In this paper, authors follow the *Journal of Fluids Engineering* editorial policy statement on the control of numerical accuracy. These statements emphasize that for a CFD simulation to be credible, the code needs to be verified and validated (comparison with reliable experimental results, DNS or analytical solution if available).

Code verification will not be addressed; it is assumed that the commercial code ANSYS CFX 12.0, used in this paper, itself has been verified independently by many authors that have been using this code for numerical simulations and have published their results. ANSYS CFX has been used to consider flow structures in experimental channels such as the Flood Channel Facility (Morvan *et al.* 2002; Morvan 2005).

Furthermore, work on CFD based on large eddy simulation (LES) has been performed by Sterling *et al.* (2008) to detail the physics of rectangular channel flows.

Despite all these applications, there has been almost no attention given in compound channel flow studies to the

issue of solution credibility. The work carried out here aims to evaluate the level of accuracy of CFD calculations compared with experimental data. For compound channel flow solution verification, where the correct solution is unknown, the authors have adopted a Grid Convergence Index (GCI). In the case of small value variables, the GCI approach results in 'unrealistic' high GCI values, and therefore the approach was complemented with a linear regression analysis that seems more appropriated to deal with low magnitude variables, like v and w velocity components and Reynolds stresses.

For validation of the solution, comparison of numerical results obtained by turbulence closure Explicit Algebraic Reynolds Stress Model (EARSM) with the experimental data measured by a Laser Doppler Velocimeter (LDV) was performed.

GRID CONVERGENCE INDEX (GCI)

The GCI was proposed by Roache (1994) and it represents a simple method for reporting grid-convergence studies without any restriction to integer refinement (e.g., grid doubling). The GCI is based on generalized theory of Richardson extrapolation involving comparison of solutions at different grid spacing. The GCI can be computed using two levels of grid; however, three levels are recommended in order to accurately estimate the order of convergence and to check that the solutions are within the asymptotic range of convergence. The authors have adopted the procedure for estimation of GCI proposed by Celik *et al.* (2008).

For three-dimensional (3D) calculations, a local grid size h_i was calculated using

$$h_i = \left[\frac{1}{N}\sum_{i=1}^{N}(\Delta V_i)\right]^{1/3} \tag{1}$$

where ΔV_i is the volume of the ith cell, and N is the total number of cells of the calculation domain. In this paper, the local cell size was used since the variables of interest were local, i.e. all local quantities depended on the position within the cross-section.

The simulations were run on three different sets of grids with a global constant refinement factor between the coarse and fine grids $\overline{r_{21}} = \overline{h_2}/\overline{h_1}$ and $\overline{r_{32}} = \overline{h_3}/\overline{h_2}$, where $\overline{h_1} < \overline{h_2} < \overline{h_3}$ and $\overline{h_1}$, $\overline{h_2}$ and $\overline{h_3}$ are the global grid sizes for fine, medium and coarse meshes accordingly. The local refinement factors $r_{21,i}$ and $r_{32,i}$ are dependent on the local cell size and therefore vary along the cross-section. The calculation of the local apparent order of accuracy p_i was performed using the expressions:

$$p_i = \frac{1}{\ln(r_{21,i})}\left|\ln\left|\varepsilon_{32,i}/\varepsilon_{21,i}\right| + q_i(p_i)\right| \tag{2a}$$

$$q_i(p_i) = \ln\left(\frac{r_{21,i}^{p_i} - s_i}{r_{32,i}^{p_i} - s_i}\right) \tag{2b}$$

$$s_i = 1 \cdot \mathrm{sign}\left(\varepsilon_{32,i}/\varepsilon_{21,i}\right) \tag{2c}$$

where $\varepsilon_{32,i} = f_{3,i} - f_{2,i}$, $\varepsilon_{21,i} = f_{2,i} - f_{1,i}$, where $f_{1,i}$, $f_{2,i}$ and $f_{3,i}$ are the fine-, medium- and coarse-grid local solution of the variable of interest obtained with grid spacing $h_{1,i}$, $h_{2,i}$ and $h_{3,i}$, respectively. The local order of accuracy p_i is computed applying Newton–Raphson method to Equation (2a). This is an iterative procedure which does not work if either $\varepsilon_{32,i}$ or $\varepsilon_{21,i}$ is 'very close' to zero, i.e. when the difference between the local results obtained with the two adjacent meshes is almost negligible.

Local approximate relative error was calculated using:

$$e_{a,i}^{21} = \left|\frac{f_{1,i} - f_{2,i}}{f_{1,i}}\right| \text{ and } e_{a,i}^{32} = \left|\frac{f_{2,i} - f_{3,i}}{f_{2,i}}\right| \tag{3}$$

Roache (1997) defined the GCI for a particular grid as the error estimate multiplied by a factor of safety F_s:

$$\mathrm{GCI}_i^{21} = \frac{F_s e_{a,i}^{21}}{r_{21,i}^{p_i} - 1} \tag{4}$$

$$\mathrm{GCI}_i^{32} = \frac{F_s e_{a,i}^{32}}{r_{32,i}^{p_i} - 1} \tag{5}$$

where $F_s = 1.25$ has been adopted in this paper (Roache 1997).

NUMERICAL MODELLING

Calculation domain and boundary conditions

The domain, 0.785 m wide and 10 m long with a bottom slope 0.001, is exactly coincident with the experimental flume (Figure 1), and was discretized using three different meshes with hexahedral elements aligned to the main flow direction and refined close to the walls, free surface and transition zone between the main channel (MC) and the floodplain (FP). In Figure 1, H is the water level above channel bottom, h_b is the bankfull level above channel bottom, b is the MC bottom width, and B is the section width. For turbulence modelling purposes, the non-dimensional vertical coordinate, z^+, of the element closest to the bottom wall was kept around 30 for the FP and 50 for the MC, allowing the use of wall functions. The flow is biphasic (water + air) and therefore the free surface is within the calculation domain. A uniform velocity field with a water depth of 0.102 m and 5% turbulence intensity was prescribed at the inlet; while a hydrostatic pressure profile with zero velocity derivatives was set at the outlet. The upper boundary condition was prescribed on the air, at 0.05 m above the expected free surface, with free-slip wall to allow the free motion of the air along the channel, while facilitating the numerical robustness of the simulation. The bottom and side walls were prescribed with a non-slip boundary condition and an absolute roughness of 0.384 mm, obtained from the experiments.

Numerical scheme

The flow field was calculated using the commercial 3D CFD code ANSYS CFX 12.0. This code is based on the finite element-based control volume method, where the governing equations are discretized over each control volume. Advection terms in Reynolds Averaged Navier-Stokes (RANS) equations are discretized using a second-order upwind scheme. Linear shape functions are used to evaluate spatial derivatives for all the diffusion terms and pressure gradient terms. The resulting system is then solved in a coupled manner, and the results are interpolated to the grid nodes. In this paper, the flow dynamics is modelled by numerically solving RANS equations for the water-air combination using the volume of fluid (VOF) method based on the idea of volume fraction (Hirt & Nichols 1981). There is a closure equation for the volume fraction, which states that both phases of volume fraction must add up to one at every computational cell. The free surface model is accompanied by an interphase sharpening algorithm, which guarantees a minimum diffusion of the volume fraction around the free surface. The stopping criterion for iterative calculations was set to be 10^{-5} for the normalized error in all equations, which led to an error of global mass flow imbalance smaller than 0.1%.

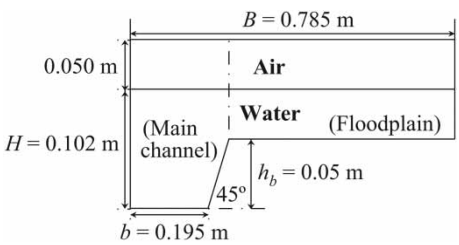

Figure 1 | Cross-section of the calculation domain of the compound channel.

Turbulence closure model

The steady-state simulations were performed using the EARSM for the turbulence calculation in the RANS equations. The implementation is based on the EARSM of Wallin & Johansson (2000) in the form given by Hellsten (2004) for 3D flows. The EARSM represents an extension of the standard $k-\varepsilon$ model, and solves algebraic equations for six Reynolds stresses; the model is derived from the Reynolds stress transport differential equations and gives a nonlinear relation between the Reynolds stresses and the mean strain-rate and vorticity tensors (Wallin & Johansson 2000). The model solves the higher order anisotropic terms and thus, it is suitable to capture effects associated with secondary flows.

Method of analysis

Determination of the GCI in this paper, as described above, is based on the solution of large- and small-magnitude, yet very important, variables of interest. Particularly, all three water velocity components, turbulence kinetic energy (TKE), dissipation and Reynolds stresses, obtained with three different meshes were considered in the analysis. By calculating a GCI on three meshes and looking at the behaviour of GCI terms between two adjacent grids (i.e., between

meshes 1 and 2, and between meshes 2 and 3), one can make an assumption whether the solutions are within the convergence radius. Roache (1994, 1997) noted that it is neither necessary nor often desirable to use global grid refinement factor $\bar{r} = 2$ (the global refinement factor $\bar{r}$ was defined before in the GCI section), i.e. grid doubling (halving), instead he recommended a minimum 10% change in $\bar{r}$. In this paper, the authors adopted $\overline{r_{21}} = \overline{r_{32}} \approx 1.2$ in the cross-section direction of the flow for the water region where the turbulence terms are more sensitive to the grid resolution. The local refinement factors $r_{21,i}$ and $r_{32,i}$ range from 1 to 2.0 and from 1 to 3.4, respectively. In the streamwise direction of the flow, the mesh was not refined since it is the least sensitive flow direction, as expected for a developed flow; thus, the computational time of the simulation can be reduced without any direct effect on the credibility of the simulation (Hardy *et al.* 2003).

RESULTS AND DISCUSSION

Verification (GCI)

Since mesh doubling was not performed, for inter-mesh point-to-point comparison purposes, a cubic interpolation was performed between meshes 1 and 3 and meshes 2 and 3, corresponding to 1,843,200 elements in mesh 1, 1,337,600 elements in mesh 2, and 1,065,600 elements in mesh 3. For all three meshes, the number of elements in the x direction was kept equal to 200. The number of elements for the water region in the y and z directions for mesh 1, 2 and 3 are: 192×32, 152×28 and 148×20, respectively. In the air region, the number of mesh elements in the z direction was kept constant and equal to 16 elements. The GCI was determined for three components of velocity, TKE, dissipation and tangential Reynolds stresses only for the water region by considering a cross-section at 7.5 m from the inlet, where uniform flow was considered to be established. GCI values have been calculated for the 3,427 common data points (nodes) when meshes 1 and 2 were compared against mesh 3.

Figure 2 provides the results of the three velocity components obtained by meshes 1, 2 and 3, and presented only for the water region of the cross-section. The contours of u, v and w velocity components do not demonstrate significant evolution in response to grid resolution.

The averaged values over the cross-section, $\overline{\mathrm{GCI}}$ and $\overline{p}$, are given in Table 1. As expected, the lowest absolute values of $\overline{\mathrm{GCI}}$, 0.39 and 0.47%, are for the u velocity component, while the highest $\overline{\mathrm{GCI}}$ values are for v and w velocity components, and Reynolds stresses *RSxy* and *RSyz*. This is not surprising because these variables,

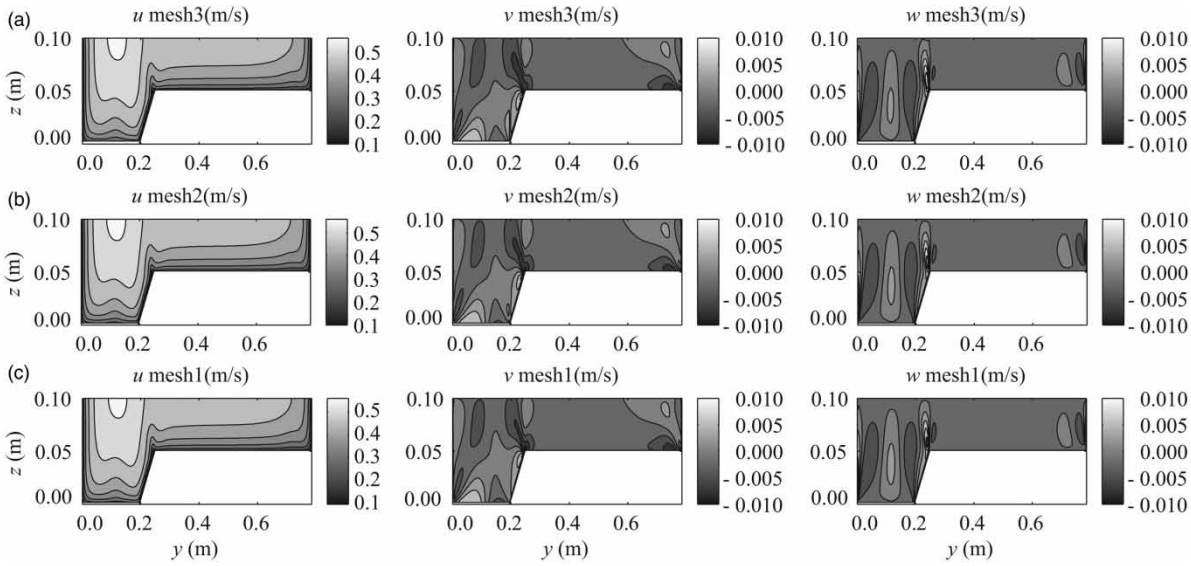

Figure 2 | Velocity components in the cross-section for water region: (a) mesh 3; (b) mesh 2; (c) mesh 1.

Table 1 | Averaged $\overline{GCI}$ and $\overline{p}$ over the cross-section

Variable of interest	$\overline{GCI32}$ (%)	$\overline{GCI21}$(%)	$\overline{p}$ (–)
u component	0.47	0.39	6.3
v component	50.11	125.42	5.4
w component	806.45	220.21	5.6
TKE	6.42	5.68	4.2
Dissipation	−5.30	−6.27	3.5
Reynolds stress *RSxy*	76.65	41.67	5.9
Reynolds stress *RSxz*	9.99	8.95	3.2
Reynolds stress *RSyz*	195.43	77.83	5.9

representing secondary flow, have small magnitude and therefore are highly sensitive to grid resolution. Thus, high $\overline{GCI}$ values for v and w velocity components indicate that mesh resolution is not yet good for predicting secondary flow. But from Table 1 it is clear that, except for the v velocity component and dissipation, the $\overline{GCI}$ values decrease with the mesh refinement, thus $\overline{GCI21}$ shows better results than $\overline{GCI32}$. The averaged apparent order of accuracy $\overline{p}$ is always higher than the algorithm order (2nd order). It should be mentioned that for all variables there are negative values of local p_i near the wall, which means that asymptotic convergence is not achieved in that region.

The cross-section contours GCI21 and GCI32 for three velocity components, TKE, dissipation and tangential Reynolds stresses are presented in Figure 3. The scales in Figure 3 were limited to a maximum GCI value of 5% for each variable. The white spots on the plots represent the zones where the GCI is higher than 5%. For example, such zones of high GCI appear in the MC, near the interface region between MC and FP, where the secondary flows dominate, for v and w velocity components. For the u component, such zones of high GCI are much smaller and appear near the MC wall, where lower velocities are expected. For TKE and dissipation, these zones appear in both MC and FP and close to the walls, which means that is very likely that mesh resolution for these zones was not enough since it is well known that the largest dissipation rate occurs close to the walls (e.g., Fulgosi *et al.* 2003; Li *et al.* 2010). As for tangential Reynolds stresses, *RSxy* and *RSyz* present the worst results, for the former the white zones are mainly located in the region where the mixing (shear) layer develops, while for the latter those zones are present in both MC and FP, where secondary flow is expected to be significant. Therefore, a higher spatial density of grid points is required to generate an adequate system definition of the shear layer and of secondary circulation, even though the streamwise flow is within a reasonable margin of error.

In order to reduce the $\overline{GCI}$ values, based on the GCI contours (Figure 3), meshes 1 and 2 were refined in transversal and vertical directions for the water region, mesh 3 was kept the same. The refinement was made in the horizontal direction near the lateral wall and in the mixing layer region, and in the vertical direction near the bottom and free-surface region. Afterwards, the global refinement factor became $\overline{r_{21}} = \overline{r_{32}} \approx 1.31$. The local refinement factors $r_{21,i}$ and $r_{32,i}$ range from 1 to 2.4 and from 1 to 3.7, respectively. The EARSM simulation was performed again on mesh 1 refined containing 2,436,000 hexahedron elements and on mesh 2 refined containing 1,564,000 hexahedron elements, corresponding to the number of elements in the y and z direction for the water region of 210×42 and 170×30, respectively. Then, these results together with the results of mesh 3 were used to calculate GCI21r (mesh 2 refined versus mesh 1 refined) and GCI32r (mesh 2 refined versus mesh 3), using the same methodology as mentioned above.

The new averaged values over the cross-section obtained with refined meshes, $\overline{GCIr}$ and $\overline{p_r}$, are shown in Table 2. The numerical results obtained with the refined meshes 2 and 1 did not show significant differences in general for all variables of interest. The refined $\overline{GCI21r}$ values (Table 2) are smaller than the non-refined $\overline{GCI21}$ values (Table 1) for some variables, as expected for u, v and w velocity components, but the opposite occurs for the other variables related to turbulence, which indicates that asymptotic convergence is still not attained. The averaged apparent order of accuracy $\overline{p_r}$ values (Table 2) are always smaller than the values obtained for non-refined meshes (Table 1), but closer to the algorithm order (2^{nd} order).

All contours of GCI presented in Figure 4 show similar patterns; the white zones, that represent the areas where GCI is higher than 5%, are localized in the same positions as for the non-refined meshes (Figure 3), except for TKE and dissipation where those areas are pushed into the FP wall in the refined meshes. There are some nodes where the GCI is much higher than the average GCI of the cross-section, especially close to the wall where a special mesh

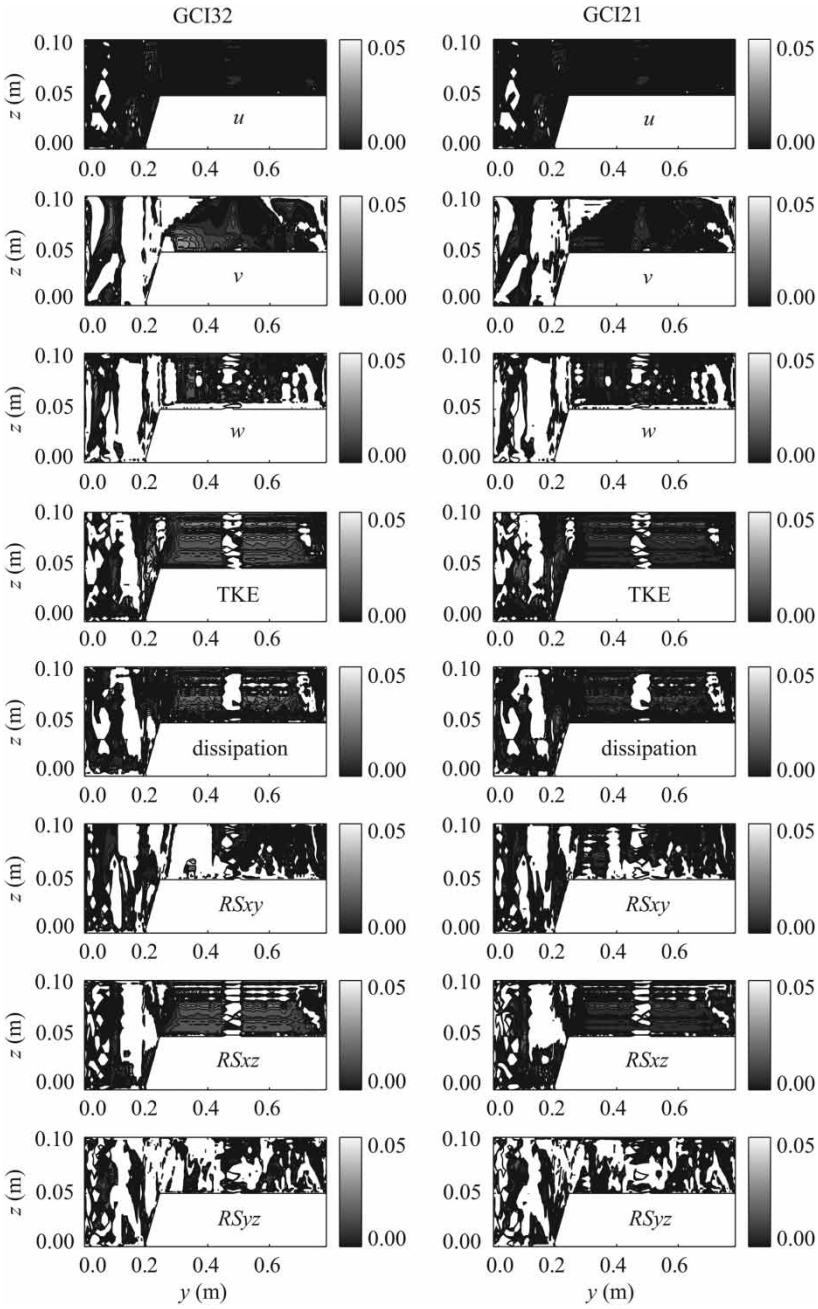

Figure 3 | Contours of GCI for the three velocity components, TKE, dissipation and for the tangential Reynolds stresses at cross-section 7.5 m downstream from inlet.

resolution is required. When we compare the contours of Reynolds stress *RSxy* before (Figure 3) and after refinement (Figure 4), we can conclude that the area of white zones, where the GCI is higher than 5%, has decreased significantly according to the mesh refinement performed in the mixing (shear) layer region. However, the averaged $\overline{GCI}$ value for Reynolds stress *RSxy* has increased in comparison to the non-refined mesh results (Tables 1 and 2, respectively), which is very likely due to the non-uniform spatial procedure of grid refinement and the high sensibility of this low magnitude variable to numerical inaccuracies. These inaccuracies are well explained by the lack of good resolution of the

Table 2 | Averaged $\overline{GCI}$ and $\overline{p_r}$ over the cross-section obtained with mesh 3, mesh 2 refined and mesh 1 refined

Variable of interest	$\overline{GCI32r}$ (%)	$\overline{GCI21r}$ (%)	$\overline{p_r}$ (–)
u component	0.50	0.23	1.8
v component	137.91	76.16	2.9
w component	50.77	165.93	2.2
TKE	18.72	17.74	1.8
Dissipation	32.83	31.62	1.4
Reynolds stress *RSxy*	592.59	106.42	2.9
Reynolds stress *RSxz*	46.90	44.30	1.6
Reynolds stress *RSyz*	97.09	89.60	2.2

viscous and buffer layers where important TKE, dissipation and Reynolds stresses are expected. Therefore, to reduce the GCI for the turbulence quantities, we need not only to refine the mesh, but also to provide an appropriate resolution of the close-to-wall turbulence, not obtained by $k-\varepsilon$ type wall functions as those used in this work. Nevertheless, further refinement of the mesh around the interface, where secondary flows are quite important, should improve results of GCI, especially for spanwise (v) and vertical (w) velocities, which are directly associated with these flows.

Analysing the last GCI results (Table 2) we can conclude that the numerical scheme is of an acceptable accuracy, especially for the u velocity component since the $\overline{GCI}$ is less than 1%. However, when the secondary variables are considered, like v and w components of velocity, and Reynolds stresses *RSxy* and *RSyz*, the $\overline{GCI}$ values are dramatically high. Therefore, the typically very small v and w components, which are around 1–2% of the maximum streamwise velocity, are largely affected by interpolation and discretization errors implicit in calculation of the GCI (Equations (4) and (5)). Furthermore, there are few nodes within the flow section, where the values are much larger than 5%, mostly close to walls where large gradients are expected, affecting substantially the average cross-section $\overline{GCI}$. It is an issue as to which variable a scheme should be verified on. If the aim is to capture only the maximum longitudinal velocity, it can be assumed that the scheme has converged and the numerical accuracy is acceptable. However, if the aim is to capture all the processes of mass and momentum transfer between the MC and FP and secondary flows, the numerical accuracy of the scheme might not be enough to predict lateral and vertical movement of the water. In such case, a further mesh refinement is necessary, or alternatively, the use of a higher order of the numerical scheme. Both alternatives lead to a more expensive computational cost.

Recalling the v and w results presented in Figure 2, they are quite similar for the three meshes and no visible improvement is seen, namely in what concerns intensity and location of secondary cells. This contradicts the GCI analysis that indicates a non-converged solution. Therefore, before trying a further mesh refinement the authors have decided to verify mesh quality using a different method. Thus, a linear regression analysis was performed between three data sets.

Linear regression analysis between meshes

In order to gain insight into discrepancies in the GCI values, the actual values of the different variables for mesh 3, and refined meshes 2 and 1 are considered. As with the GCI results, comparisons of refined meshes 1 and 2 are made to corresponding points on mesh 3, using a cubic interpolation. The results for u, v and w velocity components, TKE, dissipation and tangential Reynolds stresses are presented in Figure 5, where the solid line represents a linear regression line with zero intercept and dots represent the values of the variables in corresponding nodes between the two meshes. The comparison of variables in mesh 3 and refined mesh 2 (Figure 5) shows, taking into account correlation coefficients R close to unity, that velocities are overestimated by the coarser mesh, especially v and w; on the other hand turbulence quantities are underestimated, in particular dissipation and Reynolds stress *RSyz*. A clear improvement with mesh refinement can be seen by slopes closer to unity in refined meshes 2 and 1. The worst slope is obtained for dissipation, which is due to the fact that its values are higher near the boundaries and it is therefore a variable which is highly sensitive to grid resolution.

When the GCI values for the u velocity component are compared with the correlation coefficient and line slope, one can see that both methods give good results. Thus, we can conclude that mesh resolution is good enough and the results of streamwise velocity are mesh independent. However, when v and w velocity components and turbulence quantities are considered for refined meshes 1 and 2, there

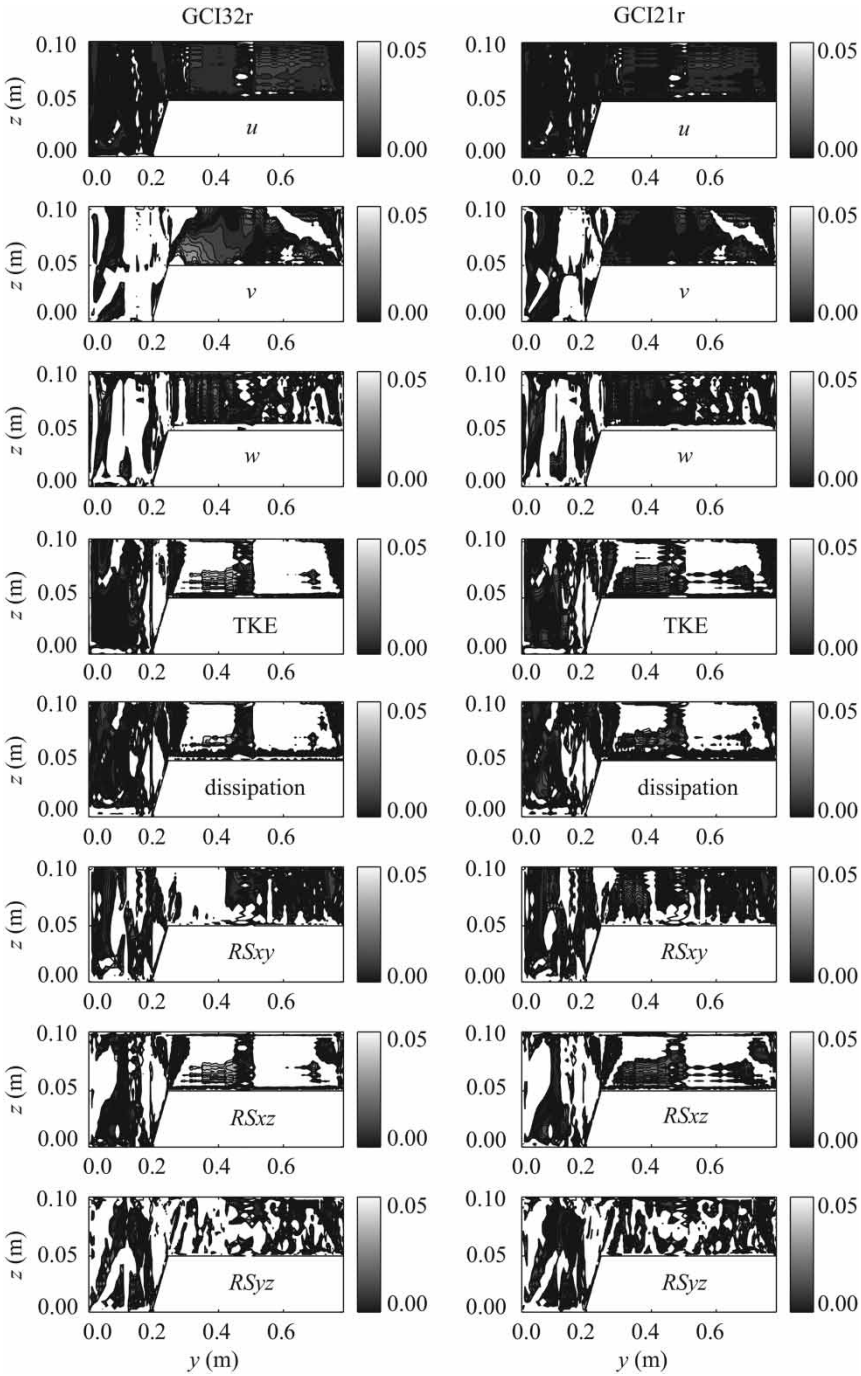

Figure 4 | Contours of GCI for the three velocity components, TKE, dissipation and for the tangential Reynolds stresses at cross-section 7.5 m downstream from inlet obtained with refined meshes 1 and 2 and mesh 3.

is a fair agreement between the meshes with regression line slopes around 1 ± 0.08, in apparent contradiction with the GCI results. It means that for the compound channel case we cannot rely only on the GCI method in verifying the mesh quality. The GCI method is very sensitive when calculating low magnitude values, resulting in 'unrealistic' very large errors. However, both methods together are good for assessing the mesh quality.

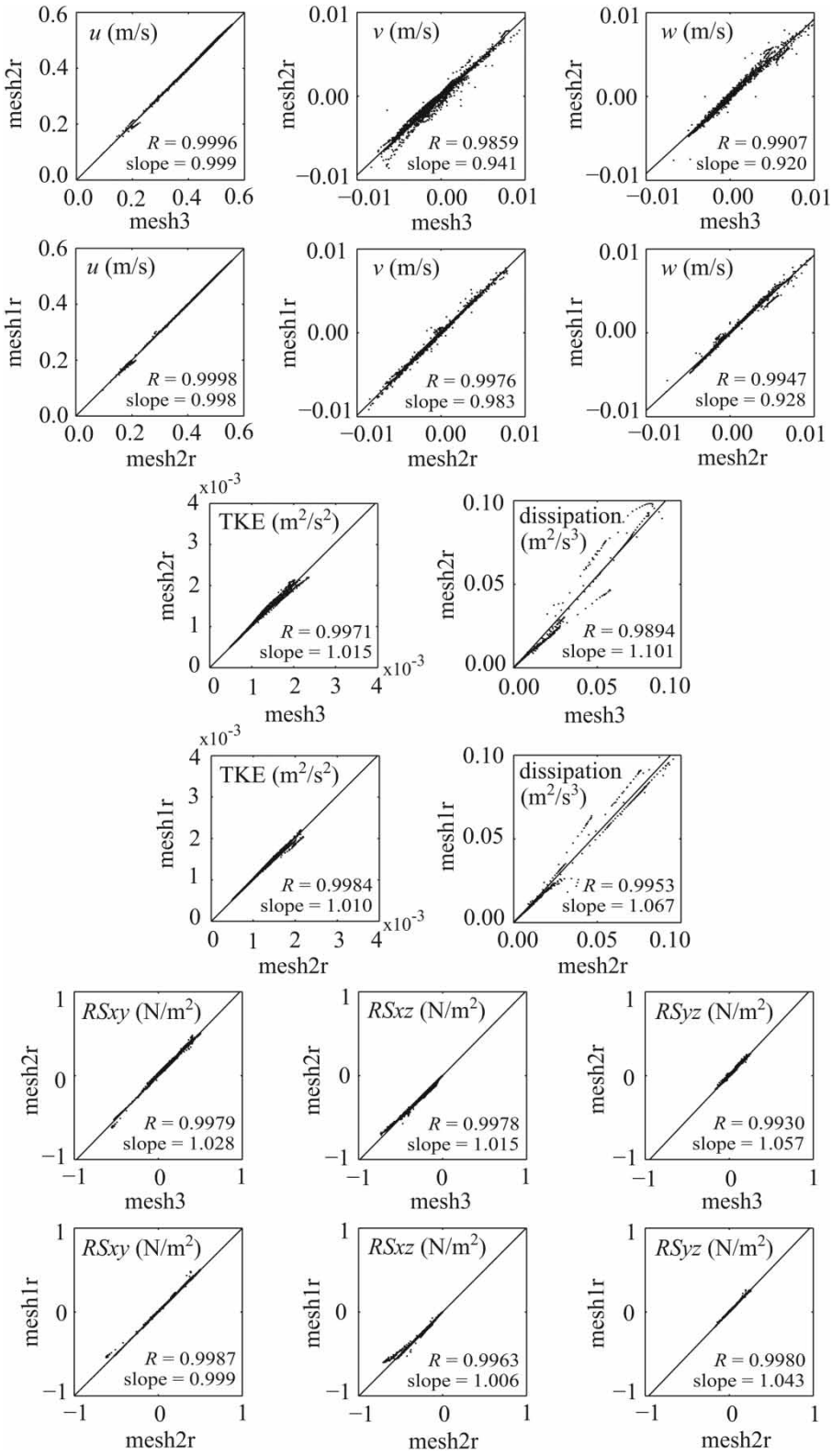

Figure 5 | Linear regression analysis of *u*, *v* and *w* velocity components, TKE, dissipation and tangential Reynolds stresses for mesh 3 vs. mesh 2 refined and for mesh 2 refined vs. mesh 1 refined.

In summary, based on the results of linear regression analysis, as well as on GCI values, we can conclude that the use of both methods can overcome some drawbacks of GCI analysis and that mesh 2 refined is fine enough for 3D modelling, except for accurately predicting w, dissipation, Rxz and Ryz, especially near the walls.

Validation (experimental data)

In this part of the paper, the comparison of numerical and experimental results is performed. The experimental study was carried out in the Hydraulics Laboratory of the University of Beira Interior in a prismatic flume with a bed slope $S_0 = 0.001$, 10 m in length and with an asymmetric trapezoidal compound section (Figure 1). The uniform flow was established by imposing a discharge of 23.0 l/s which corresponds to a relative depth $h_r = (H–h_b)/H \approx 0.5$. The streamwise u and vertical w flow velocities were measured using a LDV. Positioning of the system was controlled by computer with 0.1 mm precision. The measurements were performed in back-scattering mode through the lateral glass-wall of the flume. The water depth was measured using a point gauge and acoustic probes; the total discharge was measured using an electromagnetic flow-meter installed in the recirculation pipe of the flume.

Numerical results are based on mesh 1 refined, described in previous sections. Figure 6 presents the numerical and experimental results for u and w velocity components for a cross-section 7.5 m downstream from the flume inlet. The experimental results presented here are only until lateral position $y = 0.4$ m, the maximum distance that LDV can measure in the experimental facility.

The numerical and experimental contours of the u velocity component show similar behaviour: the isovels bulge significantly upward near the upper interface as a result of secondary flow cells generated by wall turbulence anisotropy. The difference between numerical results and experimental data is essentially that the numerical model cannot capture the effect of free surface, where the maximum velocities occur below the free surface (Nezu 1994). This might be due to the missing modelling of free surface tension phenomenon in the computational model.

The numerical and experimental contours of the w component of velocity show a similar pattern: the positive and negative velocities are almost in the same locations, slightly shifted to the MC wall in the case of the experimental values. The presence of two secondary cells is observed, one rotating counter-clockwise located in the interface region and another rotating clockwise located in the MC, between the sidewall and the centre. The first secondary flow cell is responsible for pushing upwards particles with smaller velocities near the upper interface, causing the inflection of the isovels (Figures 6(a, b)). The intensity of this cell is slightly higher for the experimental results, which confirms the fact that Algebraic Stress Models underestimate the secondary flow (Bradshaw 1987). In the MC, near the lower interface, the interaction can be observed of the two secondary cells that direct the flow downwards and

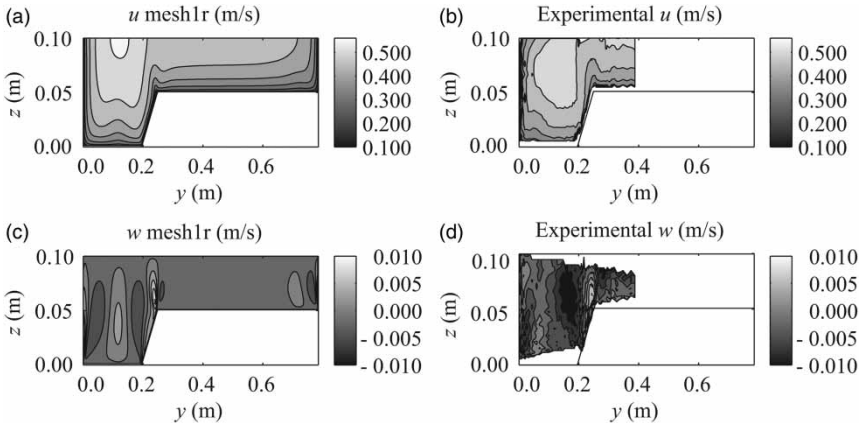

Figure 6 | Comparison of u and w velocity components obtained numerically (a and c, respectively) and experimentally (b and d, respectively) at a cross-section 7.5 m downstream from inlet.

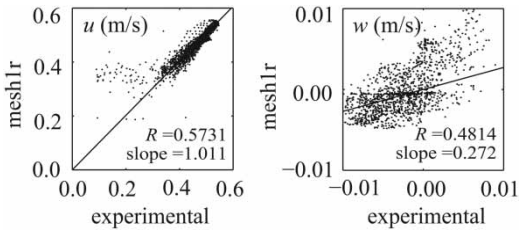

Figure 7 | Comparison between the velocity components u and w for mesh 1 refined and experimental data using linear regression analysis.

therefore inflect the isovels in that direction (Figure 6(a)). The numerical secondary flow cell in the MC (Figure 6(c)) shows the same effect, but the experimental one is significantly weaker and is not able to inflect the isovels downwards.

Linear regression analysis for u and w velocity components obtained experimentally and numerically is presented on Figure 7, for all points where experimental measurements were made. The comparison of the u velocity component, obtained numerically with mesh 1 refined and experimentally, suggests a good level of agreement. The major discrepancies are found for the lower velocities where the numerical model overestimates the experimental data, the low correlation coefficient also explains this, indicating that the model does not capture well what is happening near the walls. When a comparison is made for the w velocity component, a distinct area of disagreement exists. The dispersion of the results reflects the differences in experimental and numerical locations of the secondary cells. It is observed that generally the numerical model underestimates the experimental w velocity component.

The cross-section average relative error between numerical and experimental results for the u velocity component is 1.15%, and 329.52% for the w velocity component. The relative error for vertical velocity w is too high; this is due to very small values of the w velocity component and the previously mentioned error in secondary flow. The value of vertical velocity w is two orders of magnitude smaller than the value of longitudinal velocity u and any, even very small, difference in the value between numerical results and experimental data results in a large relative error. Also there is an influence of the cubic interpolation of numerical results into the coarse experimental mesh.

CONCLUSION

In this paper, the GCI method was adopted for the verification of 3D CFD simulations of compound channel flow. The GCI is a recognized technique which follows a standard editorial policy statement for the control of numerical accuracy.

The verification has shown that when meshes 1, 2 and 3 are considered for calculations, the GCI has the smallest values for downstream component of velocity (u) and the highest for higher order parameters. After the refinement of the mesh, although some improvements in $\overline{\text{GCI}}$ can be observed, the higher order variables still present an oscillating $\overline{\text{GCI}}$ behaviour, either increasing from coarse to finer meshes or from non-refined to refined meshes. It must be noted that the high $\overline{\text{GCI}}$ values are mostly due to a few number of cells located near the walls, where clearly one cannot assume that asymptotic convergence is achieved.

In addition to the GCI method, the authors have adopted a linear regression analysis to verify the mesh quality. This analysis has shown a much better level of agreement between the meshes with regression line slopes close to unity for most variables, and converging to unity with mesh refinement. Nevertheless, velocity components v and w are overestimated and turbulent quantities are underestimated by coarser meshes (mesh 3 and mesh 2 refined), in particular dissipation and Reynolds stress *RSyz*. The dissipation rate is known to be one of the most difficult turbulence parameters to model and the Reynolds stress *RSyz* is linked to bottom turbulence. The Reynolds stress *RSxy* presents very good results for the finer mesh, indicating that the refinement in the mixing layer region was more effective than near the walls. Merging GCI and linear regression analysis, we can conclude that the refined mesh has satisfactorily converged for most variables.

The validation has shown a fair agreement between numerical and experimental results. For the streamwise velocity (u), the model is capable of simulating the entire flow field, except the near-wall region. For the vertical velocity (w), the results show that the model is able to simulate secondary flow, although the location and intensity of secondary cells differs from the experimental ones. This is a known characteristic of Algebraic Stress Models, and

therefore should not be totally attributed to mesh dependence.

Summarizing, it can be stated that the methods for solution verification used in this paper, GCI method and linear regression analysis, are good for assessing the credibility of the simulations. From the discussion above, it is clear that, although the GCI method is mathematically well-founded, when small value variables are considered the method should be complemented with other methods, such as linear regression analysis.

ACKNOWLEDGEMENTS

The authors wish to acknowledge the financial support of the Portuguese Foundation for Science and Technology through the project PTDC/ECM/70652/2006. The first and second authors wish to acknowledge the financial support of the Portuguese Foundation for Science and Technology through the Grants No. SFRH/BD/64337/2009 and SFRH/BD/33646/2009, respectively.

REFERENCES

Bradshaw, P. 1987 Turbulent secondary flows. *Ann. Rev. Fluid Mech.* **19**, 53–74.

Celik, I., Chen, C. J., Roache, P. J. & Scheurer, G. 1993 Quantification of uncertainty in computational fluid dynamics. ASME Fluids Engineering Division Summer Meeting, ASME Publ. No. FED-Vol. 158, Washington, DC, Jun. 20–24.

Celik, I., Ghia, U., Roache, P. J., Freitas, C. J., Coleman, H. & Raad, P. E. 2008 Procedure for estimation and reporting of uncertainty due to discretization in CFD applications. *J. Fluids Eng.* **130**, 078001-1–078001-4.

Celik, I., Hassan, Y., Hughes, D., Johnson, R. & Sommerfeld, M. 1994 *Experimental and Computational Aspects of Validation of Multiphase flow CFD Codes*. The American Society of Mechanical Engineers United Engineering Center, FED-Vol. 180, New York.

Coleman, H. W. & Stern, F. 1997 Uncertainties and CFD code validation. *J. Fluids Eng.* **119**, 795–803.

Freitas, C. J. 1993 Journal of fluids engineering editorial policy statement on the control of numerical accuracy. *ASME J. Fluids Eng.* **115**, 339–340.

Fulgosi, M., Lakehal, D., Banerjee, S. & De Angelis, V. 2003 Direct numerical simulation of turbulence in a sheared air-water flow with a deformable interface. *J. Fluid Mech.* **482**, 319–345.

Hardy, R. J., Lane, S. N., Ferguson, R. I. & Parsons, D. R. 2003 Assessing the credibility of a series of computational fluid dynamic simulations of open channel flow. *Hydrol. Processes* **17**, 1539–1560.

Hellsten, A. 2004 New Two-Equation Turbulence Model for Aerodynamics Applications. Laboratory of Aerodynamics, Report No. A-21, Helsinki University of Technology, Series A, 2004, ISBN 951-22-6933-3. Doctoral dissertation.

Hirt, C. W. & Nichols, B. D. 1981 Volume of fluid (VOF) method for the dynamics of free boundaries. *J. Comput. Phys.* **39** (1), 201–225.

Li, X.-X., Liu, C.-H. & Leung, D. Y. C. 2010 Parallel FEM LES with one-equation subgrid-scale model for incompressible flows. *Int. J. Comput. Fluid Dyn.* **24**, 37–49.

Morvan, H. P. 2005 Channel shape and turbulence issues in flood flow hydraulics. *J. Hydraul. Eng.* **131**, 862–865.

Morvan, H. P., Pender, G., Wright, N. G. & Ervine, D. A. 2002 Three-dimensional hydrodynamics of meandering compound channels. *J. Hydraul. Eng.* **128** (7), 674–682.

Nezu, I. 1994 Compound open-channel turbulence and its role in river environment – Significance of secondary currents. 9th Congress of APD-IAHR, Keynote Address, Singapore.

Oberkampf, W. L. 1994 A proposed framework for computational fluid dynamics code calibration/validation. *AIAA Paper No. 94-2540, 18th AIAA Aerospace Ground Testing Conference*, Colorado Springs, CO.

Oberkampf, W. L. & Trucano, T. G. 2002 Verification and Validation in Computational Fluid Dynamics. Sandia Report SAND2002-0529. Sandia National Laboratories, Albuquerque, NM.

Roache, P. J. 1994 Perspective: a method for uniform reporting of grid refinement studies. *J. Fluids Eng.* **116**, 405–413.

Roache, P. J. 1997 Quantification of uncertainty in computational fluid dynamics. *Ann. Rev. Fluid Mech.* **29**, 123–160.

Roache, P. J. 1998a *Verification and Validation in Computational Science and Engineering*. Hermosa Publishers, Albuquerque, NM.

Roache, P. J. 1998b Verification of codes and calculations. *AIAA J.* **36** (5), 696–702.

Roache, P. J., Ghia, K. N. & White, F. M. 1986 Editorial policy statement on control of numerical accuracy. *ASME J. Fluids Eng.* **108**, 2.

Sterling, M., Beaman, F., Morvan, H. & Wright, N. 2008 Bed-shear stress characteristics of a simple, prismatic, rectangular channel. *J. Eng. Mech.* **134** (12), 1085–1094.

Wallin, S. & Johansson, A. V. 2000 An explicit algebraic Reynolds stress model for incompressible and compressible turbulent flows. *J. Fluid Mech.* **403**, 89–132.

First received 30 November 2011; accepted in revised form 23 January 2013. Available online 18 February 2013

Paper II

SIMULATION OF THE VELOCITY FIELD IN COMPOUND CHANNEL FLOW USING DIFFERENT CLOSURE MODELS

Marina Filonovich, Ricardo Azevedo, Luis R. Rojas-Solórzano, João Bento Leal

1st European IAHR Congress, Edinburgh, UK, 2010

SIMULATION OF THE VELOCITY FIELD IN COMPOUND CHANNEL FLOW USING DIFFERENT CLOSURE MODELS

M. Filonovich[1,3], R. Azevedo[1], L. R. Rojas-Solorzano[2] and J. B. Leal[1,3]

[1] Universidade Nova de Lisboa, Faculdade de Ciências e Tecnologia, Caparica, Portugal
[2] Universidad Simón Bolívar, Caracas, Venezuela
[3] CEHIDRO, Instituto Superior Técnico, Lisbon, Portugal

ABSTRACT
In this study a comparison of three turbulence closure models (two isotropic and one anisotropic) with experimental data is performed. The interaction between the main channel (MC) flow and the floodplain (FP) generates a complex flow structure. A shallow mixing layer develops between the MC flow and the slower FP flow generating a high horizontal shear layer, streamwise and vertical vortices, momentum transfer and other phenomena, related to velocity retardation and acceleration. This phenomenon dissipates part of the kinetic energy and contributes to the reduction of the velocity differences between the MC and the FP. The large scale vortices that are generated in the shear layer are anisotropic, provoking the formation of secondary flow cells that influence the primary velocity distribution. These three-dimensional turbulent structures can be reasonable well reproduced by a simple anisotropic model (Algebraic Stress Model). The isotropic models are capable of simulating the boundary layer, especially the model base in *k*-ω equations, but cannot simulate the shear layer that develops at the interface.

INTRODUCTION
Most natural rivers have compound cross-section composed by a main channel and by one or more floodplains on the lateral sides. For most of the time the water flows only in the main channel, however, when flooding occurs the water depth exceeds the bank full depth of the main channel and thus overflow occurs on the floodplains. The fast flow in the main channel is retarded by the slower flow on the floodplains, causing lateral momentum transfer. The shear layer that develops at the interface of the main channel and the floodplain by the difference of velocities affects turbulence structures and streamwise and vertical vortices are developed. Turbulent structures in compound channel flow indicate three-dimensional (3D) behavior (Fig. 1). There are two kinds of vortices that are generated at the interface between the main channel and the floodplain; one is a horizontal vortex due to shear layer of the streamwise flow, first observed by Sellin (1964), and the other is the secondary flow in the cross section due to anisotropy of turbulence, also called secondary flow of 2nd kind (*cf.* Nezu and Nakagawa, 1993). These effects have been observed experimentally by Shiono and Knight (1991), and Tominaga and Nezu (1991) using fiber-optic Laser-Doppler anemometer (LDA) and numerically by Naot *et al*. (1993), using an algebraic Reynolds stress model (ARSM), by Shiono and Lin (1992) and Pezzinga (1994), using a non-linear *k*-ε model and by Cokljat and Younis (1995), using the full Reynolds-stress transport model. They have found a significant influence of secondary flows onto momentum transfer and boundary shear stress.

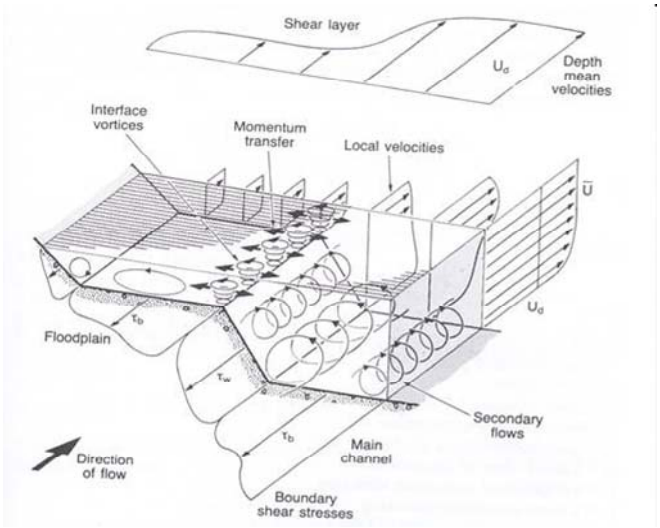

Figure 1. Three dimensional description of compound channel flow by Shiono and Knight (1991).

It is very difficult to predict secondary flows because the governing equation for the streamwise vorticity, besides using the very computational expensive DNS, cannot be solved without any modeling. Various turbulence models have been used for predicting the secondary flows and turbulence in compound channels. Numerical studies based on 3D Reynolds Averaged Navier Stokes (RANS) equations have been performed in recent years by several investigators (among others, Naot *et al*., 1993; Pezzinga, 1994; Cokljat and Younis, 1995; Lin and Shiono, 1995). If the appropriate turbulence model

is used, then secondary flows are accurately simulated and the distribution of mean primary velocity and the wall shear stress are also accurately reproduced. But the main difficulty lies in the choice of the turbulence model. Thus, isotropic eddy viscosity models, like the standard k-ε model, are robust and economic but are incapable of producing secondary flows. Instead, the ARSM is being often used lately; it reasonably predicts secondary flows and is computationally economic compared to Direct Numerical Simulation, DNS, or more complex models (*e.g.* Large Eddy Simulation, LES).

The present study simulates the uniform flow in compound channel for high relative depth (≈ 50%), using ANSYS CFX Computational Fluid Dynamics (CFD) code. For this purpose k-ε model, Shear Stress Transport (SST) model and Explicit Algebraic Reynolds Stress Model (EARSM) were employed. The k-ε model and SST model are isotropic models based on Boussinesq's approximation and do not produce secondary flows, while EARSM is derived from the Reynolds stress transport equations and is able to simulate secondary flows caused by turbulence anisotropy . The main purpose of the study is comparison of the numerical results obtained by isotropic and anisotropic models with the experimental velocity results obtained by a Laser Doppler Velocimeter (LDV).

EXPERIMENTAL SET-UP AND EXPERIMENTS DETAILS

The experimental studies were carried out in the Hydraulics Laboratory of the University of Beira Interior in prismatic channel (Fig. 2a) with a bed slope $i = 0.001$, 10 m length and with asymmetric trapezoidal compound section. The compound channel geometry and dimensions are shown in Figure 3. In this figure H is the water level above channel bottom, h is the bankfull level above channel bottom, b main channel bottom width, and B section width. The uniform regime was established by imposing a discharge of 24.7 l/s which corresponds to a relative height $h_r = (H - h)/H \approx 50\%$. The streamwise instantaneous velocity of the flow was measured using a LDV. Positioning of the system probe was achieved with 0.1 mm precision positioning system controlled by computer. The measurements were performed in back-scattering mode through the lateral glass of the channel (Fig. 2b). The water depth was measured using a point gauge and acoustic probes; the total discharge was measured using an electromagnetic flow meter installed in the recirculation pipe of the channel.

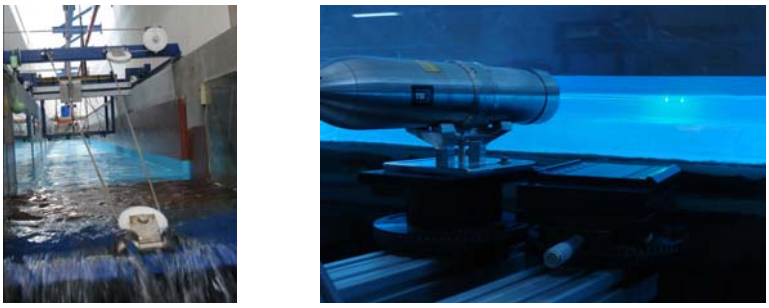

Figure 2. a) Photo with donstream view of the channel; b) Photo of the LDV measuring laterally.

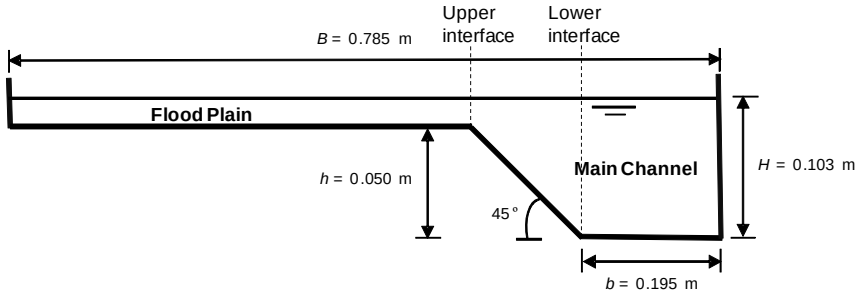

Figure 3. Cross- section of the compound channel

In simple geometries and for smooth bed, subcritical uniform open-channel flow conditions are easy to establish in a laboratory facility, as long as the flow depth is constant throughout the flume and the turbulent boundary layer is fully developed. In more complex geometries, as compound cross-section, the additional interaction between main channel and floodplain flow creates a shear layer (see Fig. 1) that difficults the establishment of uniform flow conditions in relatively short experimental flumes (*cf.* Bousmar *et al.*, 2005). To ensure uniform flow conditions the following procedure was adopted: i) the discharge computed with the Divided Channel Method (DCM, *e.g.* Chow, 1954) was inputted upstream; ii) the vertical tail gate downstream was operated in order to have almost constant flow depth throughout the channel (maximum difference of 0.1 mm). In order to confirm uniform flow conditions, vertical profiles of time-averaged velocity, U, were measured in the floodplain, in the upper and lower interfaces (Fig. 3), and in the middle of the main channel, at four cross-sections (x = 3, 4, 6 and 7 m). The results are presented in Fig. 4 and show a constancy of the profiles throughout the flume indicating that uniform flow was attained and that the turbulent boundary and shear layers are developed, especially in the floodplain.

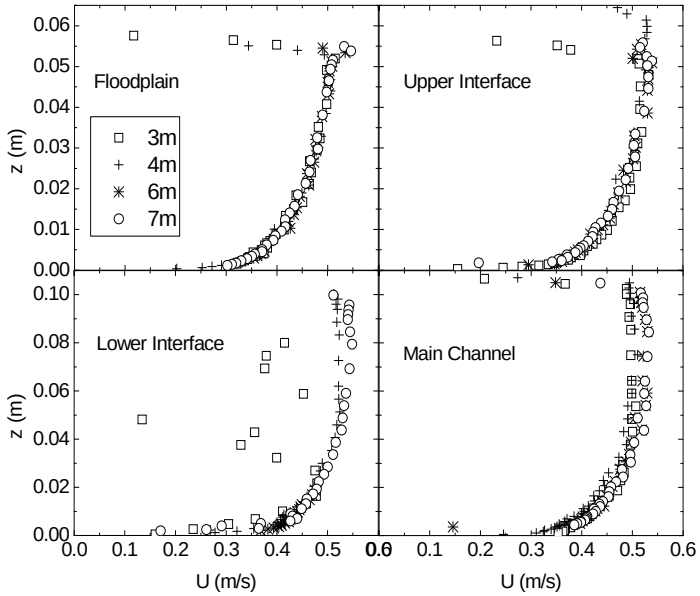

Figure 4. Measured vertical profiles of time-averaged velocity in the floodplain, in the upper and lower interfaces (Fig. 3), and in the middle of the main channel, at cross-sections x = 3, 4, 6 and 7 m.

NUMERICAL MODELLING

The flow field was calculated using a commercial 3D CFD code (ANSYS CFX 12.0). This code uses a control-volume-based finite element method, where the governing equations are discretized over each control volume, using a second-order upwind scheme for the advection terms in momentum and turbulence equations. The resulting system is then solved in a coupled manner, and the results are then interpolated to the grid nodes. The convergence criterion was settled when a global mass imbalance was less than 0.1%.

In this work, the flow dynamics is modeled by numerically solving the Reynolds Averaged Navier-Stokes (RANS) equations for the water-air combination. To model the air-water segregated flow, the mass conservation of each phase is solved, while the momentum equation (RANS) for each phase is added up to eliminate the interphase momentum transfer term. There is a closure equation for the volume fraction, which states that both phases volume fraction must add up to one at every fluid cell. The free surface model is accompanied by an interphase sharpening algorithm, which guarantees a minimum diffusion of the volume fraction around the interphase.

The domain, exactly coincident with the experimental flume, was discretized using approximately 1,200,000 regular hexahedral elements aligned to the main directions. For turbulence modeling purposes, the z^+ of the element closest to the bottom walls were kept around 20 for the floodplain and 50 for the main channel, using therefore, wall functions for all the turbulent models here explored.

A uniform velocity field with a water depth of 0.103m and 5% of turbulence intensity was prescribed at the inlet; while a hydrostatic pressure profile with zero velocity derivatives was set at the outlet. The upper boundary condition was prescribed on the air, at 0.05 m above the expected free surface, with free-slip wall to allow the free motion of the air along the channel, while facilitating the numerical robustness of the simulation. The bottom wall was prescribed with a non-slip boundary condition and an absolute roughness of 0.0002m.

Three different turbulence models were used; all based on the basic RANS equations: k-ε model; Shear Stress (SST) model; and Explicit Algebraic Reynolds Stress Model (EARSM). The first two models belong to the family of isotropic two-equation models, while the third model captures the natural anisotropy within the wall turbulence and therefore, solves for the 6 Reynolds stresses. The standard k-ε model with wall functions for dampening the turbulent viscosity near the walls is used (Rodi, 1993). The SST model accounts for the transport of the turbulent shear stress and uses a combination of the best features of the k-ε model for free turbulence, and the standard Wilcox k-ω model for the solution of the wall turbulence (Menter, 1994). The use of this model in this study aims to determine the possible highly accurate predictions of the onset and the amount of flow separation under adverse pressure gradients. The EARSM represents an extension of the standard k-ε two-equation model. This is derived from the Reynolds stress transport equations and gives a nonlinear relation between the Reynolds stresses and the mean strain-rate and vorticity tensors (Wallin and Johansson, 2000). This model is used in the present study due to the higher order terms it solves, such that it may be able to capture effects of secondary flows.

DISCUSSION

Vertical Profiles of Time-Averaged Velocity

The vertical profiles of time-averaged velocity measured and simulated numerically with *k*-ε, SST and EARSM turbulence models in cross-section x = 7 m are presented in Fig. 5. The figure also includes the log-law (*e.g.* Nezu and Nakagawa, 1993):

$$U^+ = \frac{1}{\kappa}\ln\left(z^+\right) + B \tag{1}$$

where $U^+ = U/u_*$ is the non-dimensional flow velocity, u_* is the shear velocity, κ is the von Kármán constant equal to 0.41, $z^+ = u_* z/\nu$ is the non-dimensional vertical coordinate, ν is the kinematic viscosity equal to $1{,}01\text{x}10^{-6}$ m^2/s at 20ºC, and B is a constant that for smooth bottoms takes the value 5.3 (*cf.* Nezu and Nakagawa, 1993). The values of u_* and B can be obtained by applying Clauser's method (*e.g.* Nezu and Nakagawa, 1993) where a linear regression is used to fit the data of ln(z) and u inside the inner layer (*i.e.*, $z/H < 20\%$). A practically constant value of u_* = 0.022 m/s was obtained, while values of B were more scattered ranging from 3 to 7.

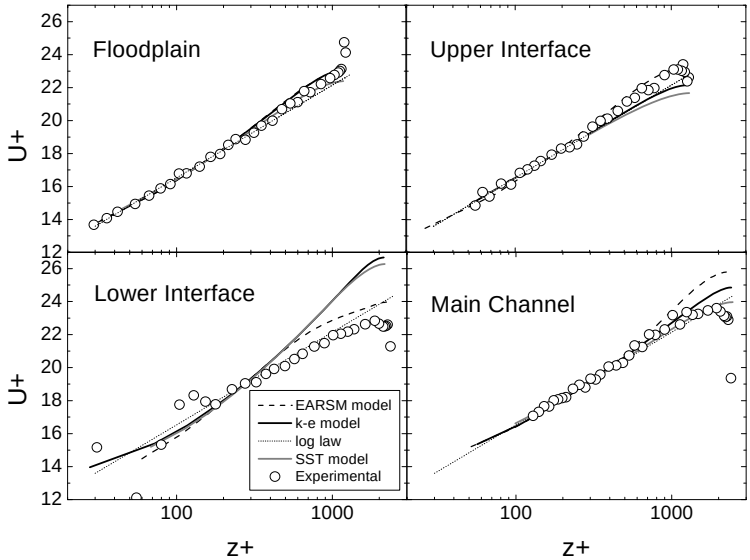

Figure 5. Measured and simulated (*k*-ε, SST and EARSM models) vertical profiles of time averaged velocity in the floodplain, in the upper and lower interfaces, and in the middle of the main channel, at cross-section x = 7 m.

Analyzing the results presented in Fig. 5 one can conclude that, in the inner layer ($z^+ < \approx 450$), all models give similar results and with good agreement with experimental data. Another conclusion is that in the floodplain and in the middle of the main channel the results seem almost independent of the turbulence model used and show good agreement with the experimental data, except near the free-surface. In the interface verticals and for the outer layer ($z^+ > \approx 450$) EARSM model gives results slightly overestimated but closer to the experimental data than the other isotropic models. This means that the depth-averaged velocity in the floodplain can be computed using simplified models (isotropic), but in the upper and lower interfaces those models will, respectively, underestimate and overestimate the depth-averaged velocity, being necessary the use of anisotropic models like EARSM.

Isovel lines, secondary flow vectors, and TKE

The isovel lines obtained numerically with *k*-ε, SST and EARSM turbulence models in cross-section x = 7 m are presented in Fig. 7. The isovel lines of EARSM (Fig. 7c) bulge significantly upward near the upper interface as a result of secondary flow cells generated by turbulence anisotropy and represented in Fig. 1 (*cf.* Nezu, 1994). The isovel lines of *k*-ε and SST don't show that behavior since they assume isotropic turbulence and therefore cannot reproduce the secondary flow.

The secondary flow vectors of EARSM are presented in Fig. 8, confirming the simulation of two secondary flow cells interacting near the upper interface and responsible for pushing upwards particles with smaller velocities, causing the inflection of the isovel lines. In the main channel, near the lower interface, it can also be observed the interaction of two secondary cells that direct the flow downwards and therefore inflect the isovel lines in that direction (Fig. 7c). The two secondary flow cells exiting in the main channel (Fig. 1) interact in the middle of the main channel directing the flow upwards (Fig. 7c), but with less intensity than what is observed in the upper interface. Near the wall, the secondary cell points downward (Fig. 7c) causing and effect similar to what has been referred for the lower interface. The ability of EARSM in reproducing secondary flow cells helps explaining its better approximation to the experimental velocity profiles (Fig. 5) in the interface region, where turbulence anisotropy was expected to occur.

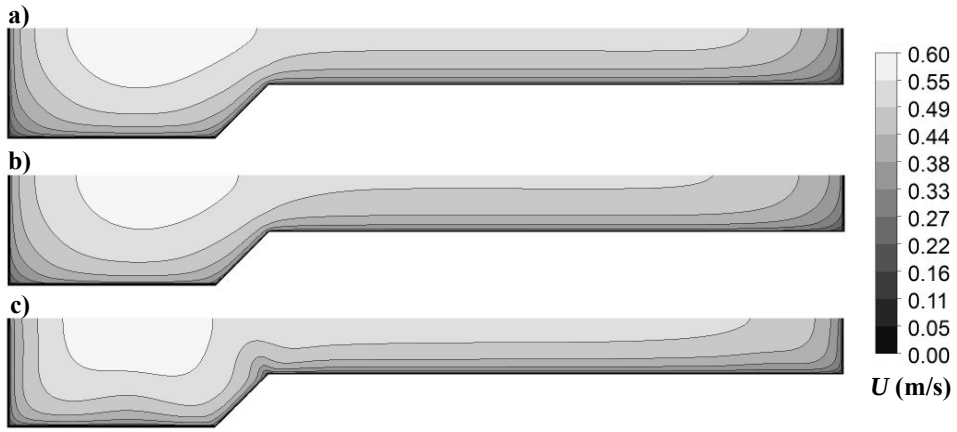

Figure 7. Isovel lines obtained numerically in cross-section x = 7 m with turbulence model: a) k-ε; b) SST; and c) EARSM.

Figure 8. Secondary flow vectors obtained numerically in cross-section x = 7 m with EARSM turbulence model.

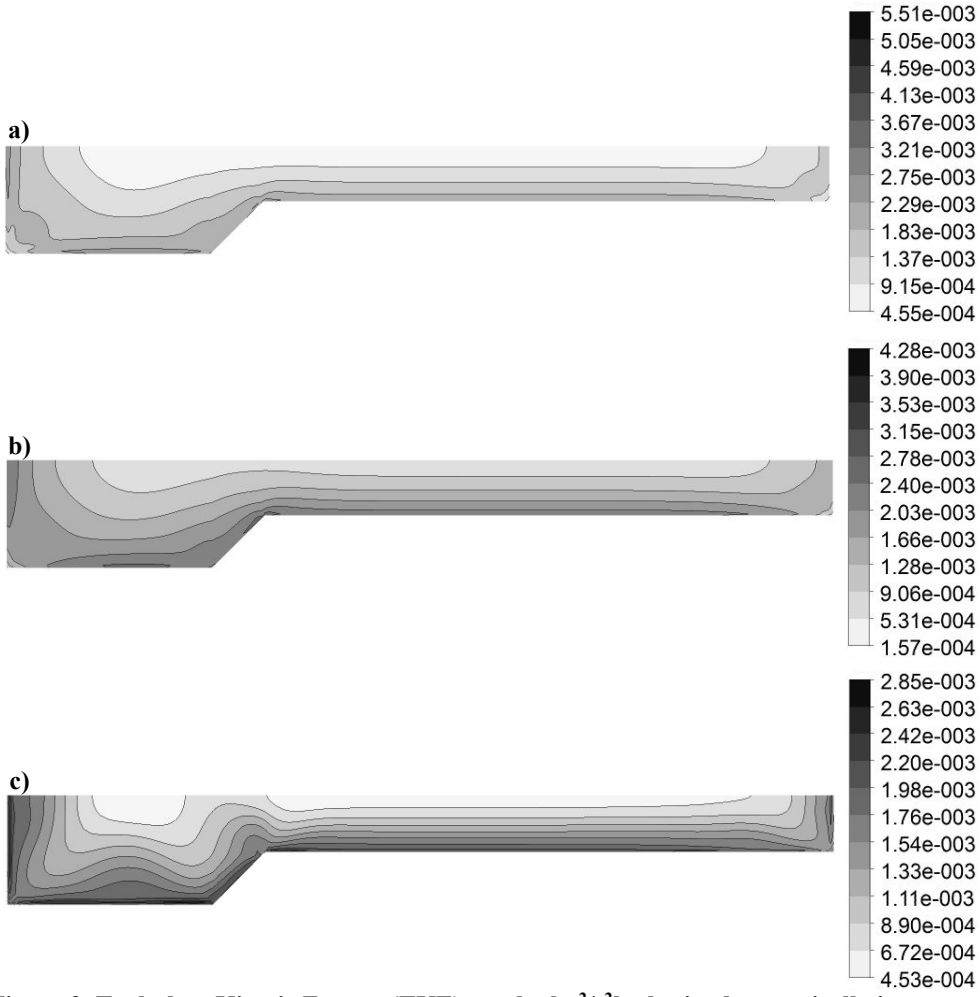

Figure 9. Turbulent Kinetic Energy (TKE) results [m^2/s^2], obtained numerically in cross-section x = 7 m with turbulence model: a) k-ε; b) SST; and c) EARSM.

Fig. 9 presents the Turbulent Kinetic Energy (TKE) results obtained numerically with k-ε, SST and EARSM turbulence models in cross-section x = 7 m. Comparing the results obtained with k-ε model (Fig. 9a) and SST model (Fig. 9b), one can conclude that the latter performs better near the walls. This is because in CFX k-ε is not optimized for boundary

layer flows, whereas SST model uses k-ω equations near the walls which allow obtaining better results (*cf*. Menter, 1994). Nevertheless, the EARSM shows the more realistic results (Fig. 9c), since it not only models the turbulence created by the walls, but it also simulates the turbulence arising from the interaction between the flows in the main channel and in the floodplain.

CONCLUSIONS

The numerical simulation of experimental results with three different turbulence models: k-ε and SST, both isotropic, and EARSM, anisotropic, allowed to verify that using anisotropic turbulence models is required if velocity profiles are to be accurately predicted in the interface region. Isotropic models underestimate velocities in the upper interface and overestimate them in the lower interface. In the main channel isotropic models perform better and in the floodplain all models give similar results. Isovel lines, secondary flow vectors, and TKE numerical results confirm the relevance of modeling anisotropy in the sense that it generates secondary flow responsible for changing the isovel lines of streamwise velocity, especially in the upper interface where a shear layer develops.

ACKNOWLEDGMENTS

The authors wish to acknowledge the financial support of the Portuguese Foundation for Science and Technology through the project PTDC/ECM/70652/2006. The first and second authors wish to acknowledge the financial support of the Portuguese Foundation for Science and Technology through the Grants No. SFRH/BD/64337/2009 and SFRH/BD/33646/2009, respectively.

REFERENCES

1. Bousmar, D.; Riviere, N.; Proust, S.; Paquier, A.; Morel, R. and Zech, Y. (2005) Upstream discharge distribution in compound-channel flumes, *Journal of Hydraulic Engineering*, 131(5): 408-412.
2. Chow, V.T. (1959) *Open channel hydraulics*, McGraw Hill, New York.
3. Cokljat, D. and Younis, B. (1995) Second Order Closure Study of Open-channel Flows, *Journal of Hydraulic Engineering*, 121(2): 94-107.
4. Lin, B. and Shiono, K. (1995) Numerical Modelling of Solute Transport in Compound Channel Flows, *Journal Hydraulic Research*, 33(6): 773-788.
5. Menter, F.R. (1994) Two-equation eddy-viscosity turbulence models for engineering applications, *AIAA Journal*, 32(8): 1598-1605.
6. Naot, D., Nezu, I. and Nakagawa, H. (1993) Calculation of compound open channel flow. *Journal Hydraulic Engineering*, 119(12): 1418-1426.
7. Nezu, I. (1994) Compound open-channel turbulence and its role in river environment, *9th Congress of the Asian and Pacific Division of IAHR*, Keynote address, Singapore.
8. Nezu, I. and Nakagawa, H. (1993) *Turbulence in open-channel flows*, IAHR Monograph Series, A.A. Balkema, Rotterdam, Netherlands.
9. Pezzinga, G. (1994) Velocity distribution in compound channel flows by numerical modeling. *Journal of Hydraulic Engineering*, 120(10): 1176-1197.
10. Rodi, W. (1993) Turbulence Models and their Application in Hydraulics, a State of the Art Review, IAHR Monograph Series, 3rd edition, Delft.
11. Sellin, R.H.J. (1964) A laboratory investigation into the interaction between the flow in the channel of a river and that over its floodplain, *La Houille Blanche*, 7: 793-802.
12. Shiono, K. and Knight, D.W. (1991) Turbulent open-channel flows with variable depth across the channel, *Journal of Fluid Mechanics*, 222: 617-646.
13. Shiono, K. and Lin, B. (1992) Three Dimensional Numerical Models for Two Stage Open Channel Flows, *Hydrocomp '92, International Conference of Computational Methods and Measurements in Hydraulics and Hydrology*, Ed. Gayer, Starosolszky, Maksimovic, pp. 123–130.
14. Sofialidis, D. and Prinos, P. (1998) Compound open-channel flow modeling with nonlinear low-reynolds k-ε models, *Journal of Hydraulic Engineering*, 124(3): 253-262.
15. Tominaga, A. and Nezu, I. (1991) Turbulent structure in compound open channel flows. *Journal of Hydraulic Engineering*, 117(1): 21-40.
16. Wallin, S. and Johansson, A. (2000) A complete explicit algebraic Reynolds stress model for incompressible and compressible flows, *Journal of Fluid Mechanics*,403: 89-132.
17. Yakhot, V.; Orszag, S.A.; Thangam, S.; Gatski, T.B. and Speziale, C.G. (1992) Development of turbulence models for shear flows by a double expansion technique, *Physic of Fluids*, A4: 1510-1520.

Paper III

PREDICTION OF COMPOUND CHANNEL SECONDARY FLOWS USING ANISOTROPIC TURBULENCE MODELS

Marina Filonovich, Luis R. Rojas-Solórzano, João Bento Leal

River Flow 2014 – the 7th International Conference on Fluvial Hydraulics
EPFL, Lausanne, Switzerland, 2014

River Flow 2014 – Schleiss et al. (Eds)
© 2014 Taylor & Francis Group, London, ISBN 978-1-138-02674-2

Prediction of compound channel secondary flows using anisotropic turbulence models

M.S. Filonovich
FCT/UNL, Caparica, Portugal
CEHIDRO, IST, Lisbon, Portugal

J.B. Leal
FCT/UNL, Caparica, Portugal
CEHIDRO, IST, Lisbon, Portugal
University of Agder, Grimstad, Norway

L.R. Rojas-Solórzano
Nazarbayev University, Astana, Kazakhstan

ABSTRACT: In this study the results of Baseline Explicit Algebraic Reynolds Stress model (BSL EARSM), Baseline Reynolds Stress model (BSL RSM) and Speziale-Sarkar-Gatski Reynolds Stress model (SSG RSM) of turbulent flow in an asymmetric compound channel are presented. The numerical results are validated with experimental measurements of Tominaga & Nezu (1991).

Secondary flows are captured by all turbulence models at the step-junction between the main channel and the floodplain, where a strong bulging of velocity isolines towards the free surface is observed. The Reynolds stresses are predicted with relatively close agreement to the corresponding experimental data. The turbulence anisotropy and generation of streamwise vorticity are presented and their role in promoting secondary flows is discussed. The results are also analysed in order to evaluate the influence of the underlying hypotheses of each closure model.

1 INTRODUCTION

Most natural rivers have compound cross-section composed by a main channel and by one or more floodplains on the lateral sides. During floods the water depth exceeds the bank full depth of the main channel, and thus overflow occurs on the floodplains. The fast flow in the main channel is retarded by the slower flow on the floodplains, causing lateral momentum transfer. The turbulence structures in compound channels are characterized by a shear layer that develops at the interface of the main channel and the floodplain due to the difference of velocities. In this large shear region, vortices with vertical and longitudinal axis interact. The latter are called secondary flows of second kind (Nezu & Nakagawa 1993), which are driven by the anisotropy. The secondary flows are found to influence the primary velocity field. These effects have been observed experimentally by Shiono & Knight (1991), and Tominaga & Nezu (1991) using fiber-optic Laser-Doppler Anemometer (LDA) and numerically by Naot et al. (1993), using an Algebraic Reynolds Stress Model (ARSM), by Shiono & Lin (1992) and Pezzinga (1994), using a non-linear k–ε model, by Cokljat & Younis (1995), using the full Reynolds-stress transport model, by Thomas & Williams (1995), Cater & Williams (2008) and Kara et al. (2012), using Large Eddy Simulation (LES). They have found a significant influence of secondary flows onto momentum transfer and boundary shear stress.

Secondary flows in compound channel flow are of great interest. Direct Numerical Simulation (DNS) is the most straightforward approach to the solution of the turbulent flow. However, the numerical effort of DNS is considerably high. In LES the computational demands are considerably smaller than in DNS by restricting the computational resolution to the large scales and by modelling the small scales using a subgrid model, but still LES is a quite numerical expensive model. Isotropic two-equation models are still the most popular models due to their simplicity and relatively short computational time yet have some shortcomings; for instance, poor prediction of secondary flows (e.g. Bradshaw 1987). However, with the rapid development of computation power it is feasible to use more advanced Reynolds-averaged Navier-Stokes equations (RANS) turbulence models than

the traditional two-equation models to study the detailed distribution of the flow and turbulence structures in compound channel flow.

The objective of this study is to use anisotropic models based on Reynolds stresses transport equations (namely, BSL EARSM, BSL RSM and SSG RSM) to examine the differences in results produced by each model, including different wall treatment, pressure-strain and Reynolds stresses transport equations modelling. Comparisons are made with the experimental data of Tominaga & Nezu (1991). The numerical results are analysed to investigate the contribution of terms of the governing equation for the respective models on generation of secondary flows.

2 NUMERICAL MODELLING

ANSYS CFX 13.0 code used herein is based on the finite element-based control volume method, where the governing equations are discretized over each control volume. Advection terms in Navier-Stokes equations are discretized using second-order upwind scheme. Linear shape functions are used to evaluate spatial derivatives for all the diffusion terms and pressure gradient terms. The resulting system is then solved in a coupled manner, and the results are interpolated to the grid nodes.

The simulations were run on a workstation with an i7 X980 six-core processor of 64 bits and 24GB of RAM in HP MPI local parallel run mode. The computational domain was divided into 6 partitions with one master and five slave processes.

2.1 *Mathematical models*

The steady-state simulations of the flow were performed using the BSL EARSM, BSL RSM and SSG RSM.

The BSL EARSM and BSL RSM are based on the BSL k–ω model of Menter (1994). One of the advantages of the k–ω formulation is the near wall treatment. k–ω model requires the non-dimensional vertical coordinate, z^+, of the node closest to the wall to be at least <2. However, in many flow applications it may result in a very difficult task and special attention must be paid on this regard. Menter's model represents a blending between the k–ω model near the wall and the k–ε model in the outer region. Each of the constants from Menter's BSL k–ω model is a blend of an inner (1) and outer (2) constant:

$$\phi = F\phi_1 + (1-F)\phi_2 \tag{1}$$

where blending function F is equal to 1 near the wall and decreases to a value of zero outside the boundary layer (for details see Menter 1994).

The BSL EARSM solves algebraic equations for six Reynolds stresses. The model is derived from the Reynolds stress transport equations and gives a nonlinear relation between the Reynolds stresses and the mean strain-rate and vorticity tensors. The EARSM is based on the traditional ARSM idea where advection and diffusion terms in the exact transport equation for the Reynolds stress anisotropy, a_{ij}, are neglected. The implementation is based on the EARSM of Wallin & Johansson (2000). The model solves the higher order anisotropic terms and thus, it is suitable to capture effects associated to secondary flows (Filonovich et al. 2013).

The SSG RSM uses the wall-function approach where predictions depend on the location of the node nearest to the wall and are sensitive to the near-wall meshing. According to Grotjans & Menter (1998), refining the mesh does not necessary give a unique solution of increasing accuracy. Thus, the non-dimensional vertical coordinate, z^+, of the node closest to the wall for SSG RSM was outside the viscous sublayer and buffer layer.

Both BSL RSM and SSG RSM are based on the Reynolds stress transport equations. The differences between these models lie in the use of the near-wall treatment mentioned above, and in the modelling of the pressure-strain term. Thus, in BSL RSM the "slow" pressure-strain term is linear, LRR-IP, and "rapid" term is Quasi-Isotropic, LRR-QI, after Launder et al. (1975). The constitutive relation for the pressure-strain term is given by:

$$\begin{aligned}\Pi_{ij} = {} & \beta' C_1 \omega \left(-\overline{u_i u_j} + \frac{2}{3} k \delta_{ij} \right) \\ & - \frac{C_2 + 8}{11} \left(P_{ij} - \frac{2}{3} P \delta_{ij} \right) \\ & - \frac{30 C_2 - 2}{55} k \left(\frac{\partial U_i}{\partial x_j} + \frac{\partial U_j}{\partial x_i} \right) \\ & - \frac{8 C_2 - 2}{11} \left(D_{ij} - \frac{2}{3} P \delta_{ij} \right)\end{aligned} \tag{2}$$

where $$P_{ij} = -\overline{u_i u_k} \frac{\partial U_j}{\partial x_k} - \overline{u_j u_k} \frac{\partial U_i}{\partial x_k} \tag{3}$$

and $$D_{ij} = -\overline{u_i u_k} \frac{\partial U_k}{\partial x_j} - \overline{u_j u_k} \frac{\partial U_k}{\partial x_i} \tag{4}$$

$P = P_{ii}/2$ is the rate of production of turbulence kinetic energy and the coefficients for the model are: $\beta' = 0.09$, $C_1 = 1.8$ and $C_2 = 0.52$.

The SSG RSM was developed by Speziale et al. (1991) and uses a quadratic relation for

the pressure-strain term. The general form reads:

$$\Pi_{ij,1} = -\varepsilon\left[C_{s1}a_{ij} + C_{s2}\left(a_{ik}a_{kj} - \frac{1}{3}a_{mn}a_{mn}\delta_{ij}\right)\right]$$

$$\begin{aligned}\Pi_{ij,2} = &-C_{r1}Pa_{ij} + C_{r2}kS_{ij} \\ &- C_{r3}kS_{ij}\sqrt{a_{mn}a_{mn}} \\ &+ C_{r4}k\left(a_{ik}S_{jk} + a_{jk}S_{ik} - \frac{2}{3}a_{kl}S_{kl}\delta_{ij}\right) \\ &+ C_{r5}k\left(a_{ik}\Omega_{jk} + a_{jk}\Omega_{ik}\right)\end{aligned} \quad (5)$$

where a_{ij}, S_{ij} and Ω_{ij} are anisotropy tensor, the mean rate of strain tensor and mean vorticity tensor, respectively, and are defined as:

$$a_{ij} = \frac{\overline{u_i u_j}}{k} - \frac{2}{3}\delta_{ij} \quad (6)$$

$$S_{ij} = \frac{1}{2}\left(\frac{\partial U_i}{\partial x_j} + \frac{\partial U_j}{\partial x_i}\right) \quad (7)$$

$$\Omega_{ij} = \frac{1}{2}\left(\frac{\partial U_i}{\partial x_j} - \frac{\partial U_j}{\partial x_i}\right) \quad (8)$$

The constants for the model are presented in the Table 1.

2.2 *Computational domain and boundary conditions*

The computational domain is exactly coincident with the experimental flume of Tominaga & Nezu (1991) for the S-2 case, i.e. $h/H = 0.5$, where h and H are the flow depth of the floodplain and of the main channel, respectively. The main channel width of $b = 0.2$ m and the channel top width of $B = 0.4$ m are presented in Figure 1. The flow is assumed to be statistically homogeneous in the streamwise direction and is driven by a constant pressure gradient Δp, thus periodic boundary conditions are applied. The length of the domain in streamwise direction is $12H$, which is nearly twice the recommended value of $2\pi H$ for straight smooth channels (Kara et al., 2012). The free surface is treated as a rigid lid where a free slip condition is applied. For the smooth bed, the no-slip wall boundary condition

Table 1. The values for the constants used in SSG model.

C_{s1}	C_{s2}	C_{r1}	C_{r21}	C_{r3}	C_{r4}	C_{r5}
1.7	–1.05	0.9	0.8	0.65	0.625	0.2

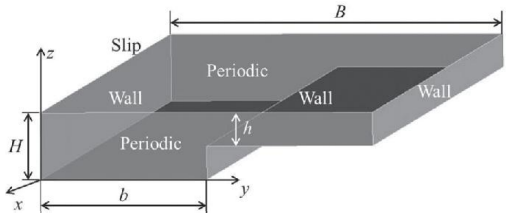

Figure 1. Computational domain and boundary conditions.

is used. The domain is discretized with uniformly spaced mesh in streamwise direction. In spanwise and in the vertical directions the mesh is refined close to the walls, free surface and transition zone between the main channel and the floodplain. Grid considered for the BSL EARSM and BSL RSM simulations is of 200 × 200 × 80 (40) hexahedral elements in x, y and z directions, respectively. The value in parenthesis indicates the number of elements in z direction on the floodplain. For the SSG RSM model the mesh of 200 × 200 × 60 (30) is used. The purpose of using different mesh for the latter model is to assure that z^+ is around 30, allowing the use of wall function.

The simulations were stopped when the convergence criteria were met. During the run three velocity components and pressure were monitored using monitor points throughout the computational domain. When the monitored values reached the asymptotic range and kept constant for at least 500 time-steps, and if the RMS (Root Mean Square) normalized values of the equation residuals were below the residual target value which is set to 10^{-7}, then the CFX-Solver terminated the run. At the end of the run the global balances are reported. The simulation is assumed to be converged if two previous criteria met and if global unbalances are less than 0.01%.

3 RESULTS AND DISCUSSION

Contours of the mean streamwise velocity (lines correspond to U/U_{max} = 0, 0.2, 0.3, 0.4, 0.5, 0.6, 0.7, 0.75, 0.8, 0.85, 0.9, 0.95 and 0.975, from the bottom to the free-surface) and vector distribution of secondary flows normalized by the maximum streamwise velocity, U_{max}, are shown in Figure 2. A plot of measured streamwise velocity contours from Tominaga & Nezu (1991) is also presented in Figure 2a.

The numerical predictions agree well with the experiments, particularly near the interface between the main channel and floodplain. The primary velocity is strongly influenced by secondary

flows. It can be seen a significant bulging upwards of the isovels at the interface due to the secondary currents generated by turbulence anisotropy. The velocity bulge is more pronounced in the BSL EARSM and BSL RSM (Figs 2b, c) than in the SSG (Fig. 2d) due to a different wall treatment between the models. This is of particular relevance in the case of the bank lateral wall, as will be discussed later.

The secondary flow vectors presented in Figure 2, confirm the presence of two secondary flow cells interacting near the interface ($1.6 \leq y/H \leq 3$) and responsible for pushing upwards particles with smaller velocities, causing the inflection of the isovel lines. In the main channel bottom corners, two secondary cells can also be observed, the so-called "bottom vortex", that direct the flow downwards and therefore inflect the isovel lines in that direction (Fig. 2). The two secondary flow cells interact in the middle of the main channel directing the isovels upward (Figs 2b, c, d), but with less intensity than what is observed in the interface.

The experiments show a similar pattern, but located closer to the main channel side wall.

Another important influence of secondary flows on the primary flow is the velocity dip in the main channel, where the maximum velocity occurs below the free surface (Fig. 2a). The isovels of lower velocities are shifted towards the middle of the main channel due to a presence of the free surface vortex, which is generated by the anisotropy of turbulence caused by the existence of the free surface and the side wall. This phenomenon is reproduced by the numerical models, but with a much lower magnitude and not extending until the middle of the main channel as observed in the experimental data. The SSG RSM seems to simulate this effect better, which should be linked with the use of a quadratic pressure strain term. From the vector plots (Fig. 2) we can conclude that secondary flow cells close to the free surface are too weak in order to be able to bring the low momentum fluid at the surface towards the center of the main channel.

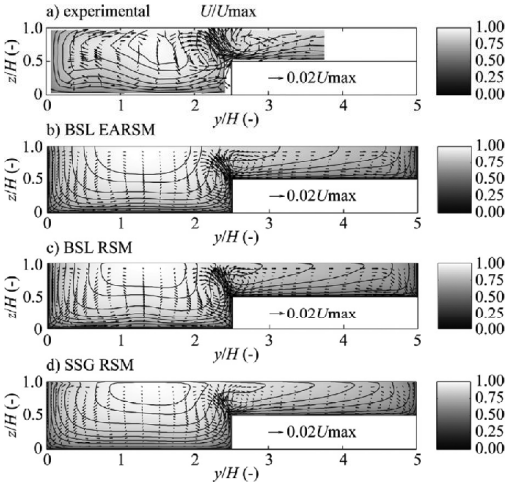

Figure 2. Isovels of mean streamwise velocity U normalized by U_{max}: a) experimental; b) BSL EARSM; c) BSL RSM; d) SSG RSM.

Overall, the agreement of the predicted vortex pairs with the experimental data is satisfactory. The maximum magnitude of the secondary flows is about 4% of U_{max} for experiments, 3.4% for the BSL EARSM, 4.8% for BSL RSM, and 4.7% for SSG RSM. The differences in terms of location and magnitude of the secondary cells may be either a result of measurement uncertainty (Kara et al. 2012), experimental flow not fully developed (Thomas & Williams 1995) or numerical modelling (wall treatment, pressure-strain term modelling, rigid lid assumption).

Figure 3 shows the distribution of normalised mean velocity $U^+ = U/u_*$ against the non-dimensional vertical coordinate $z^+ = zu_*/\nu$ at four spanwise (lateral) positions, two in the main channel and other two in the floodplain. For normalization, the shear velocity $u_* = (\tau_w / \rho)^{1/2}$ is used, where τ_w is the local wall shear stress computed at each vertical and ρ is the water density. The two-dimensional (2D) universal law is also presented for the viscous sublayer ($z^+ < 5$, linear law), the buffer layer ($5 < z^+ < \approx 30$, van Driest's law), the wall region ($z/H < \approx 0.2$, log-law) and the free-surface region ($z/H > \approx 0.6$, defect-law).

Figures 3a and 3b correspond to the positions in the main channel ($y = 0.1$ m at the middle of the main channel and $y = 0.185$ m close to the bank). The positions in the floodplain ($y = 0.205$ m close to the bank and $y = 0.3$ m at the middle of the floodplain) are presented in Figures 3c and 3d.

The computed profiles show 2D behaviour in the middle of the main channel and in the middle of the floodplain (Figs 3a, d). However, the SSG model underestimates velocities in the main channel (Fig. 3a) and overestimates in the floodplain (Fig. 3d). This might be due to a different k_s roughness applied to the bottom of the main channel and of the floodplain. The k_s were prescribed according to the material used for the experimental flume. The use of correct value of the k_s in the SSG model is essential for predicting the primary velocities since it uses a wall function (Knight et al. 2005).

The profiles in Figures 3b and 3c do not follow the 2D behaviour close to the free surface since there is a strong influence of the secondary flows. Thus, diminution of the velocities at the interface

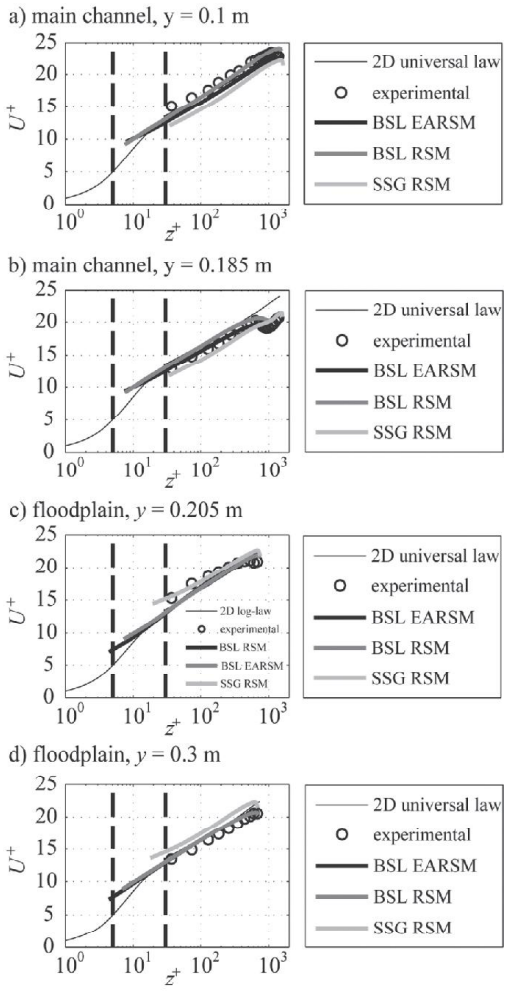

Figure 3. Log-law distribution of streamwise velocity profiles: a) main channel (middle, $y = 0.1$ m); b) main channel (close to the bank, $y = 0.185$ m); c) floodplain (close to the bank, $y = 0.205$ m); d) floodplain (middle, $y = 0.3$ m).

close to the free surface (Figs. 3b, c) is because the secondary flows push lower velocities upward. This effect is more noticeable for BSL EARSM and BSL RSM, which clearly shows that a proper wall treatment is more relevant than using a more complex turbulent closure model, as the SSG RSM.

Figures 4 and 5 show contours of the normalised shear stresses $-\overline{u'v'}$ and $-\overline{u'w'}$. The Reynolds shear stresses are related to gradients of the primary mean velocity. Thus, the distribution of the Reynolds stress $-\overline{u'v'}$ demonstrates that the high values occur near the side wall of the main channel and near the bank wall due to the lateral gradient of the streamwise velocity. The contours of the

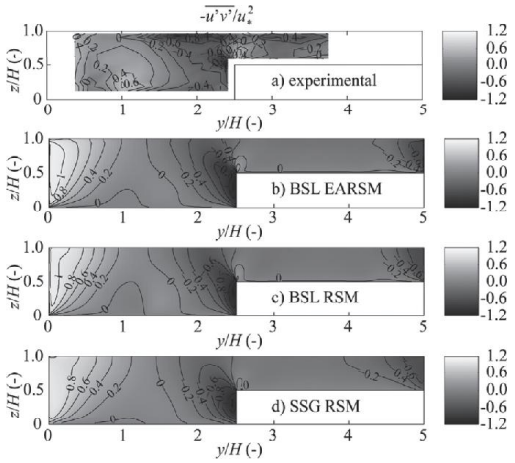

Figure 4. Normalised Reynolds Stress $-\overline{u'v'}$ distribution: a) experimental; b) BSL EARSM; c) BSL RSM; d) SSG RSM.

Reynolds stresses $-\overline{u'v'}$ are inclined towards the free surface indicating that transport of streamwise momentum due to secondary flows affects the turbulent transport (Kara et al. 2012). The high negative values of $-\overline{u'v'}$ do not overlap the interface region since there is an abrupt decrease in the velocity gradient $\partial U/\partial y$ close to the interface ($y/H \approx 2.5$), indicating that the secondary flow originated by the bank wall is predominant over the shear layer produced by the streamwise velocity lateral gradient between main channel and floodplain flow.

The highest values of the Reynolds stress $-\overline{u'w'}$ (Fig. 5) occur near the bottom in the main channel and in the floodplain for all numerical models as well as in the experiments, with the maxima occurring in the main channel.

The regions of negative values of $-\overline{u'w'}$ appear at the left hand side of the interface corner and in the free surface region of $y/H < 0.5$ for numerical models and of $y/H < 1.3$ for experiments. These negative regions of $-\overline{u'w'}$ correspond well with the regions where $\partial U/\partial z$ is negative. However, the latter region of negative $-\overline{u'w'}$ close to the free surface is smaller than in the experiments, which confirms that there is no free surface vortex developed by models, which produces strong negative wall-normal primary velocity gradients, $\partial U/\partial z$.

Figure 6 shows the contours of the difference between normal stresses ($\overline{v'v'} - \overline{w'w'}$) normalised by the squared local shear velocity. The values of ($\overline{v'v'} - \overline{w'w'}$) determine the structures of secondary currents driven by turbulence. Thus, in the main channel, the experiments (Fig. 6a) show that the value of ($\overline{v'v'} - \overline{w'w'}$) decreases with the z/H and

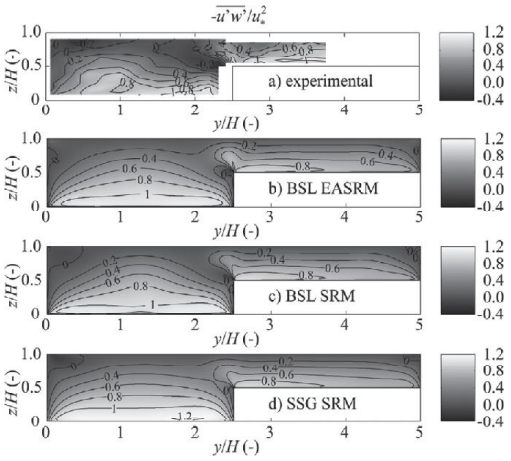

Figure 5. Normalised Reynolds Stress $-\overline{u'w'}$ distribution: a) experimental; b) BSL EARSM; c) BSL RSM; d) SSG RSM.

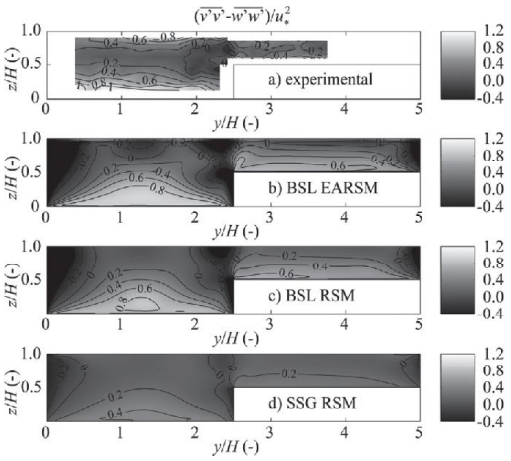

Figure 6. Normalised anisotropy $\overline{v'v'}-\overline{w'w'}$ distribution: a) experimental; b) BSL EARSM; c) BSL RSM; d) SSG RSM.

reaches the minimum value at $z/H \approx 0.6$. Then, it increases again with the increase of z/H towards the free surface. Thus, this anisotropy of turbulence generates the free-surface vortex and bottom vortex (Fig. 2a).

The pattern of $(\overline{v'v'}-\overline{w'w'})$ for numerical models (Figs. 6b-d) slightly differs from the experimental (Fig. 6a). As was mentioned above the free surface vortex is not captured by the models. However, the vortex pairs are formed in the corners of the main channel (Figs 2b-d), where the values of $(\overline{v'v'}-\overline{w'w'})$ change the sign. At the junction between the main channel and the floodplain the values of $(\overline{v'v'}-\overline{w'w'})$ have opposite signs indicating a complex behaviour. For compound channels the anisotropy at the interface leads to the formation of the two counter-rotating secondary flow cells.

The higher values of the turbulence anisotropy are observed close to the bottom walls in the main channel and in the floodplain. This is in good agreement for the BLS's models (Figs. 6b, c) with the experimental data. Despite neglecting advection and diffusion terms in the exact transport equation for the Reynolds stress anisotropy, the BSL EARSM model reproduced higher values of the turbulence anisotropy. The SSG model shows lower values of $(\overline{v'v'}-\overline{w'w'})$ (Fig. 6d) due to a different wall treatment compared to the BSL's models, which explains the secondary flow under prediction.

Figure 7 shows the vertical distributions of the normal Reynolds stresses normalized by the squared local shear velocity at the same spanwise (lateral) positions as in Figure 3. The solid lines represent the 2D theoretical linear distributions (Nezu & Nakagawa 1993). It can be seen that all models underestimate the experimental normal stresses $\overline{u'u'}$ near the bed until $z/H < 0.4$. This might be due to a wall treatment for SSG model and due to insufficient mesh refinement close to the walls for the BSL EARSM and BSL RSM models. For $z/H > 0.4$, at the center of the main channel (Fig. 7a) and at the center of the floodplain (Fig. 7b) we can conclude that normal stresses indicate 2D behaviour. In the vicinity to the interface at $y = 0.185$ m (Fig. 7b), the experimental normal Reynolds stresses exhibit waviness with a second peak in the vertical distribution. The peak occurs at $z/H \approx 0.55$ at about the bank elevation in the direction towards the free surface due to interaction between the two secondary flow cells at the junction. The BSL EARSM and BSL RSM can slightly reproduce the waviness and the peak of the normal Reynolds stresses, while SSG indicates an almost 2D behaviour. It is also clear that, contrary to the 2D behavior, the BSL's models present higher $\overline{w'w'}$ than $\overline{v'v'}$, which is in accordance with the negative region of $\overline{v'v'}-\overline{w'w'}$ (Figs. 6b, c).

Figure 8 shows the contours of the production term of the secondary currents in the streamwise equation of vorticity (Nezu & Nakagawa 1993).

The extreme values are found at the junction edge and present positive and negative peaks alternatively. This underlines the significance of the turbulence anisotropy of the normal stresses in this region.

There are also high values of the generation term in the corners of the main channel and the

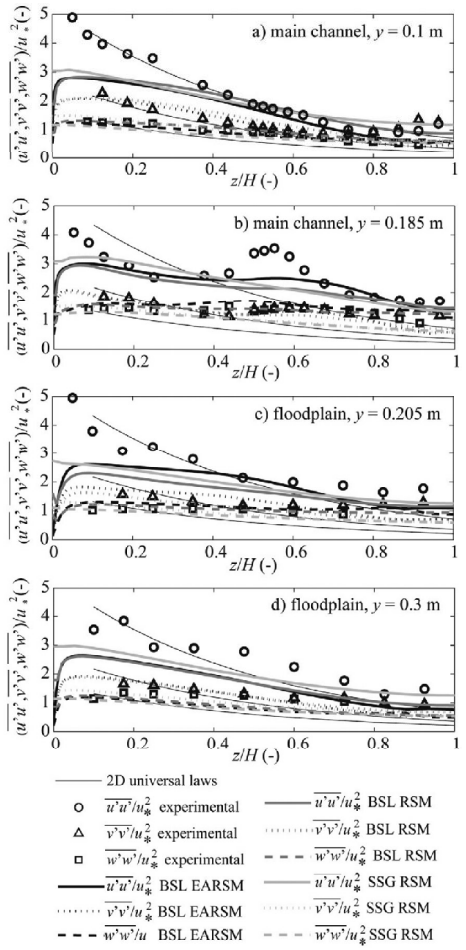

Figure 7. Normalised normal Reynolds stress profiles: a) main channel (middle, y = 0.1 m); b) main channel (close to the bank, y = 0.185 m); c) floodplain (close to the bank, y = 0.205 m); d) floodplain (middle, y = 0.3 m).

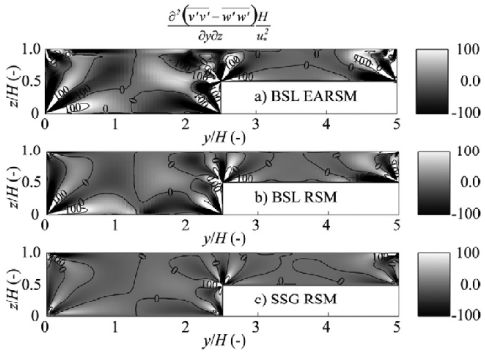

Figure 8. Normalised streamwise vorticity generation distribution: a) BSL EARSM; b) BSL RSM; c) SSG RSM.

floodplain as well as in the wall-free-surface corners. This gradient becomes a driving force in generation of secondary flows at the junction edge and in the corners of the channel. The BSL EARSM generates higher values than BSL RSM, which means that neglecting the advection and diffusion terms in the exact transport equation for the Reynolds stress anisotropy increases the vorticity generation and, consequently, secondary flows. The BSL RSM generates higher values than SSG RSM, confirming that the wall treatment is a key issue in what concerns secondary flow reproduction.

4 CONCLUSIONS

The results of BSL EARSM, BSL RSM and SSG RSM of turbulent flow in asymmetric compound open channel are presented. The simulations have reproduced the complex flow pattern of primary velocity field, secondary currents, Reynolds stresses, anisotropy of turbulence and production term of secondary currents. Overall, a good agreement was obtained between numerical results with the existing experimental data of Tominaga & Nezu (1991).

For the particular case studied (high flow depth) the flow is clearly dominated by wall turbulence and the anisotropy generated at the boundary corners. This helps to explain better performance of BSL's models against SSG RSM. Although the latter constitutes a more realistic conceptual model, since it solves the exact Reynolds transport equations using a quadratic pressure strain term, the simpler BSL's models give better results due to a better wall treatment.

It was also concluded that the simpler model (BSL EARSM) gave better results than the most complex ones (BSL RSM and SSG RSM), indicating that neglecting advection and diffusion terms in the exact transport equation for the Reynolds stress anisotropy promotes the generation of stronger secondary flow cells.

In this particular case (wall dominated anisotropic turbulence) it seems clear that a use of a simpler model can reproduce accurate results, as long as a proper wall treatment is used. This is also true if the results are compared against the LES results of Thomas & Williams (1995) and Kara et al. (2012).

ACKNOWLEDGEMENTS

The first author wishes to acknowledge the financial support of the Portuguese Foundation for Science and Technology through the Grants No. SFRH/BD/64337/2009. The first and second authors

wish to acknowledge the financial support of the Portuguese Foundation for Science and Technology through the projects PTDC/ECM/117660/2010 and RECI/ECM-HID/0371/2012. The authors are grateful to Prof. Yoshihisa Kawahara for providing us with the experimental data of Tominaga and Nezu.

REFERENCES

Bradshaw, P. 1987. Turbulent secondary flows. *Ann. Rev. Fluid Mech. 19*: 53–74.

Cater, J.E. & Williams, J.J.R. 2008. Large eddy simulation of a long assymetric compound channel. *J. Hydraulic Res*. 46(4):445–453.

Cokljat, D. & Younis, B.A. 1995. Second-order closure study of open channel flows. *J. Hydraulic Eng.* 121(2): 94–107.

Filonovich, M.S., Azevedo, R., Rojas-Solórzano, L.R. & Leal, J.B. 2013. Credibility analysis of computational fluid dynamic simulations for compound channel flow. *J. Hydroinformatics* 15(3): 926–938.

Grotjans, H. & Menter, F.R. 1998. Wall functions for general application CFD codes. *ECCOMAS 98 Proceedings of the Fourth European Computational Fluid Dynamics Conference*. John Wiley & Sons.

Kara, S., Stoesser, T. & Sturm, T.W. 2012. Turbulence statistics in compound channels with deep and shallow overbank flows. *J. Hydraulic Res.* 50(5): 482–493.

Knight, D,W., Wright, N.G. & Morvan, H.P. 2005. *Guidelines for applying commercial CFD software to open channel flow.* Report based on research work conducted under EPSRC Grants GR/R43716/01 and GR/R43723/01. 1–31.

Launder, B.E., Reece, G.J. & Rodi, W. 1975. Progress in the developments of a Reynolds-stress turbulence closure. *Journal of Fluid Mechanics* 68:537–566.

Menter, F. R. 1994. Two-Equation Eddy-Viscosity Turbulence Models for Engineering Applications. *AIAA Journal* 32(8): 1598–1605.

Naot, D., Nezu, I. & Nakagawa, H. 1993. Hydrodynamic behavior of compound rectangular open channels. *J. Hydraulic Eng.* 119(3): 390–408.

Nezu, I. & Nakagawa, H. 1993. *Turbulence in open-channel flows*. In: IAHR Monograph Series. Rotterdam: Balkema.

Pezzinga, G. 1994. Velocity distribution in compound channel flows by numerical modeling. *J. Hydraulic Eng*. 120(10):1176–1198.

Shiono, K. & Knight, D.W. 1991. Turbulent open channel flows with variable depth across the channel. *J. Fluid Mechanics* 222: 617–646.

Shiono, K. & Lin, B. 1992. Three Dimensional Numerical Models for Two Stage Open Channel Flows. *Hydrocomp '92, International Conference of Computational Methods and Measurements in Hydraulics and Hydrology*. 25–29 May, Budapest, Hungary. 123–130.

Speziale, C.G., Sarkar, S. & Gatski, T.B. 1991. Modelling the pressure-strain correlation of turbulence: an invariant dynamical systems approach. *J. Fluid Mechanics* 277: 245–272.

Thomas, T.G. & Williams, J.J.R. 1995. Large eddy simulation of turbulent flow in an asymmetric compound open channel. *J. Hydraulic Res.* 33(1): 27–41.

Tominaga, A. & Nezu, I. 1991. Turbulent structure in compound open-channel flows. *J. Hydraulic Eng.* 117(1): 21–40.

Wallin, S. & Johansson, A.V. 2000 An explicit algebraic Reynolds stress model for incompressible and compressible turbulent flows. *J. Fluid Mechanics.* 403: 89–132.

Paper IV

OPEN-CHANNEL FLOW SIMULATION WITH RSM AND EARSM

Marina Filonovich, Luis R. Rojas-Solórzano, João Bento Leal

Submitted to *Engineering Applications of Computational Fluid Mechanics.*

Open-channel secondary flow simulation with RSM and EARSM

Marina Filonovich[*&+], Luis Rojas-Solórzano[#], Joao Bento Leal[§&]

[*] *FCT/UNL, Caparica, Portugal and CEHIDRO, IST, Lisbon, Portugal*

[&] *UNIDEMI and Department of Civil Engineering, FCT, Universidade Nova de Lisboa, Portugal*

[+] *Email: m.filonovich@fct.unl.pt (Corresponding Author)*

[#] *Nazarbayev University, Astana, Kazakhstan*

[§] *Faculty of Engineering and Science, Universitetet i Agder, Norway*

ABSTRACT

The present study presents numerical Reynolds Averaged Navier-Stokes (RANS) simulations of a compound open-channel flow with strong Prandtl's second kind secondary flow. For that purpose the Reynolds Stress Model (RSM) and Explicit Algebraic Reynolds Stress Model (EARSM) were used. The budgets of transport equation for Reynolds stress and anisotropy tensor highlighted the importance of anisotropy diffusion terms in predicting secondary flow. The diffusive-transport constrain that is included in the weak-equilibrium hypothesis and grounds the EARSM, is not valid in the presence of this type of secondary flow. Furthermore, the diffusion and streamline curvature corrections of the EARSM are not able to overcome this limitation. Contrary to flows in rotating frames, the assumption of negligible anisotropy convection holds in simulated flow. Some two-dimensional approximations assumed in the explicit polynomial have significant impact on EARSM solution.

Keywords: secondary flow, turbulence anisotropy, Reynolds Stress Model (RSM), Explicit Algebraic Reynolds Stress Model (EARSM)

1. INTRODUCTION

The modelling of secondary flow is important in several applications, since it can affect the velocity and boundary shear distributions (e.g. Knight et al. 2007, Nikora and Roy 2012). The Prandtl's second kind secondary flow or turbulence-driven secondary flow (e.g. Nezu and Nakagawa 1993) arises from turbulence anisotropy and therefore cannot be simulated by isotropic eddy viscosity models (e.g. Bradshaw 1987). The use of Reynolds Stress Models (RSM) would be the natural step beyond eddy viscosity models (cf. Hanjalić 1999), but due to their computational time demand they were replaced by the use of simpler Explicit Algebraic Reynolds Stress Model (EARSM). The latter is reported to be able to simulate secondary flow in different contexts (Wallin and Johansson 2000, Naji et al. 2004, Franke et al. 2005, Filonovich et al. 2013) and appear to be more robust than RSM (Menter 2011).

The major assumption in EARSM is the weak equilibrium condition on the turbulent stress anisotropy proposed by Rodi (1976) to obtain the implicit equation (see section 2.2) and corresponds to the following two conditions (e.g. Gatski and Wallin 2004)

$$\frac{\mathrm{D}a_{ij}}{\mathrm{D}t} = 0 \tag{1}$$

$$D_{ij} = \frac{\overline{u_i' u_j'}}{k} D \tag{2}$$

where the Reynolds-stress anisotropy tensor is defined as

$$a_{ij} = \frac{\overline{u_i' u_j'}}{k} - \frac{2}{3}\delta_{ij} \tag{3}$$

and D_{ij} represents the combined effects of viscous diffusion, pressure and turbulent transport (Pope 2000)

$$D_{ij} = \underbrace{-\frac{\partial T_{lij}^{(p)}}{\partial x_l}}_{\text{pressure transport}} \underbrace{-\frac{\partial T_{lij}^{(t)}}{\partial x_l}}_{\text{turbulent transport}} \underbrace{-\frac{\partial T_{lij}^{(v)}}{\partial x_l}}_{\text{viscous diffusion}} = \\ = -\frac{\partial}{\partial x_l}\left(\frac{1}{\rho}\overline{u_i' p'}\delta_{jl} + \frac{1}{\rho}\overline{u_j' p'}\delta_{il}\right) - \frac{\partial \overline{u_i' u_j' u_l'}}{\partial x_l} + \frac{\partial}{\partial x_l}\left(\nu \frac{\partial \overline{u_i' u_j'}}{\partial x_l}\right) \quad (4)$$

where δ_{ij} is Kronecker delta.

The validity of condition (1) in rotating frames or in flows where streamline curvature effects are non-negligible has been put into question by several authors (Girimaji 1997, Speziale 1998, Gatski and Jongen 2000, Weis and Hutter 2003, Gatski and Wallin 2004). Although some of the initial arguments to support the non-validity of Eq. (1), like material frame indifference have been proven to be not universal (Barnerjee et al. 2009, Frewer 2009), it is now consensual that a weak equilibrium condition like Eq. (1) can be written in an objective form that verifies both Galilean (translation) and Euclidean transformations (rotation) (Hamba 2006). The solution for this problem is based on the introduction of an absolute/corrected rotation-rate tensor (Spalart and Shur 1997, Wallin and Johansson 2002, Naji et al. 2004, Hellsten and Wallin 2009) that is presented in section 2.4.

Contrary to Eq. (1), the validity of other part of weak-equilibrium condition Eq. (2) has not received that much attention (cf. Thomson and Mompean 2010). This condition is the diffusive-transport constrain (Qiu et al. 2008) and corresponds to neglecting the terms that are associated with the diffusion and transport processes (see section 2.3), which can result in an overestimation of the effective eddy viscosity in regions where production to dissipation ratio is small (Taulbee 1992).

As stated before the main reason to use EARSM is the computational time, this explains why there are not many studies where the EARSM simulations are thoroughly compared to more time consuming RSM simulations. An exception is the study by Grundestam et al. (2006), where the authors compared EARSM with RSM for a rotating turbulent pipe flow, concluding that the predicted turbulence kinetic energy levels vary dramatically depending on the diffusion model used.

In the present study, this comparison is made using ANSYS-CFX software for simulating a compound-channel flow where secondary flow is strong. The comparison is useful to evaluate the differences between EARSM results and RSM ones (they should be equal under the same boundary conditions), and to identify which simplifications in the EARSM are causing the differences.

2. THEORETICAL BACKGROUND

2.1. Reynolds Stress Model (RSM)

The Reynolds stress models are based on the Reynolds stress transport equation that can be written (e.g. Pope 2000)

$$\underbrace{\frac{\mathrm{D}\overline{u_i' u_j'}}{\mathrm{D}t}}_{\substack{\text{convection by}\\ \text{mean flow}}} = \underbrace{D_{ij}}_{\substack{\text{turbulent transport}\\ \text{and viscous diffusion}}} + \underbrace{P_{ij}}_{\substack{\text{turbulent}\\ \text{production}}} + \underbrace{\Pi_{ij}}_{\substack{\text{pressure–strain}\\ \text{rate correlation}}} - \underbrace{\varepsilon_{ij}}_{\substack{\text{dissipation rate}\\ \text{tensor}}} \tag{5}$$

The second and third RHS terms in the equation can be written (e.g. Pope 2000)

$$P_{ij} = -\overline{u_i' u_l'}\frac{\partial \overline{u_j}}{\partial x_l} - \overline{u_j' u_l'}\frac{\partial \overline{u_i}}{\partial x_l} \tag{6}$$

$$\Pi_{ij} = \overline{p'\left(\frac{\partial u_i'}{\partial x_j} + \frac{\partial u_j'}{\partial x_i}\right)} \tag{7}$$

Taking in consideration Eqs. (4)-(6) it is clear that the production P_{ij} and the viscous diffusion $-\partial T_{lij}^{(v)} \big/ \partial x_l$ terms do not need any modelling since they are explicit in the Reynolds stress tensor (Eqs. (6) and (4), respectively). On the other hand, the pressure and turbulent transport $-\partial T_{lij}^{(p)} \big/ \partial x_l - \partial T_{lij}^{(t)} \big/ \partial x_l$, the dissipation rate tensor ε_{ij} and the pressure-strain rate correlation tensor Π_{ij} need to be modelled.

The pressure and turbulent transport are modelled using the gradient-diffusion model due to Shir (1973)

$$-\frac{\partial T_{lij}^{(p)}}{\partial x_l} - \frac{\partial T_{lij}^{(t)}}{\partial x_l} = \frac{\partial}{\partial x_l}\left(\underbrace{\frac{\nu_t}{\sigma_k}}_{\substack{\text{diffusion} \\ \text{coefficient}}} \frac{\partial \overline{u_i' u_j'}}{\partial x_l}\right) \tag{8}$$

where the diffusion coefficient is considered to be equal to the diffusion coefficient of turbulence kinetic energy $k = \overline{u_i' u_i'} \big/ 2$ (see section 2.5). In this model the diffusion coefficient is considered isotropic, which increases the model robustness. Although, the general experience of practitioners is that the modelling of these transport terms is not critical in the overall model (cf. Pope 2000), there are some studies where inaccuracies in the calculation are attributed to limitations in the modelling of the pressure and turbulent transport (cf. Grundestam et al. 2006). This issue will be further discussed in section 4.1.

The dissipation rate tensor ε_{ij} is modelled assuming local isotropic dissipation (e.g. Pope 2000)

$$\varepsilon_{ij} = \frac{2}{3}\tilde{\varepsilon}\delta_{ij} \approx \frac{2}{3}\varepsilon\delta_{ij} \tag{9}$$

where the pseudo-dissipation rate $\tilde{\varepsilon}$ is considered approximately equal to the dissipation rate. Eq. (9) is strictly valid for high-Reynolds-number, which is not the case of near-wall regions where dissipation is anisotropic (Speziale and Gatski 1997, Jakirlić and Hanjalić 2002), especially for smooth walls (cf. Shafi and Antonia 1995). This issue will be addressed latter in the interpretation of the results (section 4.1). To determine the dissipation rate tensor an additional closure equation for the isotropic turbulent dissipation rate $\varepsilon = \varepsilon_{ii}/2$ is needed, which is established in the baseline (BSL) model described in section 2.5.

Launder et al. (1975) proposed a quasi-isotropic general linear model, called LRR-QI, for the pressure-strain rate

$$\Pi_{ij} = \underbrace{-c_1\frac{\varepsilon}{k}\left(\overline{u_i'u_j'} - \frac{2}{3}k\delta_{ij}\right)}_{\text{slow pressure-rate-of-strain}} + \underbrace{\left[-\frac{(c_2+8)}{11}\left(P_{ij} - \frac{2}{3}P\delta_{ij}\right) - \frac{(30c_2-2)}{55}k\left(\frac{\partial\overline{u_i}}{\partial x_j} + \frac{\partial\overline{u_j}}{\partial x_i}\right) - \right.}_{\text{rapid pressure-rate-of-strain}}$$

$$\underbrace{\left. + \frac{(8c_2-2)}{11}\left(\overline{u_i'u_l'}\frac{\partial\overline{u_l}}{\partial x_j} + \overline{u_j'u_l'}\frac{\partial\overline{u_l}}{\partial x_i} + \frac{2}{3}P\delta_{ij}\right)\right]}_{\text{rapid pressure-rate-of-strain}} \tag{10}$$

where $P = P_{ii}/2$ is the turbulent production, $c_1 = 1.8$ and $c_2 = 5/9$ are coefficients with values proposed by Wallin and Johansson (2000).

2.2. Explicit Algebraic Reynolds Stress Model (EARSM)

Algebraic Reynolds stress models have been developed for the Reynolds-stress anisotropy tensor instead of the Reynolds stress. The transport equation of k can be deducted from the

contraction of stress transport equation (5), using the fact that the pressure-strain redistribution term is traceless $\Pi_{ii} = 0$ (e.g. Gatski and Jongen 2000)

$$\frac{\mathrm{D}k}{\mathrm{D}t} = D + P - \varepsilon \tag{11}$$

where $D = D_{ii}/2$ represents the combined effects of viscous diffusion, pressure and turbulent transport.

Using Eqs. (5) and (11), the transport equation for Reynolds stress anisotropy tensor can be derived (e.g. Grundstam et al. 2006)

$$k \underbrace{\frac{\mathrm{D}a_{ij}}{\mathrm{D}t}}_{\substack{\text{convection of} \\ a_{ij} \text{ by mean flow}}} - \underbrace{\left(D_{ij} - \frac{\overline{u_i' u_j'}}{k} D \right)}_{\text{total diffusion of } a_{ij}} = \underbrace{-\frac{\overline{u_i' u_j'}}{k}(P - \varepsilon)}_{\substack{\text{anisotropy turbulent production} \\ \text{and viscous dissipation} \\ \text{contribution from TKE}}} + \underbrace{\left(P_{ij} + \Pi_{ij} - \varepsilon_{ij} \right)}_{\substack{\text{Reynolds stresses terms} \\ (\text{see Eq. 5})}} \tag{12}$$

which can also be presented, by using Eqs. 9 and 10 (Wallin and Johansson 2002)

$$\tau\left[\frac{\mathrm{D}a_{ij}}{\mathrm{D}t} - \frac{1}{k}\left(D_{ij} - \frac{\overline{u_i' u_j'}}{k} D \right) \right] = A_0 \left[\left(A_3 + A_4 \frac{P}{\varepsilon} \right) a_{ij} + A_1 S_{ij} - \left(a_{il}\Omega_{lj} - \Omega_{il} a_{lj} \right) + A_2 \left(a_{il} S_{lj} + S_{il} a_{lj} - \frac{2}{3} a_{mn} S_{mn} \delta_{ij} \right) \right] \tag{13}$$

where $\tau = k/\varepsilon$ is a scalar representing the characteristic turbulent time-scale, the dimensionless mean strain-rate, S_{ij}, and rotation rate tensor, Ω_{ij}, are defined by

$$S_{ij} = \frac{\tau}{2}\left(\frac{\partial \overline{u_i}}{\partial x_j} + \frac{\partial \overline{u_j}}{\partial x_i} \right) \tag{14}$$

$$\Omega_{ij} = \frac{\tau}{2}\left(\frac{\partial \overline{u_i}}{\partial x_j} - \frac{\partial \overline{u_j}}{\partial x_i} \right) \tag{15}$$

and the coefficients A depend on the pressure-strain rate coefficients (Eq. 10)

$$A_0 = -\frac{1+7c_2}{11} = -0.44 \quad A_1 = \frac{88}{15(1+7c_2)} = 1.2 \quad A_2 = \frac{5-9c_2}{1+7c_2} = 0$$
$$A_3 = \frac{11(c_1-1)}{1+7c_2} = 1.8 \qquad A_4 = \frac{11}{1+7c_2} = 2.25 \tag{16}$$

Solving the turbulent anisotropy tensor transport equation (Eq. 12 or 13) together with the turbulence kinetic energy transport equation (Eq. 11) is equivalent to solving the Reynolds stress transport equation (5). Both alternatives can be used in Reynolds Stress Models (RSM).

Substituting the weak-equilibrium conditions (Eqs. 1 and 2) in Eq. (13) with coefficients in Eq. (16), the implicit equation for the turbulence anisotropy tensor is obtained

$$Na_{ij} = -A_1 S_{ij} + \left(a_{il}\Omega_{lj} - \Omega_{il}a_{lj}\right) \tag{17}$$

with

$$N = A_3 + A_4 \frac{P}{\varepsilon} \tag{18}$$

Unfortunately, the implicit algebraic equation is not very robust. This led researchers to find explicit algebraic equation which allows a much more robust solution of the anisotropy tensor. The steps and assumptions to get the explicit solution will be explained briefly here (more details can be found in Gatski and Jogen 2000). From Eq. (17) (or from Eq. 13) it is clear that the stress anisotropy tensor has the functional dependency

$$a_{ij} = a_{ij}\left(S_{ml}, \Omega_{ml}, \tau\right) \tag{19}$$

implying that the anisotropy tensor a_{ij} elements in any Cartesian coordinate system are only functions of the two independent kinematic tensors S_{ij} and Ω_{ij} in the same coordinate system. It is therefore possible to represent the Reynolds stress anisotropy tensor as a linear combination

of basis tensors S_{ij} and Ω_{ij}, which can be represented as a projection on a tensor basis (cf. Gatski and Jongen 2000). For any choice of basis tensors, it is possible to use the Cayley-Hamilton theorem, which states that tensor polynomial terms beyond a certain order are redundant. In the three-dimensional general case this basis consists of a minimum of ten linearly independent elements (cf. Gatski and Speziale 1993) that can be written for the simplified equation (17) as a tensor polynomial with five tensor basis (cf. Wallin and Johansson 2000):

$$\begin{aligned} a_{ij}^{WJ} &= \beta_1^{WJ} S_{ij} + \beta_3^{WJ}\left(\Omega_{il}\Omega_{lj} - \frac{1}{3} II_\Omega \delta_{ij}\right) + \beta_4^{WJ}\left(S_{il}\Omega_{lj} - \Omega_{il}S_{lj}\right) + \\ &+ \beta_6^{WJ}\left(S_{il}\Omega_{lm}\Omega_{mj} + \Omega_{il}\Omega_{lm}S_{mj} - \frac{2}{3} IV\delta_{ij} - II_\Omega S_{ij}\right) + \\ &+ \beta_9^{WJ}\left(\Omega_{il}S_{lm}\Omega_{mp}\Omega_{pj} - \Omega_{il}\Omega_{lm}S_{mp}\Omega_{pj}\right) \end{aligned} \tag{20}$$

where β^{WJ} are coefficients that for general three-dimensional mean flows can be written as

$$\begin{aligned} \beta_1^{WJ} &= -\frac{N\left(2N^2 - 7II_\Omega\right)}{Q^{WJ}} \quad \beta_3^{WJ} = -\frac{12IV}{NQ^{WJ}} \\ \beta_4^{WJ} &= -\frac{2\left(N^2 - 2II_\Omega\right)}{Q^{WJ}} \quad \beta_6^{WJ} = -\frac{6N}{Q^{WJ}} \quad \beta_9^{WJ} = \frac{6}{Q^{WJ}} \end{aligned} \tag{21}$$

with

$$\begin{aligned} Q^{WJ} &= \frac{\left(N^2 - 2II_\Omega\right)\left(2N^2 - II_\Omega\right)}{A_1} \qquad II_S = S_{lm}S_{ml} \\ II_\Omega &= \Omega_{lm}\Omega_{ml} \qquad\qquad IV = S_{lm}\Omega_{mp}\Omega_{pl} \end{aligned} \tag{22}$$

In CFX-ANSYS software a simplified version of polynomial (20) with only four tensor basis is used

$$\begin{aligned} a_{ij}^{CFX} &= \beta_1^{CFX} S_{ij} + \beta_3^{CFX}\left(\Omega_{il}\Omega_{lj} - \frac{1}{3} II_\Omega \delta_{ij}\right) + \beta_4^{CFX}\left(S_{il}\Omega_{lj} - \Omega_{il}S_{lj}\right) + \\ &+ \beta_6^{CFX}\left(S_{il}\Omega_{lm}\Omega_{mj} + \Omega_{il}\Omega_{lm}S_{mj} - \frac{2}{3} IV\delta_{ij} - II_\Omega S_{ij}\right) \end{aligned} \tag{23}$$

where β^{CFX} are coefficients that for general three-dimensional mean flows can be written as

$$\begin{aligned} \beta_1^{CFX} &= -\frac{N}{Q^{CFX}} \quad \beta_3^{CFX} = -\frac{12IV}{NQ^{CFX}\left(2N^2 - II_\Omega\right)} \\ \beta_4^{CFX} &= -\frac{1}{Q^{CFX}} \quad \beta_6^{CFX} = -\frac{6N}{Q^{CFX}\left(2N^2 - II_\Omega\right)} \end{aligned} \tag{24}$$

with

$$Q^{CFX} = \frac{N^2 - 2II_\Omega}{A_1} \tag{25}$$

Comparing Wallin and Johansson (2000) explicit polynomial (Eq. 20) with the CFX one (Eq. 23), there are two main differences. First, the latter does not include the fourth-order term $\beta_9\left(\mathbf{\Omega S \Omega}^2 - \mathbf{\Omega}^2\mathbf{S\Omega}\right)$ appearing in the former. Second, the tensor basis is slightly changed according to Apsley and Leschziner (1998), who derived a stress-strain relationship formed by successive iterative approximations to an algebraic Reynolds-stress third-order polynomial. As stated by Apsley and Leschnizer (1998) their algebraic polynomial is an approximation. In fact, comparing Eqs. (20) and (23), it is simple to deduct a second-order term that is missing in the later, which can be written:

$$\frac{3II_\Omega}{Q^{WJ}\left(2N^2 - II_\Omega\right)}\left(\mathbf{S\Omega} - \mathbf{\Omega S}\right) \tag{26}$$

This difference arises because in the definition of β_4^{CFX}, the value valid for two-dimensional flows (Eq. 24, see also Wallin and Johanssson 2000) is used instead of the corresponding three-dimensional one. The influence of these two differences in the solution will be accessed in section 4.4.

In three-dimensional flows, substituting Eq. (20) or Eq. (23) in Eq. (17), a sixth order nonlinear equation is obtained for N (Wallin and Johansson 2000). Since this equation cannot be

explicitly solved, Hellsten (2004) suggested to use as approximation the solution of the cubic equation obtained for two-dimensional flows

$$N^{ap} = \begin{cases} A_3/3 + \left(P_1 + \sqrt{P_2}\right)^{1/3} + \mathrm{sgn}\left(P_1 - \sqrt{P_2}\right)\left|P_1 - \sqrt{P_2}\right|^{1/3} & \text{for} \quad P_2 \geq 0 \\ A_3/3 + 2\left(P_1^2 - P_2\right)^{1/6} \cos\left[\frac{1}{3}\arccos\left(\frac{P_1}{\sqrt{P_1^2 - P_2}}\right)\right] & \text{for} \quad P_2 < 0 \end{cases} \tag{27}$$

where

$$P_1 = A_3\left(\frac{A_3^2}{27} + \frac{A_1 A_4}{6} II_S - \frac{2}{3} II_\Omega\right) \tag{28}$$

$$P_2 = P_1^2 - \left(\frac{A_3^2}{9} + \frac{A_1 A_4}{3} II_S + \frac{2}{3} II_\Omega\right)^3 \tag{29}$$

The influence of the approximation procedure to obtain N will be discussed in section 4.4.

Finally, to obtain the characteristic turbulent time-scale (i.e. k and ε; contrary to the RSM now k also needs a closure) the full version of BSL model is used (see section 2.5).

2.3. EARSM diffusion correction

Wallin and Johansson (2000) proposed a correction for the neglected diffusion terms (Eq. 2, weak-equilibrium diffusive-transport constrain) to derive the implicit algebraic polynomial (Eq. 17) that can be modelled as:

$$\begin{aligned} D_{ij} - \frac{\overline{u_i' u_j'}}{k} D &= -C_{Diff}\, a_{ij} D \approx C_{Diff}\, a_{ij}\left(P - \varepsilon\right) \approx -C_{Diff}\, \max\left(1 - \frac{P}{\varepsilon}, 0\right)\frac{k}{\tau} a_{ij} \approx \\ &\approx -C_{Diff}\, \max\left(1 + \beta_1^{eq} II_S, 0\right)\frac{k}{\tau} a_{ij} \end{aligned} \tag{30}$$

assuming negligible the turbulent kinetic energy advection ($\mathrm{D}k/\mathrm{D}t \approx 0$ in Eq. 11, i.e. $D \approx \varepsilon - P$), introducing a limiter that ensures that the diffusion correction is 0 when $P/\varepsilon > 1$ (i.e., in regions with large strain rates) and adopting $P/\varepsilon \approx -\beta_1^{eq} II_S$, where $\beta_1^{eq} = \beta_1\left(N = N^{eq} = A_3 + A_4 = 4{,}05\right)$ is the equilibrium value ($P = \varepsilon$) of coefficient β_1 (see Eqs. 18 and 24). The diffusion correction can then be included as an additional term in coefficient A_3 appearing in the first term of N^{ap} in Eq. (27)

$$A_3' = \frac{9}{5} + \underbrace{\frac{9}{4} C_{Diff} \max\left(1 + \beta_1^{eq} II_S, 0\right)}_{\substack{\text{diffusion} \\ \text{correction}}} \tag{31}$$

The value of the constant $C_{Diff} = 2.2$ is established for vanishing strain rate (i.e. $II_S \to 0$ and consequently $P/\varepsilon \to 0$) resulting in an effective eddy viscosity $C_\mu^{eff} = -\beta_1/2 = 3/(5N) = 3/(5A_3') \approx 0.09$ which is close to the expected value $C_\mu = 0.09$. The influence of this diffusion correction will be analysed in section 4.3.

2.4. EARSM streamlines curvature correction

The streamlines curvature correction for the neglected total variation of the anisotropy (Eq. 1, weak-equilibrium) consists in replacing in Eq. (19) the rotation-rate tensor Ω_{ij} by the absolute rotation-rate tensor Ω_{ij}^* (cf. Wallin and Johansson 2002)

$$\Omega_{ij}^* = \Omega_{ij} - C_{scale} \frac{\tau}{A_0} \Omega_{ij}^{(s)} \tag{32}$$

where C_{scale} is a coefficient that takes the value 0 if no correction is introduced or the value 1 to activate the correction, and $\Omega_{ij}^{(s)}$ is a tensor that takes into account the streamlines curvature and is given by

$$\Omega_{ij}^{(s)} = -\in_{ijm} \omega_m^{(s)} \tag{33}$$

where $\in_{ijm}$ is the Levi-Chivita factor and vector and $\omega_m^{(s)}$ is a rotation-rate vector that accounts for streamline curvature effects (e.g. Speziale 1991, Gatski and Jongen 2000). The computation of this term can be performed as follows (Spalart and Shur 1997)

$$\omega_m^{(s)} = \frac{S_{in}\left(\frac{\mathrm{D}S_{nj}}{\mathrm{D}t}\right)\in_{ijm}}{2II_S} \tag{34}$$

The inclusion of streamline curvature correction in the present simulations will be addressed in the section 4.3.

2.5. Baseline (BSL) model

The baseline (BSL) model developed by Menter (1994) is used for determining the characteristic turbulent time-scale (i.e. k and ε in the case of EARSM and just ε in the case of RSM, since k is determined by the Reynolds transport equation). The BSL model takes advantage of the robust and accurate formulation of the Wilcox $k-\omega$ model in the near wall region, and also of the free-stream independence of the $k-\varepsilon$ model in the outer part of the boundary layer. The model is written (Menter 2009)

$$\frac{\mathrm{D}k}{\mathrm{D}t} = \underbrace{\frac{\partial}{\partial x_l}\left(\left[\nu + \underbrace{\frac{\nu_t}{\sigma_k}}_{\substack{\text{turbulent}\\ \text{diffusion}\\ \text{coefficient}}}\right]\frac{\partial k}{\partial x_l}\right)}_{\text{viscous and turbulent diffusion term}} + \tilde{P} - \beta^* k\omega \tag{35}$$

$$\frac{\mathrm{D}\omega}{\mathrm{D}t} = \underbrace{\frac{\partial}{\partial x_l}\left(\left[\nu + \underbrace{\frac{\nu_t}{\sigma_\omega}}_{\substack{\text{turbulent}\\ \text{diffusion}\\ \text{coefficient}}}\right]\frac{\partial \omega}{\partial x_l}\right)}_{\text{viscous and turbulent diffusion term}} + \alpha\frac{\tilde{P}\omega}{k} - \beta\omega^2 + \underbrace{2(1-F_1)\frac{1}{\sigma_{\omega 2}\omega}\frac{\partial k}{\partial x_l}\frac{\partial \omega}{\partial x_l}}_{\text{cross diffusion}} \tag{36}$$

where ν_t is the kinematic eddy viscosity defined from the turbulent-viscosity hypothesis as $\nu_t = -2\left(\overline{u_i' u_j'} - 2/3 k\delta_{ij}\right)\Big/\overline{S}_{ij}$, which can be approximated by $\nu_t = C_\mu k^2 \big/ \varepsilon$ (except close to the wall). $\omega = k/\nu_t = \varepsilon/\left(C_\mu k\right)$ is the specific dissipation, leading to isotropic diffusion coefficients for the turbulence kinetic energy and the dissipation rate. $\tilde{P} = \min\left(P, 10\beta^* k\omega\right)$ is the production obtained with a simple limiter that avoid the excessive generation of turbulence energy in the vicinity of stagnation points. Constant $\beta^* = 0.09$, and constants α, β, σ_k and σ_ω can be computed as $\phi = F_1\phi_1 + (1-F_1)\phi_2$, being ϕ_1 the value of the corresponding constant in Wilcox ω- transport equation ($\alpha_1 = 5/9$, $\beta_1 = 3/40$, $\sigma_{k1} = 2$ and $\sigma_{\omega 1} = 2$) and ϕ_2 the value of the corresponding constant in the transformed ε- transport equation that is obtained by replacing ω in the original ε- transport equation ($\alpha_2 = 0.44$, $\beta_2 = 0.0828$, $\sigma_{k2} = 1$ and $\sigma_{\omega 2} = 0.856$). The blending function F_1, which takes the value 1 near the walls and 0 far from them, is defined as:

$$F_1 = \tanh\left(\arg_1^4\right) \tag{37}$$

$$arg_1 = \min\left[\max\left(\frac{\sqrt{k}}{\beta^*\omega d};\frac{500\nu}{\omega d^2}\right),\frac{4\rho k}{CD_{k\omega}\sigma_{\omega 2}d^2}\right] \tag{38}$$

$$CD_{k\omega} = \max\left(2\rho\frac{1}{\sigma_{\omega 2}\omega}\frac{\partial k}{\partial x_l}\frac{\partial \omega}{\partial x_l},10^{-10}\right) \tag{39}$$

where d is the distance to the closest wall. It is important to mention that both the values of the constants and the blending function were obtained for 2D wall bounded flows; therefore their application to the present tri-dimensional case will be addressed in section 4.1.

3. NUMERICAL SIMULATIONS

Both models RSM and EARSM, using the BSL model, were used to simulate a compound channel flow experiment by Tominaga and Nezu (1991), namely the S-2 case, i.e. relative depth $h/H = 0.5$, where $h = 0.04$ m and $H = 0.08$ m are the flow depth of the floodplain and of the main channel, respectively. The main channel width $b = 0.2$ m and the channel top width $B = 0.4$ m are presented in Fig. 1.

The flow is assumed to be statistically homogeneous in the streamwise direction and is driven by a constant pressure gradient Δp, thus periodic boundary conditions are applied. The length of the domain in streamwise direction is $12H$, which is nearly twice the recommended value of $2\pi H$ for straight smooth channels (Kara et al. 2012). The free surface is treated as a rigid lid where a free slip condition is applied. For the smooth bed, the no-slip wall boundary condition is used. The domain is discretized with uniformly spaced mesh in streamwise direction. In spanwise and in the vertical directions the mesh is refined close to the walls, free surface and transition zone between the main channel and the floodplain. The grid is composed of 200 × 200

× 80 (40) hexahedral elements in *x*, *y* and *z* directions, respectively. The value in parenthesis indicates the number of elements in *z* direction on the floodplain.

To test the validity and influence of the underlying hypotheses of EARSM, several simulations were performed using EARSM with/without diffusion and streamlines curvature corrections and compared to a simulation using RSM. Table 1 presents a resume of the correction coefficients used in all EARSM simulations (all other coefficients were already presented in section 2).

The simulations were stopped when the convergence criteria were met. During the run three velocity components and pressure were monitored using monitor points throughout the computational domain. When the monitored values reached the asymptotic range and kept constant for at least 500 time-steps, and if the RMS (root mean square) normalized values of the equation residuals were below the residual target value of 10^{-7}, then the simulation ended, and the global balances were reported. The simulation is assumed to be converged if the two previous criteria met and if global unbalances are less than 0.01%.

4. RESULTS AND DISCUSSION

4.1. Experimental, RSM and EARSM results

The experimental and numerical Reynolds stress results demonstrate a good agreement (see Fig. 2) and are consistent to what is known from boundary-layer theory, i.e. near the bottom $\overline{u_1'u_1'} > \overline{u_2'u_2'} > \overline{u_3'u_3'}$ and $\overline{u_1'u_3'} > \overline{u_1'u_2'}$, as well as near the lateral walls $\overline{u_1'u_1'} > \overline{u_3'u_3'} > \overline{u_2'u_2'}$ and $\overline{u_1'u_2'} > \overline{u_1'u_3'}$. Despite that, the RSM and non-corrected EARSM (simulation EARSM_1) are unable to reproduce accurately the experimental $\overline{u_1}$ distribution (see Fig. 2), namely the maximum velocity that is located below the free-surface due to the interaction of two secondary cells. The RSM results are slightly better than EARSM_1, i.e. present stronger secondary flows. These results show that the use of ω closure equation (Eq. 36) along with the assumption of

isotropic dissipation rate near the walls has a strong influence on the secondary flow pattern. It should be noticed that the BSL formulation of ω was developed for 2D boundary layers and its validity is questionable in 3D boundary layers, as well as the isotropic assumption (cf. Speziale and Gatski 1997). It is clear that the closure of RSM plays a central role in the prediction of secondary flows, and that although globally the Reynolds stresses results are acceptable; the mean flow field presents the "fingerprint" of poor prediction of the secondary flow generated at the wall regions.

Comparing the RSM and EARSM_1 results also shows non negligible discrepancies in the secondary flow pattern, highlighted by the different curvatures of the $\overline{u_1}$ contours (see Fig. 2). These differences have to be related either to the weak-equilibrium hypothesis (Eqs. 1 and 2) or to the simplifications made in the solution of the explicit algebraic equation (23), which will be addressed in the next sections.

4.2. Budget of Reynolds stresses transport equations

For the primary normal Reynolds stress $\overline{u_1'u_1'}$ (see Fig. 3) there is a high turbulent production (order $O(10^2)$) near the walls that is balanced by both pressure-strain rate correlation and dissipation rate (ε_{ij} in Eq. 5, not shown here). Near the corners there is also a considerable Reynolds stress turbulent transport and viscous diffusion (although with a lower order $O(10)$), which coincides with the region of secondary cells interaction. The secondary normal stresses $\overline{u_2'u_2'}$ and $\overline{u_3'u_3'}$ show a very different budget, being the dissipation rate at the walls (not shown here) mainly balanced by the pressure-strain rate (both of $O(10^2)$), except near the corners and channel centre where turbulent production becomes important (although with a lower order $O(10)$). Also near the corners there is a smaller order turbulent transport and viscous diffusion, which again coincide with the secondary cells interface. The production of $\overline{u_2'u_2'}$ and $\overline{u_3'u_3'}$ has

opposite signs which reflects the anisotropy generated at the corners by the interaction of vertical wall and bottom boundary layers, where $\overline{u_2'u_2'}$ production increases near the vertical walls and channel centre with a correspondent diminution of $\overline{u_3'u_3'}$ production, whereas near the bottom the opposite occurs. The wall-normal Reynolds stresses $\overline{u_1'u_2'}$ (for the vertical walls) and $\overline{u_1'u_3'}$ (for the bottom) present a similar pattern near the wall where they are generated, i.e. the production of $\overline{u_1'u_2'}$ is high near the vertical walls (order $\mathrm{O}(10^2)$) and is balanced by the pressure-strain correlation, whereas the production of $\overline{u_1'u_3'}$ shows the same pattern near the bottom. For both shear stresses, a relevant Reynolds stress turbulent transport and viscous diffusion (although with a lower order $\mathrm{O}(10)$) is observed near the corners.

From what was stated before, it is clear that the production of Reynolds stresses plays an essential role in the secondary flow pattern (as pointed out by Nikora and Roy 2012) and, furthermore, turbulent transport and viscous diffusion become also relevant in the interface region of adjacent secondary cells, making the modelling of this term a key issue. This also indicates that the EARSM hypothesis of negligible anisotropy diffusion is not valid (cf. Grundstam et al. 2006), which will be further investigated in the next section.

The EARSM_1 results show appreciable differences (order $\mathrm{O}(10)$) from those of RSM for all the production terms (see Fig. 4), which influences also the pressure-strain rate correlation terms and in a minor extent the stress turbulent transport and viscous diffusion terms. The major differences occur for the primary normal Reynolds stress $\overline{u_1'u_1'}$ and the wall-normal Reynolds stresses $\overline{u_1'u_2'}$ (for the vertical walls) and $\overline{u_1'u_3'}$ (for the bottom). Namely, the EARSM_1 predicts higher primary normal and lower wall-normal Reynolds stresses production near the wall corners, which will have influence on the turbulence anisotropy, and consequently on the secondary flow pattern. This different distribution between normal ($\overline{u_1'u_1'}$ and $\overline{u_2'u_2'}$) and wall-

normal Reynolds stresses ($\overline{u_1' u_2'}$) is also observed in the channel centre, where two secondary cells interact. These results highlight a different budget of Reynolds stress transport equation between RSM and EARSM.

4.3. Budget of anisotropy tensor transport equations (diffusion and streamline curvature corrections)

The RSM results (Fig. 5) show that the convection of anisotropy has a lower order ($\mathrm{O}(1)$) than the other terms in the anisotropy tensor transport equation (12). The turbulent production and viscous dissipation contribution from TKE is also small and only has relevance (order $\mathrm{O}(10)$) near the bottom corners. The diffusion term (order $\mathrm{O}(10)$) is the only term that can compare with the magnitude of the other terms that are common in equation (5) and can be seen in Fig. 3, namely the Reynolds stresses production (order $\mathrm{O}(10)$ for the P_{22} and P_{33} components and $\mathrm{O}(10^2)$ for the other components), pressure-strain rate (order $\mathrm{O}(10^2)$) and viscous dissipation terms (order $\mathrm{O}(10^2)$). These results highlight that, for the present simulations, neglecting the anisotropy convection (Eq. 1) is a valid approach, whereas discarding the anisotropy diffusion (Eq. 2) is not valid, since its value is especially high near the corners and non-negligible through the entire cross-section. This conclusion is in line with what was stated by Taulbee (1992) and Qiu et al. (2008). These authors point out to the important role of diffusion in the near-wall region where the ratio P/ε is small, as can be seen in the change of sign of the turbulent production and viscous dissipation contribution from TKE in Fig. 5.

Furthermore, the relevance of the diffusion terms can, along with the closure for the pressure-strain rate correlation and the dissipation rate, also explain the failure of RSM in accurately reproducing the secondary flow observed experimentally (see Fig. 2). Although is commonly

assumed by practitioners that the modelling of this term is not relevant (e.g. Pope 2000), it seems that it becomes important when secondary flow exists. For rotating pipe flow, Grundestam et al. (2006) refers the importance of choosing a Daly-Harlow type of diffusion modelling, instead of the simpler gradient-diffusion model used here (Eq. 8).

The effect of the EARSM diffusion correction (see section 2.3) can be observed in Fig. 6, where the EARSM_2 results for a constant $C_{Diff} = 10$ (see Eq. 30) are presented. An exceptionally high value, compared to the $C_{Diff} = 2.2$ proposed by Wallin and Johansson (2000), was used, since that value did not produce the required diffusion correction, resulting in an artificially increased effective eddy viscosity. Comparing the results of the corrected EARSM_2 diffusion terms in Fig. 6 with the ones for RSM (see Fig. 5), it can be concluded that both models present similar patterns of anisotropy diffusion, although the magnitudes are higher for the RSM. The diffusion correction increases the secondary flow, being the maximum streamwise velocity region reduced in the centre of the main channel (corrected EARSM_2 in Fig. 6(f) and non-corrected EARSM_1 in Fig. 2(c)). Nevertheless, the correction is unable to reproduce the $\overline{u_1}$ contours inflection observed in RSM at the centre of the main channel (see Fig. 2(b)). Resuming the diffusion correction with an exceptionally high constant improves the ERASM results but fails to reproduce the RSM ones.

Since high streamline curvatures are present in the flow, it is important to evaluate its correction (see section 2.4) in the EARSM results. For that purpose a simulation EARSM_3 with streamline curvature correction (Eq. 32) was performed. The value of coefficient $A_0 = -0.72$ used in this study differs from the one presented in Eq. (16), since the introduction of the correction implies a change of this coefficient (cf. Wallin and Johansson 2002). The diffusion terms for the corrected EARSM_3 (see Fig. 7) show a similar pattern when compared with RSM (see Fig. 2) and EARSM_2 with diffusion correction (see Fig. 6), although their magnitude is smaller than in the latter ones. In fact, there are no visible differences between the

secondary flow of the corrected EARSM_3 (Fig. 7(f)) and non-corrected EARSM_1 (Fig. 2(c)). Therefore, it can be concluded that for the present flow, contrary to flows in rotating frames, the diffusion correction is more relevant than the streamline curvature correction.

4.4. Approximations included in EARSM

In section 2.2 it was mentioned that the explicit polynomial in CFX is an approximation of the exact explicit polynomial of Wallin and Johansson (2000). In Fig.8 are presented the relative errors (defined as $RE_{a_{ij}} = 100\left(a_{ij}^{CFX} - a_{ij}^{WJ}\right)/a_{ij}^{WJ}$, see Eqs. 20 and 23, with S_{ij} and Ω_{ij} given by the non-corrected EARSM_1 simulation) of the anisotropy tensor computed by both polynomials. The results show that there are significant differences (order of ± 50%). The differences are more important in the regions of interest for the normal components, i.e. the lateral walls for a_{22}, the channel bottom for a_{33}. Whereas, the differences in the cross components a_{12}, a_{13} and a_{23}, are higher in regions where there absolute value is low. In fact, neglecting the β_9^{WJ} term from Eq. (20), which only affects the cross components, gives errors below 5%, which highlights that the major source of error is the use of the two-dimensional value for β_4^{CFX} near the walls where three-dimensional effects influence the anisotropy generation. This means that the missing term (Eq. 26) in Eq. (23) is not negligible and the three-dimensional value β_4^{WJ} should be used.

The validity of the approximation made on parameter N, by using the solution of the cubic equation obtained for two-dimensional flows (see Eqs. 27-29), is evaluated by comparing the exact value N (Eq. 18) with the approximated value N^{ap} (Eq. 27), both computed with non-corrected EARSM_1 results. The N relative error, defined as $RE_N = 100\left(N^{ap} - N\right)/N$ (not presented here) shows higher values in the regions where secondary cells interact, but with

order of 5%. Therefore it can be assumed that the N approximation gives reasonably good results.

5. CONCLUSIONS

Regarding the use of Reynolds stress models (RSM and EARSM) in the simulation of open-channel flows with strong secondary currents (case of a compound channel with high relative depth), the following conclusion can be drawn:

- Both RSM and EARSM fail to reproduce accurately the experimental secondary flow. This can be attributed to the near-wall treatment (ω closure equation), to the adopted pressure-strain rate correlation model, to the isotropic dissipation rate assumption and to the diffusion terms modelling.
- RSM presents better results than EARSM, which is due to the non-negligible effect of diffusion terms near the interface region of adjacent secondary cells.
- The budget of Reynolds stresses transport equations highlights the important role of production terms in the secondary flow pattern, being those terms linked to non-negligible diffusion terms in the budget of anisotropy tensor transport equations. Since, anisotropy diffusion terms are ignored in EARSM, this results in different budgets between RSM and EARSM.
- Contrary to what is known for flows in rotating frames, the anisotropy convection weak-equilibrium hypothesis (Eq. 1) is valid for the flow studied, whereas discarding the anisotropy diffusion (Eq. 2) is not valid, since its value is especially high near the corners and non-negligible through the entire cross-section.
- The diffusion correction developed for rotating frames improved the EARSM results, but even with a high coefficient it fails to reproduce the RSM ones.

- The streamline curvature correction did not produce significant improvements on the EARSM results.
- The two-dimensional approximations assumed in the EARSM explicit polynomial revealed significant errors when compared with the three-dimensional approximation used by Wallin and Johansson (2000), especially the β_4 term.

Resuming, although the EARSM seems an attractive model, due to its lower computational effort, it is not able to accurately simulate Prandtl's second kind secondary flow due to the importance of the anisotropy diffusion terms. Available corrections for these terms did not produce the required results. Moreover, the diffusion modelling should also be an issue to take into account when using the more complex RSM.

ACKNOWLEDGMENTS

This work was partially funded by FEDER, program COMPETE, and by national funds through Portuguese Foundation for Science and Technology (FCT) projects PTDC/ECM/117660/2010 and RECI/ECM-HID/0371/2012. The first author wishes also to acknowledge the financial support of the Portuguese Foundation for Science and Technology through the Grant No. SFRH/BD/64337/2009.

REFERENCES

Apsley D, Leschziner M (1998). A new low-Reynolds number nonlinear two-equation turbulence model for complex flows. *International Journal of Heat and Fluid Flow* 19: 209-222.

Banerjee S, Ertunç Ö, Köksoy Ç, Durst F (2009). Pressure strain rate modeling of homogeneous axisymmetric turbulence. *Journal of Turbulence* 10(29): 1-39.

Bradshaw P (1987). Turbulent secondary flows. *Annual Review of Fluid Mechanics* 19: 53-74.

Filonovich MS, Azevedo R, Rojas-Solórzano L, Leal, JB (2013). Credibility Analysis of Computational Fluid Dynamic Simulations for Compound Channel Flow. *Journal of Hydroinformatics* 15(3): 926-938.

Franke M, Wallin S, Thiele F (2005). Assessment of explicit algebraic Reynolds-stress turbulence models in aerodynamic computations. *Aerospace Science and Technology* 9(7): 573-581.

Frewer M (2009). More clarity on the concept of material frame-indifference in classical continuum mechanics. *Acta Mechanica* 202: 213-246.

Gatski TB, Jongen T (2000). Nonlinear eddy viscosity and algebraic stress models for solving complex turbulent flows. *Progress in Aerospace Sciences* 36: 655-682.

Gatski TB, Speziale CG (1993). On explicit algebraic stress models for complex turbulent flows. *Journal of Fluid Mechanics* 254: 59-78.

Gatski TB, Wallin S (2004). Extending the weak-equilibrium condition for algebraic Reynolds stress models to rotating and curved flows. *Journal of Fluid Mechanics* 518: 147-155.

Girimaji SS (1997). A galilean invariant explicit algebraic Reynolds stress model for turbulent curved flows. *Physics in Fluids* 9: 1067-1077.

Grundestam O, Wallin S, Johansson AV (2006). Observations on the predictions of fully developed rotating pipe flow using differential and explicit algebraic Reynolds stress models. *European Journal of Mechanics - B/Fluids* 25(1): 95-112.

Hamba F (2006). Euclidian invariance and weak-equilibrium condition for the algebraic Reynolds stress model. *Journal of Fluid Mechanics* 569: 399-408.

Hanjalić K (1999). Second-Moment Turbulence Closures for CFD: Needs and Prospects. *International Journal of Computational Fluid Dynamics* 12(1): 67-97.

Hellsten A (2004). New two-equation turbulence model for aerodynamics applications. *PHD Thesis*. Helsinki University of Technology, Espoo, Finland, ISBN 951-22-6933-3.

Hellsten A, Wallin S (2009). Explicit algebraic Reynolds stress and non-linear eddy-viscosity Models. *International Journal of Computational Fluid Dynamics* 23(4): 349-361.

Jakirlić S, Hanjalić K (2002). A new approach to modelling near-wall turbulence energy and stress dissipation. *Journal of Fluid Mechanics* 459: 139-166.

Kara S, Stoesser T, Sturm TW (2012). Turbulence statistics in compound channels with deep and shallow overbank flows. *Journal of Hydraulic Research* 50(5): 482-493.

Knight D, Omran M, Tang X (2007). Modeling Depth-Averaged Velocity and Boundary Shear in Trapezoidal Channels with Secondary Flows. *Journal of Hydraulic Engineering* 133(1): 39-47.

Launder BE, Reece GJ, Rodi W (1975). Progress in the development of a Reynolds stress turbulence closure. *Journal of Fluid Mechanics* 68: 537-566.

Menter FR (2011). Turbulence Modeling for Engineering Flows. *Technical paper from ANSYS*, Inc.: 1-25.

Menter FR (2009). Review of the shear-stress transport turbulence model experience from an industrial perspective. *International Journal of Computational Fluid Dynamics* 23(4): 305-316.

Menter FR (1994). Two-equation eddy-viscosity turbulence models for engineering applications. *AIAA Journal* 32(8): 1598-1605.

Naji H, Mompean G, El Yahyaoui O (2004). Evaluation of explicit algebraic stress models using direct numerical simulations. *Journal of Turbulence* 5(38): 1-25.

Nezu I, Nakagawa H (1993). *Turbulence in open-channel flows*. IAHR-Monograph, Balkema, Rotterdam, The Netherlands.

Nikora V, Roy AG (2012). Secondary flows in rivers: Theoretical framework, recent advances, and current challenges. *Gravel-bed Rivers: Processes, Tools, Environments*. M. Church, P.M. Biron, A.G. Roy, eds. John Wiley & Sons, USA, 3-22.

Pope SB (2000). *Turbulent Flows*, 1st Edition, Cambridge University Press.

Qiu J-F, Obi S, Gatski TB (2008). On the weak-equilibrium condition for derivation of algebraic heat flux model. *International Journal of Heat and Fluid Flow* 29: 1628-1637.

Rodi W (1976). A new algebraic relation for calculating the Reynolds stresses. *Zeitschrift fuer angewandte Mathematik und Mechanik* 56: 219-221.

Shafi HS, Antonia RA (1995). Anisotropy of the Reynolds stresses in a turbulent boundary layer on a rough wall. *Experiments in Fluids* 18(3): 213-215.

Shir CC (1973). A preliminary study of atmospheric turbulent flow in idealized planetary boundary layer. *Journal Atmospheric Science* 30: 1327-1339.

Spalart PR, Shur M (1997). On the sensitization of turbulence models to rotation and curvature. *Aerospace Science and Technology* 1(5): 297-302.

Speziale CG (1998). A review of material frame-indifference in mechanics. *Applied Mechanics Reviews* 51(8): 489-504.

Speziale CG (1991). Analytical methods for the development of Reynolds stress closures in turbulence. *Annual Review of Fluid Mechanics* 23: 107-157.

Speziale CG, Gatski TB (1997). Analysis and modelling of anisotropies in the dissipation rate of turbulence. *Journal Fluid Mechanics* 344: 155-180.

Taulbee DB (1992). An improved algebraic Reynolds stress model and corresponding nonlinear stress model. *Physics of Fluids A* 4(11): 2555-2560.

Thomson RL, Mompean G (2010). An alternative assessment of weak-equilibrium conditions in turbulent closure modeling. *International Journal of Engineering Science* 48(11): 1633-1640.

Tominaga A, Nezu I (1991). Turbulent structure in compound open-channel flows. *Journal of Hydraulic Engineering* 117(1): 21-41.

Wallin S, Johansson AV (2002). Modeling streamline curvature effects in explicit algebraic Reynolds stress turbulence models. *International Journal of Heat and Fluid Flow* 23: 721-730.

Wallin S, Johansson AV (2000). An explicit algebraic Reynolds stress model for incompressible and compressible turbulent flows. *Journal of Fluid Mechanics* 403: 89-132.

Weis J, Hutter K (2003). On Euclidean invariance of algebraic Reynolds stress models in turbulence. *Journal of Fluid Mechanics* 476: 63-68.

FIGURES CAPTIONS

Fig. 1 Scheme of the computational domain.

Fig. 2 Time-averaged streamwise velocity and Reynolds stresses contours for experimental, RSM and EARSM_1.

Fig. 3 Contours of Reynolds stress turbulent transport and viscous diffusion (D_{ij} in Eq. 5), and turbulent production (P_{ij} in Eq. 5), and pressure-strain rate correlation (Π_{ij} in Eq. 5) for RSM.

Fig. 4 Contours of Reynolds stress turbulent transport and viscous diffusion (D_{ij} in Eq. 5), turbulent production (P_{ij} in Eq. 5) and pressure-strain rate correlation (Π_{ij} in Eq. 5) for RSM minus EARSM_1.

Fig. 5 Contours of anisotropy convection ($conv_{ij} = k\left(\mathrm{D}a_{ij}/\mathrm{D}t\right)$ in Eq. 12), diffusion ($diff_{ij} = D_{ij} - \overline{u_i'u_j'}\,D/k$ in Eq. 12) and turbulent production and viscous dissipation contribution from TKE ($TKE_{contr\,ij} = -\overline{u_i'u_j'}\left(P-\varepsilon\right)/k$ in Eq. 12) for RSM.

Fig. 6 Contours of anisotropy diffusion ($diff_{ij} = D_{ij} - \overline{u_i'u_j'}\,D/k$ in Eq. 12) and of time-averaged streamwise velocity for EARSM_2 (diffusion correction with $C_{Diff} = 10$, Eq. 30).

Fig. 7 Contours of anisotropy diffusion ($diff_{ij} = D_{ij} - \overline{u_i'u_j'}\,D/k$ in Eq. 12) and of time-averaged streamwise velocity for EARSM_3 (streamline curvature correction $A_0 = -0.72$, Eq. 32).

Fig. 8 Contours of relative errors $RE_{a_{ij}} = 100\left(a_{ij}^{CFX} - a_{ij}^{WJ}\right)/a_{ij}^{WJ}$ between anisotropy tensor using CFX explicit polynomial (Eq. 23) and using Wallin and Johansson (2000) polynomial Eq. (20), using non-corrected EARSM_1 results.

TABLES

Table 1 Simulations performed with and without diffusion and streamlines curvature corrections.

SIMULATION	Diffusion correction		Streamlines curvature correction		
	Status	Eq. (31)	Status	Eq. (32)	
		C_{Diff}		C_{scale}	A_0
EARSM_1	No	-	No	0	-
EARSM_2	Yes	10	No	0	-
EARSM_3	No	-	Yes	1	-0.72

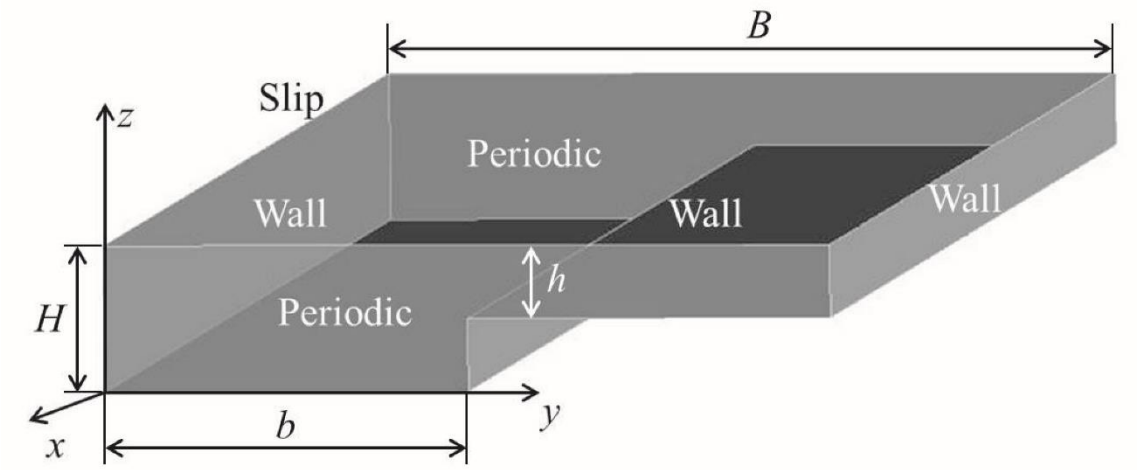

Fig. 1 Scheme of the computational domain.

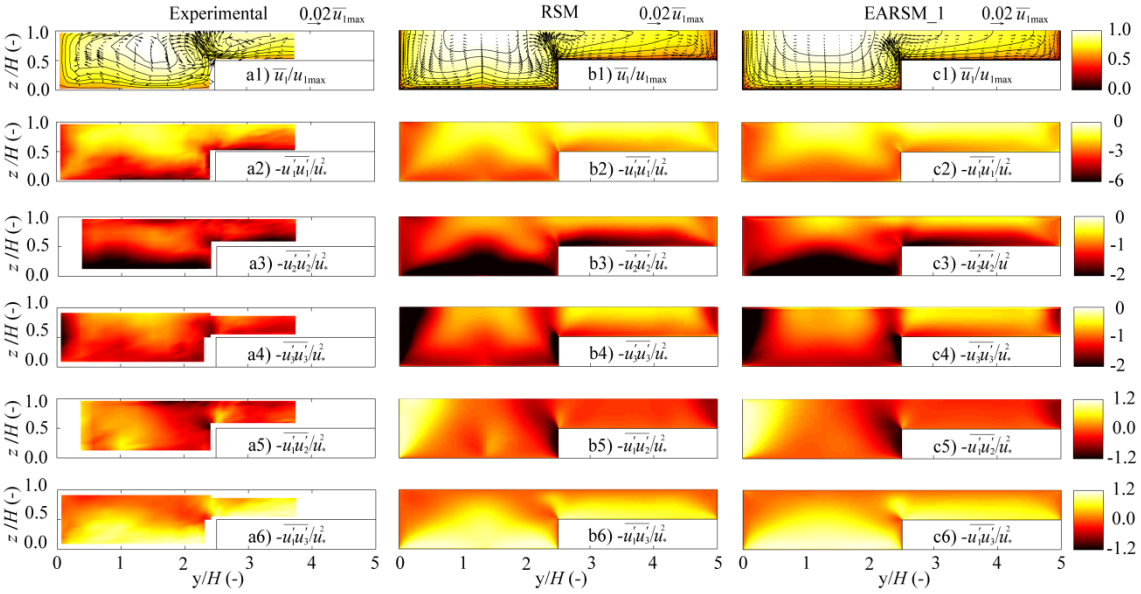

Fig. 2 Time-averaged streamwise velocity and Reynolds stresses contours for experimental, RSM and EARSM_1.

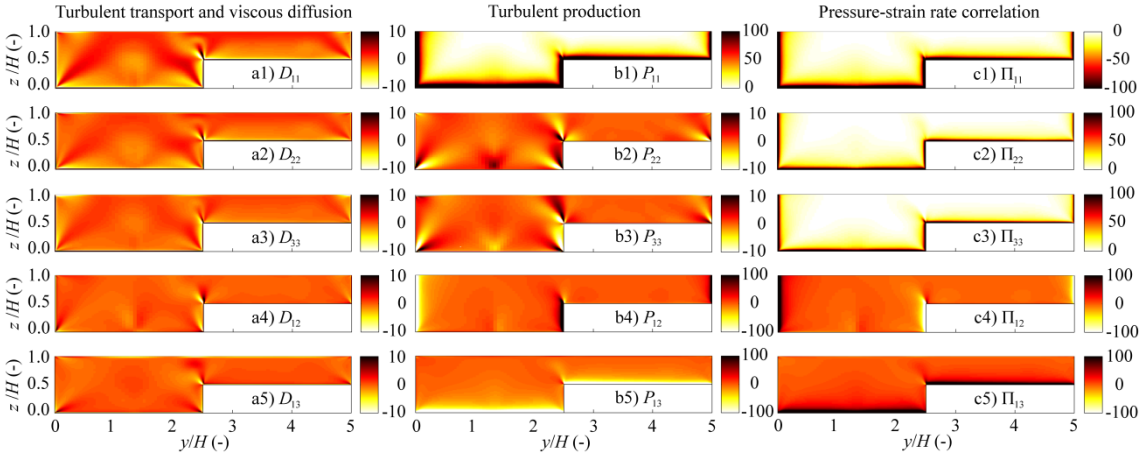

Fig. 3 Contours of Reynolds stress turbulent transport and viscous diffusion (D_{ij} in Eq. 5), and turbulent production (P_{ij} in Eq. 5), and pressure-strain rate correlation (Π_{ij} in Eq. 5) for RSM.

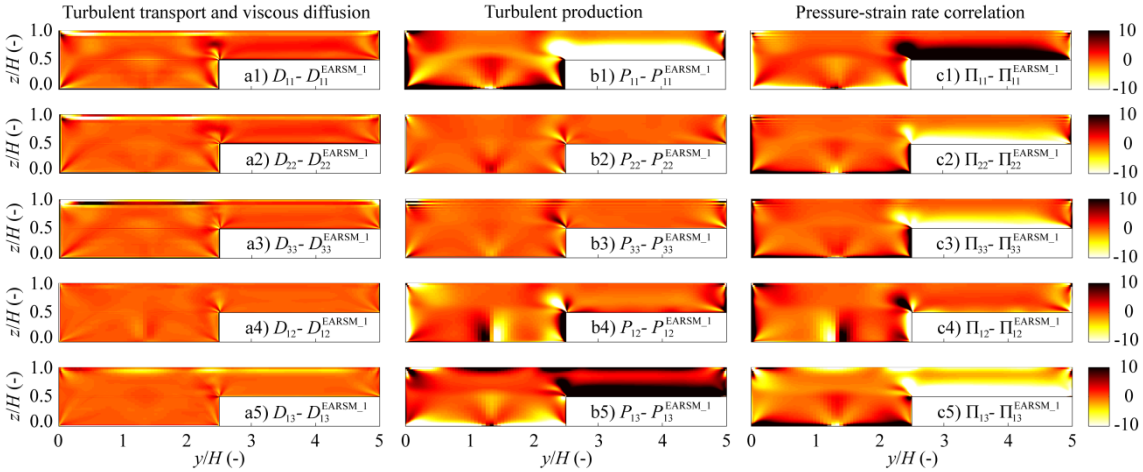

Fig. 4 Contours of Reynolds stress turbulent transport and viscous diffusion (D_{ij} in Eq. 5), turbulent production (P_{ij} in Eq. 5) and pressure-strain rate correlation (Π_{ij} in Eq. 5) for RSM minus EARSM_1.

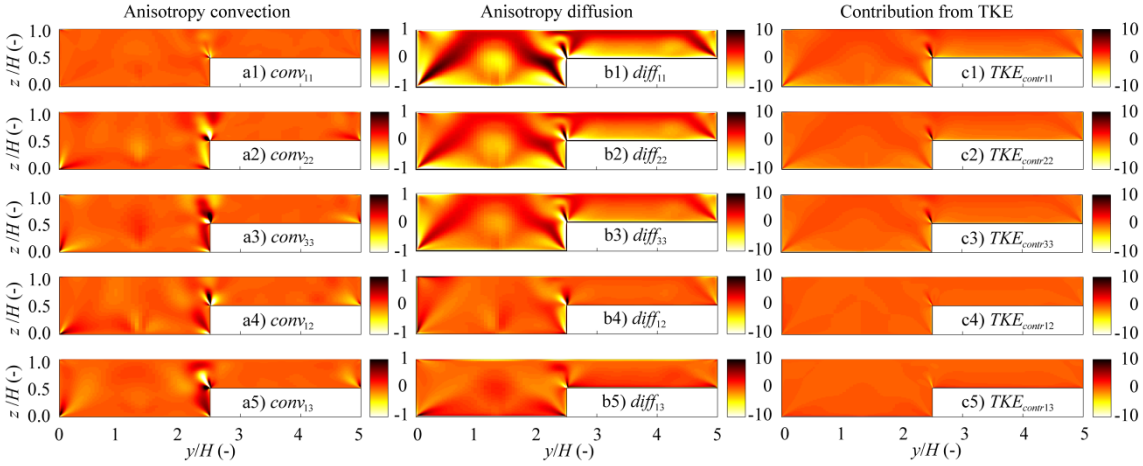

Fig. 5 Contours of anisotropy convection ($conv_{ij} = k\left(\mathrm{D}a_{ij}/\mathrm{D}t\right)$ in Eq. 12), diffusion ($diff_{ij} = D_{ij} - \overline{u_i'u_j'}\,D/k$ in Eq. 12) and turbulent production and viscous dissipation contribution from TKE ($TKE_{contr\,ij} = -\overline{u_i'u_j'}\left(P-\varepsilon\right)/k$ in Eq. 12) for RSM.

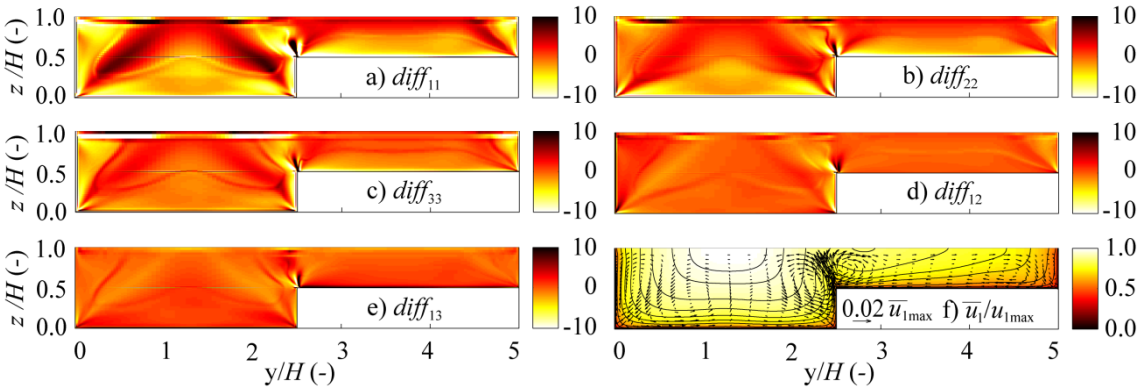

Fig. 6 Contours of anisotropy diffusion ($diff_{ij} = D_{ij} - \overline{u_i' u_j'}\, D/k$ in Eq. 12) and of time-averaged streamwise velocity for EARSM_2 (diffusion correction with $C_{Diff} = 10$, Eq. 30).

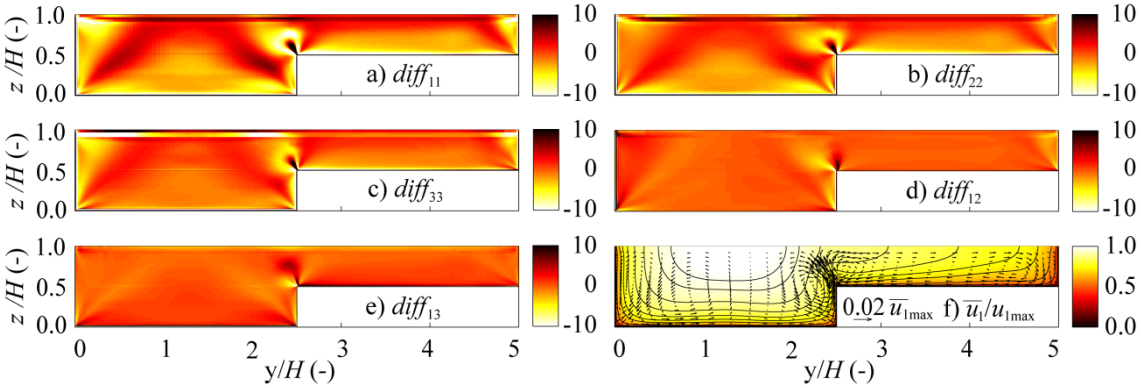

Fig. 7 Contours of anisotropy diffusion ($diff_{ij} = D_{ij} - \overline{u_i' u_j'}\, D/k$ in Eq. 12) and of time-averaged streamwise velocity for EARSM_3 (streamline curvature correction $A_0 = -0.72$, Eq. 32).

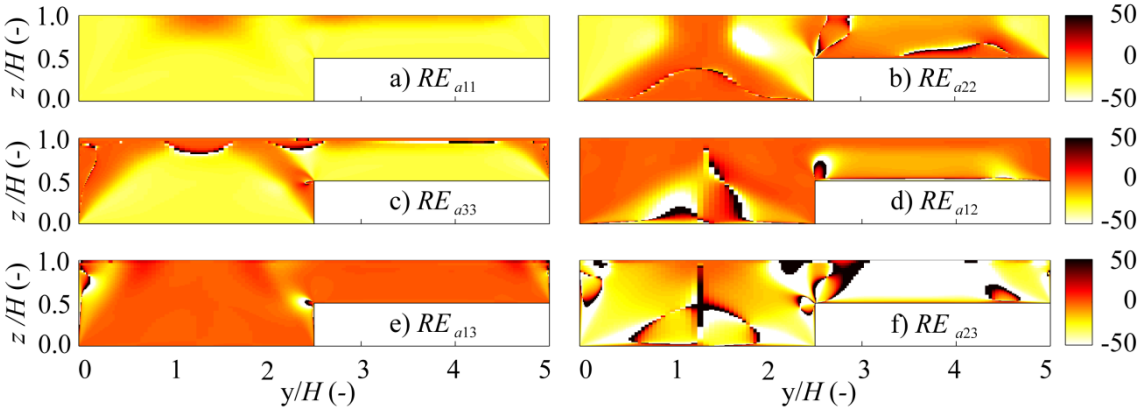

Fig. 8 Contours of relative errors $RE_{a_{ij}} = 100\left(a_{ij}^{CFX} - a_{ij}^{WJ}\right)/a_{ij}^{WJ}$ between anisotropy tensor using CFX explicit polynomial (Eq. 23) and using Wallin and Johansson (2000) polynomial Eq. (20), using non-corrected EARSM_1 results.